Physical Sciences and Technology

SCOPE AND AIM

Physical Sciences and Technology provides an original paperback for the publication of peerreviewed research and review articles in all fields of Physics and related Technology. The topics, included in the scope, especially emphasize understanding of the physics underlying modern technology.

Subject areas may include, but are not limited to the following fields: Astronomy and Space Research, Theoretical Physics and Astrophysics, Plasma Physics and Related Technology, Chemical Physics and Related Technology, Condensed Matter Physics and Related Technology, Thermal physics and Related Technology, Nuclear Physics and Related Technology, Nanomaterials and Nanotechnology, Applied Atomic and Molecular Physics, Material Sciences and Related Technology, Electronics and Related Technology, Instrumentation, Photonics and Quantum Electronics, Signal processing.

The Journal is issued under the auspices of the National Nanotechnological Laboratory of Open Type and Institute of Experimental and Theoretical Physics and is published two times a year by the «Kazakh University» Publishing House. The International Editorial Board of the Journal consists of leading researchers from different countries of the world. The Journal is wide open for contributions that both lie at the far frontiers of contemporary physics and are particularly aimed at applications of the scientific principles of physics to modern technological problems.

Revealing the noctilucent cloud fields structure
by software processing of satellite images

A.A. Solodovnik (ID) , R.A. Kleksin (ID) , P.I. Leontyev (ID) ,

B.M. Useinov* (ID) , A.G. Markova (ID) and S.A. Kassimova (ID)

M. Kozybayev North Kazakhstan University, Petropavlovsk, Kazakhstan
*e-mail: buseinov@gmail.com

Noctilucent clouds, which form during the summer months primarily over the polar regions, are also frequently observed at temperate latitudes. These regions play a key role in shaping the total area and spatial configuration of mesospheric cloud fields. As shown in previous studies, the seasonal and interseasonal evolution of these fields is largely influenced by meteorological processes in the mesosphere, though the role of geophysical fields is also considered. This work describes the development of a methodology that enables a shift from studying the integral characteristics of noctilucent clouds to analyzing their differential properties. At the initial stage, the goal is to investigate the presence of longitudinal structure by dividing satellite images of noctilucent cloud fields into 30-degree longitudinal sectors and calculating the cloud area within each. Achieving this requires the creation of specialized software, and a significant portion of the study is devoted to describing the algorithm design, programming language selection, and implementation process. The performance of the new software is compared with existing approaches, demonstrating that the developed method provides substantially improved accuracy in detecting longitudinal inhomogeneities in the global distribution of noctilucent clouds.

Key words: noctilucent clouds, digital images, longitudinal cloud structure, hydrometeorology, hydroclimatology, cloud physics and chemistry.
PACS number(s): 92.60.H-; 96.12. Jt; 95.85.-e.

1 Introduction

Although noctilucent clouds (NLC are studied across several scientific disciplines, they are of particular interest to astronomy and geophysics. This interest was initially sparked by their discovery and has since grown, especially in the context of atmospheric physics and comparative planetology.

These cloud formations are located in the mesosphere at altitudes of about 80 km, where moisture levels are extremely low, making them largely irrelevant for traditional meteorological studies. At the same time, the seasonality of their appearance, associated with a change in the nature of atmospheric circulation, the effectiveness of the influence of cosmic factors on the highest layers of the atmosphere and, finally, the presence of similar cloud formations in the atmospheres of other planets, are attractive to specialists in the field of upper atmosphere physics, climatology, planetology [1-4].

The unique conditions for observing NLC in the twilight sky and the seasonality of their appearance determined the methods for studying these objects. Their high-altitude location makes conventional meteorological tools such as balloon or aerial sounding ineffective. As a result, most scientific data on NLCs have been obtained through remote sensing techniques, including both ground-based and satellite observations. Space-based monitoring, unaffected by weather conditions, offers a far greater volume of data than ground-based methods. One of the most successful missions for investigating the nature of NLCs has been the operation of the AIM (Aeronomy of Ice in the Mesosphere) satellite [5]. Many of the measurement results collected during this mission are publicly available and provide valuable insights into the genesis and evolution of noctilucent clouds.

In our study, the objective was to investigate the spatial structure of global noctilucent cloud (NLC) fields, with a particular focus on determining whether

these cloud formations exhibit longitudinal symmetry or contain significant inhomogeneities.

2 The influence of meteorological factors on the state of noctilucent clouds fields

By now, there is a fairly accurate picture of the seasonal occurrence description of the mesospheric cloud fields. This picture is based on the change in the nature of atmospheric circulation at the heights of the mesosphere and stratosphere during the «winter-summer» transition. The main role is played by the ascending flows of air masses, leading to a significant decrease in temperatures in the upper part of the mesosphere in summer. In this case, water vapor in the mesosphere becomes supersaturated and condensation occurs. Taking into account the fact that these processes are characteristic for subpolar latitudes, the annual formation of the polar mesospheric clouds "caps" in the summer seasons should be associated with them [6 – 8].

However, in the summer seasons, NLC are also observed in temperate latitudes. It is not at all necessary that their appearance is associated only with the drift (advection) of mesospheric cloud formations in the meridional direction. The appearance of NLC in temperate latitudes is also explained by the influence on the temperature regime of the mesosphere of internal gravity waves (IGW) – density waves propagating in horizontal and vertical directions. An adiabatic decrease in the temperature of the mesosphere at the crests of such waves contributes to the condensation of water vapor and the formation of high-altitude clouds [9 – 11].

The source of IGW can be various processes associated with large-scale energy release, but most likely they owe their origin to meteorological processes in the troposphere – the movement of atmospheric vortices and fronts, occlusions, orographic effects. Currently, the study of the influence of IGW on the genesis and evolution of NLC fields reveals its high relevance [12].

Of course, considering the evolution of NLC fields, it is impossible to exclude from consideration the influence of the water vapor inflow processes into the mesosphere. But general research in this direction is hampered by the lack of accurate data on the content of water vapor both at different height levels and at different latitudes and longitudes in the upper atmosphere.

Recent (2018) studies [13-14] show that NLC fields may be associated with climate change, and, specifically, with an increase in the amount of green-

house gases in the atmosphere. Large-scale atmospheric processes, such as increases in ocean surface temperatures or changes in air circulation patterns, can lead to changes in the distribution and intensity of NLC. The results of research in this area are quite unexpected and clearly demonstrate the lack of the process and consequences understanding of climate change in the last few centuries, creating another relevant area for research.

Thus, large-scale atmospheric processes play a significant role in the formation and development of NLC fields. Research in this area helps to better understand atmospheric interactions and their influence on climate processes. However, to conduct such research it is necessary to obtain data in a convenient for study format (mainly comparative). To obtain such data, we can use the method of synthetic mapping. This method is based on the analysis of data obtained from spacecraft and allows you to create maps that reflect the distribution of NLC at various latitudes and longitudes. This method also makes it possible to more accurately monitor changes in cloud distribution dynamics and identify possible trends.

Synthetic map is a map that provides an integral image of an object or phenomenon in unified synthetic indicators [15]. In our case, synthetic maps are a combination of photographic observations along a separate orbit of the spacecraft as shown in figure 3.

3 Methods for studying tropospheric-mesospheric relations

The methodology of studying the influence of tropospheric processes on the evolution of NLC in temperate latitudes has proved to be extremely productive. This approach is based on a cartographic analysis of data on the daily dynamics of NLC in the northern hemisphere, correlated to the maximum extent with data on meteorological phenomena occurring at the same time [16-19]. When constructing images of the NLC field, data from the AIM mission was used [5], while meteorological information was received from relevant sources. The analysis of such maps has shown that in most cases there is a relation between the nature of the meteorological events development in the troposphere and the formation of the NLC field features. The main factors influencing mesospheric processes are the following: the movement of cyclones in the zonal direction with the intersection of the Ural Mountains, the meridional (from north to south) movement of cyclones, the development of occlusions and thunderstorm foci, as well as the oncoming movement of atmospheric fronts.

These processes are effective sources of density waves (IGW) that reach the mesosphere and influence the temperature regime at significant heights.
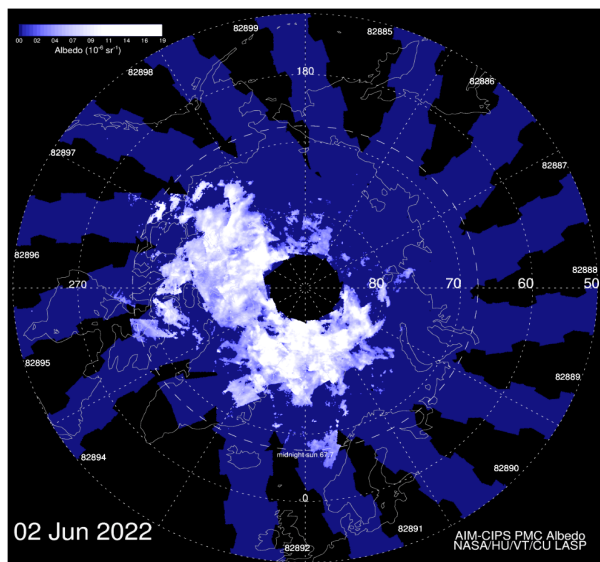

Figure 1 – Synthetic map of noctilucent cloud fields
in the northern hemisphere
obtained by the AIM satellite.

On the other hand, the analysis of the tropospheric processes effect on NLC generation included a study of the temperature regime effect in Antarctica on the formation of mesospheric clouds in the southern hemisphere. In this context, high correlations were found between temperature changes in the South Pole region and changes in the total area of the NLC field [20]. A special feature here is the detected characteristic time lag between these two parameters, the graph showing this correlation is given in figure 2 [14].

Shown results are surface area of the noctilucent clouds for the southern hemisphere (red) and average daily temperatures of the South Pole (blue) for two seasons. Here it is important to note the climatic feature of Antarctica, where temperature changes in the pole region essentially reflect changes in the average temperature for the entire continent. When studying the relationship between temperature changes and changes in the area of the NLC field in the North Pole region, it is necessary to move from determining the general characteristics of the NLC field to a differential representation, that is, to studying the longitude distribution of mesospheric clouds. But this requires the development of a new software package and processing of a large array of images with its help.
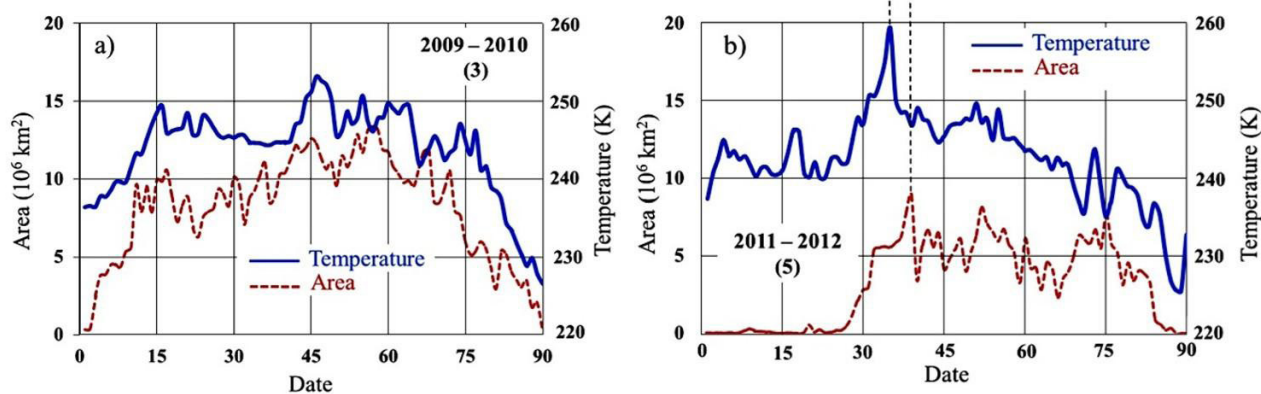
Figure 2 – Seasonal changes in the NLC field area.

4 Structure and algorithm of the satellite image processing program

To develop the program, the high-level, object-oriented, multi-paradigm programming language *Python* was chosen. In the context of the problem being solved, its main advantage was its modularity, which allows, using the simplest commands within the environment and the compiler, to integrate specialized code libraries into the created program. The free *PyCharm Community Edition*, which has a large list of tips and built-in documentation for the language, was used as a compiler. The development environment is made virtual using the *Anaconda* distribution for ease of handling libraries. The program must meet the following requirements: the ability to work

with an entire array at once, dividing each image in the array into 12 sectors of 30 degrees, calculating the area of the NLC in each of them and saving the result in an Excel table. This functionality allows you to reduce the time for obtaining data necessary for analyzing the development of an object.

Each image is accompanied by a file with data encoded in it, including the area in each pixel. This is necessary to convert the results of the program. The document file is in IDL dataset format. To extract this data, you will need a separate IDL reader program. Since the data of the entire dataset is not needed, it is advisable to create a compact version of the IDL reader that reads only the indicator that interests us. In figure 3 the code of such reader is presented.

```
1   from netCOF4 import Dataset
2
3   # Specify the data array
4   nc_file = Dataset('cips_sci_3a_2020-153_v05.20_r05.nc', 'r')
5   # Specify the required variable
6   data_varlablel = nc_flie.variables['KM_PER_PIXEL'][:]
7   # Output the result to the compiler console
8   print("km per pixel", data_varlablel)
9   # Close file
10  nc_file.close()
```

Figure 3 – Algorithm for converting cloud image elements into
the format required for software processing.

If necessary, you can always increase the number of variables extracted from the array at a time by adding *Python* variables: *data_variable2, data_variable3, data_variable4*, etc. After that, having received the names of the necessary variables from the AIM website (or another source), to indicate for each the correspondence with the contents of the array. If you use the latest version of the data (they are always available), the desired variable does not change, and you can then use it in all calculations.

To check the effectiveness of the developed software package, a control image was created and is shown in figure 4, the required information on which is easily accessible for direct calculation.

The image is represented by a background on which a white square of 100 by 100 pixels is placed. The area of this object is precisely calculated: 10,000 pixels are multiplied by 7.5 sq. km/pixel, which gives a result of 75 thousand sq. km. To eliminate the influence of the background, a complex method was chosen: a combination of threshold filtering, background subtraction and zones of interest.
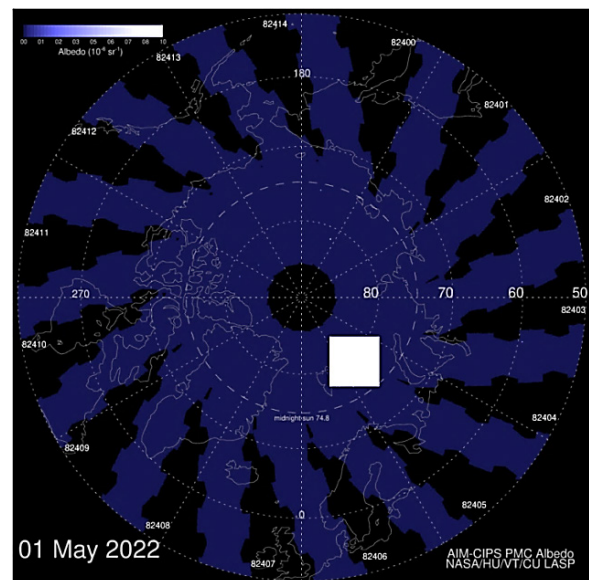

Figure 4 – An image of the circumpolar region with a
background. The area is highlighted
with a square to control the accuracy.

5 Description of the algorithm and logic of individual solutions

To perform the assigned tasks, specialized libraries were selected and are listed below.

OpenCV (cv2): used for reading, processing and analyzing images using a wide range of methods.

NumPy: used for introducing advanced mathematical operations and working with arrays into code.

- *Pandas*: provides data structuring and tools for their analysis. Responsible for exporting to Excel.

- *Tkinter*: serves to create a graphical interface allowing the user to select directories.

- *MatPlotLib*: allows you to demonstrate *cv2* and *numpy* operations; it was used for calibration and adjustment.

- *Os*: a helper library used to interact with a computer's file system.

Then the program algorithm was set up, as shown further.

1. Setting up GUI for directory selection: *Tkinter* is used to create an interface through which the user can select a directory of images for analysis.

2. Reading the image: using *OpenCV*, the program reads images from the selected directory, then *os* indexes and sorts them.

3. Binarization: OpenCV converts images into matrix form and applies threshold filtering.

4. Background subtraction: the absolute difference between the "background" matrix and the target image matrix is calculated.

5. Creating masks: a mask is created that completely covers the image with zero pixels, then a mask is created in the shape of a circle of a certain radius. Inside this mask, based on the angular geometry, masks of individual sectors are created, which in turn cancel the "shading" effect and allow the calculation algorithm to operate within its geometry.

6. Calculation of the sectors area: the number of pixels not covered by "shading" masks is counted and the area covered by the sector is calculated, converting the number of pixels into square kilometers.

7. Saving results: The results of sector area analysis are saved to an Excel file. After which cycle 2-6 is repeated until all images have been processed.

Two functions stand out in the general code. The «*slice_mask*» function accepts image and sector parameters, creating a mask to highlight the area of a particular sector. This is achieved by drawing lines and arcs that define the inner and outer boundaries of the sector. The areas of the image that lie outside the boundaries of the sectors are filled with zeros and excluded from the calculation. The «*calculate_sector_areas*» function applies a background subtraction algorithm, converts the image to binary format and uses masks created by the first function to determine the area of each sector [22].

Two program blocks are responsible for determining the initial and final sectors and working with angles in the program, one block for each function. For example, the block shown in Figure 5 is responsible for working with angles.

```
sector_areas = np.zeros(12)
for i in range(12):
    start_angle = 90 – (i + 1) * 30   # Start sector angle
    end_angle = 90 – (i) * 30         # End sector angle

    # Creation the sector mask
    sector_mask = slice_mask(image,center,inner_radius,outer_radius,start_angle,end_angle)
```

Figure 5 – Algorithm for selecting a longitudinal sector in processed images.

In mathematical expression, the point search algorithm looks like this:

$$x = \left(c[0] + r \cdot \cos(\alpha)\right), \quad y = \left(c[1] + r \cdot \sin(\alpha)\right) \quad (1)$$

where x is a point, c is the center (0 and 1 mean the axes, for each of which the center is determined separately), r is the radius, α is the angle, which is determined by the block shown in Figure 5.

Before data can be stored in Excel, it is collected and organized according to a format that is most readable and easy to analyze [24]. To organize the results of sector area measurements, the *DataFrame* method from the *Pandas* library is used. Each row of the *DataFrame* corresponds to one image, and the columns represent individual sectors. The program goes through all the images in the selected directory, analyzes them and fills the *DataFrame* with the received data. To save the *DataFrame* in Excel, the *to_excel* method is used, which is part of the *Pandas* library. This method specifies the path to the file where the data will be saved and the label for the index (index_label='Image'), which provides the addition of descriptive headers for rows in an Excel file.

As a result of executing the algorithm, the user, after a few seconds (depending on the size of the directory), receives an Excel file convenient for analysis with accurate and systematized data on the areas of the analyzed images sectors. For example, Table 1 shows data for two images: a test image and one working image, for June 1, 2020. The cells of the table show the sector areas for the conditional image (Figure 4) and the NLC fields (Figure 1), calculated in square kilometers, according to the described method. For the test image (Figure 4), a nominal value of 75 thousand km^2 is known.

Table 1 – Results of image processing shown in Figures 4 and 1.

	Sectors													
	1	2	3	4	5	6	7	8	9	10	11	12	Calc.	Nom.
Fig. 4	14775	60135	1103	0	0	0	0	0	0	0	0	0	76013	75000
Fig. 1	102975	61605	27645	9960	4553	21255	20243	131152	122888	107295	71505	107505	-	-

We can compare this value with the calculated sum of indicators for all sectors obtained during the program: 76 thousand km^2. The observed error of 1 thousand km^2 (1.3%) can be caused by background dispersion when changing images as shown in figure 6. It is also possible that the error is partially caused by the shot effect, which is characteristic of any discrete objects. The error varies depending on the threshold filtering parameter, but if this parameter is too high, there is a risk of data loss.
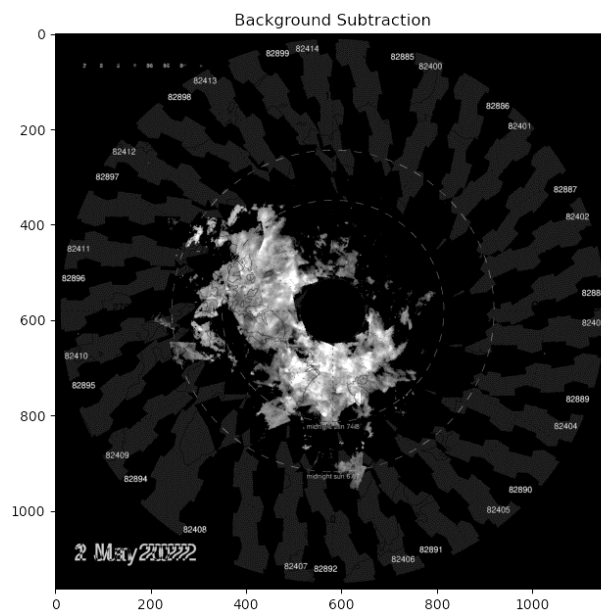

Figure 6 – View of the global noctilucent cloud field
after removing the background influence.

6 Some results of image processing of mesospheric cloud fields

Naturally, the main indicator of the practical value of the program can only be the results of processing satellite images of global NLC fields. In our case, we are talking about the seasons of their evolution from 2007 to 2022 (excluding the 2018 season). The lack of data on the AIM mission website for the 2018 summer season is due to technical reasons.

Table 2 – Final data on the distribution of the cloud fields area.

		Sectors											
		1	2	3	4	5	6	7	8	9	10	11	12
Seasons	2007	122601	124411	126350	124846	*121474*	129181	128701	**137061**	128037	122211	130344	**135432**
	2008	128283	120842	117123	118101	113286	117337	128473	118477	*111245*	*111287*	112750	**135556**
	2009	113429	113032	114379	*105623*	*106856*	119411	125047	124442	115057	108336	117975	**135387**
	2010	123277	126652	123245	118194	*113971*	126455	126258	**130122**	118444	*113009*	119484	**130812**
	2011	137475	136082	139701	138750	127739	131639	**144846**	143298	129263	*115371*	125453	**149688**
	2012	**132468**	123818	116832	121792	120925	124937	126614	124328	114381	*112243*	*112557*	**132203**
	2013	133645	123876	127421	127109	125155	133381	141900	137145	124888	*122010*	127701	**146562**
	2014	110886	104807	112024	108717	*102969*	*102125*	114820	115719	*102782*	104463	105302	**119809**
	2015	**144096**	133663	128889	*119840*	120822	127821	**140253**	138878	127618	124345	*120545*	137663
	2016	115647	98901	100761	100280	106067	105318	110933	**119256**	94661	96254	*88684*	100782
	2017	116102	110429	110199	104461	*101964*	107566	123241	**125878**	106725	113296	111475	106830
	2019	124333	124859	123104	118423	112784	*111894*	125015	**131895**	122845	113811	126065	121269
	2020	128248	134339	130372	123670	123854	127481	128995	**146412**	122379	*112798*	132670	132079
	2021	123580	126311	121126	121557	119537	122826	128685	**135952**	119991	*115836*	127007	124207
	2022	116016	116254	120530	114892	107116	113135	117100	**122985**	112432	*110530*	118948	**126343**
	Aver.	124672	121218	120804	117750	114968	120034	127392	130123	116716	113053	118464	128975
	Norm.	1,029	1,000	0,997	0,972	0,949	0,991	1,051	1,074	0,963	0,932	0,979	1,064

In each season, 90 daily pictures were included in the processing, that is, the total number of images studied was about 1350. In this case, the time required was no more than 10 hours. The final data on the distribution of the cloud fields area, expressed in square kilometers, for 12 longitudinal sectors on average per season are presented in Table 2.

The last lines show the average cloud area for all seasons (second line from the bottom) and the same values normalized to the average cloud area in all sectors and for all seasons. Cells corresponding to the maximum cloud field areas in the sector for a given season are highlighted in bold (differences of 1-2% are considered acceptable). Sectors with the minimum area of the cloud field are highlighted in italics and gray shading.

The table data indicates the existence of stable trends, that is, sectors with a predominance of maximum or minimum areas of cloud fields in relation to the average in the sectors. This fact is clearly illustrated in Figure 7, where the differences in the longitudinal structure are shown in the form of a bar graph.
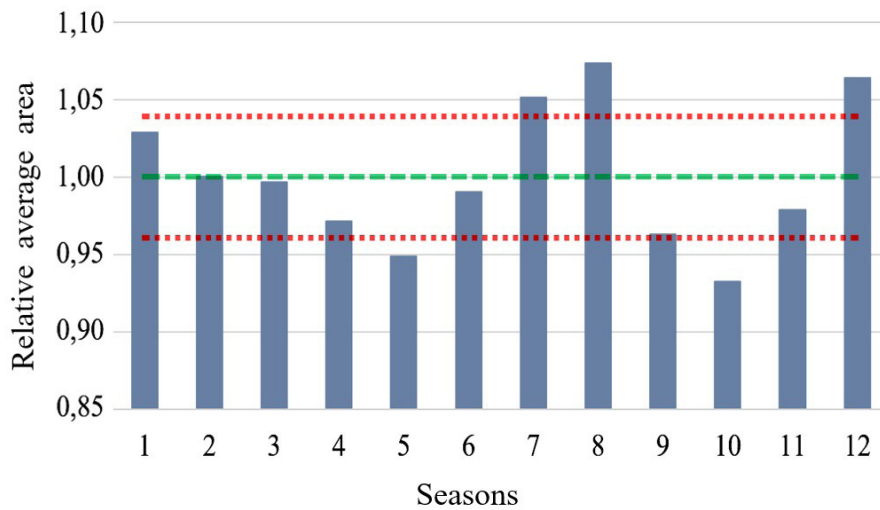
Figure 7 – Distribution of normalized average field area values
NLC in the northern hemisphere by longitudinal sectors for all seasons.

It should be noted that Figure 7 shows both the average value of the relative area of the cloud field and the maximum deviations of these values, corresponding to a confidence level of 98% (plus or minus triple the root mean square error of the average value). Thus, we can confidently speak about the existence of stable maxima in the development of the cloud field in sectors 7, 8 and 12. At the same time, minimal development of the area of NLC fields is typical for sectors 5 and 10. These facts, in our opinion, deserve further study as it can lead to discovery of new NLC relations with geophysical events or phenomena.

7 Conclusion

The developed program is a convenient tool for analyzing longitudinal variations of NLC fields, being a reliable foundation in studies of the connection between various physical processes and the evolution of NLC. The program not only provides accurate data, but also allows you to automate routine image processing, which speeds up data analysis and improves its quality.

Acceptable accuracy has been achieved when processing working arrays. Distortions in the result caused by background dispersion create an insignificant error and, in the future, can be eliminated using machine learning algorithms or background subtraction methods. The structure of the program and its development environment are flexible enough to allow modification in the future. As an advantage over analogues, we can highlight the fact that the version from the current work, if necessary, can be provided with an executive file and a compact directory with the necessary libraries, which will allow it to be used with a minimum of presets.

Using the created program, a general analysis of the satellite images array of the northern hemisphere global NLC field was carried out over a long period of time. The results obtained reliably indicate the presence of longitude sectors with statistically significant differences in the development of mesospheric clouds. This suggests the need to continue research in this direction.

References

1. Gadsden, M., and Schroder W. Noctilucent Clouds. – New York: Springer – 1989. – P. 125-130.

2. Grishin, N.I. Studies of Mesospheric Clouds. // In Proceedings of Meteorological Studies. Physics of the Mesosphere and Mesospheric Clouds, edited by O.B. Vasyl'ev. – Moscow: Nauka – 1975. – P. 23–32. (In Russian)

3. Bronshten, V.A., Grishin N.I. Noctilucent Clouds. – Moscow: Nauka – 1970. – 359 p. (In Russian)

4. Turco, R.P., Toon O.B., Whitten R.C., Keesee R.G., Hollenbach D. Noctilucent Clouds: Simulation Studies of Their Genesis, Properties, and Global Influences. // Planetary and Space Science 30. – 1982. – no. 11 P. 1147–1181.

5. Aim Mission Overview. AIM. Exploring Clouds at the Edge of Space. http://aim.hamptonu.edu/mission/index.html (accessed May 27, 2025).

6. Olivero J.J., Thomas G.E. Climatology of polar mesospheric clouds // Journal of the Atmospheric Sciences 43. – 1986. – no. 12 – P. 1263–1274.

7. Berger U., Lübken F.-J. Trends in mesospheric ice layers in the northern hemisphere during 1961–2013 // Journal of Geophysical Research: Atmospheres 120. – 2015. – P. 11.277–11.298. https://doi.org/10.1002/2015JD023355

8. Thurairajah B., Cullens C.Y., Bailey S.M. Characteristics of a mesospheric front observed in polar mesospheric cloud fields // Journal of Atmospheric and Solar-Terrestrial Physics. – 2021. -P. -Vol. 208. – Art. 105627. https://doi.org/10.1016/j.jastp.2021.105627

9. Shevchuk N., Pertsev N., Dalin P., Perminov V. Wave-induced variations in noctilucent cloud brightness: Model and experimental studies // Journal of Atmospheric and Solar-Terrestrial Physics. – 2020. -P. Vol. 203. – Art. 105257. https://doi.org/10.1016/j.jastp.2020.105257

10. Chandran A., Rusch D.W., Thomas G.E., Palo S.E., Baumgarten G., Jensen E.J., Merkel A.W. Atmospheric gravity wave effects on polar mesospheric clouds: A comparison of numerical simulations from CARMA 2D with AIM observations // Journal of Geophysical Research. – 2012. -Vol. 117. – Art. D20104. https://doi.org/10.1029/2012JD017794

11. Dalin P., Gavrilov N., Pertsev N., Perminov V., Pogoreltsev A., Shevchuk N., Dubietis A., Völger P., Zalcik M., Ling A., Kulikov S., Zadorozhny A., Salakhutdinov G., Grigoryeva I. A case study of long gravity wave crests in noctilucent clouds and their origin in the upper tropospheric jet stream // Journal of Geophysical Research: Atmospheres. – 2016. -Vol. 121. – No. 23. -P. 14.102-14.116. https://doi.org/10.1002/2016JD025422

12. DeLand M.T., Shettle E.P., Thomas G.E., Olivero J.J. A quarter-century of satellite polar mesospheric cloud observations // Journal of Atmospheric and Solar-Terrestrial Physics. – 2006. P. -Vol. 68. -P. 9–29. https://doi.org/10.1016/j.jastp.2005.08.003

13. Gao H., Li L., Bu L., Zhang Q., Tang Y., Wang Z. Effect of small-scale gravity waves on polar mesospheric clouds observed from CIPS/AIM // Journal of Geophysical Research: Space Physics. – 2018. -Vol. 123. – P. 4026–4045. https://doi.org/10.1029/2017JA024855

14. Shitikov V.K., Rosenberg G.S., Kostina N.V. Metody sinteticheskogo kartografirovaniya territorii (Na primere ekologo-informacionnoi sistemy «Region-Volgabas») https://ecograde.bio.msu.ru/library/books/_pdf_rozenberg/3-2.pdf (accessed May 27, 2025). (In Russian)

15. Solodovnik, A. A., Leontyev P. I., Dalin P. Studies of the influence of tropospheric factors on the formation of noctilucent clouds by a cartographic method // Journal of Atmospheric and Solar-Terrestrial Physics. – 2020. -Vol. 200. – Art. 105224. https://doi.org/10.1016/j.jastp.2020.105224

16. Kudabaeva D.A., Solodovnik A.A. Variation in the area of the global field of noctilucent clouds of the northern hemisphere in 2007–2012 seasons // Geomagnetism and Aeronomy. – 2015. -Vol. 55. -No. 2. – P. 261–265. https://doi.org/10.1134/S0016793215020139

17. Solodovnik, A., Baibusinova A., Kudabaeva D. Dynamics of the development of the field of noctilucent clouds in the northern hemisphere in the period 2013–2020 // Bulletin of KazNTU. – 2020a.- -Vol. 4. -No. 140. – P. 138–144.

18. Solodovnik, A.A., Baibusinova A.K. Features of the seasonal development of the fields of noctilucent clouds of the northern and southern hemispheres of the Earth // Eurasian Union of Scientists (EUS) 5. – 2020b. – No. 74. – P. 10–16.

19. Solodovnik A., Leontiev P., Dalin P., Takenov B., Alyoshin D. Seasonal evolution and interseasonal changes in polar mesospheric clouds at high latitudes in the southern hemisphere // Journal of Atmospheric and Solar-Terrestrial Physics. – 2021. -Vol. 226. – Art. 105787. https://doi.org/10.1016/j.jastp.2021.105787

20. Cole A. E., Kantor A. J. Air force reference atmospheres. – Hanscom AFB, Massachusetts: Air Force Geophysics Laboratory, Air Force Systems Command, United States Air Force. – 1978. – P. 76.

21. Bradski G., Kaehler A. Learning OpenCV: Computer vision with the OpenCV library. – O'Reilly Media. – 2008. -P. 577.

22. McKinney W. Python for data analysis. – O'Reilly Media. – 2012. – P. 541.

23. Langtangen, H. P. A primer on scientific programming with Python. – Springer. – 2016. – P. 716.

24. Summerfield M. Programming in Python 3: A Complete introduction to the Python language. – Addison-Wesley. – 2015. – 636 p.

25. Solodovnik A.A., Zyryanov R.O, Leontyev P.I., Useinov B.M., Gololobova E.G., Zhuravlev P.L. Experience of noctilucent clouds registering in the near infrared spectrum region // Physical Sciences and Technology. – 2024. – Vol. 11 (No. 1-2). – P. 85-93. https://doi.org/10.26577/phst2024v11i1a10

26. Solodovnik A.A., Leontyev P.I., Useinov B.M., Kadyrmin A.D., Zyryanov R.O. Application of electronic receivers for recording infrared images of celestial phenomena at the CAR of the NKU // Physical Sciences and Technology. – 2023. – Vol. 10 (No. 1-2). -P. 50-57. https://doi.org/10.26577/phst.2023.v10.i1.07

Information about authors:

Solodovnik Andrey, Candidate of Physico-Mathematical Sciences is a Professor at the M. Kozybayev North Kazakhstan University (Petropavlovsk, Kazakhstan), e-mail: asolodovnik@ku.edu.kz

Kleksin Roman is a Laboratory assistant at the M. Kozybayev North Kazakhstan University (Petropavlovsk, Kazakhstan), e-mail: fjolkunnigr@yandex.kz

Leontyev Pavel, Candidate of Physico-Mathematical Sciences is an Associate professor at the M. Kozybayev North Kazakhstan University (Petropavlovsk, Kazakhstan), e-mail: pleontyev@mail.ru, pleontiev@ku.edu.kz

Useinov Beibut, Candidate of Physico-Mathematical Sciences is a Professor at the M. Kozybayev North Kazakhstan University (Petropavlovsk, Kazakhstan) e-mail: buseinov@gmail.com

Markova Agniya is a Senior lecturer at the M. Kozybayev North Kazakhstan University (Petropavlovsk, Kazakhstan), e-mail: agni.m@bk.ru

Kassimova Svetlana is a Senior lecturer at the M. Kozybayev North Kazakhstan University (Petropavlovsk, Kazakhstan), e-mail: kassedy_sa@mail.ru

Impact of gas pressure and spray distance on coating formation in electric arc metallization

B.K. Rakhadilov [1] , N.M. Magazov [2] , Y.S. Molbossynov [2*] ,

A.K. Apsezhanova [2] and A.Y. Kussainov [2]

[1]PlasmaScience LLP, Ust-Kamenogorsk, Kazakhstan
[2]Daulet Serikbayev East Kazakhstan Technical University, Ust-Kamenogorsk, Kazakhstan
*e-mail: molbossynov.ye@edu.ektu.kz

This study investigates the technological parameters of electric arc metallization applied to 30KHGSA steel, focusing on the effects of varying the spraying distance (100–250 mm) and gas pressure (6–9 Pa) on the resulting coating structure and properties. The spraying was performed using an SX-600 electric arc metallizer. Electron microscopy and metallographic analysis revealed that the coatings possess a layered structure consisting of solidified convective metal flows, micro-welded particles, and oxide inclusions. The optimal spraying parameters–150 mm distance and 7 Pa pressure–yielded the maximum coating thickness (729.58–733.62 μm) and the lowest porosity (4.02–4.33%). It was observed that increasing the spraying distance beyond 150 mm leads to reduced coating thickness, while deviations from the optimal gas pressure result in decreased structural density and homogeneity. Electric arc metallization of 30KHGSA steel under optimal conditions enables the formation of coatings with enhanced wear resistance and mechanical strength. Specifically, spraying distances over 150 mm and pressures outside the 7–8 Pa range negatively affect the coating's density, uniformity, and tribological performance. The identified optimal range (150–200 mm, 7–8 Pa) promotes the development of coatings with low surface roughness, reduced friction coefficient, and improved wear resistance.

Key words: arc spraying, steel coatings, microstructure, Vickers hardness, porosity, thickness.
PACS number(s): 81.15.-z, 81.20.-n, 81.40.-z.

1 Introduction

Arc spraying is a technique that utilizes the heat of an electric arc to melt various metallic materials [1]. Among the coating methods, arc spraying process seems to be more preferred by the criteria of thermal efficiency, cost of atomized materials and ease of maintenance [2,3]. In this method, two consumable wire electrodes are automatically fed into the arc zone. The arc arising between the electrodes melts the wire tips. The principle of arc atomization is based on the atomization of molten metal with compressed air and its deposition on the substrate at high speed, forming a protective coating.

Due to its high productivity and cost-effectiveness, electric arc metallization is widely used in various industries including mechanical engineering, shipbuilding, agricultural and mining machinery. However, the quality of the resulting coatings is highly dependent on spraying parameters such as

spray distance and gas pressure. Improper selection of these parameters can lead to defects, increased porosity and deterioration of mechanical properties of the coating. Therefore, optimization of process conditions is an important task to improve the performance of sprayed coatings.

In this paper, coatings of 30KHGSA steel deposited by electric arc metallization on a substrate of 65G steel are investigated. Special attention is paid to the influence of technological parameters of the process – in particular, spraying distance and gas pressure – on the coating formation, its microstructure, thickness, porosity, hardness and surface roughness. Optimization of these parameters will improve the performance properties of coatings and expand their application in agricultural engineering.

Recent progress in electric arc spraying technologies has highlighted the importance of optimizing process parameters to improve coating performance. In particular, steel grade 30KHGSA has emerged

as a promising material due to its high mechanical strength, wear resistance, and structural stability under high dynamic loads [1,2]. Its successful application in arc metallization processes is supported by recent works demonstrating its effectiveness in improving surface hardness and adhesion [3]. Thus, selecting 30KHGSA as the coating material is justified by its advantageous performance in demanding industrial environments.

2 Materials and methods

2.1 Equipment and instrumentation

Coating was carried out using supersonic electric arc metallizer SX-600 developed by Guangzhou Sanxin Metal Technology Co (Guangzhou, China). This system consists of power supply, supersonic spray gun, control system and compressed air supply system.
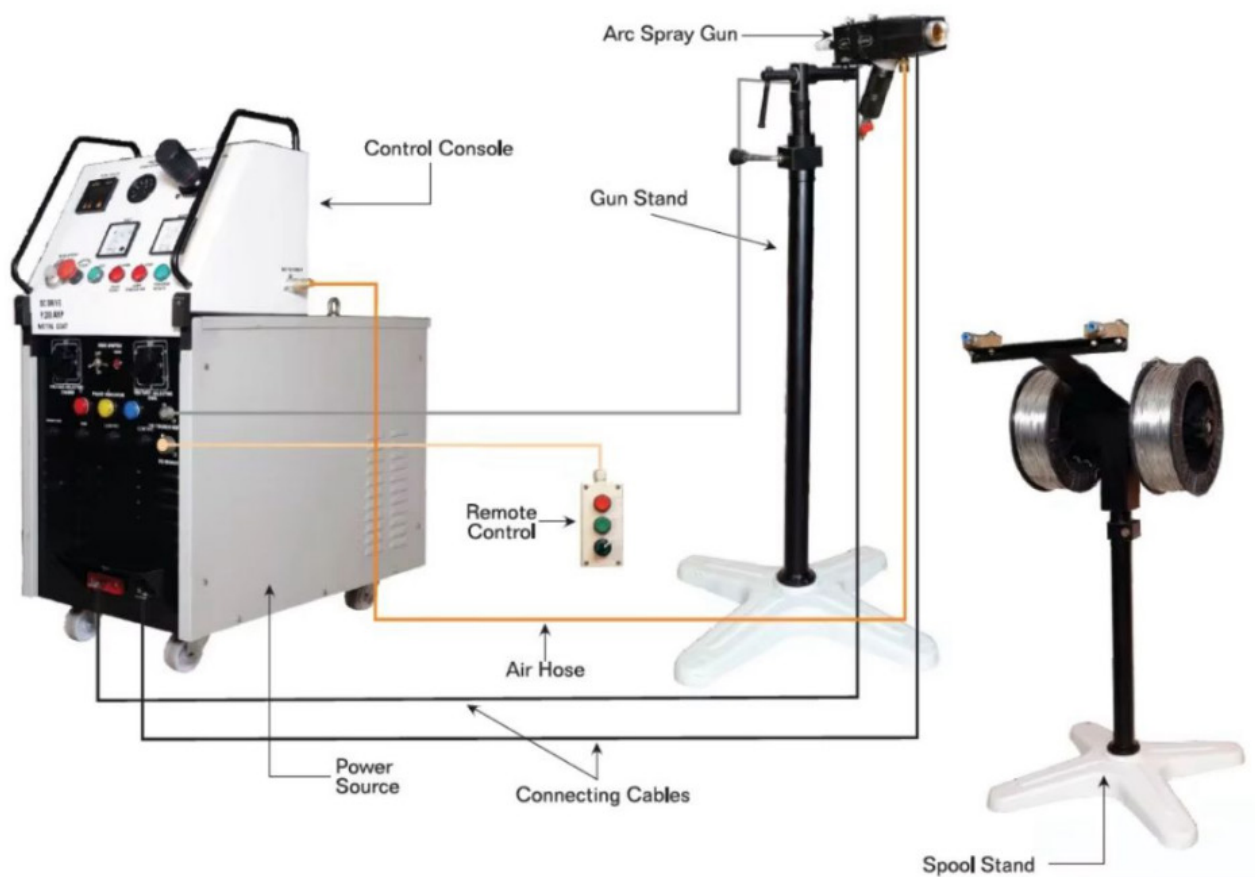

Figure 1 – Schematic diagram of the electric arc metallization setup**.**

The spraying process was conducted according to the modes shown in Table 1, with the parameters varied by varying the gas pressure (P) and spraying distance (D). The substrate temperature was not controlled during the experiment. Future studies will investigate the effect of substrate temperature on coating quality. During the spraying process, the voltage was maintained at the levels shown in Table 1. Air was used as the atomizing gas. Each sample was sprayed for 10 seconds over the entire substrate surface to form a uniform layer. The spraying was

carried out under atmospheric conditions. Each experimental condition was repeated 3 times to ensure consistency, with measurements averaged across all trials.

In this work 65G steel (GOST 103-2006) was used as a substrate material. Its ability to harden by hardening significantly increases the service life and wear resistance of parts. Due to these properties, steel 65G is used for the manufacture of springs, springs, washers, friction disks, brake belts, gears, bearing housings, flanges, as well as clamping and feeding

collets. This list is not exhaustive, since the universal characteristics of this alloy make it in demand in the production of parts operating under conditions of intensive wear. Steel 65G is widely used in mechanical engineering, machine tool construction, shipbuild-

ing, as well as in the production of heavy military, agricultural and mining equipment. It can be found in almost any mechanism where springs and springs are used. Chemical composition of steel 65G in accordance with GOST 14959-79 is presented in Table 2.

Table 1 – Spraying modes.

Sample	P, Pa	D, mm	I, A	U, B	V, cm/s
D1	9	100	300	45	12
D2	9	150	300	45	12
D3	9	200	300	45	12
D4	9	250	300	45	12
P1	6	200	300	45	12
P2	7	200	300	45	12
P3	8	200	300	45	12
P4	9	200	300	45	12

Table 2 – Chemical composition of steel 65G according to GOST 14959-79.

C	Si	Mn	Ni	S	P	Cr	Cu
0.62 – 0.7	0.17 – 0.37	0.9 – 1.2	to 0.25	to 0.035	to 0.035	to 0.25	to 0.2

The coating material used was 30KHGSA steel wire with a diameter of 1.4 mm. This alloy is characterized by high strength, rigidity, as well as good weldability and machinability. Due to these characteristics, 30CrHSA steel is widely used in mechanical engineering and automotive industry. In the automotive industry it is in demand due to its high wear resistance, which makes it an optimal material for the

production of crankshafts, connecting rods, cylinder heads and other parts operating under significant loads. In mechanical engineering and construction equipment steel 30CrHSA is used for the manufacture of shafts, axles, gears, bolts and nuts designed for high operating loads. Chemical composition of steel 30KHGSA according to GOST 4543-71 is given in Table 3.

Table 3 – Chemical composition of 30KHGSA steel according to GOST 4543-71.

C	Si	Mn	Ni	S	P	Cr	Cu
0.28 – 0.34	0.9 – 1.2	0.8 – 1.1	to 0.3	to 0.025	to 0.025	0.8 – 1.1	to 0.3

2.2 Characterization methods for coatings

To study the structure and porosity of coatings, cross-sections of samples were prepared. Their fabrication was carried out by standard methods of sectioning with subsequent grinding and mechanical polishing. Grinding was carried out using silicon carbide (SiC) based sandpaper with 120 to 3000 grit, and polishing was performed on velvet cloth using 3M polishing paste on a METAPOL 2200P automated

grinding machine (Laizhou Lyric Testing Equipment Co., Shandong, China, 2022)[4]. The porosity of the coatings was analyzed using an Olympus BX53M optical microscope (Tokyo, Japan, 2024) [5], at 5× and 10× magnification. Quantification of porosity was performed using Metallographic Analysis Software in accordance with ASTM E2109. The average coating thickness was determined based on five measurements for each image.Roughness measurement

was performed by contact profilometry using a 130 profilometer (Proton, Zelenograd, Russia, 2018) [6]. To ensure repeatability of the results and increase the accuracy, five measurements were performed on each sample at random points [7], with subsequent calculation of the parameters Ra (arithmetic mean deviation of the profile) and Rz (the greatest height of the profile) in accordance with GOST 2789-73. Evaluation of surface roughness allowed to determine the influence of different spraying parameters[8].Hardness analysis on the depth of the samples was carried out by the Vickers method using a semi-automatic micro-hardness tester Metolab 502 (St. Petersburg, Russia) in accordance with GOST 2999-75. The optimal combination of these parameters ensures maximum coating durability. Hardness and surface roughness measurements were repeated three times, with measurement errors of ± 5 HV and ± 0.2 μm, respectively. The standard deviations were 2.5 HV and 0.1 μm. Tribological tests were carried out on tribometer TRb3 Anton Paar (international standards ASTM G 133-95 and ASTM G99) under dry friction conditions at room temperature using the standard «ball-disk» method. A 100Cr6 ball of 6 mm diameter was used as the contour[9]. The tests took place at a load of 10 N and a linear velocity of 10 cm/s, the radius of curvature of wear was 3 mm, and the friction path was 400 m.

3 Results and discussions

3 .1 Microstructure

As shown in Figure 2, the microstructure of steel coatings made of 30KHGSA steel by electric arc metallization is a complex heterogeneous system formed as a result of the rapid cooling of molten metal particles during their deposition on the substrate. It consists of individual layer-by-layer deposited splatters (melt droplets of the spraying material), spread and solidified on the substrate [10]. Metallographic analysis of cross-sections reveals a structure characteristic of arc-sprayed coatings, with pronounced layering and heterogeneity [11]. The thickness of individual layers varies widely, and distinct inter-splat boundaries are visible throughout the structure. Spherical and irregular pores are mostly located along the splat boundaries, resulting from gas entrapment and incomplete fusion. Several microcracks, typically oriented perpendicular to the coating surface, can be observed propagating between splats, likely due to thermal shrinkage during rapid solidification. These features – splat boundaries, porosity, and crack networks – confirm the complex interplay between thermal gradients and particle dynamics during deposition, which ultimately affect the mechanical, tribological, and corrosion properties of the coating.
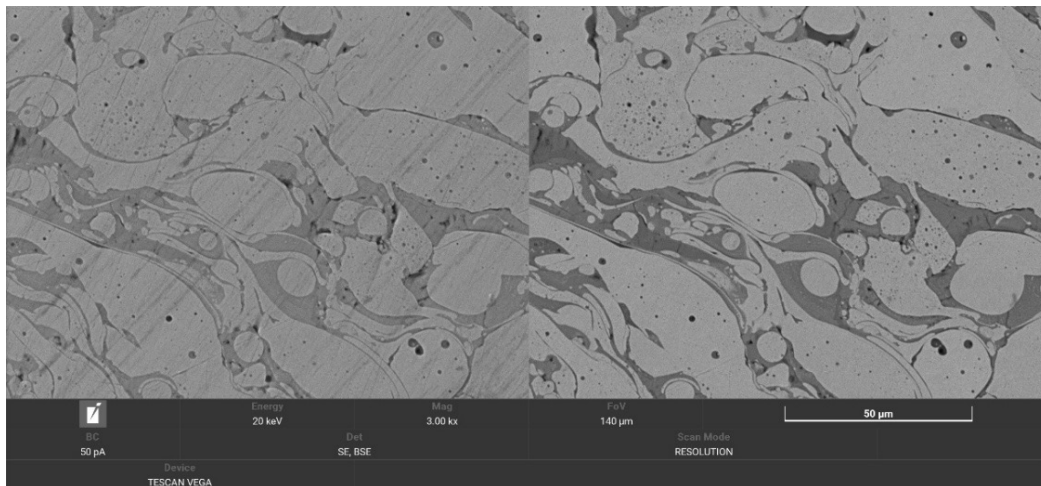

Figure 2 – Layered microstructure of the cross section
of the coatings at a magnification of 3.00 kx.

3.2 Thickness and porosity

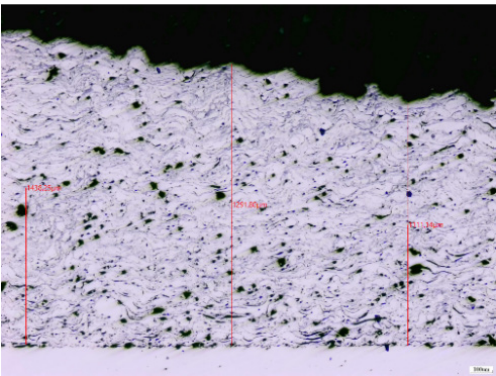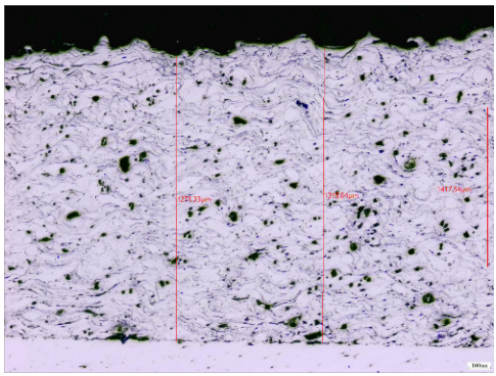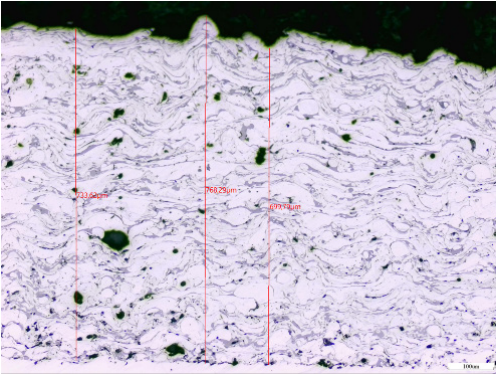The coating thickness affects wear resistance and protective properties, while porosity affects density and strength. The relationship between coating thickness and porosity is complex: in a certain range of spraying modes, increasing the distance contributes to a decrease in porosity, but with further increase in distance and gas pressure, there is an increase in

porosity due to an increase in the dispersion of particles in the flow[12]. The optimum combination of these parameters ensures maximum durability of the coating.

Table 4 shows the effect of spraying distance (D) on the thickness and porosity of the coating deposited by electric arc metallization. When the distance is increased from 100 to 150 mm, the coating thickness increases from 1291.80 to 1315.04 μm and porosity decreases from 13.92% to 9.80%. However, when the distance is further increased to 200 mm, the thickness decreases sharply to 733.62 μm but the porosity drops to 4.33%. At a distance of 250 mm, the coating thickness becomes minimum (416.27 μm) and porosity increases to 7.21%. This indicates that increasing the distance leads to particle dispersion, reducing the coating thickness. [13]

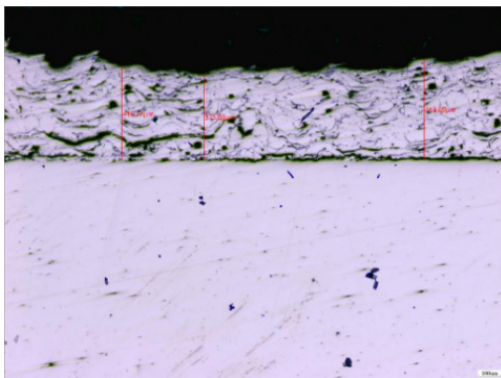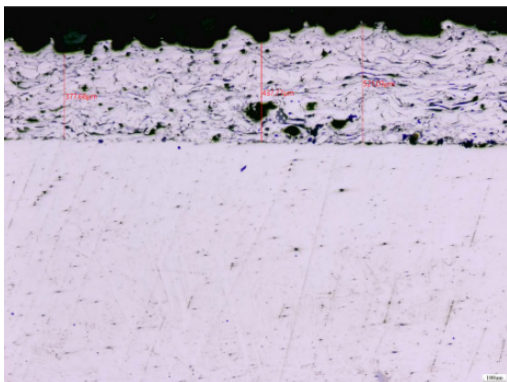**Table 4** – Dependence of thickness and porosity on distance.

№	Distance dependence of coverage(D)	Coating thickness μm	Photos obtained with metallographic microscope	Porosity of coatings %
D1	100	1291,80		13,92
D2	150	1315,04		9,80
D3	200	733,62		4,33

Continuation of the table

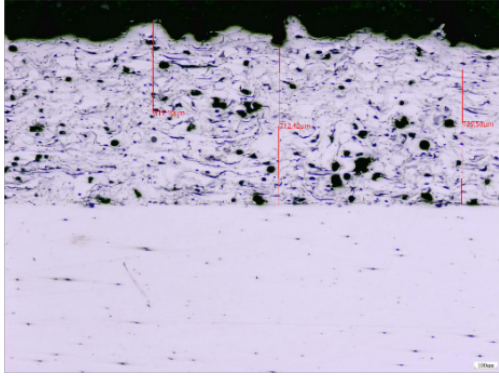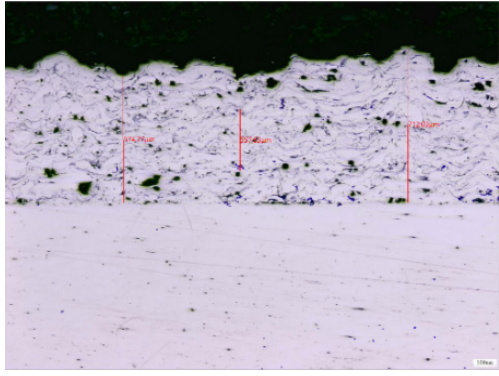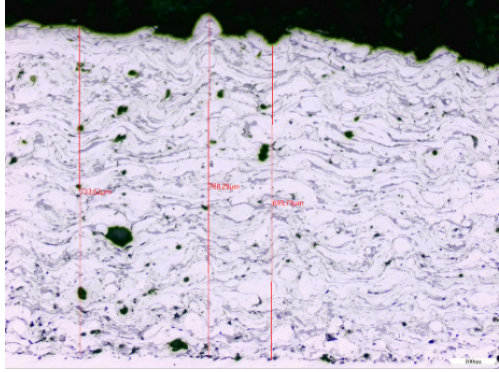| №	Distance dependence of coverage(D)	Coating thickness μm	Photos obtained with metallographic microscope	Porosity of coatings %
D4	250	416,27		7,21

Table 5 shows the effect of gas pressure (P) on the thickness and porosity of the coating deposited by electric arc metallization. At a pressure of 6 Pa, the thickness of the coating is 437.77 μm and the porosity is 9.80%. When the pressure is increased to 7 Pa, the thickness increases to 729.58 μm and the porosity decreases to 4.02%. However, when the pressure is further increased to 8 Pa, the thickness decreases to 557.63 μm and the porosity increases to 5.84%. At 9 Pa, the thickness increases again to 733.62 μm and the porosity remains low (4.33%). These data show that the optimum pressure range is 7-9 Pa, as it achieves the highest coating thickness with low porosity.

Table 5 – Dependence of thickness and porosity on gas pressure.

№	Gas pressire of coverage(D)	Coating thickness μm	Photos obtained with metallographic microscope	Porosity of coatings %
P1	6	437,77		9,80

Impact of gas pressure and spray distance...

Phys. Sci. Technol., Vol. 12 (No. 1-2), 2025: 14-26

Continuation of the table

№	Gas pressire of coverage(D)	Coating thickness μm	Photos obtained with metallographic microscope	Porosity of coatings %
P2	7	729,58		4,02
P3	8	557,63		5,84
P4	9	733,62		4,33

Analysis of the data from both tables shows that the thickness and porosity of the coating deposited by electric arc metallization significantly depend on both the spraying distance (D) and the gas pressure (P). The optimum distance interval is 150 – 200 mm. At 150 mm, the maximum coating thickness (1315.04 μm) with moderate porosity (9.80%) is achieved, while at 200 mm, the lowest porosity (4.33%) with the average thickness (733.62 μm) is achieved. Increasing the distance beyond 200 mm leads to a greater reduction in thickness and an increase in coating porosity due to particle dispersion during the spraying process. Regarding the gas pressure, the most favorable range is between 7-9 Pa, since at these values the highest coating thickness (729.58-733.62 μm) with minimum porosity (4.02-4.33%) is achieved. Thus, it is recommended to use a spraying distance of 150-200 mm and gas pressure of 7-9 Pa to obtain an optimal coating.

3.3 Hardness of steel coatings

The hardness of the coating is one of the key parameters determining its wear resistance, durability and mechanical strength. High hardness contributes to the coating's resistance to abrasive wear, shock loads and deformation, which is especially important for parts operating under intensive friction and high loads.
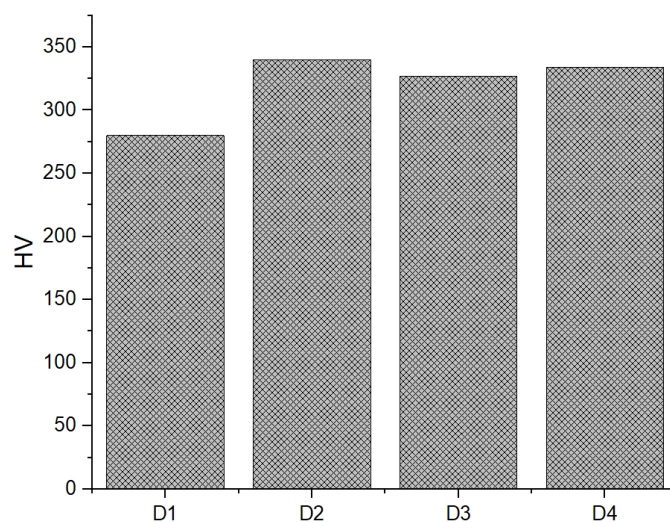

Figure 3 – Variation of coating hardness as a function of varying the distance
from the gun to the substrate surface (D is the spraying mode indicated in Table 1).

The graph shows the dependence of the hardness of coatings obtained by electric arc metallization on the spraying distance. The horizontal axis shows different spraying modes (D1-D4). The maximum hardness (340 HV) is achieved in the second mode, whereas in the other cases it decreases to 280 HV.

The data analysis indicates a deterioration in the hardness of the coatings at a spraying distance of 100 mm. A slight increase in the distance improves the hardness, but at a distance of 200-250 mm the values are lower than at 150 mm. Therefore, the optimum spraying distance to achieve the best hardness is 150 mm (Figure 3).
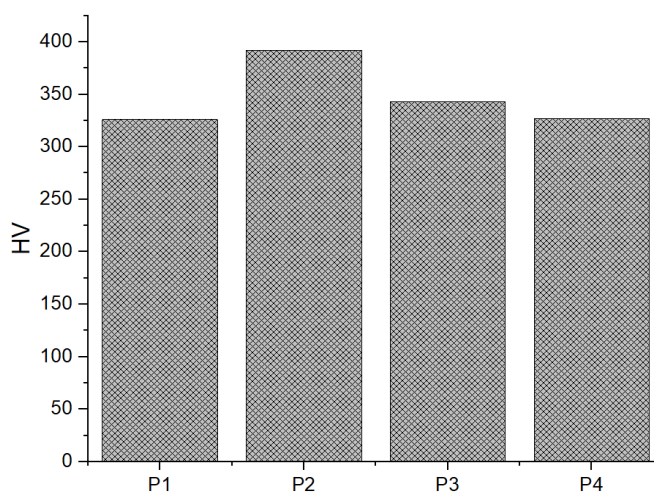

Figure 4 – Variation of coating hardness as a function of varying gas pressure
(P is the spraying mode indicated in Table 1).

The graph shows the dependence of the hardness of coatings obtained by electric arc metallization on gas pressure. The horizontal axis shows different spraying modes (1-4).

The maximum hardness (392 HV) is achieved in the second mode at a pressure of 7 Pa, while at other pressure values fluctuations in the range of 326-343 HV are observed. This indicates that both at too low and too high pressures, the coating properties deteriorate, which negatively affects its hardness. Consequently, in this case the optimum pressure is 7 Pa (mode 2).[14,15]

Thus, based on the presented data, we can conclude that both the distance of spraying and gas pressure have a significant effect on the hardness of coatings obtained by electric arc metallization.Therefore, to obtain coatings with maximum hardness, it is necessary to carefully select the spraying parameters, optimizing the distance of 150 mm and gas pressure of 7 Pa.[16](Figure 4).

While the highest hardness observed during the variation of spraying distance alone is achieved at 150 mm (340 HV), the overall maximum hardness of **392.6 HV** is recorded when the spraying distance is **200 mm** and the gas pressure is **7 Pa**. This indicates that the hardness is not solely dependent on a single parameter but results from the **combined optimization** of both spraying distance and gas pressure. Therefore, the best mechanical performance is achieved at 200 mm and 7 Pa, which should be considered the true optimum condition for maximum hardness.

3.4 Roughness

Surface roughness affects the wear resistance, corrosion resistance, adhesion, of materials. The optimum level of roughness is necessary to achieve the best performance characteristics depending on the conditions of use.

Ra (the absolute average deviation relative to the base length) is a parameter that characterizes the average of the deviations of the surface height from its mean value, measured over the entire length of the profile. It is calculated as the arithmetic mean of absolute deviations of the profile height from the mean value. Ra is one of the main roughness indices, where smaller values indicate a smoother surface and larger values indicate a more pronounced roughness.
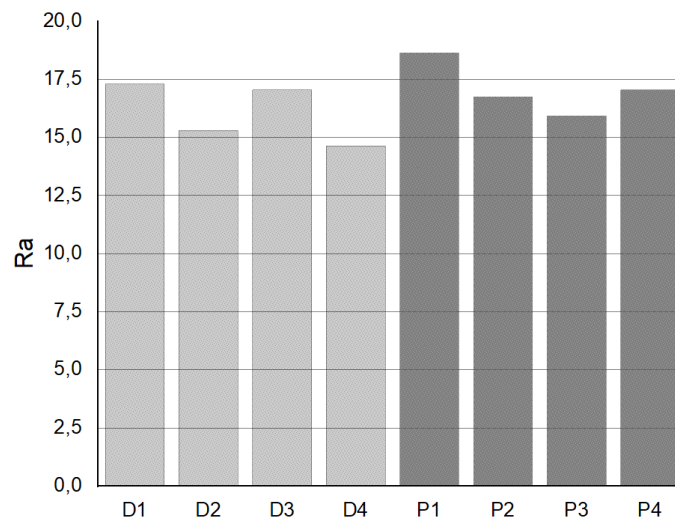

Figure 5 – Variation of coating roughness as a function of varying spraying parameters
(D is the distance from the gun to the substrate surface, P is the gas pressure).

As shown in Figure 5, varying the spraying distance affects the surface roughness depending on the selected values. At distances of 100 mm and 200 mm, maximum roughness values of 17.3 μm and 17.04 μm were recorded, respectively. In contrast, the lowest roughness values were observed at spraying distances of 150 mm and 250 mm. At the same time, as the gas pressure (P) increases, the surface roughness initially decreases, reaching a minimum of 15.93 μm; however, further increases in pressure

result in a rise in roughness up to 17.04 μm. This be-havior may be attributed to the changing dynamics of particle motion in the gas flow. Optimal coating roughness values are achieved through a balanced combination of spraying distance and gas pressure parameters.

Gas pressure plays a critical role in controlling the dynamics of molten particles during arc spray-ing. As the atomizing gas (typically air) accelerates the molten metal droplets toward the substrate, the pressure determines their velocity, trajectory, de-gree of fragmentation, and cooling rate. At low pres-sures (e.g., 6 Pa), particle acceleration is insufficient, which results in lower impact energy, poor flattening, and weak adhesion. This leads to increased porosity and rough surface morphology due to partial fusion and uneven deposition.

When the pressure is increased to an optimal range (7–8 Pa), particles reach a higher velocity and achieve better spreading upon impact, forming flatter splats and denser microstructures with lower porosity. This also improves mechanical properties such as hardness and wear resistance. However, ex-cessive gas pressure (e.g., 9 Pa) may cause high tur-bulence and particle rebound, leading to inhomoge-neous coating, surface defects, and even increased cooling rates that can cause microcracking due to thermal stress.

Therefore, gas pressure must be optimized to en-sure a balance between particle speed, splat morphol-ogy, cooling behavior, and coating integrity. These effects are consistent with previous studies on high-velocity arc and flame spraying systems [17,18]

3.5 Tribological tests

The spraying distance affects the kinetic energy and degree of oxidation of the coating particles. At the minimum distance (D1, 100 mm), particles are deposited with high energy, forming a dense but potentially overheated coating [19]. Increasing the distance to 150-200 mm (D2, D3) promotes uniform layer formation, reducing the likelihood of defects [20]. At the maximum distance (D4, 250 mm), the particles lose a significant part of energy, which can lead to an increase in porosity and changes in the tri-bological characteristics of the coating.
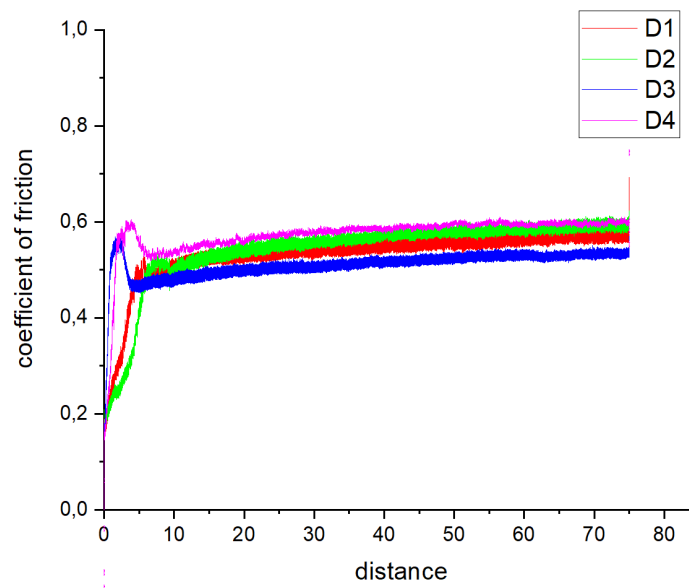

Figure 6 – Dependence of friction coefficient on distance.
(D1-D4 are the spraying mode indicated in Table 1).

Figures 6 and 7 illustrate how spraying distance and gas pressure influence the friction coefficient. As the distance increases, particles acquire different ki-netic energies, affecting the wear resistance and tri-bological properties of the coating. Optimal param-eters (distance of 150–200 mm, pressure of 7–8 Pa) result in coatings with a reduced friction coefficient and improved wear resistance. In particular, at a pres-sure of 7 Pa (P2) and a distance of 150 mm (D2), the most stable and lowest friction coefficient values are observed, correlating with a denser structure and lower surface roughness.
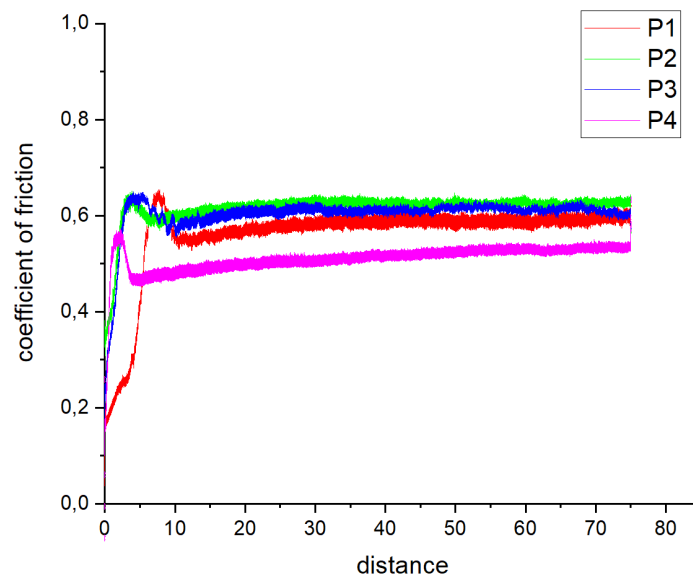
Figure 7 – Dependence of friction coefficient on distance.
(P1-P4 are the spraying mode indicated in Table 1).

Gas pressure determines the atomization rate and the distribution of particles in the flow. At low pressure (P1, 6 Pa) particles have lower kinetic energy, which increases coating roughness and friction coefficient. Increasing pressure (P2-P3, 7-8 Pa) improves the adhesion and density of the coating, making it more homogeneous. At maximum pressure (P4, 9 Pa), excessive particle acceleration is possible, resulting in increased material rebound and inhomogeneity of the coating.

Optimal modes of spraying distance and gas pressure are determined by the balance between the coating density, its adhesion to the substrate and tribological characteristics. Moderate values of distance (150-200 mm) and pressure (7-8 Pa) provide the best combination of friction coefficient and wear resistance of the coating.[21]

4 Conclusion

The conducted study of microstructure and properties of steel 30KHGSA coatings obtained by electric arc metallization has shown that the process of coating formation is accompanied by rapid cooling of molten particles, which leads to the formation of layer-by-layer stacked splats. Optimization of spraying parameters, such as distance and gas pressure, allows achieving the best performance characteristics of the coating, such as maximum thickness

(729.58–733.62 μm) and minimum porosity (4.02–4.33%) at a distance of 150 mm and gas pressure of 7–9 Pa. Increasing the spraying distance above 150 mm decreases the coating thickness, and deviation of gas pressure from the optimum values worsens the density and homogeneity of the structure. The influence of spraying distance and gas pressure on the coating hardness is also important: increasing the distance from 100 mm to 150 mm increases the hardness from 280.8 HV to 340.7 HV, and the maximum hardness (392.6 HV) is achieved at a distance of 200 mm and a gas pressure of 7 Pa. The graphical representation showed that the reduction of coating roughness is achieved at certain values of distance, while increasing the gas pressure initially decreases the roughness, but at a certain stage leads to an increase. This behavior can be attributed to the influence of gas pressure on particle velocity and splat formation: at low pressures, insufficient kinetic energy leads to poor adhesion and porosity; optimal pressures enhance particle acceleration, improve splat flattening, and promote rapid solidification; excessive pressure may result in turbulence, rebound effects, and coating inhomogeneity. Thus, parameters such as spraying distance and gas pressure need to be carefully controlled to achieve the required performance properties and increase the mechanical strength of the coating. Analysis of tribological characteristics showed that the distance

and gas pressure significantly affect the friction coefficient. Optimal parameters (150–200 mm, 7–8 Pa) provide uniform coating, minimum roughness and high wear resistance.

References

1. Steffens H. D., Babiak Z., Wewel M. Recent developments in arc spraying // IEEE Transactions on Plasma Science. – 1990. – Vol. 18. – P. 974–979. https://doi.org/10.1109/27.61512

2. Shynarbek A., Rahadilov B., Stepanova O., Kusainov R., Zhasulan A., Daumova G. Issledovanie processa elektrodugovoj metallizacii pokrytij iz stali 30HGSA // Eurasian Physical Technical Journal. – 2024. – Vol. 20, No. 4(46). – P. 67–73. https://doi.org/10.31489/2023No4/67-73 (In Russian)

3. Gargasas J., Valiulis A. V., Gedzevičius I., Mikaliūnas Š., Nagurnas S., Pokhmurska H. Optimization of the arc spraying process parameters of the Fe–base Mn-Si-Cr-Mo-Ni coatings for the best wear performance // Materials Science. – 2016. – Vol. 22. – P. 20–24. https://doi.org/10.5755/j01.ms.22.1.7339

4. Mussabek G., Kalimoldayev M., Lysenko V., Dikhanbayev K., Baiganatova S., Amirkhanova G. Modern achievements in the field of development of methods for obtaining porous titanium structures for medical applications // Recent Contributions to Physics. – 2020. – Vol. 75(4). – P. 46–60. https://doi.org/10.26577/RCPh.2020.v75.i4.06

5. Khan M. A., et al. Influence of electric arc deposition parameters on the microstructure and porosity of coatings // Surface and Coatings Technology. – 2019. – Vol. 372. – P. 135–142. https://doi.org/10.1016/j.surfcoat.2019.05.010

6. Rysin A. V., et al. Vyvod sootnosheniya mass protona i elektrona na osnove zakonov mirozdaniya i termodinamicheskogo ravnovesiya // Sciences of Europe. – 2017. – No. 19(19). (in Russian)

7. Mussabek G., Sivakov V. Synthesis and microstructure of p-type porous gallium phosphide layers // Physical Sciences and Technology. – 2017. – Vol. 4(2). – P. 54–58. https://phst.kaznu.kz/index.php/journal/article/view/134

8. Baktygerey S. B., Mussabek G., Zhylkybayeva N., Yermukhamed D., Zhumabekova V., Gumarova S., Boldyrieva O., Lisnyak V. Palladium catalysts supported on carbonized porous silicon for H$\square$/O$\square$ recombination // Physical Sciences and Technology. – 2023. – Vol. 10(3–4). – P. 40–47. https://phst.kaznu.kz/index.php/journal/article/view/359

9. Bazarbekov S. A. Application of high-speed gas-flame technology for hardening the surfaces of machines and robots of automatic gas-flame spraying // Physical Sciences and Technology. – 2021. – Vol. 8(1–2). – P. 47–52. https://doi.org/10.26577/phst.2021.v8.i1.06

10. Borisova M. Z., Struchkov N. F., Vinokurov G. G. Analiz struktury iznosostojkogo pokrytiya, poluchennogo elektrodugovoj metallizaciej poroshkovoj provoloki s tugoplavkimi dobavkami // Prirodnye resursy Arktiki i Subarktiki. – 2016. – No. 2(82). – P. 76–80. (in Russian)

11. Rakhadilov B., Magazov N., Kakimzhanov D., Apsezhanova A., Molbossynov Y., Kengesbekov A. Influence of spraying process parameters on the characteristics of steel coatings produced by arc spraying method // Coatings. – 2024. – Vol. 14. – Article 1145. https://doi.org/10.3390/coatings14091145

12. Tamargazin A. A., Lopata L. A., Brusilo Yu. V., Dovzhuk S. A. Vliyanie faktorov processa elektrodugovogo napyleniya na strukturoobrazovanie i svojstva pokrytij // Zbirnik naukovih prac' KNTU. – 2010. – Vip. 23. – P. 287–297. (in Russian)

13. Zhukeshov A., Gabdullina A., Amrenova A., Fermahan K., Serik K., Ahmetzhanova N., Erenbayeva Z., Rysbekova Z. The specifics of copper coatings production by pulsed arc method // Physical Sciences and Technology. – 2016. – Vol. 2(2). – P. 49–52. https://doi.org/10.26577/2409-6121-2015-2-2-49-52

14. Ilyasov A. M., Zhamanbalin M. B. Features of the production and calibration of reference hardness test blocks // Physical Sciences and Technology. – 2022. – Vol. 9(3–4). – P. 32–38. https://doi.org/10.26577/phst.2022.v9.i2.05

15. Iqbal A., Siddique S., Maqsood M., Atiq Ur Rehman M., Yasir M. Comparative analysis on the structure and properties of iron-based amorphous coating sprayed with the thermal spraying techniques // Coatings. – 2020. – Vol. 10(10). – P. 1006. https://doi.org/10.3390/coatings10101006

16. Logachev V. N., Litovchenko N. N. Electric arc metallization: ways to improve equipment and technology // Proceedings of GOSNITI. – 2014. – Vol. 117. – P. 228–234. (in Russian)

17. Johnston A. L., Hall A. C., McCloskey J. F. Effect of process inputs on coating properties in the twin-wire arc zinc process // Journal of Thermal Spray Technology. – 2013. – Vol. 22. – P. 856–863. https://doi.org/10.1007/s11666-013-9949-0

18. Kang S., et al. Influence of deposition parameters on the surface roughness and mechanical properties of coatings in thermal spray process // Journal of Thermal Spray Technology. – 2017. – Vol. 26(2). – P. 214–224. https://doi.org/10.1007/s11666-017-0526-7

19. Raza A., Ahmad F., Badri T. M., Raza M. R., Malik K. An influence of oxygen flow rate and spray distance on the porosity of HVOF coating and its effects on corrosion – A review // Materials. – 2022. – Vol. 15. – P. 6329. https://doi.org/10.3390/ma15186329

20. Chen W. L., Liu M., Xiao X. L., Zhang X. Effect of spray distance on the microstructure and high temperature oxidation resistance of plasma spray-physical vapor deposition 7YSZ thermal barrier coating // Materials Science Forum. – 2021. – Vol. 1035. – P. 511–520. https://doi.org/10.4028/www.scientific.net/MSF.1035.511

21. Syzdykova A. Sh. Tribologicheskie svojstva stal'nykh pokrytij, legirovannykh med'yu // Master's Journal. – 2015. – No. 2. – P. 66–70. (in Russian)

Information about authors:

Rakhadilov Baurzhan Korabayevich, PhD is a Director of PlasmaScienfce LLP (Ust-Kamenogorsk, Kazakhstan), e-mail: rakhadilovb@gmail.com

Magazov Nurtoleu Magzumbekovich, PhD candidate is a Researcher at the D. Serikbayev East Kazakhstan Technical University (Ust-Kamenogorsk, Kazakhstan), e-mail: magazovn@gmail.com

Molbossynov Yermakhan Serikuly, Bachelor of Sc. is a Technician at the D. Serikbayev East Kazakhstan Technical University (Ust-Kamenogorsk, Kazakhstan), e-mail: molbossynov.ye@edu.ektu.kz

Apsezhanova Akbota Kudaibergenkyzy is a Researcher at the D. Serikbayev East Kazakhstan Technical University (Ust-Kamenogorsk, Kazakhstan), e-mail: akbotaapsezhanova@gmail.com
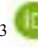
Kussainov Arystanbek Yerlanovich, PhD candidate is a Junior researcher at the D. Serikbayev East Kazakhstan Technical University (Ust-Kamenogorsk, Kazakhstan), e-mail: arys20055@gmai.com

Non-relativistic solutions of the modified Hylleraas potential in the presence of external magnetic and Aharonov-Bohm flux fields for heteronuclear diatomic molecules

E.P. Inyang[1] * , C.C. Ekechukwu[2] , I.M. Nwachukwu[1] ,

E.A. Thompson[2] , E.S. William[3] and K.M. Lawal[1]

[1]Department of Physics, National Open University of Nigeria, Jabi-Abuja, Nigeria
[2]Department of Physics, University of Calabar, Calabar, Nigeria
[3]Department of Physics, School of Pure and Applied Sciences, Federal University of Technology, Ikot Abasi, Nigeria
*e-mail: etidophysics@gmail.com; einyang@noun.edu.ng
(Received October 4, 2024; received in revised form March 13, 2025; accepted April 6, 2025)

In this study, we solve the Schrödinger equation with the modified Hylleraas potential (MHP) using the Nikiforov-Uvarov method in the presence of external magnetic and Aharonov-Bohm (AB) flux fields. We determine non-relativistic energy eigenvalues for various vibrational and magnetic quantum numbers, and examine the energy spectra of the MHP with and without these external fields for heteronuclear diatomic molecules like Carbon monoxide (CO) and hydrogen chloride (HCl). We observe that the presence of these fields increases the energy spectrum and breaks degeneracy. These findings could enable precision molecular spectroscopy, quantum control in molecular devices, and energy storage technologies. Additionally, we discover that the AB flux field has a more significant impact on the energy spectrum compared to the magnetic field. We also analyze the system's thermodynamic properties, including the partition function, mean energy, specific heat capacity, free energy, and entropy, providing valuable insights into its behavior. Generally, this study lays a foundation for further investigation into various quantum chemistry topics, highlighting how external fields can significantly influence the properties and behavior of molecular systems.

Key words: Thermodynamic properties; Schrödinger equation; Modified Hylleraas potential; Nikiforov-Uvarov method; Aharonov-Bohm flux.
PACS number(s): 03.65.Ge, 31.15.-p, 31.50.Bc, 33.20.Vq.

1 Introduction

The Schrödinger equation indeed lies at the focal point of the non-relativistic quantum mechanics, providing a fundamental framework for understanding the behavior of quantum systems. It's fascinating how, once solved, it encapsulates so much about a system, offering insights into its energy levels and wavefunctions [1-3]. Various potential models have been devised to describe interactions within quantum systems [4-6], and the modified Hylleraas potential model is one such approach. It is particularly useful in contexts where two charged particles interact, such as the nuclei in a diatomic molecule. The modified Hylleraas potential is valuable for understanding molecular structure and dynamics, offering unique advantages by accurately modeling both short- and long-range interactions. Unlike other potentials, it captures

complex quantum behaviors and allows precise exploration of field-induced effects on molecular energy spectra, providing deeper insights into molecular dynamics and enhancing quantum chemistry applications.The diverse methods researchers have developed to solve the Schrödinger equation with these potential models demonstrate the depth of exploration in quantum mechanics and the ongoing quest to understand complex systems at the quantum level [7-11]. The modified Hylleraas potential is given as;

$$V(r) = \frac{V_o}{b} \frac{\left(a - e^{-2\alpha r}\right)}{\left(1 - e^{-2\alpha r}\right)} \qquad (1)$$

where V_o is the depth of the potential well, a and b are the potential parameters, α is the screening parameter. The modified Hylleraas potential (MHP)

model is a short-range potential that can be used to describe interactions within molecular, atomic, or nuclear systems [12]. The MHP has been used extensively in recent studies involving diatomic molecules [13,14]. Currently, the effect of *magnetic* and Aharanov-Bohm (AB) flux fields on energy spectrum of quantum systems have been on the forefront research [15,16]. For instance, the investigation by Edet [17] on the Yukawa potential energy spectra and the work by Horchani et al. [18] on the inversely quadratic Yukawa potential highlight the importance of understanding how external fields affect these systems. Additionally, Ikot et al. [19] contribute by emphasizing the significance of external fields on energy spectra and magnetic properties. The appealing effects of magnetic and AB field on the energy spectra, thermodynamics and magnetic properties of systems motivates us to study the impact of these fields on the modified Hylleraas potential. The motivation comes from the fact that this potential model fines very useful application in a wide area of specialties in physics and chemical physics. In this paper, we present the solution to the Schrodinger equation (SE) for the MHP model in the presence of magnetic and AB flux fields using the Nikifarov-Uvarov method. Then the energy obtained is applied to measure the partition function and other thermodynamic functions such as; entropy, mean energy, free energy, and specific heat capacity. This paper is structured as follows: In Section 2, we provide the solution to the Schrodinger equation for the modified Hylleraas potential, accounting for magnetic and AB fields. In Section 3, the thermodynamic properties of the potential model under consideration are evaluated. The discussion of our findings is presented in Section 4, and our conclusion is presented in Section 5.

2 Theoretical frameworks

The Schrodinger equation for a particle moving in a cylindrical coordinate system within the modified Hylleraas potential under the combined effect of magnetic and AB fields can be stated as;

$$\left[\frac{1}{2\mu}\left(i\hbar\vec{\nabla} - \frac{e}{c}\vec{A} \right)^2 + \frac{V_o}{b}\frac{\left(a - e^{-2\alpha r}\right)}{\left(1 - e^{-2\alpha r}\right)} \right]\psi\left(r,\varphi\right) = E_{mn}\psi\left(r,\varphi\right) \tag{2}$$

where E_{mn} is the energy eigenvalues, r is inter nuclear distance and μ is the reduced mass of the system. $\vec{A}$ is the vector potential written as a superposition of two terms $\vec{A} = \vec{A}_1 + \vec{A}_2$ [16] having azimuthal component and external magnetic field with $\vec{\nabla}\times\vec{A}_1 = \vec{B}; \vec{\nabla}\times\vec{A}_2 = 0$, where $\vec{A}_1 = \frac{1}{2}\left(\vec{B}\times\vec{r}\right) = \frac{\vec{B}r}{2}\hat{\varphi}$, $\vec{B}$ is the magnetic field perpendicular to the plane of transversal motion of the particle, and $\vec{A}_2 = \frac{\phi_{AB}}{2\pi r}\hat{\varphi}$, ϕ_{AB} is the addition AB field created by a solenoid in a cylindrical coordinate [20].

The vector potential can be written more explicitly as;

$$\vec{A} = \left(\frac{\vec{B}r}{2} + \frac{\phi_{AB}}{2\pi r} \right)\hat{\varphi} \tag{3}$$

We define the wave function in Eq. (2) as $\psi\left(r,\varphi\right) = \frac{R(r)}{\sqrt{2\pi r}}e^{-im\varphi}$ where m is the magnetic quantum number and R(r) is the radial part of the wave function. Substituting the wave function and Eq. (3) into Eq. (2), we obtain a second order differential equation given as;

$$\frac{d^2R\left(r\right)}{d^2r} + \Im\frac{R(r)}{r^2} + \left(\frac{2\mu E}{\hbar^2} - \frac{\pi mB}{\phi_o} - \frac{\pi^2 B^2 r^2}{\phi_o^2} - \frac{2\pi\zeta B}{\phi_o} - \frac{2\mu V_o(a - e^{-2\alpha r})}{\hbar^2 b(1 - e^{-2\alpha r})} \right)R(r) = 0 \tag{4}$$

where $\quad \Im = \dfrac{1}{4} - m^2 - m\zeta - \zeta^2, \quad \phi_o = \dfrac{hc}{e} \quad$ and

$$\zeta = \dfrac{\phi_{AB}}{\phi_o}$$

The exact solution of Eq. (4) cannot be obtained; hence we find the approximate solution by introducing the Greene and Aldrich approximation [21] stated by Eq. (5) to handle the centrifugal term,

$$\frac{1}{r^2} = \frac{\alpha^2}{\left(1 - e^{-2\alpha r}\right)^2} \qquad (5)$$

The approximation here is valid for very small values of the screening parameter α. The Greene and Aldrich approximation simplifies the centrifugal term by replacing the angular momentum term with an effective potential, making the problem analytically solvable. However, this approximation assumes that the centrifugal force is weak, which may not hold in systems with high angular momentum or when the external fields significantly alter the molecular dynamics. This limitation could lead to reduced accuracy, especially for higher quantum numbers or stronger field strengths, where the centrifugal term plays a more prominent role. Considering the approximation stated in Eq. (5) and the transformation $z = e^{-2\alpha r}$, Eq. (4) is rewritten in terms of the new variable z as

$$\frac{d^2 R(z)}{dz^2} + \frac{(1-z)}{z(1-z)} \frac{dR(z)}{dz} + \frac{1}{z^2(1-z)^2}\left[-\gamma_1 z^2 + \gamma_2 z - \gamma_3 \right] R(z) = 0 \qquad (6)$$

where

$$\gamma_1 = \frac{2\mu E}{4\alpha^2 \hbar^2} - \frac{\pi m B}{4\alpha^2 \phi_o} - \frac{\pi \zeta B}{2\alpha^2 \phi_o} - \frac{\mu V_o}{2\alpha^2 \hbar^2 b}$$

$$\gamma_2 = -2\frac{2\mu E}{4\alpha^2 \hbar^2} + 2\frac{\pi m B}{4\alpha^2 \phi_o} + 2\frac{\pi \zeta B}{2\alpha^2 \phi_o} + a\frac{\mu V_o}{2\alpha^2 \hbar^2 b} + \frac{\mu V_o}{2\alpha^2 \hbar^2 b}$$

$$\gamma_3 = \frac{2\mu E}{4\alpha^2 \hbar^2} + \frac{\Im}{4} - a\frac{\mu V_o}{2\alpha^2 \hbar^2 b} - \frac{\pi m B}{4\alpha^2 \phi_o} - \frac{\pi^2 B^2}{4\phi_o^2} - \frac{\pi \zeta B}{2\alpha^2 \phi_o}$$

Equation (6) is a hypergeometric type second order differential equation which solvable by the Nikiforov-Uvarov (NU) method. Comparing the Eq. (6) to the standard NU equation [22] stated by Eq. (7), we obtain the requisite polynomials given by (8).

$$\psi^{\|}(z) + \frac{\tilde{\tau}(z)}{\sigma(z)} \psi^{\|}(z) + \frac{\tilde{\sigma}(z)}{\sigma^2(z)} \psi(z) = 0 \qquad (7)$$

$$\left. \begin{aligned} \tilde{\tau}(z) &= 1 - z \\ \sigma(z) &= z(1-z) \\ \sigma^2(z) &= z^2(1-z)^2 \\ \tilde{\sigma} &= \gamma_1 z^2 + \gamma_2 z + \gamma_3 \end{aligned} \right\} \qquad (8)$$

Using the polynomials in Eq. (8), another useful polynomial $\pi(z)$ is obtained as prescribed by the NU method. A brief review of the NU method is as presented by [22]. The Nikiforov-Uvarov method is chosen for its efficiency in providing better analytical solutions to second-order differential equations, simplifying complex potential models like the modified Hylleraas potential under external fields.

$$\pi(z) = -\frac{Z}{2} \pm \sqrt{\left(\beta - k\right)Z^2 + \left(\gamma_2 + k\right)Z + \gamma_3} \qquad (9)$$

where $\beta = \dfrac{1}{4} + \gamma_1$

Equating the discriminant of the quadratic expression within the square root sign to zero, and solving the ensuring equation for k.

$$k = -\left(\gamma_2 + 2\gamma_3\right) \pm 2\sqrt{\gamma_3}\sqrt{\beta + \gamma_2 + \gamma_3} \qquad (10)$$

Accepting the negative solution of k and substituting it into Eq.(9), we have

$$\pi(z) = -\frac{z}{2} \pm$$
$$\pm\left(\sqrt{\gamma_3} + \sqrt{\beta + \gamma_2 + \gamma_3}\right)z - \sqrt{\gamma_3} \quad (11)$$

We apply the relationship

$$\tau(z) = \breve{\tau}(z) + 2\pi(z) \quad (12)$$

Using Eqs. (8) and (11) another useful polynomial is obtained;

$$\tau(z) = 1 - 2z -$$
$$-2\left(\sqrt{\gamma_3} + \sqrt{\beta + \gamma_2 + \gamma_3}\right)z - 2\sqrt{\gamma_3} \quad (13)$$

Taking the first derivative of $\tau(z)$, we have;

$$\tau'(z) = -2 - 2\sqrt{\gamma_3} - 2\sqrt{\beta + \gamma_2 + \gamma_3} \quad (14)$$

Equating the parameter λ defined by Eqs. (15) and (16) respectively, we obtain a quantity which contain the energy eigenvalues as given by Eq. (17)

$$\lambda_n = -n\tau'(z) + \frac{n(n-1)}{2}\sigma''(z) = 0 \quad (15)$$

$$\lambda = k_- + \pi'_-(z) \quad (16)$$

$$\gamma_3 = \left[\frac{-\frac{1}{2}\left[\left(n + \frac{1}{2} + \sqrt{\chi}\right)^2 + \frac{1}{4} + \rho\right]}{\left(n + \frac{1}{2} + \sqrt{\chi}\right)}\right]^2 \quad (17)$$

where
$$\chi = \beta + \gamma_2 + \gamma_3$$
$$\rho = \gamma_3 - \beta$$

Substituting the parameters γ_1, γ_2 and γ_3 as earlier defined into Eq. (17), we obtain the non-relativistic energy eigenvalue of the MHP;

$$E_{nm} = \left[aV_o + \frac{\hbar\omega_c}{4}(m+\zeta) + \frac{\alpha^2\mu\omega_c^2}{8} - \frac{1}{4}\left(\frac{1}{4} - m^2 - m\zeta - \zeta^2\right) - \frac{1}{4}\left\{\frac{\left(n+\frac{1}{2}+\sqrt{\chi}\right)^2 + \frac{\pi^2B^2}{4\phi_o^2} + \frac{a\mu V_o}{2\alpha^2\hbar^2b} - \frac{\mu V_o}{2\alpha^2\hbar^2b}}{\left(n+\frac{1}{2}+\sqrt{\chi}\right)}\right\}\right] \quad (18)$$

where
$$\chi = \frac{1}{4} + \frac{\pi^2B^2}{4\phi_o^2} - \frac{1}{4}\left(\frac{1}{4} - m^2 - m\zeta - \zeta^2\right),$$

$\omega_c = \dfrac{eB}{hc}$ is the cyclotron frequency and m is the magnetic quantum number given as $m = \ell + \dfrac{1}{2}$. For our purpose Eq. (18) can written in a more compact form as

$$E_{nm} = A_1 - \frac{\hbar^2\alpha^2}{2\mu}\left[\frac{(n+A_2)^2 + A_3}{n+A_2}\right]^2 \quad (19)$$

where

$$A_1 = aV_o + \frac{\hbar\omega_c}{4}(m+\zeta) + \frac{\alpha^2\mu\omega_c^2}{8} - \frac{1}{4}\left(\frac{1}{4} - m^2 - m\zeta - \zeta^2\right)$$

$$A_2 = \frac{1}{2} + \frac{1}{2}\sqrt{1 + \frac{\pi^2B^2}{\phi_o^2} - \left(\frac{1}{4} - m^2 - m\zeta - \zeta^2\right)}$$

$$A_3 = \frac{\pi^2B^2}{4\phi_o^2} + \frac{a\mu V_o}{2\alpha^2\hbar^2b} - \frac{\mu V_o}{2\alpha^2\hbar^2b}$$

3 Thermodynamic properties of the modifed Hylleraas potential

The thermodynamic properties of a system are easily obtained when the partition function of the system is known [23]. However, the partition function (PF) is determined by obtaining the summation of all possible vibration energy of the system. Given the energy spectrum of stated in Eq. (19), the partition function $Z(\beta)$ for the MHP at a finite temperature T, is calculated in terms of the Boltzmann factor.

$$Z(\beta) = \sum_{n=0}^{n_{max}} e^{(-\beta E_{mn})} \tag{20}$$

where $\beta = \dfrac{1}{k_B T}$, k_B is the Boltzmann constant.

By substituting the energy spectrum in Eq. (19) into Eq. (20), the partition function is given as

$$Z(\beta) =$$
$$= \sum_{n=0}^{n_{max}} \text{Exp}\left\{-\beta\left(A_1 - \frac{\hbar^2\alpha^2}{2\mu}\left[\frac{(n+A_2)^2 + A_3}{n+A_2}\right]^2\right)\right\} \tag{21}$$

Let $x = \dfrac{\hbar^2\alpha^2}{2\mu}, q = -A_1, t = n + A_2, p = xA_3^2$

The partition function $Z(\beta)$ becomes;

$$Z(\beta) = \sum_{n=0}^{n_{max}} \text{Exp}\left[\beta q + \beta x t^2 - \frac{\beta p}{t^2}\right] \tag{22}$$

Writing Eq. (22) in integral form we have;

$$Z(\beta) = \int_0^{n_{max}} e^{xt^2\beta - \frac{p\beta}{t^2} + \beta q} dt \tag{23}$$

Using Maple 10.0 version, the partition function of Eq. (23) can be evaluated as

$$Z(\beta) = \frac{e^{xt\beta + \beta q\sqrt{-p\beta}}\left(\dfrac{2n_{max}e^{\frac{p\beta}{n_{max}^2}}}{\sqrt{-p\beta}} - 2\sqrt{p}\sqrt{\beta}\sqrt{\pi}\dfrac{\text{erfi}\left(\dfrac{\sqrt{p}\sqrt{\beta}}{n_{max}}\right)}{\sqrt{-p\beta}} - 2\sqrt{\pi}\right)}{2} \tag{24}$$

And the imaginary error function *erfi*(y) is defined as follows

$$erfi(y) = \frac{erf(iy)}{i} = \frac{2}{\sqrt{\pi}}\int_0^y e^{t^2} dt. \tag{25}$$

Using Eq. (24) other thermodynamic relations are found as follows:

(a) vibrational mean energy

$$U(\beta) = -\frac{\partial InZ(\beta)}{\partial\beta} \tag{26}$$

(b) Vibrational specific heat capacity

$$C(\beta) = k_B\beta^2\left(\frac{\partial^2 InZ(\beta)}{\partial^2\beta}\right) \tag{27}$$

(c) Vibrational free energy

$$F(\beta) = -k_B T InZ(\beta) \tag{28}$$

(d) Vibrational entropy

$$S(\beta) = k_B InZ(\beta) - k_B\beta\frac{\partial InZ(\beta)}{\partial\beta} \tag{29}$$

31

4 Results and discussion

The study of heteronuclear diatomic molecules such as carbon monoxide (CO) and hydrogen chloride (HCl) is crucial due to their diverse applications in atmospheric science, spectroscopy, and industrial processes. Their unique bond properties, dipole moments, and vibrational-rotational spectra provide critical insights into molecular dynamics, advancing chemical analysis, environmental monitoring, and quantum information systems. To validate our findings, we employed spectroscopic data from Table 1 to analyze the energy levels of HCl and CO under external magnetic and Aharonov-Bohm (AB) flux fields. The analysis utilized the following referenced values:

$$1 \text{ amu} = 931.494028 \text{ MeV}/c^2,$$
$$1 \text{ } cm^{-1} = 1.239841875 \times 10^{-4} eV, \text{ and}$$
$$\hbar c = 1973.29 \text{ eV A}$$

[24] in our calculations. Tables 2 and 3 present the energy levels for the modified Hylleraas potential of HCl and CO, respectively, considering the influence of AB flux field (ζ) and external magnetic field (B) across various magnetic (m) and vibrational (n) quantum numbers using Equation (19). The Aharonov-Bohm (AB) effect is a quantum mechanical phenomenon where a charged particle experiences a phase shift when moving around a region with a magnetic field, even if the magnetic field is zero along the particle's path. The AB flux field represents the effect of this phenomenon on the molecule's energy levels. We observed degeneracy when both fields are absent (ζ = B = 0) for m = 1 and m = -1. Under the exclusive influence of the magnetic field (B $\neq$ 0; ζ = 0), energy levels rise, eliminating degeneracy while retaining quasi-degeneracy. Sole exposure to the AB field (B = 0; $\zeta \neq 0$) abolishes degeneracy, confining the system further. Consequently, the combined impact of both fields surpasses individual effects, causing a significant shift in the system's energy spectrum. This suggests that the interaction between the AB flux field and the external magnetic field alters the energy levels in a more pronounced manner than either field acting alone. In Figures 1 to 5, we plotted the thermodynamic functions against the temperature for selected heteronuclear diatomic molecules. Figure 1 depicts the partition function for HCl and CO. It was observed that as the temperature

increases the molecules energy decreases. This implies that at higher temperatures, the distribution of these molecules among their energy states decreases rather than increases. Also, Fig 2 indicates a shape increase in the mean energy at almost zero temperature and an exponential decrease as the temperature increases. This behavior is consistent with the Boltzmann distribution, which describes the distribution of energy among the different energy states of a system at thermal equilibrium. At higher temperatures, particles are distributed among a greater number of energy states, resulting in a decrease in the average energy per particle. In Fig. 3 we observed that there is a linear increase between the two molecules as both the specific heat capacity and temperature increases. The linear increase in specific heat capacity with temperature may be indicative of various physical processes occurring within the molecules as temperature rises. For example, in gases, increasing temperature leads to greater molecular motion and vibrational modes becoming active, which require more energy to excite. In solids, higher temperatures may lead to increased thermal expansion and more pronounced lattice vibrations, contributing to higher specific heat capacities. Fig. 4 shows a rapid increase in free energy at a constant temperature and it begins to converge when the temperature increases. The rapid increase in free energy at constant temperature may correspond to the onset of a phase transition or chemical reaction, where the system undergoes a significant change in its internal structure or composition. The convergence of free energy with increasing temperature may indicate the stabilization of the system as temperature increases, leading to a reduction in the rate of change of free energy with temperature. The entropy against temperature is plotted in Fig. 5. We observed that as the temperature increase, the molecules entropy is seen to increase. The observed increase in entropy with increasing temperature is consistent with the general trend observed in many systems. As the temperature rises, the molecules in the system gain more thermal energy, leading to increased molecular motion and a greater number of accessible microstates. This increased molecular disorder contributes to an overall increase in the system's entropy. The increase in entropy with temperature has significant implications for various physical and chemical processes. For example, in phase transitions such as melting or vaporization, the increase in entropy with temperature plays a crucial role in determining the conditions under which these transitions occur.

Table 1 – Spectroscopic parameters of the selected heteronuclear diatomic molecules [25].

Molecules	$D_e(eV)$	$\alpha^{-9}\left(\overset{\circ}{A}^{-1}\right)$	$r_e(\dot{A})$	$\mu(MeV)$
HCl	4.6190309050	1.86770	1.2746	0.09129614886
CO	11.225600000	2.29940	1.1283	0.63906749030

Table 2 – Eigenvalues (eV) for the modified Hylleraas potential for CO molecule with and without *B* and *AB* flux fields.

m	n	B = 0; ζ = 0	B = 5 T; ζ = 0	B = 0; ζ = 5	B = 5 T; ζ = 5
1	0	-10:89413685	-10:89412694	-10:88701166	-10:88700163
	1	-10:79366351	-10:79365356	-10:78663755	-10:78662748
	2	-10:69458650	-10:69457650	-10:68765794	-10:68764782
	3	-10:59688007	-10:59687002	-10:59004712	-10:59003695
0	0	-10:89437452	-10:89436462	-10:88843594	-10:88842593
	1	-10:79389787	-10:79388793	-10:78804200	-10:78803194
	2	-10:69481761	-10:69480762	-10:68904293	-10:68903282
	3	-10:59710798	-10:59709795	-10:59141299	-10:59140284
-1	0	-10:89413685	-10:89412696	-10:88938567	-10:88937567
	1	-10:79366351	-10:79365358	-10:78897851	-10:78896846
	2	-10:69458650	-10:69457652	-10:68996645	-10:68995636
	3	-10:59688007	-10:59687004	-10:59232377	-10:59231363

Table 3 – Eigenvalues (eV) for the modified Hylleraas potential for HCl molecule with and without *B* and *AB* flux fields.

| m	n	B = 0; ζ = 0	B = 5 T; ζ = 0	B = 0; ζ = 5	B = 5 T; ζ = 5
1	0	-3:962892968	-3:962876513	-3:911543641	-3:911526223
	1	-3:805044609	-3:805027813	-3:756800366	-3:756782607
	2	-3:656677388	-3:656660250	-3:611292839	-3:611274738
	3	-3:517046921	-3:517029442	-3:474300445	-3:474282003
0	0	-3:964628515	-3:964612149	-3:921703713	-3:921686402
	1	-3:806674860	-3:806658153	-3:766347643	-3:766329991
	2	-3:658210692	-3:658193643	-3:620275626	-3:620257633
	3	-3:518490814	-3:518473424	-3:482762382	-3:482744047
-1	0	-3:962892968	-3:962876683	-3:928507319	-3:928490109
	1	-3:805044609	-3:805027984	-3:772740459	-3:772722907
	2	-3:656677388	-3:656660421	-3:626290068	-3:626272175
	3	-3:517046921	-3:517029612	-3:488427730	-3:488409495
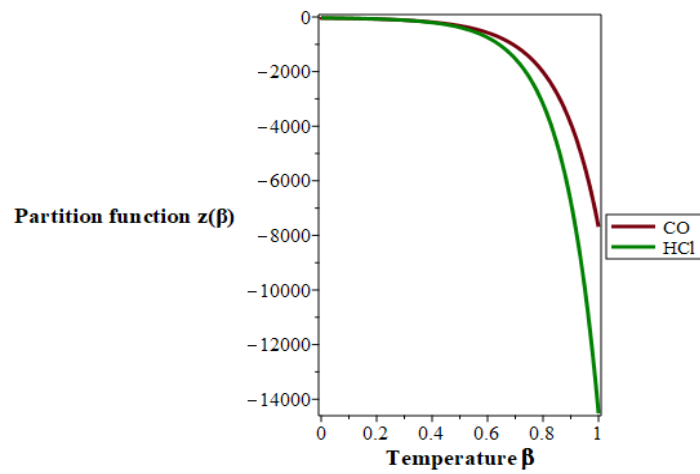
Figure 1 – Variation of the partition function $Z(\beta)$ versus temperature (β) for selected heteronuclear diatomic molecules.
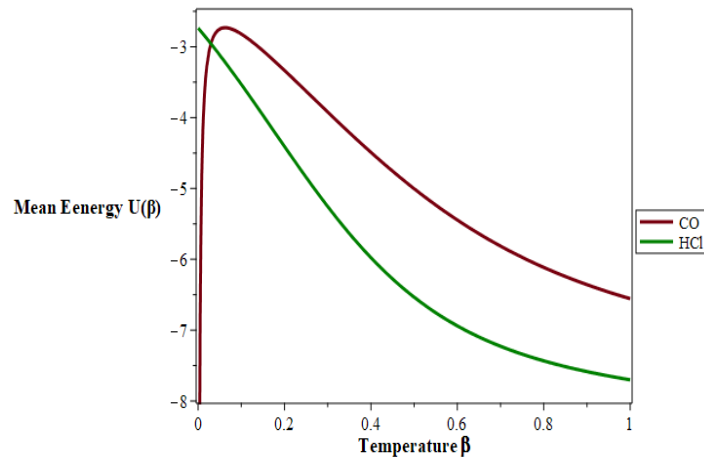

Figure 2 – Variation of the mean energy $U(\beta)$ versus temperature (β) for selected heteronuclear diatomic molecules.
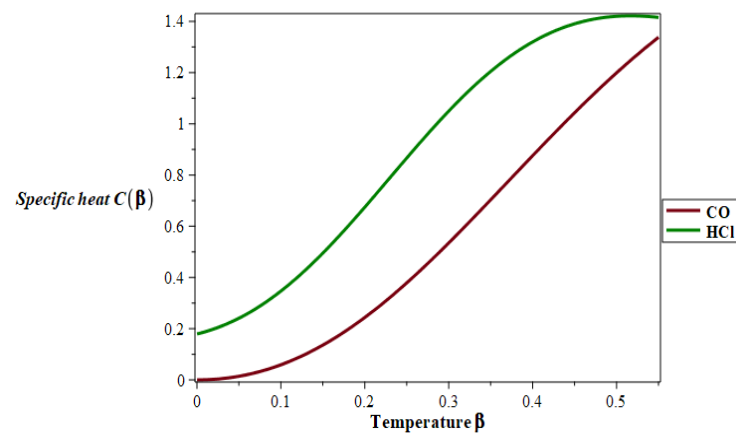

Figure 3 – Variation of the specific heat $C(\beta)$ versus temperature (β) for selected heteronuclear diatomic molecules.
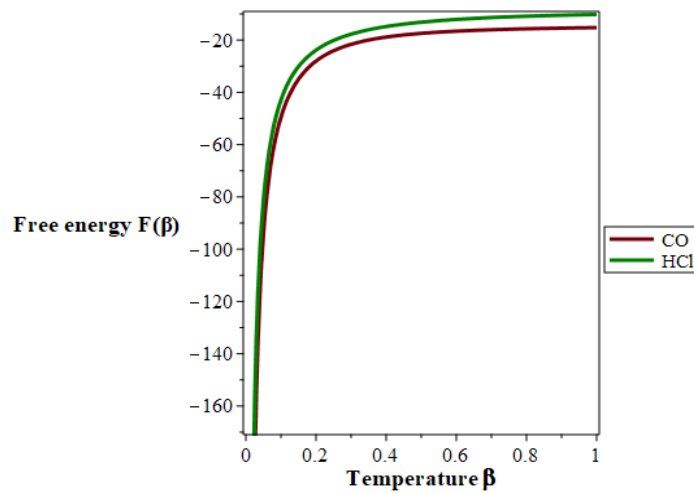
Figure 4 – Variation of the free energy $F(\beta)$ versus temperature (β) for selected heteronuclear diatomic molecules.
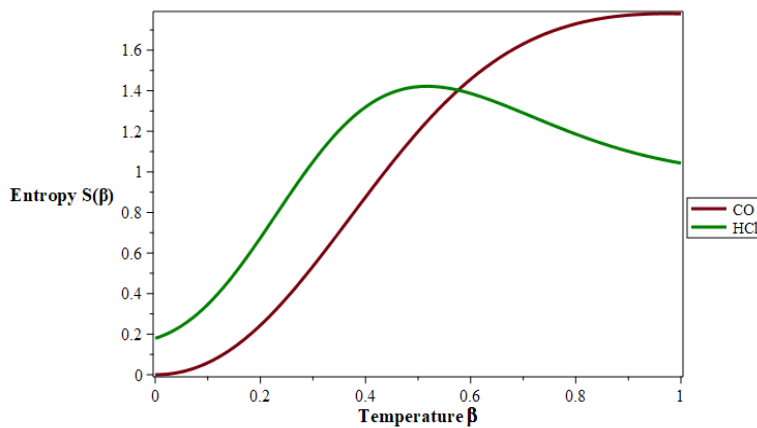

Figure 5 – Variation of the entropy $S(\beta)$ versus temperature (β) for selected heteronuclear diatomic molecules.

5 Conclusion

This work presents an analytical solution to the Schrödinger equation (SE) with the modified Hylleraas potential using the Nikiforov-Uvarov (NU) method, incorporating external magnetic and Aharonov-Bohm (AB) flux fields. The study calculates non-relativistic energy eigenvalues for various vibrational and magnetic quantum numbers and examines the influence of these fields on the energy spectra of heteronuclear diatomic molecules like CO and HCl. Degeneracy is observed in the absence of external fields, while the application of a magnetic field increases energy eigenvalues, breaking degeneracy but leaving some quasi-degeneracy. The AB field has a stronger effect, further reducing degeneracy and raising energy levels compared to the magnetic field. When both fields are applied, their combined impact exceeds their individual effects. The thermodynamic properties of the system, including the partition function, mean energy, specific heat capacity, free energy, and entropy, are analyzed and visualized, providing deeper insights into molecular behavior under external fields. This study establishes a foundation for exploring various quantum chemistry topics, illustrating how external fields can significantly influence molecular properties. The findings have implications for quantum technology development

and molecular physics, enabling advancements in field-tunable molecular systems for quantum sensors, quantum information processing, and advanced material design. Future research could extend these methods to more complex molecular systems and investigate the effects of diverse external field configurations.

References

1. Thompson E. A., Inyang E. P., William E. S. Analytical determination of the non-relativistic quantum mechanical properties of near doubly magic nuclei // Physical Sciences and Technology. -2021. -Vol. 8. -No.3-4. -P. 10-21. https://doi.org/10.26577/phst.2021.v8.i2.02

2. Inyang E.P., Obisung E.O., Amajama J., Bassey D.E., William E.S., Okon I.B. The effect of topological defect on the mass spectra of heavy and heavy-light quarkonia // Eurasian Physical Technical Journal. – 2022. – Vol. 19. – No. 4. – P. 78–87. https://doi.org/10.31489/2022No4/78-87

3. Nwabuzor P., Edet C., Ikot A.N., Okorie U., Ramantswana M., Horchani R., Abdel-Aty A., Rampho G. Analyzing the effects of topological defect (TD) on the energy spectra and thermal properties of LiH, TiC and I_2 diatomic molecules // Entropy. – 2021. – Vol. 23. – No. 8. – P. 1060. https://doi.org/10.3390/e23081060

4. Eyube E.S., Yusuf I., Omugbe E., Makasson C.R., Onate C.A., Mohammed B.D., Balami B.Y., Tahir A.M. Energy spectrum and magnetic susceptibility of the improved Pöschl-Teller potential // Physica B: Condensed Matter. – 2024. – Vol. 694. – P. 416483. https://doi.org/10.1016/j.physb.2024.416483

5. Allosh M., Mustafa Y., Ahmed N.K., Mustafa A.S. Ground and excited state mass spectra and properties of heavy-light mesons // Few-Body Systems. – 2021. – Vol. 62. – P. 26. https://doi.org/10.1007/s00601-021-01608-1

6. Mutuk H. Cornell Potential: A neural network approach // Advances in High Energy Physics. – 2019. – Vol. 2019. – P. 3105373. https://doi.org/10.1155/2019/3105373

7. Kumar R., Singh R.M., Bhahardivaj S.B., Rani R., Chand F. Analytical solutions to the Schrödinger equation for generalized cornell potential and its application to diatomic molecules and heavy mesons // Modern Physics Letters A. – 2022. – Vol. 37. – P. 2250010. https://doi.org/10.1142/S0217732322500109

8. Kharusi A.I., Omama, Horchani R., Ikot A. Non-relativistic and relativistic energy of molecules in external fields with time-dependent moving boundaries // The European Physical Journal Plus. – 2024. – Vol. 139. – No. 9. – P. 818. https://doi.org/10.1140/epjp/s13360-024-05603-3

9. Abu-Shady M., Inyang E.P. Heavy-light meson masses in the framework of trigonometric Rosen-Morse potential using the generalized fractional derivative // East European Journal of Physics. – 2022. – Vol. 4. – P. 80–87. https://doi.org/10.26565/2312-4334-2022-4-06

10. Ikot A.N., Okorie U.S., Amadi P.O., Edet C.O., Rampho G.J., Sever R. The Nikiforov-Uvarov–functional analysis (NUFA) method: A new approach for solving exponential-type potentials // Few-Body Systems. – 2021. – Vol. 62. – P. 9. https://doi.org/10.1007/s00601-021-021-01593-5

11. Edet C.O., Osang J.E., Ali N., Agbo E.P., Aljunid S.A., Endut R., et al. Non-relativistic energy spectra of the modified Hylleraas potential and its thermodynamic properties in arbitrary dimensions // Quantum Reports. – 2022. – Vol. 4. – No. 3. – P. 238–250. https://doi.org/10.3390/quantum4030016

12. Ikot A.N., Awoga O.A., Antia A.D. Bound state solutions of d–dimensional Schrödinger equation with Eckart potential plus modified deformed Hylleraas potential // Chinese Physics B. – 2013. – Vol. 22. – No. 2. – P. 304-324.

13. Ikot A.N. Solution of Dirac equation with generalised Hylleraas potential // Communications in Theoretical Physics. – 2013. – Vol. 59. – No. 3. – P. 268–272. https://doi.org/10.1088/0253-6102/59/3/04

14. Onyeaju M.C., Ikot A.N., Onate C.A., Ebomwonyi O., Udoh M.E., Idiodi J.O. Approximate bound state solutions of the Dirac equation with some thermodynamic properties for the deformed Hylleraas plus deformed Woods-Saxon potential // The European Physical Journal Plus. – 2017. – Vol. 132. – P. 302. https://doi.org/10.1140/epjp/i2017-11573-x

15. Karayer H. Study of the radial Schrödinger equation with external magnetic and AB flux fields by the extended Nikiforov–Uvarov method // The European Physical Journal Plus. – 2020. – Vol. 135. – No. 1. – P. 1–10. https://doi.org/10.1140/epjp/s13360-020-00131-2

16. Antonakos C., Terzis A.F. Aharonov–Bohm effect as a diffusion phenomenon // Foundations of Physics. – 2024. – Vol. 54. – No. 4. – P. 53. https://doi.org/10.48550/arXiv.2307.06683

17. Edet C.O., Ikot A.N., Okorie U.S., Rampho G.J., Ramantswana M., Horchani R., et al. Persistent current, magnetic susceptibility and thermal properties for a class of Yukawa potential in the presence of external magnetic and Aharonov–Bohm fields // International Journal of Thermophysics. – 2021. – Vol. 42. – P. 138.

18. Horchani R., Al-Aamri H., Al-Kindi N., Ikot A.N., Okorie U.S., Rampho G.J., Jelassi H. Energy Spectra and Magnetic Properties of Diatomic Molecules in the Presence of Magnetic and AB Fields with the Inversely Quadratic Yukawa Potential // The European Physical Journal D. – 2021. – Vol. 75. – No. 1. – P. 1–13. https://doi.org/10.1140/epjd/s10053-021-00038-2

19. Ikot A.N., Rampho G.J., Edet C.O., Okorie U.S. Energy spectra and thermal properties of diatomic molecules in the presence of magnetic and AB field with improved Kratzer potential // Molecular Physics. – 2020. https://doi.org/10.1080/00268976.202.1821922

20. Okorie U.S., Edet C.O., Ikot A.N., Rampho G.J., Sever R. Thermodynamic functions for diatomic molecules with modified Kratzer plus screened Coulomb potential // Indian Journal of Physics. – 2019. – Vol. 19. – P. 12648. https://doi.org/10.1007/s12648-019-01670-w

21. Greene R. L., Aldrich C. Variational wave functions for a screened Coulomb potential // Phys. Rev. A. -1976. -Vol.14. -P. 2363. https://doi.org/10.1103/PhysRevA.14.2363

22. Nikiforov S.K., Uvarov V.B. Special functions of mathematical physics. – Basel: Birkhäuser, 1988.

23. Okorie U.S., Ikot A.N., Chukwuocha E.O., Onyeaju M.C., Amadi P.O., Sithole M.J., Rampho G.J. Energies spectra and thermodynamic properties of hyperbolic Pöschl–Teller potential (HPTP) model // International Journal of Thermophysics. – 2020. – Vol. 41. – P. 1–15. https://doi.org/10.1007/s10765-020-02671-2

24. Reggab K. Approximate resolutions of the Schrödinger theory applying the WKB approximation for certain diatomic molecular interactions // Journal of Molecular Modeling. – 2024. – Vol. 30. – No. 10. – P. 358. https://doi.org/10.1007/s00894-024-06143-4

25. Inyang E.P., William E.S., Ntibi J.E., Obu J.A., Iwuji P.C., Inyang E.P. Approximate Solutions of the Schrödinger Equation with Hulthen Plus Screened Kratzer Potential Using the Nikiforov-Uvarov-Functional Analysis Method: An Application to Diatomic Molecules // Canadian Journal of Physics. – 2022. – Vol. 100. – No. 10. https://doi.org/10.1139/cjp-2022-0030

Information about authors:

Etido P. Inyang, PhD is a Lecturer at the Department of Physics, National Open University of Nigeria (Jabi-Abuja, Nigeria), email: etidophysics@gmail.com , einyang@noun.edu.ng

Christopher C. Ekechukwu, MSc is a Lecturer at the Department of Physics, University of Calabar, (Calabar, Nigeria), e-mail: ekehmore@gmail.com

Iheke M. Nwachukwu, PhD is a Lecturer at the Department of Physics, National Open University of Nigeria (Jabi-Abuja,Nigeria), e-mail: inwachukwu@noun.edu.ng

Edet A. Thompson, PhD is a Lecturer at the Department of Physics, University of Calabar (Calabar, Nigeria), e-mail: edyythompson@gmail.com

Eddy S. William, PhD is a Lecturer at the Department of Physics, School of Pure and Applied Sciences, Federal University of Technology (Ikot Abasi, Nigeria), e-mail: williameddyphysics@gmail.com

Kolawole M. Lawal, PhD is a Lecturer at the Department of Physics, National Open University of Nigeria (Jabi-Abuja,Nigeria), e-mail: kmlawal@noun.edu.ng

Solar magnetic activity and its terrestrial impact through correlations with drought indices

A. Sarsembayeva[1*] ID , L. Ryssaliyeva [1] ,

F. Belissarova[1] ID and A. Sarsembay[2] ID

[1]Al-Farabi Kazakh National University, Almaty, Kazakhstan
[2]CSI «Kyzylorda Regional Educational Center (Methodological Office)»
of the Department of Education of Kyzylorda Region, Kyzylorda, Kazakhstan
*e-mail: sarsembaeva.a@kaznu.kz
(Received April 5, 2025; received in revised form May 17, 2025; accepted May 26, 2025)

Solar activity manifests itself in the form of sunspots on the solar surface and solar flares, which can influence Earth's climatic conditions, including drought in mid-latitude regions. This study examines the impact of solar flares on drought conditions in Northern Kazakhstan and analyzes the relationship between solar activity parameters and drought indices. Twelve solar flares of classes X and M recorded in 2014 were analyzed using multi-wavelength data from SDO/AIA, GOES, and HMI/SOLIS magnetograms. Key physical parameters of the flares were determined, including duration, spatial scale, and magnetic reconnection rate. The reconnection rates ranged from 10^{-4} to 10^{-3} and showed an inverse dependence on the GOES classification, consistent with the Petschek reconnection theory. Additionally, correlation links were investigated between solar activity indices (WSN, SSN), atmospheric oscillations (NAO, AO), and drought indices (SPI3, HTC). Significant strong correlations were established: between WSN and NAO ($r = 0.63$), NAO and SPI3 ($r = 0.70$), as well as a strong negative correlation between SSN and HTC ($r = -0.66$), indicating a potential connection between solar activity and drought formation in temperate regions.

Key words: solar flares, magnetic reconnection, sunspot activity, drought indices, atmospheric oscillations.
PACS number(s): 96.60.−j; 96.60.Iv; 96.60.qe.

1 Introduction

Solar activity plays a crucial role in driving dynamic processes within the solar atmosphere and throughout the heliosphere, exerting measurable influence on the Earth's magnetosphere, ionosphere, and atmospheric systems [1]. Among the most energetic manifestations of solar activity are solar flares – sudden, intense releases of energy across the entire electromagnetic spectrum. These events are accompanied by bursts of X-rays, ultraviolet radiation, and radio waves, reflecting the rapid acceleration of charged particles and the presence of high-temperature plasma. The primary mechanism responsible for such rapid energy release is magnetic reconnection, which occurs in regions of strongly sheared or oppositely directed magnetic fields in the solar corona [2-3].

Solar flares are well known for their impact on space weather conditions, including transient increases in high-energy particle fluxes, cosmic ray modulation, and the intensification of the solar wind. These phenomena lead to compression of the Earth's magnetosphere, often resulting in geomagnetic storms with an observed delay of approximately 36 hours after the flare event. Observational data from missions such as SOHO, STEREO, and the Solar Dynamics Observatory (SDO) have enabled high-resolution, multi-wavelength imaging of these events, allowing detailed reconstruction of their physical parameters. Nevertheless, the volume and cadence of full-disk, high-temporal-resolution imagery present computational challenges for data access and processing [4].

In this study, we analyze 12 major X- and M-class solar flares recorded between January 2014 and December 2024, employing multi-wavelength imaging from AIA/SDO and magnetograms from HMI, SOLIS, and GOES. We estimate key physical properties of these flares – including duration, spatial scale, magnetic flux density, and reconnection rate – to characterize the flare energetics and reconnection dynamics. Our results

reveal notable trends, including a broader size distribution for weaker GOES classes, a lower threshold in magnetic flux density that depends on flare class, and a decreasing reconnection rate with increasing flare magnitude. Calculated inflow velocities range from a few to several tens of kilometers per second, while estimated coronal Alfvén velocity fall within the 10^3–10^4 km/s range, yielding dimensionless reconnection rates on the order of 10^{-3} – consistent with theoretical predictions from fast reconnection models.

Beyond the immediate impacts on the near-Earth environment, long-term solar variability, as indexed by sunspot numbers such as SSN, WSN, and GSN, is increasingly recognized as a potential driver of terrestrial climate modulation. These indices follow an approximate 11-year solar cycle [5-6] and have been statistically associated with cyclic variations in surface temperature, precipitation, and large-scale atmospheric oscillations. Although the overall variation in total solar irradiance is small (~0.04%), the resulting changes in upper atmospheric dynamics – particularly through enhanced UV radiation and stratospheric heating – can significantly influence tropospheric circulation patterns. Empirical studies have linked solar activity to modulations in the El Niño–Southern Oscillation (ENSO), Arctic Oscillation (AO), and North Atlantic Oscillation (NAO), which serve as critical regulators of climate variability, particularly in the Northern Hemisphere [7-9].

However, the climatic response to solar forcing is region-dependent and often non-linear. In West Africa, for instance, positive correlations between solar activity and both temperature and precipitation have been reported, particularly during solar minima, often resulting in intensified heat extremes [10-11]. Similarly, studies in India have identified links between solar cycles and monsoonal variability [12-13]. In contrast, regions such as East Africa, the United States, and Saudi Arabia show weaker or statistically insignificant correlations [14-15], potentially due to hemispheric asymmetry in sunspot distribution and flare emergence [16].

Given these complexities, the current study takes an interdisciplinary approach, bridging solar physics and atmospheric science to investigate the impact of solar magnetic activity and flare energy release on regional drought conditions. Specifically, we explore how flare-scale parameters – such as reconnection rate and spatial scale – correlate with

climate indicators including the Standardized Precipitation Index (SPI3) and the Selyaninov Hydrothermal Coefficient (HTC), using data from Northern Kazakhstan, a region highly vulnerable to agricultural drought. We further examine the role of atmospheric teleconnections such as NAO and AO, which may act as intermediaries in the solar–climate interaction.

2 Data analysis

The energy released during a solar flare can be attributed to the magnetic energy stored in the solar corona, which is generally expressed as a function of the flare's characteristic spatial scale and the magnetic flux density present in the active region [17].

$$E_{flare} \sim E_{mag} = \frac{B_{cor}^2}{8\pi} L^3 \qquad (1)$$

Since the liberated magnetic energy corresponds to the energy transported into the magnetic reconnection region, the rate of energy release can be formulated based on the inflow velocity of plasma into this region [18-20].

$$\left|\frac{dE_{mag}}{dt}\right| \sim 2\frac{B_{cor}^2}{4\pi} V_{in} L^2 \qquad (2)$$

Accordingly, the duration required for this inflow to supply the total energy released by the flare provides an estimate of the flare's characteristic timescale.

$$\tau_{flare} \sim E_{flare}\left(\left|\frac{dE_{mag}}{dt}\right|\right)^{-1} \sim \frac{L}{4V_{in}} \qquad (3)$$

This relationship allows for the determination of the plasma inflow velocity using observationally derived timescale values.

$$V_{in} \sim \frac{L}{4\tau_{flare}} \qquad (4)$$

To assess the reconnection process $M_A \equiv \frac{V_{in}}{V_A}$, in a dimensionless framework, we must estimate the Alfvén velocity $V_A = \frac{B_{cor}}{(4\pi\rho)^{1/2}}$ in the inflow region, which depends on the coronal magnetic field strength and plasma density. Therefore, by measuring the coronal density B_{cor}, flare size L,

magnetic field strength, and flare duration τ_{flare}, it becomes possible to compute key physical parameters: the plasma inflow velocity V_{in}, the Alfvén velocity V_A, and the corresponding magnetic reconnection rate M_A [21-22].

Observational data for this analysis is provided in near real-time by the Geostationary Operational Environmental Satellites (GOES), which monitor solar flares and associated energetic particles. In particular, data from GOES-13, GOES-14, and GOES-15 were used to track X-ray flux variations during flare events.

Beyond solar flare diagnostics, this study also investigates the climatic impact of solar activity on regional drought in Northern Kazakhstan – a region of significant agricultural importance and sensitivity to climate variability. In particular, drought events pose a major threat to wheat production, with losses reaching up to 50% in dry years and leading to substantial economic damage.

Meteorological data for the year 2014 were obtained from the Republican State Enterprise "Kazhydromet", under the Ministry of Ecology and Natural Resources. These data include monthly total precipitation and daily mean air temperature from 11 ground-based weather stations across the North Kazakhstan region. Based on these inputs, two drought indices were computed: the Standardized Precipitation Index (SPI) and the Selyaninov Hydrothermal Coefficient (HTC).

The SPI is a globally recognized index recommended by the World Meteorological Organization (WMO). It is based solely on precipitation and is suitable for assessing drought over various time scales. SPI is calculated by fitting precipitation data to a gamma distribution, which is then transformed into a normal distribution. Positive SPI values indicate wetter-than-average conditions, while negative values reflect meteorological drought [23].

The Selyaninov Hydrothermal Coefficient (HTC) is commonly used in agricultural climatology to assess moisture availability. It is defined as:

$$HTC = \frac{\sum R}{0.1 \sum t} \qquad (5)$$

where: t is the sum of average daily air temperatures during the period when air temperatures are above +10 °C, and R is the total precipitation during the same period, in mm [24].

Additionally, the North Atlantic Oscillation (NAO) and Arctic Oscillation (AO) indices were incorporated to assess atmospheric circulation influences. NAO data were retrieved from the National Centers for Environmental Information (NCEI) under NOAA, while AO data were obtained from the Physical Sciences Laboratory (PSL) of NOAA's Earth System Research Laboratories [25-26].

By integrating solar flare diagnostics with regional drought indices and large-scale atmospheric oscillation data, we aim to quantify the extent to which solar magnetic activity and flare dynamics may influence terrestrial climate variability and drought risk across continental mid-latitudes.

3 Results

This study integrates solar flare diagnostics with atmospheric circulation and drought indices to investigate the potential solar-terrestrial coupling mechanisms influencing regional hydrometeorological variability in Northern Kazakhstan. We present results from two complementary domains: (1) the physical characterization of solar flares based on reconnection dynamics and flare morphology, and (2) the statistical correlation between solar activity indices and atmospheric/drought indicators throughout the year 2014.
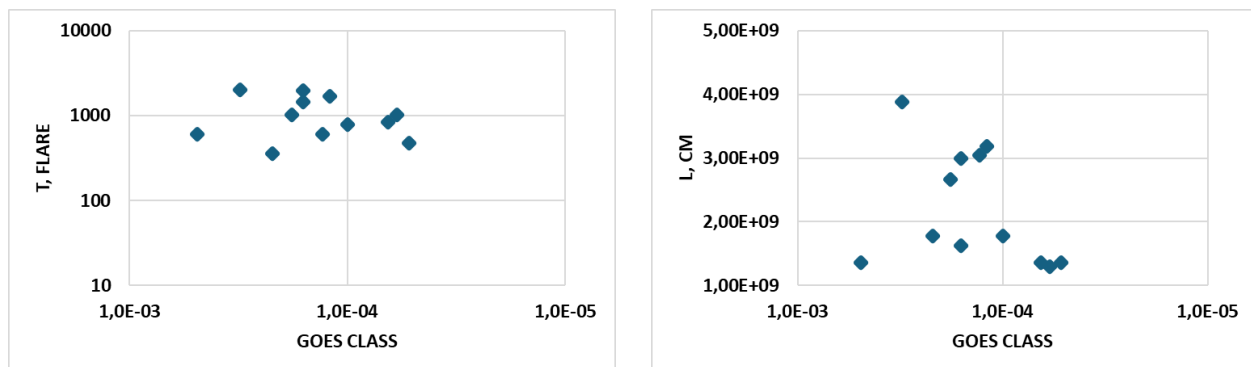

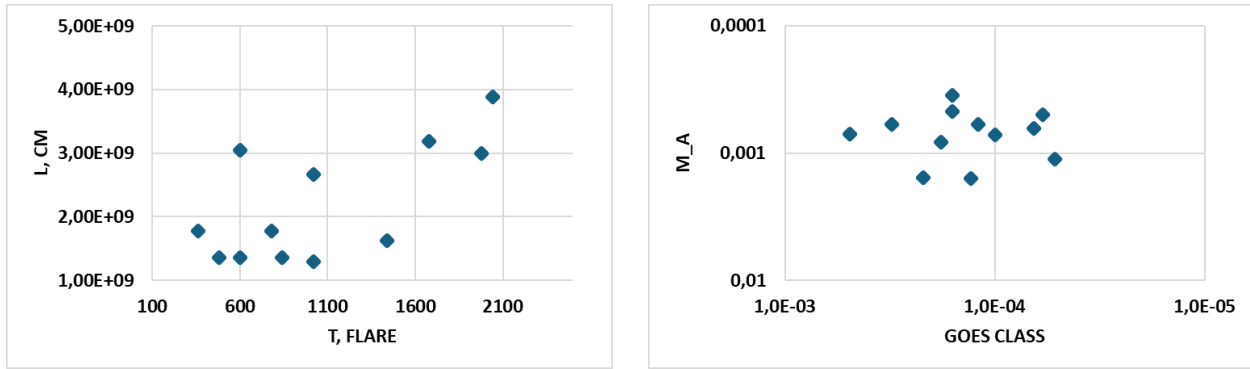**Figure 1** – Physical parameters of each flare plotted against the GOES class (a); Timescale τ_{flare}. Size L (b)

Figure 2 – Timescale τ_{flare} plotted against L (a); Reconnection rate M_A plotted against GOES class (b)

3.1. Physical parameters of solar flares

In this study, we analyzed 12 major X- and M-class solar flares observed during the year 2014 to investigate the physical parameters governing energy release through magnetic reconnection. Using multi-wavelength observations and magnetogram data, we derived flare timescales (τ_{flare}), characteristic sizes (L), reconnection rates (M_A), and compared these parameters with GOES peak X-ray flux to explore physical trends and potential scaling relations.

3.1.1 Flare duration vs. GOES class

Fig. 1a displays the relationship between the flare timescale (τ_{flare}) and the GOES class on a log-log scale. The flare durations range from approximately 500 to 2000 seconds. The scatter plot shows a weak inverse trend, suggesting that higher GOES-class flares tend to have slightly shorter durations, while weaker flares exhibit a broader range of timescales (Fig.1a).

3.1.2 Flare size vs. GOES class

In Fig. 1b, the characteristic spatial size of the flare loops (L) is plotted against the GOES class. Flare sizes range from $\sim 1.3 \times 10^9$ cm to 3.8×10^9 cm. The results reveal a weak inverse relationship, where stronger flares (higher GOES class) are associated with slightly smaller-scale structures. While larger flares can occur across a range of GOES classes, the most compact events are concentrated in the higher flux range (Fig.1b).

3.1.3 Flare size vs. timescale

Fig. 2a examines the correlation between flare size (L) and flare duration (τ_{flare}). A moderate positive trend is observed: flares with larger spatial dimensions tend to last longer, supporting reconnection-based scaling laws such as $\tau_{flare} \propto \frac{L}{V_{in}}$. This suggests that in larger coronal structures, the reconnection process operates over extended timescales, likely due to slower inflow or extended energy release regions (Fig.2a).

3.1.4 Reconnection rate vs. GOES class

Fig. 2b presents the distribution of the magnetic reconnection rate (M_A) versus GOES class. The reconnection rates, calculated from inflow velocity and Alfvén velocity, lie within the range (10^{-4} to 10^{-3}) (Fig.2a). A slight downward trend is evident, indicating that higher GOES-class flares tend to occur with lower normalized reconnection rates. This suggests that the intense energy output of strong flares may not necessarily stem from faster reconnection, but from larger magnetic flux density or more efficient energy conversion in smaller volumes. All reconnection rates fall within one order of magnitude of the theoretical limit predicted by the Petschek model, affirming the fast reconnection regime observed in the solar corona.

3.2 Solar activity and atmospheric/drought variability

Time series data for 2014 demonstrate that solar activity indices such as the Wolf Sunspot Number (WSN) and Sunspot Number (SSN) exhibited moderate variability, with WSN ranging between 80 and 120, and SSN between 100 and 140. As shown in Figure 4, atmospheric indices NAO and AO displayed significant seasonal dynamics. NAO declined from +0.8 in February to –0.97 in June, followed by sharp oscillations from –1.68 in August

Solar magnetic activity and its terrestrial impact through ...

Phys. Sci. Technol., Vol. 12 (No. 1-2), 2025: 38-44

to +2.0 in December. Similarly, AO showed a drop from +1.21 in March to –1.13 in October.

Correlation analysis revealed a moderately strong positive correlation between WSN and NAO (r = 0.63 at zero lag; r = 0.43 at two-month lag), suggesting that solar variability may influence mid-latitude circulation patterns both immediately and with short delay. The SPI3 drought index, which showed a strong correlation with NAO (r = 0.70), mirrored this variability – indicating drought intensification from March to June, followed by a recovery phase toward the end of the year. Furthermore, a moderately strong correlation

between WSN and SPI3 (r = 0.57) supports the hypothesis that solar activity, directly or indirectly, modulates regional drought conditions.

In parallel, the Hydrothermal Coefficient (HTC) showed a strong negative correlation with AO (r = –0.75), and AO itself correlated positively with SSN (r = 0.51), suggesting a solar-mediated influence on Arctic atmospheric patterns. Additionally, a strong negative correlation between SSN and HTC (r = –0.66) was observed, reinforcing the link between increased solar activity and suppressed precipitation in the mid-latitude continental region.
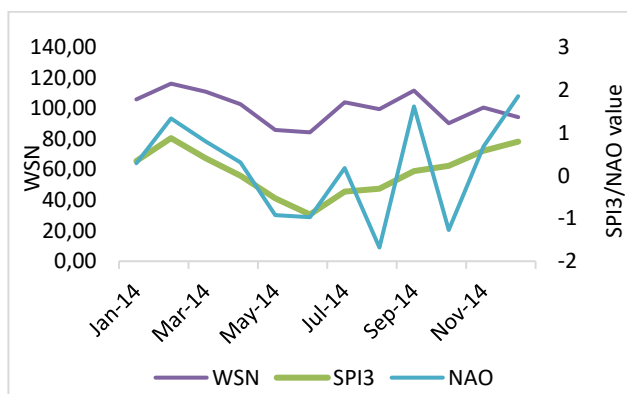

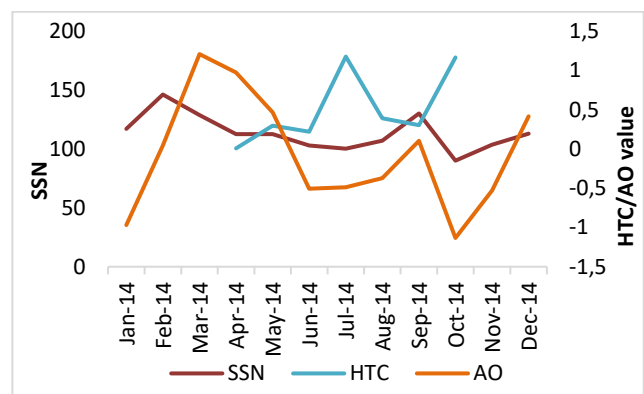**Figure 3** – Time variation of: WSN, SPI3, NAO

Figure 4 – Time variation of: SSN, HTC, AO

Figures 3 and 4 illustrate the temporal evolution of solar activity, atmospheric circulation indices, and drought indicators. Throughout 2014, the Wolf Sunspot Number (WSN) fluctuated between 80 and 120. The North Atlantic Oscillation (NAO) index declined steadily from February to June, reaching –0.97, and showed sharp variability during the summer, ranging from –1.68 in August to +2.0 in September and December. The SPI3 drought index, which exhibits a strong correlation with NAO (r = 0.70), indicated progressive drought intensification from March to June, followed by a trend toward wetter conditions by the end of the year.

Correlation analysis revealed a consistent and moderately strong positive relationship between WSN and NAO, with a maximum correlation coefficient of r = 0.63 at zero lag, decreasing to r = 0.43 with a two-month lag. Additionally, a moderately strong positive correlation between WSN and SPI3 was identified (r = 0.57), suggesting a potential solar influence on short-term hydrometeorological variability.

As shown in Figure 4, sunspot numbers (SSN) ranged between 100 and 140. The Arctic Oscillation (AO) index displayed significant seasonal variability, increasing from +1.21 in March to a minimum of –1.13 in October. The Hydrothermal Coefficient (HTC), which is strongly negatively correlated with AO (r = –0.75), showed persistently dry conditions from April to October. Correlation analysis revealed a moderately strong positive relationship between SSN and AO (r = 0.51) within a one-month lag. Furthermore, a strong negative correlation between SSN and HTC (r = –0.66) was established, indicating that elevated solar activity may be associated with increased meteorological drought conditions in mid-latitudes.

4 Conclusion

This study provides a comprehensive investigation into the solar-terrestrial connection by integrating detailed physical analysis of solar flare dynamics with regional atmospheric and

hydrometeorological responses. From the solar physics perspective, we estimated the physical parameters of 12 X- and M-class solar flares observed between January and December 2014, focusing on energy release rates and reconnection dynamics. The calculated reconnection rates ranged from 10^{-4} to 10^{-3}, and exhibited an inverse relationship with GOES flare class. These results are consistent with the theoretical predictions of the Petschek reconnection model, supporting the validity of magnetic reconnection as the dominant mechanism behind flare energy release. The energy output, derived from multi-wavelength observations, provides an important physical basis for quantifying solar forcing in Earth's upper atmosphere.

On the meteorological side, the findings highlight a coherent and statistically significant link between solar activity and large-scale atmospheric oscillations. A moderately strong correlation between WSN and NAO (r = 0.63 at zero lag; r = 0.43 at a two-month lag) suggests both immediate and delayed influences of solar variability – likely mediated through UV-induced stratospheric heating and subsequent modulation of planetary wave dynamics. These oscillatory responses appear to cascade into regional hydrometeorological effects, as evidenced by a strong positive correlation between NAO and SPI3 (r = 0.70), indicating that the positive phase of NAO is associated with increased precipitation and reduced short-term drought in Northern Kazakhstan.

Importantly, the study also identifies a moderately strong direct relationship between solar activity and SPI3 (r = 0.57), further reinforcing the hypothesis that solar variability – particularly flarerelated energetic events – can influence regional drought regimes. A significant negative correlation between sunspot numbers and the Hydrothermal Coefficient (HTC) (r = -0.66) in mid-latitudes suggests that enhanced solar activity may correspond to drier conditions. This is further supported by a chain of correlations involving Arctic Oscillation (AO), where solar activity and AO exhibit a positive correlation (r = 0.51), and AO and HTC are strongly negatively correlated (r=-0.75). These results collectively point to a multi-step coupling mechanism, whereby solar magnetic activity modulates high-latitude atmospheric circulation (e.g., AO), which in turn affects surfacelevel climate indicators such as drought severity.

References

1. Petschek H. E. Magnetic field annihilation. In *Physics of solar flares*, edited by W. N. Hess. NASA SP-50. Washington, DC, USA: NASA, 1964. –P. 425–439.

2. Parker E. N. Sweet's mechanism for merging magnetic fields in conducting fluids // Journal of Geophysical Research. –1957. –Vol. 62. –P. 509–520. https://doi.org/10.1029/jz062i004p00509

3. Parker E. N. The solar flare phenomenon and theory of reconnection and annihilation of magnetic fields // Astrophysical Journal Supplement Series. –1963. –Vol. 8. –P. 177–211.

4. Sweet P. A. Electromagnetic phenomena in cosmical physics. Cambridge: Cambridge University Press, 1958.

5. Schwabe S. Die Sonne // Astronomical Notes. –1843. –Vol. 20, No. 17. https://doi.org/10.1002/asna.18430201706

6. Wolf J. R. Mittheilungen über die Sonnenflecken // Vierteljahrsschrift der Naturforschenden Gesellschaft in Zürich. –1856. –Vol. 1. –P. 151–161. (In German)

7. Pol M., Binyamin J. Impact of climate change and variability on wheat and corn production in Buenos Aires, Argentina // American Journal of Climate Change. –2014. –Vol. 3, No. 2. –P. 145–152. https://doi.org/10.4236/ajcc.2014.32013

8. Liu Xiaokang, et al. Holocene solar activity imprint on centennial- to multidecadal-scale hydroclimatic oscillations in arid Central Asia // Journal of Geophysical Research: Atmospheres. –2019. –Vol. 124, No. 5. –P. 2562–2573. https://doi.org/10.1029/2018jd029699

9. Bojariu R., et al. Cryosphere–atmosphere interaction related to variability and change of Northern Hemisphere annular mode // Annals of the New York Academy of Sciences. –2008. –Vol. 1146, No. 1. –P. 50–59. https://doi.org/10.1196/annals.1446.018

10. Sawadogo Y., Koala S., and Zerbo J. L. Rainfall and temperature variations over Burkina Faso: Possible influence of geomagnetic activity, solar activity and associated energies from 1975 to 2020 // Atmospheric and Climate Sciences. –2022. –Vol. 12, No. 4. –P. 603–612. https://doi.org/10.4236/acs.2022.124034

11. Owoicho A. M., and Okeke F. N. Seasonal variability of rainfall and its decadal anomaly over Nigeria: Possible role of solar and geomagnetic activities // International Journal of Advanced Engineering Research and Science. –2018. –Vol. 5, No. 9. –P. 325–335. https://doi.org/10.22161/ijaers.5.9.39

12. Kodera K. Solar influence on the Indian Ocean monsoon through dynamical processes // Geophysical Research Letters. – 2004. –Vol. 31, No. 24. https://doi.org/10.1029/2004gl020928

13. Mathpal M. C., Pande B., and Pande S. Dependence of rainfall on solar activity features // Journal of Mountain Research. – 2019. –Vol. 14, No. 1. https://doi.org/10.51220/jmr.v14i1.18

14. Mohamed M. A., and El-Mahdy M. E.-S. Impact of sunspot activity on the rainfall patterns over Eastern Africa: A case study of Sudan and South Sudan // Journal of Water and Climate Change. –2021. –Vol. 12, No. 5. –P. 2104–2124. https://doi.org/10.2166/wcc.2021.312

15. Maghrabi A. H., Alamoudi H. A., and Alruhaili A. S. Investigation of a possible link between solar activity and climate change in Saudi Arabia: Rainfall patterns // Atmospheric and Climate Sciences. –2023. –Vol. 13. –P. 478–490. https://doi.org/10.4236/acs.2023.134027

16. Zharkova V., et al. Heartbeat of the Sun from principal component analysis and prediction of solar activity on a millennium timescale // Scientific Reports. –2015. –Vol. 5. –P. 15689. https://doi.org/10.1038/srep15689

17. Nagashima K. Statistical study of the reconnection rate in solar flares observed with Yohkoh SXT // Astrophysical Journal. – 2006. –Vol. 647. –P. 654.

18. Sarsembayeva A., Odsuren M., Belisarova F., Sarsembay A., Maftunzada S. A. L. Detecting the Sun's active region using image processing techniques // Physical Sciences and Technology. –2021. –Vol. 8(3–4). –P. 48–53. https://doi.org/10.26577/phst.2021.v8.i2.07

19. Sarsembayeva A., Belisarova F., Odsuren M., Sarsembay A. February 25, 2014 solar flare data analysis in SunPy // Physical Sciences and Technology. –2020. –Vol. 7(3–4). –P. 21–25. https://doi.org/10.26577/phst.2020.v7.i2.03

20. Sarsembayeva A., Belisarova F., Odsuren M., Sarsembay A. A new Java-based application in solar physics // Physical Sciences and Technology. –2019. –Vol. 6(3–4). –P. 22–27. https://doi.org/10.26577/phst-2019-2-p3

21. Garcia H. A. Forecasting methods for occurrence and magnitude of proton storms with solar hard X rays // Space Weather. – 2004. –Vol. 2. –P. S06003. https://doi.org/10.1029/2003SW000035

22. Isobe H., Takasaki H., and Shibata K. Measurement of the energy release rate and the reconnection rate in solar flares // Astrophysical Journal. –2005. –Vol. 632. –P. 1184. https://doi.org/10.1086/444490

23. Vicente-Serrano S. M., Beguería S., and López-Moreno J. I. A multiscalar drought index sensitive to global warming: The standardized precipitation evapotranspiration index // Journal of Climate. –2010. –Vol. 23. –P. 1696–1718. https://doi.org/10.1175/2009JCLI2909.1

24. Selyaninov G. T. Proiskhozhdenie i dinamika zasukh [Origin and dynamics of droughts]. In Zasukh v SSSR, ikh proiskhozhdenie, povtoryaemost' i vliyanie na urozhai, edited by A. Rudenko, –P. 36–44. Leningrad: Gidrometeoizdat, 1958. (In Russian)

25. NOAA National Centers for Environmental Information. North Atlantic Oscillation (NAO) index page. https://www.ncei.noaa.gov/access/monitoring/nao/ (accessed April 21, 2025).

26. NOAA Physical Sciences Laboratory. Monthly AO index (Arctic Oscillation). https://psl.noaa.gov/data/timeseries/month/AO/ (accessed April 21, 2025).

Information about the author:

Sarsembayeva Aiganym, PhD is an Associate professor at the Department of Theoretical and Nuclear Physics, Al-Farabi Kazakh National University (Almaty, Kazakhstan), e-mail: sarsembaeva.a@kaznu.kz;

Ryssaliyeva Laura Sergeevna is a Senior researcher at the Department of Meteorology and Hydrology, Al-Farabi Kazakh National University (Almaty, Kazakhstan), e-mail: ryssaliyeva.laura@kaznu.kz;

Belissarova Farida, PhD is an Associate professor at the Department of Theoretical and Nuclear Physics, Al-Farabi Kazakh National University (Almaty, Kazakhstan), e-mail: farida.belisarova@kaznu.kz;

Sarsembay Akmaral, M.Sc., is a CSI «Kyzylorda Regional Educational Center (Methodological Office)» of the Department of Education of Kyzylorda Region,(Kyzylorda, Kazakhstan), e-mail: akmaral_sarsembay@mail.ru.

Method for determining the physical parameters
of hot supergiants based on spectral energy distribution analysis

A.T. Gyuchtash [1] , Sh.T. Nurmakhametova[1] , N.L. Vaidman[1] ,

S.A. Khokhlov , A.T. Agishev[1*] and A. Bakhytkyzy[2]

[1]Fesenkov Astrophysical Institute, Observatory, Almaty, Kazakhstan
[2]Department of Physics and Astronomy, University of North Carolina – Greensboro, Greensboro, NC, USA
*e-mail: Aldiyar.Agishev@gmail.com

This study determines the physical parameters of B- and A-type hot supergiants through the construction and analysis of their spectral energy distributions (SEDs). These luminous stars are in the late stages of stellar evolution and are important for understanding stellar structure and the chemical evolution of galaxies. Although previous spectroscopic studies provided extensive information, our application of the comprehensive SED analysis represents a novel approach to further refine and validate these parameters. We refined the effective temperature Teff, surface gravity (log g), and interstellar extinction A_V for a sample of 16 supergiants using multiwavelength photometry spanning from the ultraviolet to the infrared. A dedicated software package written in Fortran was used to convert observed magnitudes into physical fluxes and compare them with synthetic photometry derived from Castelli & Kurucz model atmospheres. The optimal parameter set for each star was obtained by minimizing the deviations between the observed and model SEDs, iterating over A_V values. The resulting parameters show good agreement with those published in the literature, confirming the reliability of our approach.

Key words: supergiants, spectral energy distribution, interstellar extinction, effective temperature, surface gravity.
PACS number(s): 97.20.Pm, 97.10.Ex

1 Introduction

Hot supergiants are stars in the late stages of their evolution. They can serve as standard candles to measure extragalactic distances and are important for understanding stellar evolution processes. One of the most effective tools for studying such objects is the construction of spectral energy distributions (SED), which allows us to accurately determine their physical parameters, such as the effective temperature (Teff), surface gravity (log(g)), and interstellar reddening (Av).

The choice of this research topic is due to the need for a deeper understanding of the physics of hot supergiants. Despite significant progress in astronomy, their fundamental parameters remain poorly understood and are not well-constrained. Numerous studies, such as those by [1], [2] and [3], have made a huge contribution to the study of hot supergiants, but there is still a lack of comprehensive studies covering a wide range of such stars, which emphasizes the relevance of this project.

Although previous spectroscopic studies provided extensive information, our application of comprehensive SED analysis represents a novel approach to further refine and validate these parameters.

The aim of the present study is to use the SED construction method to determine the parameters of hot B-A supergiants. The objectives of the study include constructing the SED for 16 stars, analyzing their spectral data, and applying extrapolation and modeling methods to refine the values of Teff, log(g), and Av. Selected stars span a temperature range from 8 000 to 13 000 K, which provides good coverage of the main types of hot supergiants (spectral classes B and A). This makes the sample representative in terms of physical diversity and suitable for testing the method. Moreover, selected stars are the most interesting and intriguing ones investigated earlier. The SED-method was never

used for them before, though different spectroscopic methods were used, so our investigation is very representative for this sample of objects. In addition, all selected stars have reliable multi-band photometric data, which is essential for constructing accurate SED.

We will compare our derived parameters with previously obtained values from other studies to assess the accuracy and consistency of our results. This comparison will help to confirm the reliability of our methods and provide a broader context for the physical parameters of hot supergiants. By comparing our results with those from established studies, we aim to identify any discrepancies or confirm the results, thereby contributing to a more accurate understanding of the stellar characteristics of the selected supergiants.

The methods used in this study include the use of modern astronomical databases and tools for analyzing observational data, such as tools for constructing and analyzing SEDs, as well as statistical methods for data processing, including optimization methods for fitting models. The approach proposed in the paper is based on the use of new data, which significantly improves the accuracy of determining the parameters of supergiants.

The theoretical significance of the work lies in improving the methods for determining the physical parameters of hot supergiants and expanding knowledge about the processes occurring in stars at late stages of their evolution. The practical significance lies in the possibility of using the obtained data to refine the models of stellar evolution and applying the SED method to the study of other types of stars.

Literature review

HD 87737. HD 87737 is classified as an A0 Ib supergiant and has been extensively studied to determine its fundamental parameters. $T_{eff} = 10\,400 \pm 300$ K and $\log(g) = 2.05 \pm 0.20$ were reported [4]. Two options for the effective temperature were given as $T_{eff} = 9\,460 / 8\,920$ K [5], while $T_{eff} = 9\,400$ K was estimated [6]. A higher estimate of $T_{eff} = 10\,500$ K and $\log(g) = 2.2$ was provided [7]. T_{eff} was refined to $10\,200 \pm 370$ K, with $\log(g) = 1.9 \pm 0.4$ [8]. $T_{eff} = 9\,650 \pm 200$ K and $\log(g) = 1.95 \pm 0.10$ were derived based on the ionization equilibrium of Mg I/Mg II [9].

Earlier works contributed to the understanding of HD 87737's parameters. Initial evaluations of equivalent widths of spectral lines were provided

[10, 11], and using these values, the parameters were recalculated by [3], resulting in $T_{eff} = 9\,500$ K and $\log(g) = 1.1$, and $T_{eff} = 9\,300$ K and $\log(g) = 0.9$. Then, in [3] new data was used to derive $T_{eff} = 9\,700$ K and $\log(g) = 2.0$.

Subsequent studies reported slightly different values. $T_{eff} = 9\,600 \pm 150$ K and $\log(g) = 2.00 \pm 0.15$ were derived [12], and $T_{eff} = 9\,730$ K and $\log(g) = 1.97$ were estimated using the MILES spectral library [13]. $T_{eff} = 9\,820 \pm 340$ K and $E(B–V) = 0.053$ were provided [14]. Later, $T_{eff} = 9\,600 \pm 150$ K and $\log(g) = 2.00 \pm 0.10$ were reported [15], and $T_{eff} = 9,600 \pm 200$ K and $\log(g) = 2.05 \pm 0.10$ with $E(B-V) = 0.02 \pm 0.02$ were determined [1]. Thus, HD 87737 has been studied extensively over the years, providing a wide range of determined fundamental parameters.

HD 46300. HD 46300 is a supergiant, classified as an A0 Ib, which has been studied several times through years. In [5] two evaluations for the effective temperature are derived, $T_{eff} = 8\,940 / 8\,800$ K. In [4] T_{eff} is determined to be $9\,800 \pm 200$ K, with $\log(g) = 2.15 \pm 0.10$. As for HD 87737, initial estimates provided by [10] and [11] were recalculated, and in the follow-up work in [3] obtained $T_{eff} = 9\,500$ K and $\log(g) = 1.0$ for [10] and $T_{eff} = 9700$ K and $\log(g) = 1.5$ for [11]. Using her own data, [3] refined the parameters of her previous work to $T_{eff} = 9\,700$ K and $\log(g) = 2.1$.

The parameters were then refined by further studies, such as in [2], who derived $T_{eff} = 9\,750$ K and $\log(g) = 2.0$. In [2] it is also noted that in [16] T_{eff} equals $9\,730$ K. Then, [14] estimated $T_{eff} = 9\,800 \pm 340$ K and $E(B-V) = 0.083$. More recently, [1] reported $T_{eff} = 11\,000 \pm 200$ K and $\log(g) = 2.15 \pm 0.10$, with $E(B–V) = 0.07 \pm 0.02$.

BD +60 2582. BD +60 2582 is a supergiant classified as a B7 Iab. It was studied mainly by [1], who reported $T_{eff} = 11\,900 \pm 200$ K and $\log(g) = 1.85 \pm 0.10$ using spectroscopic data and refined model atmospheres. Additionally, they estimated $E(B–V) = 0.85 \pm 0.02$, which nearly corresponds to the previous measurement by [17], who obtained an evaluation for the interstellar reddening $A_V = 2.34$.

HD 5776. HD 5776 is classified as an A2 Iab supergiant. [17] estimated the interstellar reddening as $A_V = 1.53$. Fundamental parameters of the star were reported by [18], who derived $T_{eff} = 10\,715$ K based on spectroscopic analysis. Later, [2] provided a lower temperature estimate of $T_{eff} = 9\,500$ K and $\log(g) = 1.0$. In this paper it is also noted that the estimation given by [16] is $T_{eff} = 9730$.

BD +61 153. BD +61 153 is classified as an A2 Iab supergiant, which was not studied a lot as well. [17] obtained A_V = 2.49. Fundamental parameters of the star were determined by [2], who provided the effective temperature Teff = 9 750 K and log(g) = 1.5. Moreover, in [2] the effective temperature was noted, which was estimated by [16].

HD 161695. HD 161695 is classified as an A0 Ib supergiant. According to the [13], it has an effective temperature of Teff = 9 950 K and a surface gravity of log(g) = 2.2. These values were included in MILES stellar library.

HD 175687. HD 175687 is classified as a B9/A0 Ib supergiant. In [3], the effective temperature for HD 175687 was calculated to be Teff = 9 400 K, with log(g) = 2.3. These parameters were obtained by observing hydrogen line profiles and using ionization equilibrium.

HD 16778. HD 16778, classified as an A1 Ia supergiant, was studied by [18], who estimated its effective temperature Teff to be 9 550 K. This estimate was derived from the spectroscopic analysis.

HD 202850. HD 202850 is classified as a B9 Iab supergiant and was studied several times. In [19] determined Teff = 11 000 K and log(g) = 1.87. In [20] derived an estimate for the interstellar reddening, reporting E(B–V) = 0.13, Further studies, such as [14], estimated Teff = 11 170 ± 450 K and reported E(B–V) = 0.2. In [15] and [1] consistently reported Teff = 10 800 ± 200 K and log(g) = 1.85 ± 0.10, with E(B–V) values of 0.19 ± 0.02.

HD 40589. HD 40589 is classified as an A0 Iab supergiant. It was studied by [21], who determined Teff = 12 000 and log(g) = 1.8. Later, in [14] estimated the effective temperature of HD 40589 to be Teff = 11 660 ± 490 K, based on atmospheric modeling and comparisons with observed photometric data. In [22] the parameters for this star were refined, reporting Teff = 10 750 ± 150 K and log(g) = 1.65 ± 0.2, using a combination of atmospheric models and the parallax method.

HD 46769. HD 46769, classified as a B7 Ib supergiant, has been studied in several key works. In [23], the effective temperature was estimated to be Teff = 12 000 K, with surface gravity values of log(g) = 2.57. In [14] derived Teff = 13 920 ± 710 K, along with E(B–V) = 0.151, which provides a more refined temperature estimate along with a better understanding of the reddening effect for the star. In [24] the parameters were refined further, reporting Teff = 13 000 ± 1 000 K and log(g) = 2.7 ± 0.1.

HD 59612. HD 59612, classified as an A5/7 Iab/II supergiant, has been studied by [3], who estimated Teff = 8 100 K and log(g) = 1.45, based on spectroscopic data and model fitting. In [2] the parameters were refined to Teff = 8 500 K and log(g) = 1.5. Additionally it is noted that in [16] T_{eff} = 8 510 K is received. In [13] Teff = 8 330 K and log(g) = 1.45 is estimated, and in [25] Teff = 8 620 K and log(g) = 1.78 is reported.

HD 67456. HD 67456, classified as an A3 Ib/II supergiant, has been studied mainly by [26], who provided initial estimates, which were recalculated by [3] based on previous measurements of equivalent widths. In [3] the effective temperature for HD 67456 is derived as Teff = 9 500 K and log(g) = 1.2. In [3] the parameters for HD 67456 were recalculated using new data, reporting Teff = 8 300 K and log(g) = 2.5, which is noticeably lower than those from earlier estimates.

HD 71833. HD 71833, classified as a B8 II supergiant, was studied by [27], who determined its effective temperature to be Teff = 12 985 K using the calibration of Strömgren photometric parameters [28].

HD 35600. HD 35600 is classified as a B9 Ib supergiant. In [29] Teff = 11 500 K and log(g) = 2.10 are reported, based on spectroscopic analysis and model fitting. Later, in [21] the parameters were refined, estimating Teff = 11 000 K and log(g) = 1.9.

HD 212593. HD 212593, classified as a B9 Iab-Ib supergiant, has been extensively studied. Early estimates [6] provided Teff = 9 932 K, followed by [2] with Teff = 10 000 K and log(g) = 1.5. It is also noted that in [16] T_{eff} = 10 300 K is estimated. Later studies refined these values, with Teff = 10 350 K and log(g) = 1.92 [30], and in [19] a higher estimate of Teff = 11 800 K and log(g) = 2.19 is provided.

Subsequent studies, including [15] and [1], consistently reported Teff = 11 200 ± 200 K and log(g) = 2.10 ± 0.10, with E(B–V) = 0.17 ± 0.02. In [14] Teff = 11 150 ± 440 K is estimated, and in [31] E(B–V) = 0.120 is confirmed. In [32], the most recent study, the effective temperature was derived as Teff = 13 642 K with log(g) = 3.00.

2 Materials and methods

To assemble the SED for the selected stars, we collected photometric measurements spanning a wide wavelength range–from the ultraviolet through the far-infrared. These data were sourced from

several major catalogs available via the Vizier service [33] and the General Catalogue of Photometric Data (GCPD) [34], covering various photometric systems.

For the ultraviolet region, we used measurements from the TD1 space survey [35], which provides fluxes in four bands centered at 1565, 1965, 2365, and 2740 Å. These observations were obtained with the ultraviolet telescope aboard the ESRO satellite.

In the optical range, photometry in the Johnson UBVRI system [36] formed the core dataset. This was complemented by data in the Strömgren uvby system, drawn from both earlier [37] and recent [38] observations. When available, the color indices m1 and c1 were used to reconstruct individual filter magnitudes algorithmically within the input format of our SED-processing tool.

Near-infrared data were taken from the 2MASS catalog by [39], which includes the J, H, and K bands. To account for possible saturation effects in very bright sources, especially in the K band, we additionally included fluxes from the pre-1999 CIO catalog [40].

At longer wavelengths, we incorporated mid- and far-infrared data from the WISE mission [41]. The four WISE bands – W1 (3.4 μm), W2 (4.5 μm), W3 (11.6 μm), and W4 (22 μm) – provided high-precision photometry across the entire sample, within the survey's brightness limits.

Supplementary photometric measurements in the UBV, Strömgren, and JHK systems were also obtained from the GCPD to ensure consistency and maximize coverage across filters.

In cases where the input file included the letter "J" after the spectral classification, this denoted that the V−R and R−I color indices were specified in the Johnson photometric system. If, instead, the file contained the symbol "N", it indicated that these measurements were not provided. Once the full set of available magnitudes was assembled, each value was converted into an absolute flux using standard zero-points based on the flux calibration of Vega (i.e., corresponding to magnitudes of zero), together with the transmission profiles of the relevant filters.

While systematic catalog offsets were not explicitly corrected within the software, careful pre-selection and manual vetting of the photometric data minimized potential biases.

To determine stellar parameters from photometric data, we developed a custom software suite written in Fortran. It comprises three main modules, each responsible for a distinct stage of the parameter estimation process, which together form a complete optimization pipeline.

The first module preprocesses the input spectra from the Castelli-Kurucz model [42] grid by trimming them to the relevant wavelength range, converting flux units as needed, and applying normalization – typically with respect to the V-band–to ensure numerical stability during further analysis.

The second module performs synthetic photometry by convolving the normalized spectra with the transmission curves of the selected filters. The resulting integrated fluxes are then converted to synthetic magnitudes using standard zero-points, providing a direct comparison to the observed photometric data.

The final module performs the core fitting and optimization. It loads the observed multi-band magnitudes, converts them into physical fluxes, and applies interstellar extinction to each trial model while systematically varying Teff, log(g), and Av. For every combination of parameters, the program evaluates how well the model matches the observed data and selects the best fitting set by minimizing the deviation. The output includes the derived physical parameters along with visual diagnostic plots comparing models to observations.

Because photometric observations are usually expressed in magnitudes, which follow a logarithmic scale, the data are first converted to linear flux units using the standard relation:

$$F_\lambda = F_0 \times 10^{-0.4m} \qquad (1)$$

where F_λ− observed flux at wavelength λ; F_0 – reference (zero-point) flux corresponding to m=0; m – stellar magnitude in the given photometric band.

However, the absolute flux level of the observed SED depends not only on the star's effective temperature and surface gravity, but also on its radius and distance, which are generally unknown or not constrained in photometric fitting. Therefore, the model SED is normalized to match the observed flux in a reference band (typically the V band), and the comparison is performed in relative units. As a result, the absolute scaling of the SED is not fixed during the fitting process.

Instead, the fitting process focuses on the relative shape of the SED. Both the observed and model fluxes are normalized to a reference photometric band – typically the V-band in the

optical – so that their overall levels match. In effect,

the model is scaled to align with the observed flux in that band. This removes the dependence on distance and stellar size, allowing a direct comparison of the SED profiles. Only the relative differences in flux across wavelengths – driven by Teff, log(g), and Av–are considered, while absolute offsets are intentionally ignored.

Our calculations rely on a grid of model stellar spectra computed by Castelli and Kurucz [42], which provide theoretical flux distributions as functions of wavelength, parameterized by effective temperature Teff, log(g), and chemical composition. In this study, we used a broad range of models covering temperatures from approximately 3500 K to 50,000 K and surface gravities from log(g) = 0.0 to 5.0 (in cgs units), making it possible to model a wide variety of stars–from cool supergiants to hot main-sequence stars. Unless otherwise specified, solar metallicity was assumed, although adjustments can be made if the chemical composition of the target star is known.

The model spectra used in this study are provided at a sufficiently high spectral resolution to ensure accurate integration across broad photometric passbands. In the first module, each spectrum is processed to match the requirements of the filter set: it is interpolated or truncated as necessary to cover the relevant wavelength range and may be smoothed or resampled depending on the task. The spectra can also be normalized – for example, to the bolometric flux or the flux in a specific photometric band – to facilitate comparison with observational data.

Since the original models are computed in absolute physical units (erg cm^{-2} s^{-1} Å^{-1}) at the stellar surface, a direct comparison with observational fluxes – which are distance-dependent – would require conversion to apparent fluxes received at Earth. In practice, however, such comparisons focus on the relative shape of the SED, not on its absolute level. To this end, both model and observed fluxes are scaled to a common reference, typically the V band, effectively removing the dependence on distance and stellar radius.

Synthetic photometry is then generated by convolving the model spectrum with the response curves of the selected filters. The resulting fluxes are converted to magnitudes using the adopted photometric zero-points, making them directly comparable with the observed photometric data.

In the final stage, the fitting and optimization module (final module) compares the observed and synthetic SEDs to determine the best-fit stellar parameters. Observed magnitudes are first converted into physical fluxes and normalized. For each trial model (i.e., a combination of Teff and log(g)) , the program iteratively applies interstellar extinction for a range of A$_V$ values using an extinction law [43] (2) adjusts the model SED accordingly, and calculates the deviation from the observed SED.

$$F_\lambda^{dered} = F_\lambda^{obs} \times 10^{0.4A(\lambda)} \qquad (2)$$

where F_λ^{dered} – de-reddened (intrinsic) flux at wavelength λ; F_λ^{obs} – observed flux at wavelength λ; A(λ) – total extinction at wavelength, given by A(λ)=A$_V$ k(λ), k(λ) – extinction curve normalized to A$_V$ (e.g., [43]).

The deviation is quantified using a weighted relative deviation metric σ, which is calculated from the relative difference between the de-reddened observed and model fluxes, weighted by the inverse squared photometric uncertainties:

$$\sigma = \sqrt{\frac{1}{N-1}\sum_{i=1}^{N} \quad (1 - \frac{F_{\lambda,i}^{dered}}{F_{\lambda,i}^{mod}})^2 \times \omega_i} \qquad (3)$$

where σ – weighted standard deviation of the relative residuals; $F_{\lambda,i}^{dered}$ – de-reddened observed flux at wavelength λ_i; $F_{\lambda,i}^{mod}$ – model flux at wavelength λ_i; $\omega_i = 1/\sigma_i^2$ – weight factor based on the squared photometric uncertainty σ_i; N – number of photometric data points used in the comparison. Outliers were identified based on significant deviations from the model or large photometric errors, with thresholds applied manually based on data quality and visual inspection. The optimization process is repeated over the entire model grid to find the minimum σ value.

The parameter set that yields the lowest deviation is adopted as the best solution. The parameter set that yields the lowest deviation is adopted as the best solution. Sensitivity to initial parameter guesses is not evaluated, as the selection is performed via full-grid search. However, sensitivity to extinction A$_V$ is indirectly accounted for through the sampling density and range defined in the input grid, though no formal stability analysis of the solutions is performed. If required, the code also examines how sensitive the solution is to

changes in the parameters and whether other minima exist nearby.

The program outputs the optimal physical parameters – Teff, log(g), and A_V – as well as the corresponding model SED expressed in logarithmic form: log(λ), log ($\lambda F\lambda$ / $\lambda\nu F\nu$), suitable for SED visualization. This allows not only a quantitative comparison with observational data, but also a visual assessment of the fit. Deviations in the infrared, for instance, may signal the presence of excess emission from circumstellar dust.

Although our method generally yields effective temperatures and extinction values that are in good agreement with the literature, the derived surface gravities for some stars are noticeably higher than expected (typically $\log(g) \approx$ 1.0–2.0 for supergiants). This discrepancy likely arises from the intrinsic limitations of SED fitting based solely on photometric data, as surface gravity has a relatively weak effect on broadband fluxes. As a result, the procedure may prioritize minimizing residuals over maintaining physical plausibility in $\log(g)$.

To address this limitation and assess the validity of the derived $\log(g)$ values, we strongly recommend additional high-resolution spectroscopic observations and line-profile analysis. Spectroscopic diagnostics are more sensitive to gravity-dependent features and offer a direct, independent means of constraining surface gravity. Incorporating such constraints would substantially improve the physical reliability and consistency of the derived parameters, ensuring better alignment with the evolutionary status of the stars.

3 Results and discussion

This study focused on determining the physical parameters of 16 hot supergiants by constructing and analyzing their SED across a broad wavelength range, extending from the ultraviolet to the far-infrared. Using a model-fitting procedure that incorporates interstellar extinction, we derived updated estimates of effective temperature Teff, surface gravity log(g), and extinction interstellar A_V for each target star. These parameters are summaryzed in Table 1, and representative comparisons between the dereddened observed SEDs and the best-fitting models are shown in Figure 1.

Table 1 – Physical parameters of the supergiants in the sample.

| Star name	Teff [K]	log(g)	Av	σ
HD 87737	9 500	2.00	0.13	0.185
HD 46300	9 500	2.00	0.17	0.048
BD+60_2582	14 000	2.50	3.06	0.060
HD 5776	11 000	3.50	1.88	0.028
BD+61 153	10 750	3.50	2.89	0.027
HD 161695	9 750	2.00	0.20	0.040
HD 175687	9 500	2.00	0.63	0.051
HD 16778	10 250	2.00	3.07	0.040
HD 202850	11 000	2.00	0.67	0.093
HD 40589	11 750	2.00	1.14	0.087
HD 46769	12 250	3.00	0.22	0.047
HD 59612	7 000	2.00	0.07	0.064
HD 67456	8 750	3.00	0.31	0.034
HD 71833	12 000	3.00	0.08	0.035
HD 35600	10 750	2.00	0.87	0.072
HD 212593	10 750	2.00	0.48	0.055
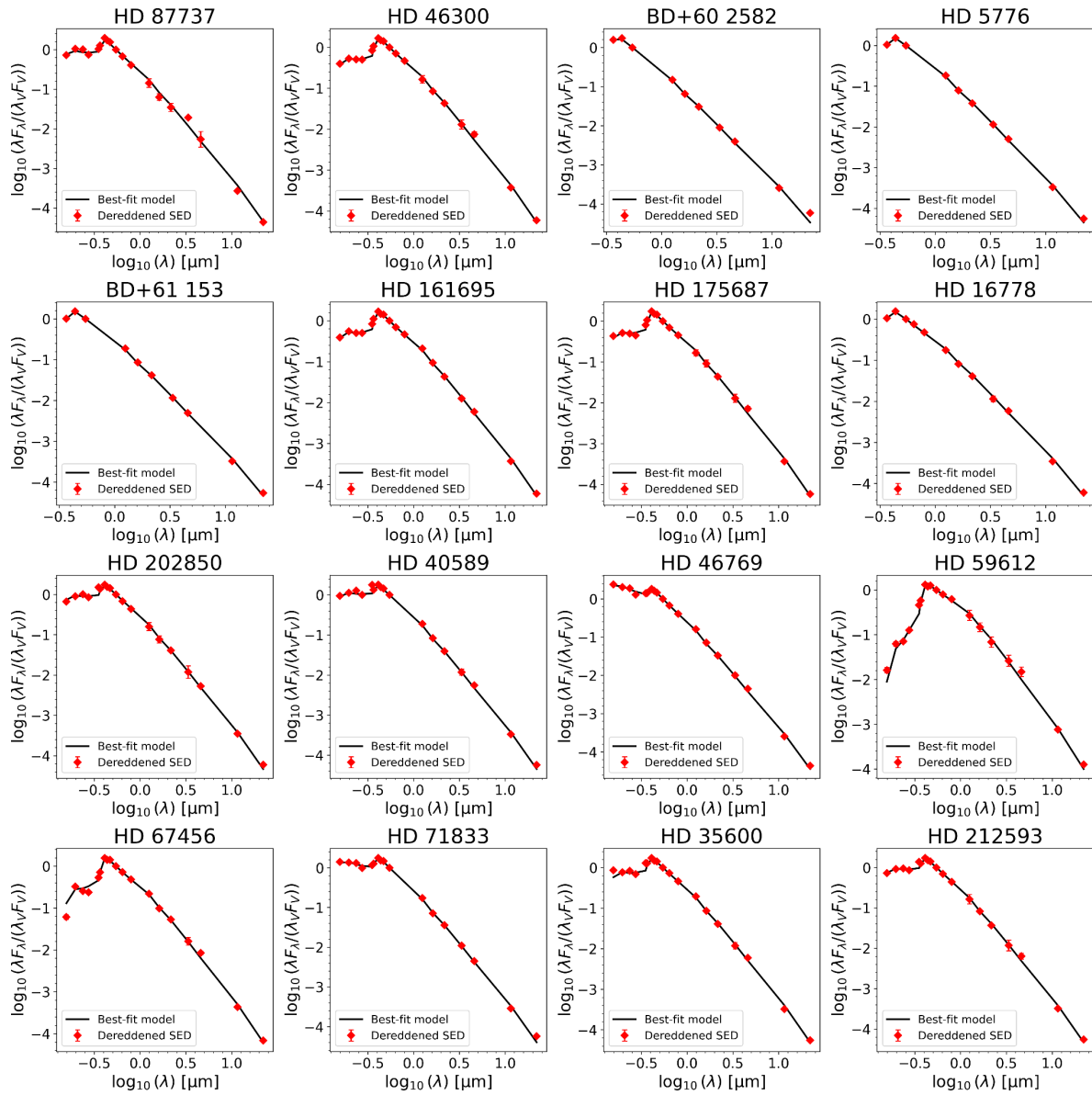
Figure 1 – Comparison between observed and modeled spectral energy distributions for a sample of 16 supergiant stars.
The black solid lines represent the best-fitting model SEDs, normalized to the V-band flux.
The red diamonds indicate the observed photometric data points, corrected for interstellar extinction
and shown with corresponding observational uncertainties. Both axes are plotted on a logarithmic scale.

For most stars, the observed SEDs are well reproduced by the atmospheric models of Castelli & Kurucz, with residuals generally remaining within the expected photometric uncertainties. The good agreement between our results and literature values (as reviewed in the corresponding section) further validates the reliability of the SED-fitting approach. For well-studied supergiants such as HD 87737 and HD 46300 our determinations of Teff**,** and log(g) agree well with those obtained via high-resolution spectroscopy and spectrophotometry. This confirms

that SED analysis, when based on high-quality multi-band photometry and robust extinction modeling, provides a reliable approach to estimate stellar parameters.

In some cases, the shape of the observed SED can offer valuable clues about the star's surrounding environment. A sharp drop in flux in the optical and ultraviolet regions, for instance, often points to strong interstellar extinction and may require a higher A_V value to accurately match the model. On the other hand, an unexpected rise in infrared flux –

especially in the WISE or IRAS bands – may hint at the presence of circumstellar dust, such as disks or extended shells that absorb stellar light and re-emit it at longer wavelengths. Such features typically reveal themselves as systematic deviations from the model fit and may serve as indirect evidence of dust in the immediate vicinity of the star.

The method also proved robust even when only partial photometric coverage was available. The robustness of the fitting procedure is ensured by a grid-search algorithm over a broad parameter space, using multi-band photometry from UV to IR, which allows convergence even when several photometric points are missing or uncertain. The normalization and extinction-fitting procedures enabled the derivation of reliable stellar parameters, despite gaps in some wavelength regions.

Comparing derived results of fundamental parameters with several previous investigations

(Table 2), it is clear that the resulting parameters show good agreement with those published in the literature, confirming the reliability of our approach. The SED-method was never used before to determine parameters of these stars, and our investigation clearly shows that it may be used in future.

In summary, the results confirm that SED fitting is a reliable and effective technique for determining the fundamental parameters of hot supergiants. Moreover, it offers a way to identify secondary signatures such as infrared excess, which may indicate mass loss or circumstellar material. The derived parameters can be used to update stellar evolution models, improve distance estimates, and characterize stellar environments. This methodology is well-suited for extension to larger samples and could be integrated into automated pipelines for next-generation photometric surveys.

Table 2 – Comparison between fundamental parameters derived in this paper with the previous ones. *E(B–V) converted using the formula Av = 3.1E(B–V) [43].

Name	Research	Teff [K]	log g	AV
HD 87737	This paper	9 500	2.00	0.13
	Venn, 1995 [3]	9 700	2.0	
	Przybilla & Butler, 2001 [12]	9 600 ± 150	2.00 ± 0.15	
	Cenarro, 2007 [13]	9 730	1.97	
	Zorec, 2009 [14]	9 820 ± 340		0.16 *
	Firnstein & Przybilla, 2012 [1]	9 600 ± 200	2.05 ± 0.10	0.06 ± 0.06 *
HD 46300	This paper	9 500	2.00	0.17
	Schmidt-Kaler, 1982 [16]	9 730		
	Venn, 1995 [3]	9 700	2.1	
	Verdugo, 1999 [2]	9 750	2.0	
	Zorec, 2009 [14]	9 800 ± 340		0.26 *
	Firnstein & Przybilla, 2012 [1]	11 000 ± 200	2.15 ± 0.10	0.22 ± 0.06 *
BD+60 2582	This paper	14 000	2.50	3.06
	Humphreys, 1978 [17]			2.34
	Firnstein & Przybilla, 2012 [1]	11 900 ± 200	1.85 ± 0.10	2.64 ± 0.06 *
HD 5776	This paper	11 000	3.50	1.88
	Humphreys, 1978 [17]			1.53
	Schmidt-Kaler, 1982 [16]	9 730		
	Garmany & Stencel, 1992 [18]	10 715		
	Verdugo, 1999 [2]	9 500	1.0	
BD+61 153	This paper	10 750	3.50	2.89
	Humphreys, 1978 [17]			2.49
	Schmidt-Kaler, 1982 [16]	9 730		

Continuation of the table

	Verdugo, 1999 [2]	9 750	1.5	
HD 161695	This paper	9 750	2.00	0.20
	Cenarro, 2007 [13]	9 950	2.2	
HD 175687	This paper	9 500	2.00	0.63
	Venn, 1995 [3]	9 400	2.3	
HD 16778	This paper	10 250	2.00	3.07
	Garmany & Stencel, 1992 [18]	9 550		
	Verdugo, 1999 [2]	9 080		
HD 202850	This paper	11 000	2.00	0.67
	Wegner, 2002 [20]			0.40 *
	Markova & Puls, 2008 [19]	11 000	1.87	
	Zorec, 2009 [14]	11 170 ± 450		0.62 *
	Firnstein & Przybilla, 2012 [1]	10 800 ± 200	1.85 ± 0.10	0.40 *
HD 40589	This paper	11 750	2.00	1.14
	Goranova, 2002 [21]	12 000	1.8	
	Zorec, 2009 [14]	11 660 ± 490		
	Samedov, 2023 [22]	10 750 ± 150	1.65 ± 0.2	
HD 46769	This paper	12 250	3.00	0.22
	Lefever, 2007 [23]	12 000	2.57	
	Zorec, 2009 [14]	13 920 ± 710		0.47 *
	Aerts, 2013 [24]	13 000 ± 1000	2.7 ± 0.1	
HD 59612	This paper	7 000	2.00	0.07
	Schmidt-Kaler, 1982 [16]	8 510		
	Venn, 1995 [3]	8 100	1.45	
	Verdugo, 1999 [2]	8 500	1.5	
	Cenarro, 2007 [13]	8 330	1.45	
	Lyubimkov, 2010 [25]	8 620 ± 200	1.78	
HD 67456	This paper	8 750	3.00	0.31
	Przybylski, 1972 [26]	9 500	1.2	
	Venn, 1995 [3]	8 300	2.5	
HD 71833	This paper	12 000	3.00	0.08
	Makaganiuk, 2011 [27]	12 985		
HD 35600	This paper	10 750	2.00	0.87
	Goranova, 2002 [21]	11 000	1.9	
HD 212593	This paper	10 750	2.00	0.48
	Schmidt-Kaler, 1982 [16]	10 300		
	Verdugo, 1999 [2]	10 000	1.5	
	Yuece, 2005 [30]	10 350	1.92	
	Markova & Puls, 2008 [19]	11 800	2.19	
	Zorec, 2009 [14]	11 150 ± 440		
	Firnstein & Przybilla, 2012 [1]	11 200 ± 200	2.10 ± 0.10	0.53 ± 0.06 *
	Wang, 2015 [31]			0.37 *

4 Conclusion

The primary aim of this study was to determine the fundamental parameters of hot supergiants of spectral types B and A through the construction and analysis of SED. The research objectives encompassed the compilation of multiwavelength photometric data, the standardization and conversion of stellar magnitudes into physical fluxes, the construction of SEDs, and their comparison with synthetic photometry derived from model stellar spectra. For this purpose, we employed modern computational techniques, utilized a variety of astronomical databases, and developed specialized software based on the Castelli & Kurucz atmospheric models.

As a result, SEDs were constructed for a sample of 16 stars, and their effective temperatures, surface gravities, and interstellar extinction values were derived. In most cases, the obtained parameters are in good agreement with previously published data, thereby validating the accuracy and robustness of our methodology. For several objects, we identified an excess in the infrared domain, which may indicate the presence of circumstellar dust environments and warrants further spectroscopic and photometric investigation. In some instances, discrepancies between observed and modeled data highlight the need for refinement in the current grid of theoretical models and support the importance of enlarging the stellar sample for improved statistical reliability.

Overall, this study demonstrates the effectiveness of SED analysis as a reliable technique for constraining the physical properties of hot supergiants. The derived results contribute to a more systematic and consistent understanding of evolved massive stars and provide a foundation for future studies involving the calibration of stellar evolutionary models and the investigation of circumstellar phenomena. Looking forward, the methodology presented here can be adapted to larger and more diverse stellar samples and can potentially be integrated with machine learning approaches to enable automated processing of photometric data in next-generation astronomical surveys. To make this approach suitable for large-scale automated applications, a few improvements are needed. These include automatic loading and preparation of photometric data from catalogs, reliable ways to identify and exclude outliers, and the use of prior knowledge – for example, typical log(g) values for different spectral types – to avoid unrealistic solutions. It would also be important to add tools that can estimate uncertainties in the results, such as Bayesian methods.

In addition to these practical improvements, the physical parameters obtained in this study can also help inform models of stellar evolution. Although the focus here was on methodology, the results provide more accurate observational constraints for hot supergiants – an important step toward improving evolutionary tracks and deepening our understanding of how massive stars evolve beyond the main sequence. The precise values of T_{eff} and log(g) allow for more accurate determinations of star's luminosity, radius, and mass, which are fundamental to understanding the internal processes of stars as they evolve through different phases. Thus, these observational constraints serve as valuable benchmarks for testing and calibrating theoretical stellar evolutionary models.

References

1. Firnstein M., Przybilla N. Quantitative Spectroscopy of Galactic BA-type supergiants. I. Atmospheric parameters // Astronomy & Astrophysics. – 2012, – Vol. 543. A. 80. – P. 17. https://doi.org/10.1051/0004-6361/201219034

2. Verdugo E., Talavera A., Gómez de Castro A. Understanding A-type supergiants II. Atmospheric parameters and rotational velocities of Galactic A-type supergiants // Astronomy & Astrophysics. – 1999. – Vol. 346. – P. 819-830. https://ui.adsabs.harvard.edu/abs/1999A&A...346..819V

3. Venn K. A. Atmospheric Parameters and LTE abundances for 22 galactic, A-type supergiants // The Astrophysical Journal Supplement Series. – 1995. – Vol. 99. – P. 659-692. https://doi.org/10.1086/192201

4. Wolf B. The atmosphere of the A0 Ib supergiant eta Leonis // Astronomy & Astrophysics. – 1971. – Vol. 10. – P. 383-400. https://ui.adsabs.harvard.edu/abs/1971A%26A....10..383W

5. Böhm-Vitense E. Effective temperatures of A and F stars // The Astrophysical Journal. – 1982. – Vol. 255. – P. 191-199. https://doi.org/10.1086/159817

6.   Underhill A., Doazan V. B Stars with and without emission lines // NASA SP-456. – 1982. – Vol. 57. – P. 485. https://ui.adsabs.harvard.edu/abs/1982bsww.book.....U

7.   Lambert D., Hinkle K. H., Luck R. E. The peculiar supergiant HR 4049 // The Astrophysical Journal. – 1988. – Vol. 333. – P. 917-924. https://doi.org/10.1086/166800

8.   Lobel A., Achmad L, de Jager C., Nieuwehnuijzen H. Atmospheric model and dynamical state of the atmosphere of the supergiant Eta Leonis (A0Ib) // Astronomy & Astrophysics. – 1992. – Vol. 256. – P. 159-165. https://ui.adsabs.harvard.edu/abs/1992A&A...256..159L

9.   Venn K. A. CNO abundances and the evolutionary status of three A-type supergiants // The Astrophysical Journal. – 1993. – Vol. 414. – P. 316-332. https://ui.adsabs.harvard.edu/abs/1993ApJ...414..316V

10.   Przybylski A. The analysis of the low gravity halo star HD 214539 // MNRAS. – 1969. – Vol. 146. – P. 71-90. https://doi.org/10.1093/mnras/146.1.71

11.   Boyarchuk A. A. A quantitative analysis of the chemical composition of the atmosphere of the bright component of β – Lyrae // Soviet Astronomy. – 1959. – Vol. 3. – P. 748-758. https://ui.adsabs.harvard.edu/abs/1959SvA.....3..748B

12.   Przybilla N., Butler K. Non-LTE line formation for N I/II: Abundances and stellar parameters. Model atom and first results on BA-type stars // Astronomy & Astrophysics. – 2001. – Vol. 379. – P. 955-975. https://doi.org/10.1051/0004-6361:20011393

13.   Cenarro A. J., Peletier R. F., Sánchez-Blázquez P. et al. Medium-resolution Isaac Newton Telescope library of empirical spectra – II. The stellar atmospheric parameters // MNRAS. – 2007. – Vol. 374. – P. 664-690. https://doi.org/10.1111/j.1365-2966.2006.11196.x

14.   Zorec J., Cidale L., Arias M. L. et al. Fundamental parameters of B supergiants from the BCD system. I. Calibration of the (λ_1, D) parameters into T_{eff} // Astronomy & Astrophysics. – 2009. – Vol. 501. – P. 297-320. https://doi.org/10.1051/0004-6361/200811147

15.   Przybilla N., Firnstein M., Nieva M. F., Meynet G., Maeder A. Mixing of CNO-cycled matter in massive stars // Astronomy & Astrophysics. – 2010, – Vol. 517. – A. 38. – P. 6. https://doi.org/10.1051/0004-6361/201014164

16.   Schmidt-Kaler Th. 4.1.4 Effective temperatures, bolometric corrections and luminosities // Landolt-Boernstein – Group VI Astronomy and Astrophysics. – 1982. – Vol. 2. – SubVol. B. – P. 455. https://doi.org/10.1007/b20014

17.   Humphreys R. M. Studies of luminous stars in nearby galaxies. I. Supergiants and O stars in the Milky Way // The Astrophysical Journal Supplement Series. – 1978. – Vol. 38. – P. 309-350. https://ui.adsabs.harvard.edu/abs/1978ApJS...38..309H

18.   Garmany C. D., Stencel R. E. Galactic OB associations in the northern Milky Way galaxy. I. Longitudes 55 to 150 // Astronomy & Astrophysics Supplement Series. – 1992. – Vol. 94. – P. 211-244. https://ui.adsabs.harvard.edu/abs/1992A&AS...94..211G

19.   Markova N., Puls J. Bright OB stars in the galaxy. IV. Stellar and wind parameters of early to late B supergiants // Astronomy & Astrophysics. – 2008. – Vol. 478. – P. 823-842. https://doi.org/10.1051/0004-6361:20077919

20.   Wegner W. Atlas of interstellar extinction curves of OB stars covering the whole available wavelength range // Baltic Astronomy. – 2002. – Vol. 11. – P. 1-74. https://ui.adsabs.harvard.edu/abs/2002BaltA..11....1W

21.   Goranova Yu.; Georgiev Ts., Iliev L. et al. Radial velocities of B-stars towards the galactic anti-center // Publ. Astron. Obs. Belgrade. – 2002. – Vol. 73. – P. 153-157. https://www.researchgate.net/publication/253486235

22.   Samedov Z. A., Rustem U. R., Hajiyeva G. M., Aliyeva Z. F. Fundamental parameters of supergiant star HD 40589 (A0Iab) // Odessa Astronomical publications. – 2023. – Vol. 36. – P. 86-87. https://doi.org/10.18524/1810-4215.2023.36.290802

23.   Lefever K., Puls J., Aerts C. Statistical properties of a sample of periodically variable B-type supergiants. Evidence for opacity-driven gravity-mode oscillations // Astronomy & Astrophysics. – 2007. – Vol. 463. – P. 1093-1109. https://doi.org/10.1051/0004-6361:20066038

24.   Aerts C., Simón-Díaz S., Catala C. et al. Low-amplitude rotational modulation rather than pulsations in the CoRoT B-type supergiant HD 46769 // Astronomy & Astrophysics. – 2013. – Vol. 557. – A. 114. – P. 9. https://doi.org/10.1051/0004-6361/201322097

25.   Lyubimkov L. S., Lambert D. L., Rostopchin S. I. et al. Accurate fundamental parameters for A, F, and G-type supergiants in the solar neighbourhood (Paper I) // MNRAS. – 2010. – Vol. 402. – P. 12. https://doi.org/10.1111/j.1365-2966.2009.15979.x

26.   Przybylski A. The analysis of the small magellanic cloud supergiant HD 7583 // MNRAS. – 1972. – Vol. 159. – P. 155-163. https://doi.org/10.1093/mnras/159.2.155

27.   Makaganiuk V., Kochukhov O., Piskunov N. et al. The search for magnetic fields in mercury-manganese stars // Astronomy & Astrophysics. – 2011. – Vol. 525. – A. 97. – P. 275-284. https://doi.org/10.1051/0004-6361/201015666

28.   Moon T. T., Dworetsky M. M. Grids for the determination of effective temperature and surface gravity of B, A and F stars using *uvby*β photometry // MNRAS. – 1985. – Vol. 217. – P. 305-315. https://doi.org/10.1093/mnras/217.2.305

29.   Takeda Y., Takada-Hidai M. Helium and carbon abundances in late-B and early-A supergiants // Publications of the Astronomical Society of Japan. – 2000. – Vol. 52. – P. 113-125. https://ui.adsabs.harvard.edu/abs/2000PASJ...52..113T

30.   Yüce K. Spectral analysis of 4 Lacertae and ν Cephei // Baltic Astronomy. – 2005. – Vol. 14. – P. 51-82. https://ui.adsabs.harvard.edu/abs/2005BaltA..14...51Y

31.   Wang X., Hummel C. A., Ren S. et al. The three-dimensional orbit and physical parameters of 47 Oph // The Astronomical Journal. – 2015. – Vol. 149:110. – P. 7. https://doi.org/10.1088/0004-6256/149/3/110

32.   Lorenzo-Gutiérrez A., Alfaro E. J., Maíz-Appellániz J. et al. Deriving stellar parameters from GALANTE photometry: bias and precision // MNRAS. – 2020. – Vol. 494. – P. 3342-3357. https://doi.org/10.1093/mnras/staa892

33.   Ochsenbein F., Bauer P., Marcout J. The VizieR database of astronomical catalogues // Astronomy and Astrophysics Supplement Series. – 2000. – Vol. 143(1). – P. 23-32. https://doi.org/10.1051/aas:2000169

34.   Mermilliod J.-C., Hauck B., Mermilliod M. The general catalogue of photometric data (GCPD). II // Astronomy and Astrophysics Supplement Series. – 1997. – Vol. 124(2). – P. 349-352. https://doi.org/10.1051/aas:1997197

35. Thompson G. I., Nandy K., Jamar C. et al. Catalogue of stellar ultraviolet fluxes from the TD-1 Satellite // ESRO SP-56, European Space Research Organisation. – 1978. – P. 295. https://ui.adsabs.harvard.edu/abs/1978csuf.book.....T

36. Lanz T. Photoelectric photometric catalogue in the Johnson *UBVRI* system // Astronomy & Astrophysics Supplement Series. – 1986. – Vol. 65. – P. 195-197. https://ui.adsabs.harvard.edu/abs/1986A%26AS...65..195L

37. Hauck B., Mermilliod M. *uvbyβ* photoelectric photometric catalogue, 1953-1996 // Astronomy and Astrophysics Supplement Series. – 1998. – Vol. 129. – P. 431-433. https://doi.org/10.1051/aas:1998195

38. Paunzen E. A new catalogue of Strömgren-Crawford *uvbyβ* photometry // Astronomy and Astrophysics. – 2015. – Vol. 580. – A. 23. https://doi.org/10.1051/0004-6361/201526413

39. Skrutskie M. F., Cutri R. M., Stiening R. et al. The two micron all sky survey (2MASS) // Astronomical Journal. – 2006. – Vol. 131(2). – P. 1163-1183. https://doi.org/10.1086/498708

40. Gezari D. Y., Schmitz M., Pitts P. S. Catalog of infrared observations. 5th edition // NASA RP-1294. – 1999. – P. 384. https://ui.adsabs.harvard.edu/abs/1999yCat.2225....0G

41. Wright E. L., Eisenhardt P. R. M., Mainzer A. K. et al. The wide-field infrared survey explorer (WISE) Mission // Astronomical Journal. – 2010. – Vol. 140(6). – P. 1868-1881. https://doi.org/10.1088/0004-6256/140/6/1868

42. Castelli F., Kurucz R. L. New grids of ATLAS9 model atmospheres // IAU Symp. No 210, Modeling of Stellar Atmospheres. – 2003. – A. 20. https://doi.org/10.48550/arXiv.astro-ph/0405087

43. Cardelli J. A., Clayton G. C., Mathis J. S. The relationship between infrared, optical, and ultraviolet extinction // The Astrophysical Journal. – 1989. – Vol. 345. – P. 245-256. https://doi.org/10.1086/167900

Information about authors:

Alina Gyuchtash, BSc in Physics and Astronomy is a Research assistant at the Fesenkov Astrophysical Institute (Almaty, Kazakhstan), e-mail: AlinaGyuchtash@gmail.com

Shakhida Tashmakhomedovna Nurmakhametova, BSc in Physics and Astronomy is a Research assistant at the Fesenkov Astrophysical Institute (Almaty, Kazakhstan), e-mail: shahidanurmahametova@gmail.com

Nadezhda Leonidovna Vaidman, MSc in Physics and Astronomy is a Research associate at the Fesenkov Astrophysical Institute (Almaty, Kazakhstan), e-mail: nva1dmann@gmail.com

Serik Anatolyevich Khokhlov, PhD is a Chief Investigator at the Fesenkov Astrophysical Institute (Almaty, Kazakhstan), email: skhokh88@gmail.com

Aldiyar Talgatovich Agishev, PhD is a Senior researcher at the Fesenkov Astrophysical Institute, (Almaty, Kazakhstan), e-mail: aldiyar.agishev@gmail.com

Aigerim Bakhytkyzy, MSc is a Visiting Scholar at the Department of Physics and Astronomy, University of North Carolina – Greensboro (Greensboro, USA), e-mail: aigerim423113@gmail.com

In-situ raman analysis of carbon nanowalls during electrochemical measurement

R.Ye. Zhumadilov[1,2,3*] , B.Ye. Zhumadilov[1,2] , R.R. Nemkayeva[1,2] ,

H. Kondo[4] , A.A. Markhabayeva[1,2] , Y. Yerlanuly[1,2,3*] ,

M.T. Gabdullin[1,2,3] and M. Hori[5]

[1]Kazakh-British Technical University, Almaty, Kazakhstan
[2]Al-Farabi Kazakh National University, Almaty, Kazakhstan
[3]Institute of Applied Science and Information Technologies, Almaty, Kazakhstan
[4]Kyushu University, Fukuoka, Japan
[5]Center for Low-temperature Plasma Sciences, Nagoya University, Nagoya, Japan
*e-mail: rakimzhan@gmail.com, yerlanuly@physics.kz
(Received February 27, 2025; received in revised form May 12, 2025; accepted May 28, 2025)

This study focuses on the synthesis of carbon nanowalls (CNWs) and nitrogen-doped CNWs using the RI-PECVD method and their investigation through in situ Raman spectroscopy during voltammetric cycling and potentiostatic charging under both reduction and oxidation potentials. CNWs were synthesized on Ti/SiO$_2$/Si substrates. Electrochemical experiments were conducted in a three-electrode cell with CNWs as the working electrode, and analytes such as urea, citric acid, and hydrogen peroxide (H$_2$O$_2$) were used to study their effects during in situ Raman measurements. The Raman spectra of CNWs and N-doped CNWs were recorded in a voltage range of -1 V to 1 V (vs. Ag/AgCl), revealing no significant shifts in peak positions but showing an increase in the G to 2D peak ratio at higher voltages, indicating strong electron doping. The cyclic voltammetry results demonstrated that nitrogen doping enhances the reductive current of CNWs, with a clear reduction peak observed at -0.7 V across all analytes. The ID/IG peak ratio of N-doped CNWs increased upon analyte addition, suggesting the introduction of defects and restoration of sp2 domains. Furthermore, the position of the G and 2D peaks shifted significantly in response to different analytes. Sharper fluctuations were observed in N-doped CNWs. These results not only provide valuable insights into the electrochemical properties of CNWs but also highlight their potential for electrochemical sensing applications, offering a promising avenue for future research and development in this field.

Key words: carbon nanowalls, in situ raman, nitrogen doping, electrochemical reduction.
PACS number(s): 61.46.−w.

1 Introduction

Raman spectroscopy, particularly in its in situ form, plays a crucial role in the study of electrochemical reactions. This technique, which is the preferred method for characterizing graphene and other carbon-based materials due to its non-destructive nature, provides real-time insights into several important areas, including interfacial phenomena, doping, interlayer coupling, structural defects, and chemical functionalization [1]. In-situ Raman spectroscopy is particularly valuable as it enables the real-time visualization and monitoring of electrochemical reactions [2–8]. The emergence of vibrational bands, which correspond to the presence of specific bonds or compounds, under applied potentials can reveal the reasons behind improved electrocatalytic performance [9]. Additionally, peak position shifts often indicate chemical composition changes resulting from chemical interactions, providing critical information about reaction mechanisms. This feature is fundamentally significant because certain chemical changes related to the reaction mechanism occur exclusively during the reaction itself and are reversed afterward. Changes detected through ex-situ techniques may not appear in in-situ characterization measurements and could, therefore, be entirely unrelated to the actual reaction [10]. Such spectroscopic data can be used

to gather diverse information about electrochemical reactions, including the structural transitions of electrocatalysts, interfacial species on surfaces, and localized species in the electrolyte within the electrical double layer (EDL) region [1]. During the electrochemical process, electrodes coated with active materials are exposed to harsh chemical and electrochemical conditions. Consequently, many materials are unable to preserve their structure under these operating conditions. Structural changes frequently take place either just before or at the early stages of electrocatalysis. Structural changes are commonly caused by redox reactions, where electrochemical reduction or oxidation leads to the transformation of electrocatalysts into species with varying oxidation states. Additionally, phase transitions occur when a chemically unstable phase converts to a stable one, and decomposition happens when electrochemically unstable materials with weak internal bonds break down [2, 11–13].

The integration of Raman spectroscopy with electrochemistry, known as Raman spectroelectrochemistry, has already demonstrated its effectiveness in investigating graphene, fullerenes, and carbon nanotubes [14]. In graphene's Raman spectra, the G and 2D modes, symmetry allowed features, are of particular interest [15, 16]. While these modes are also observed in Raman spectra of graphene-derived materials, their specific Raman shifts, line widths, and intensities are influenced by factors such as laser excitation energy, the number of graphene layers, doping levels, and strain [17, 18]. Additionally, the D peak may appear in the Raman spectra of certain graphene samples, indicating the presence of symmetry disrupting perturbations. Recent research has explored the spectroelectrochemical behavior of the D band, highlighting its tunability in response to applied potential, both reversibly and irreversibly [12, 19]. In recent years, the electrochemical properties of graphene-based nanomaterials have been studied in detail using in-situ Raman spectroscopy. For example, Milan Bouša et al. investigated graphene oxide and graphene nanoplatelets with in-situ spectroelectrochemistry during voltammetric cycling and potentiostatic charging at both reductive and mildly oxidative potentials [12]. Minkyung Choi et al. conducted in-situ Raman measurements of a graphene microbridge on SiO_2/Si substrates in air at a current density of up to 2.58×10^8 A/cm^2 [20]. Additionally, in a study by Binder et al., the authors induced hydrogen chemisorption on a bilayer graphene sample by intentionally applying a high gate voltage. The chemisorption process was investigated using in-situ Raman spectroscopy, observing the emergence of Si-H

and C-H modes and an increase in the intensity of the D-band. This process was partially reversible when negative gate voltages were applied. Thus, by varying the gate voltage, the authors achieved an electrical switch for hydrogen chemisorption on graphene [21]. However, despite these advancements, there is no information in the literature on the study of the electrochemical properties of CNWs using in-situ Raman spectroscopy. In addition, due to high specific area and peculiar morphology, CNWs are expected to react on external changes (electrolyte media and potential) noticeably strongly.

Carbon nanowalls (CNWs) are a form of carbon allotrope composed of three-dimensional networks of vertically aligned graphene sheets [22]. They are attracting increasing interest as a novel material for electrochemical sensing devices due to their high electrical and thermal conductivity, excellent electrocatalytic activity, large surface area, and high sensitivity to various analytes. The free bonds at the edges of the vertically aligned graphene sheets make CNWs a promising electrode material for electrochemical probing [23–29]. Despite their unique behavior as electrode materials, the mechanisms behind many of their specific properties are still not fully understood. The impact of different analytes such as urea, hydrogen peroxide (H_2O_2), and citric acid on the electrochemical properties of CNWs can be thoroughly examined using in-situ Raman spectroscopy. Urea is a key biomarker in medical diagnostics, particularly for kidney function monitoring, while hydrogen peroxide is widely used as an indicator of oxidative stress and plays a critical role in biochemical and environmental processes. Citric acid, on the other hand, is an important organic acid involved in metabolic pathways and is commonly found in food and pharmaceutical industries.

Thus, the work focuses on the synthesis of CNWs and nitrogen-doped CNWs, which are synthesized using the RI-PECVD method. The CNWs were investigated using in situ Raman spectroscopy during voltammetric cycling, a process involving the measurement of Raman spectra of the CNWs at different electrochemical potentials, as well as potentiostatic charging at both reducing and oxidizing potentials. This investigation provides insights into the changes in the structure and properties of CNWs under different electrochemical conditions.

2 Materials and methods

2.1 Methods
The synthesis of CNWs films is carried out using the RI-PECVD method. The experimental setup,

synthesis processes are described in detail in previous work [26, 30]. CNWs were synthesized on Ti\SiO$_2$\Si substrates (4 × 4 cm² in size), with both Ti and SiO$_2$ layers having a thickness of 200 nm. A gas mixture of CH$_4$ (100 sccm) and H$_2$ (50 sccm) was introduced into the chamber for growth without nitrogen addition, while for nitrogen-assisted growth, 20 sccm of N$_2$ was also introduced. The total gas pressure was maintained at 3 Pa. Both the surface-wave plasma (SWP) microwave source and the capacitively coupled plasma (CCP) very high frequency (VHF) source operated at 400 W. During the CNW growth, the substrate heater temperature was consistently maintained at 800 °C. All in-situ electrochemical experiments were conducted using a three-electrode electrochemical cell with a 30 mL volume (Dek Research) [31–33], where the CNWs film served as the working electrode, as illustrated in Figure 1. A Pt wire was used as counter electrode, while a Ag/AgCl (3 M KCl, E° = 0.197 V) electrode was used as reference electrode. The 0.1 M phosphate buffer solution (PBS (pH 7.2, Sigma Aldrich)) was used as supporting electrolyte. The Metrohm potentiostat (µStat-i 400) was used to perform the electrochemical measurements. Urea (98%), citric acid (99%) and hydrogen peroxide (30%), purchased from Sigma-Aldrich, were used as analytes to investigate the electrochemical reaction during in-situ Raman measurements.

The Raman spectra were recorded by Raman spectrometer (NT-MDT Solver Spectrum). A 473 nm diode laser was focused on the surface of the CNWs films utilizing a 50× long working distance microscope objective. The laser power was maintained at 0.7 mW and exposure time was set to 60 seconds.
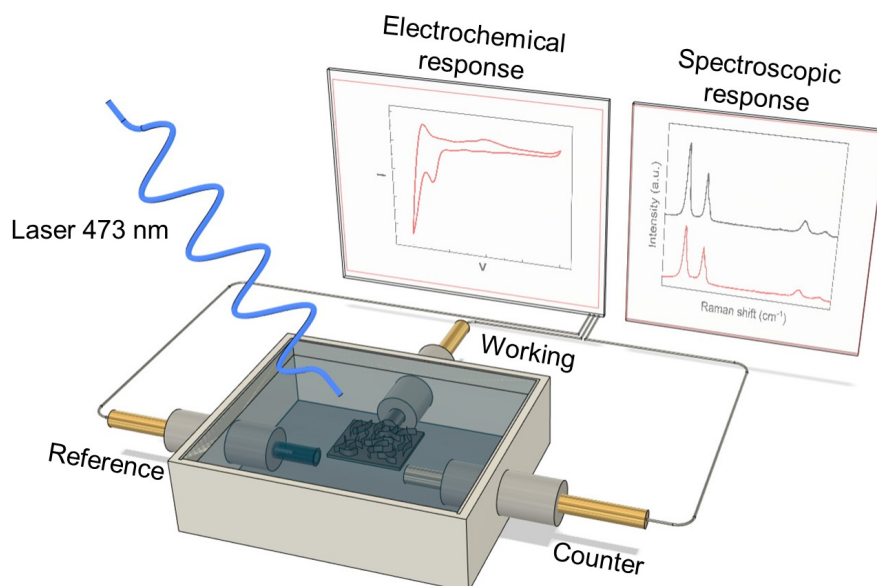
Figure 1 – Schematic illustration of in-situ Raman spectroscopy system.

3 Results and discussion

Figure 2 shows the Raman spectra of CNWs films synthesized at 0 and 20 sccm nitrogen flow rates. Typical D, G, D′, G′ (2D), and G + D peaks are observed in the CNWs Raman spectra [34]. The D peak is characteristic of samples with defects in sp²-structures. The presence of the G peak indicates the synthesis of graphitized carbon. The D′ shoulder peak arises from edges as well as lattice defects in the graphene structure and indicates disorder in the final dimensions of the sp² crystal. The appearance of the G′ peak indicates long-range order in the structure [35, 36].

Figure 3 presents the Raman spectra for (a) CNWs and (b) N-doped CNWs, recorded over a potential range of -1 V to 1 V (vs. Ag/AgCl) in 0.2 V increments during electrochemical measurements in PBS. The voltage range of -1 to 1 V was selected, as further increases in both negative and positive voltages result in material degradation and detachment from the substrate. Analysis indicates no significant effect on the peak positions with increased voltage. Moreover, the analysis of the D to G peak intensity

ratio demonstrated minimal variation, whereas the G to 2D peak ratio exhibited an increase at higher voltages of +1 V (see Figure S1). This behaviour is indicative of strong electron doping [37–39]. Doping will increase the number of charge carriers, thereby increasing the probability of a scattering event. Consequently, the 2D peak intensity should decrease [2, 3, 40].
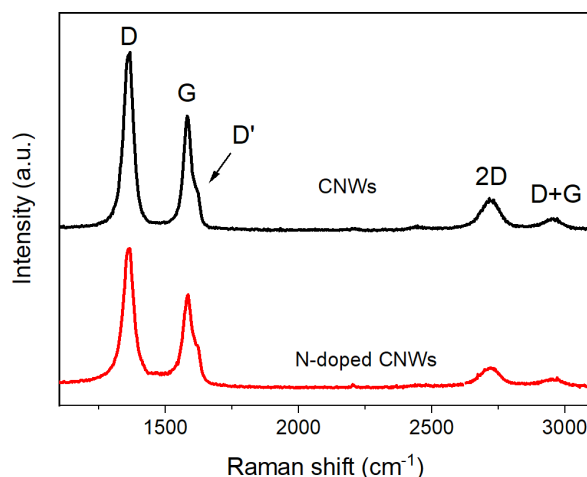

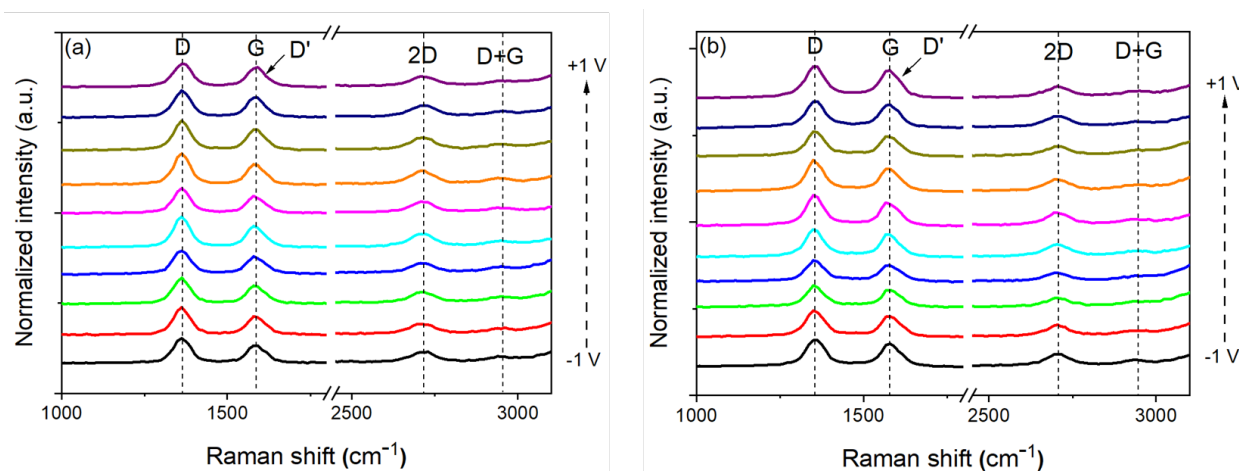**Figure 2** – Raman spectroscopy analysis of the CNWs films synthesized at 0 and 20sccm nitrogen flow rate.

Figure 3 – Raman spectra of (a) CNWs and (b) N-doped CNWs, recorded in the potential range from -1 V to 1 V (vs. Ag/AgCl) with a step of 0.2 V in the PBS electrolyte.

The electrochemical characteristics of CNW films were assessed using a three-electrode setup with 0.1 M PBS solution serving as the electrolyte. Figure 4 shows the cyclic voltammetry (CV) of CNWs, and N-doped CNWs between -1 V and 1 V (vs. Ag/AgCl) at a scan rate of 20 mV/s in the (a) bare PBS solution, and in the presence of 5 mM (b) urea, (c) H_2O_2, (d) citric acid. As the potential is swept in a cyclic voltammogram, a peak current is produced within a certain potential range where the working electrode interacts with the substance, indicating the occurrence of the reaction. It is notable from Figure 4 that reductive current significantly increases in the case of N-doped CNWs (after nitrogen doping of CNWs). A clear reduction peak can be observed for CNWs and N-doped CNWs in all studied analytes at -0.7 V versus Ag/AgCl.
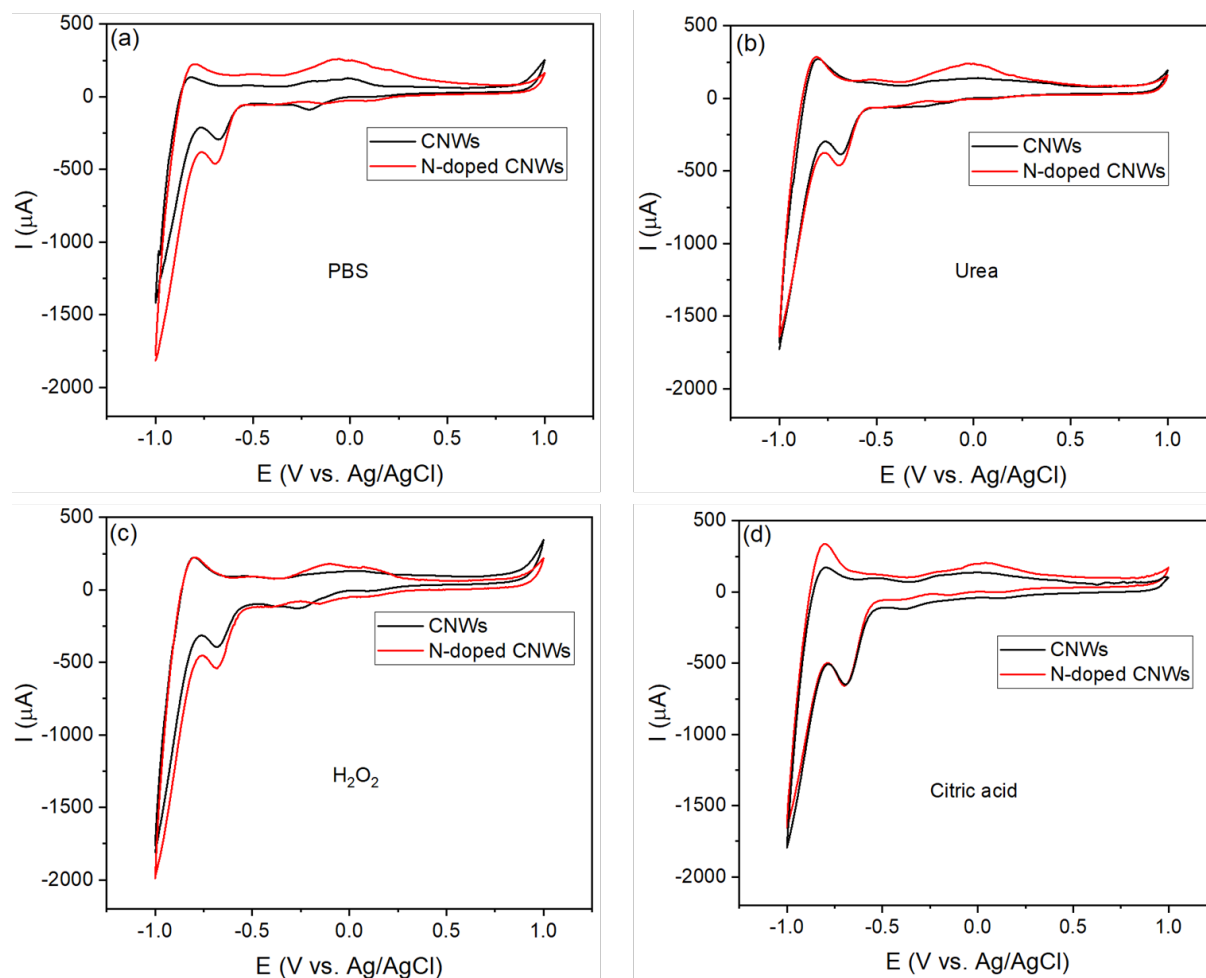
Figure 4 – Cyclic voltammograms obtained using undoped CNWs (a),
and N-doped CNWs (b) in the PBS solution, and in the presence of 5 mM urea, H_2O_2, citric acid.

Figure 5a shows the ratio of ID/IG peak when 5mM of different analytes were added to the surface of the CNWs and N-doped CNWs films. The ID/IG peak ratio of the CNWs remains unchanged upon the addition of analytes. In contrast, for N-doped CNWs, the initial ID/IG ratio is 1.4 and increases to 1.6 upon the addition of analytes such as H_2O_2, citric acid, and urea. An increase in the ID/IG ratio suggests the restoration of sp² domains caused by the introduction of defects of various types (e.g., vacancies, functionalization) [41–43]. The observed changes might be attributed to the intercalation of H+ ions from acidic electrolytes or the incorporation of water molecules into the CNWs film. These processes can cause distortions in the periodic lattice structure of CNWs [41].

Figure 5b shows the ratio of the ID/IG peaks of CNWs in PBS solution and in different analytes at applied -0.7 V negative potential to the CNWs film. The analysis indicates that applying a negative potential has no significant effect on the ID/IG peak ratio, demonstrating the structural stability of the CNWs. The specifics of the Raman spectra analysis of the CNWs films can be found in the Supporting Information (see Figure S2).

Summarizing, the addition of analytes such as urea, H_2O_2, and citric acid to the surface of CNWs results in the formation of a defective material (without applying an external potential). To gain deeper insights into the mechanism of electrochemical reduction of CNWs, a constant potential of -0.7 V was applied to the electrodes in a PBS solution with the addition of various analytes, and the resulting electrodes were characterized using Raman spectroscopy (Fig. 5). As shown, regardless of the type of analyte, the electrochemically reduced CNWs exhibited minimal modification of structural parameters (with the ID/IG ratio remaining nearly unchanged). This may be attributed to the lower efficiency of O-group removal, leading to a reduced number of defects [44, 45].
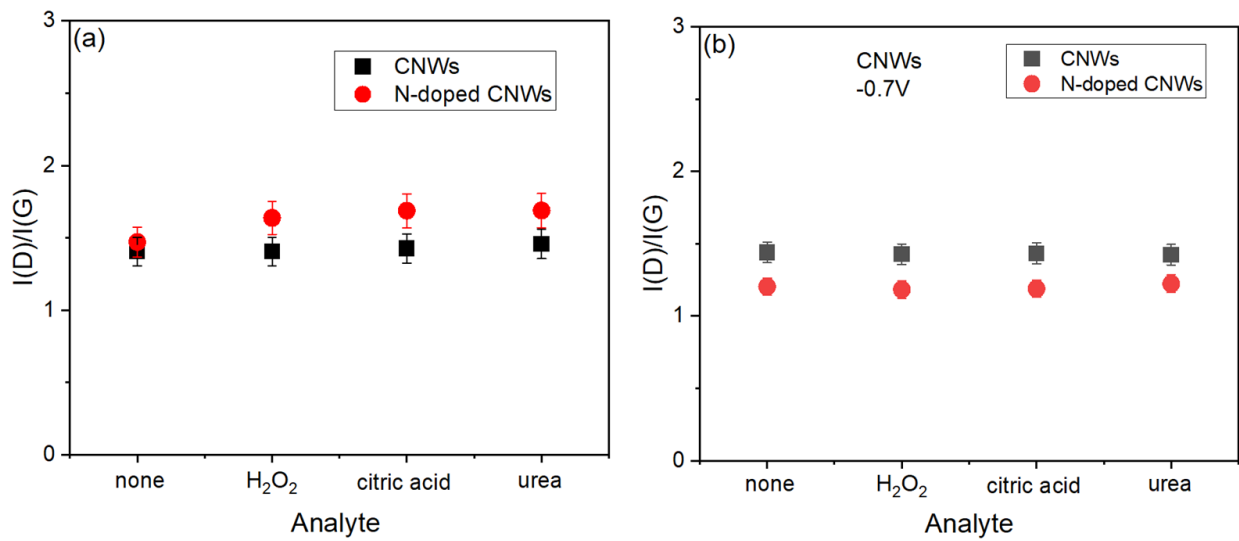
Figure 5 – (a) Ratio of the ID/IG peaks of CNWs when 0.5 mM of different analytes
were added to the surface of the CNWs film. (b) Ratio of the ID/IG peaks of CNWs
in PBS solution and in different analytes at applied -0.7 V negative potential to the CNWs film.

Figure 6(a) and (b) clearly demonstrates the effect of different analytes on the position of the G and 2D peaks, respectively. The positions of the G and 2D peaks are changed by +2 and +3 cm^{-1}, respectively, upon addition of analytes. The fluctuations in the Raman spectra of N-doped CNWs are much sharper, with the position of the G and 2D peaks changing by +4 and +9 cm^{-1}, respectively, upon addition of analytes. The G and 2D band shifts are governed by mild oxidation/reduction and/or by charging-induced lattice expansion and lattice contraction upon addition of different analytes. The blue shift observed in the Raman bands, moving to higher wavenumbers, is attributed to the growing structural disorder resulting from the presence of oxygen-containing functional groups attached to the graphene sheets. These imperfections stem from intrinsic defects introduced by the attachment of oxygen functional groups to the plane and edges of graphene sheets [46–49].
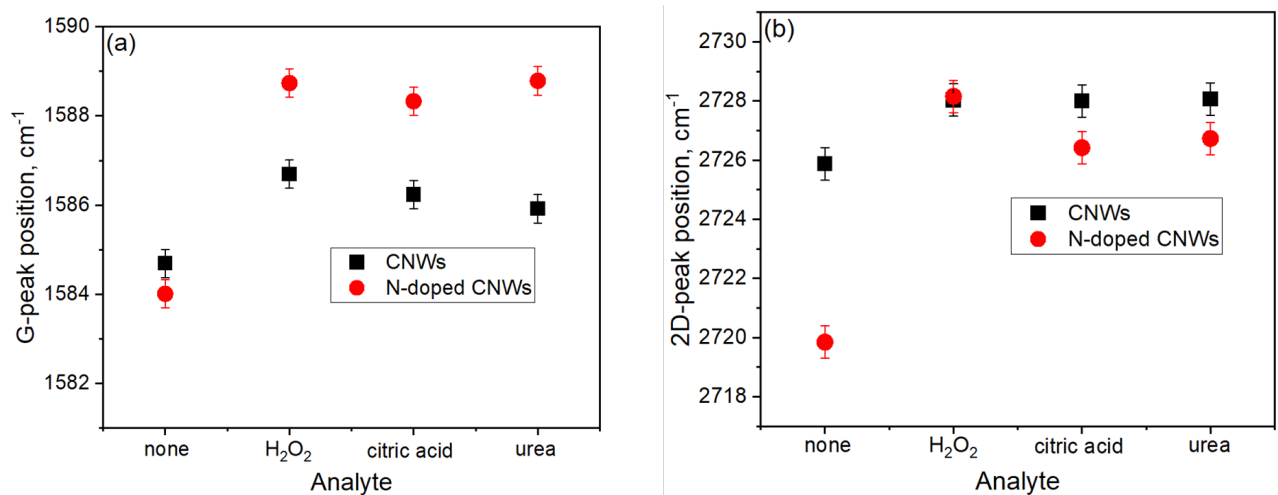
Figure 6 – The G-peak (a), and 2D-peak (b) position extracted from
the in-situ Raman spectrum vs different analytes.

4 Conclusions

In conclusion, this study comprehensively investigated the structural and electrochemical properties of CNWs and N-doped CNWs through Raman spectroscopy and cyclic voltammetry under varying conditions. The introduction of analytes such as urea, H_2O_2, and citric acid led to noticeable changes in the structural parameters of the CNWs, with the ID/IG ratio increasing in N-doped CNWs, indicating defect formation and restoration of sp² domains. Electrochemical measurements demonstrated that applying a constant potential of -0.7 V in the presence of analytes minimally affected the structural integrity of the CNWs, as evidenced by the stable ID/IG ratio. However, N-doped CNWs exhibited sharper fluctuations in the positions of the G and 2D peaks, reflecting their enhanced sensitivity to analytes and structural changes due to oxidation/reduction processes. The observed blue shifts in Raman bands were attributed to structural disorder induced by oxygen functional groups.

Overall, the results highlight the structural stability and tunable properties of CNWs and N-doped CNWs, making them promising materials for applications requiring robust electrochemical performance and analyte sensitivity. Further studies focusing on the mechanisms of defect formation and reduction processes could provide deeper insights into optimizing their functionality for specific applications.

References

1.   Zheng W. Beginner's Guide to Raman spectroelectrochemistry for electrocatalysis study // Chemistry–Methods. – 2023. – Vol. 3. – Art. e202200042. https://doi.org/10.1002/cmtd.202200042

2.   Parpal M., El Sachat A., Sotomayor Torres C.M., Gómez-Romero P., Rueda-García D., Chavez-Angel E. In situ Raman analysis of reduced-graphene oxide-based electroactive nanofluids // Diam Relat Mater. – 2024. – Vol. 141. – Art. 110541. https://doi.org/10.1016/j.diamond.2023.110541

3.   Yadav R., Joshi P., Hara M., Yoshimura M. *In situ* electrochemical Raman investigation of charge storage in rGO and N-doped rGO // Physical Chemistry Chemical Physics. – 2021. – Vol. 23. – P. 11789–11796. https://doi.org/10.1039/D1CP00248A

4.   Deng Y., Yeo B.S. Characterization of electrocatalytic water splitting and CO_2 reduction reactions using in situ/operando Raman spectroscopy // ACS Catal. – 2017. – Vol. 7. – P. 7873–7889. https://doi.org/10.1021/acscatal.7b02561

5.   Liu S., Zhang G., Feng K., Han Y., He T., You J., Wu Y. *In Situ* Raman spectroscopy studies on $La_2 CaB_{10}O_{19}$ crystal growth // Cryst Growth Des. – 2020. – Vol. 20. – P. 6604–6609. https://doi.org/10.1021/acs.cgd.0c00761

6.   Zhu H., Yu G., Guo Q., Wang X. In situ Raman spectroscopy study on catalytic pyrolysis of a bituminous coal // Energy & Fuels. – 2017. Vol. 31. – P. 5817–5827. https://doi.org/10.1021/acs.energyfuels.6b03042

7.   Wu H.-L., Huff L.A., Gewirth A.A. In situ Raman spectroscopy of sulfur speciation in lithium–sulfur batteries // ACS Appl Mater Interfaces. – 2015. – Vol. 7. – P. 1709–1719. https://doi.org/10.1021/am5072942

8.   Ou J.Z., Campbell J.L., Yao D., Wlodarski W., Kalantar-zadeh K. In situ Raman spectroscopy of H_2 gas interaction with layered MoO_3 // The Journal of Physical Chemistry C. – 2011. – Vol. 115. – P. 10757–10763. https://doi.org/10.1021/jp202123a

9.   Wain A.J., O'Connell M.A. Advances in surface-enhanced vibrational spectroscopy at electrochemical interfaces // Adv Phys X. – 2017. – Vol. 2. – P. 188–209. https://doi.org/10.1080/23746149.2016.1268931

10. Yoo R.M.S., Yesudoss D., Johnson D., Djire A. A Review on the application of In-situ Raman spectroelectrochemistry to understand the mechanisms of hydrogen evolution reaction // ACS Catal. – 2023. Vol. 13. – P. 10570–10601. https://doi.org/10.1021/acscatal.3c01687

11. van den Beld W.T.E., Odijk M., Vervuurt R.H.J., Weber J.-W., Bol A.A., van den Berg A., Eijkel J.C.T. In-situ Raman spectroscopy to elucidate the influence of adsorption in graphene electrochemistry // Sci Rep. – 2017. – Vol. 7. – Art. 45080. https://doi.org/10.1038/srep45080

12. Bouša M., Frank O., Jirka I., Kavan L. *In situ* Raman spectroelectrochemistry of graphene oxide // physica status solidi (b). – 2013. – Vol. 250. – P. 2662–2667. https://doi.org/10.1002/pssb.201300105

13. Frank O., Dresselhaus M.S., Kalbac M. Raman spectroscopy and *in Situ* Raman spectroelectrochemistry of isotopically engineered graphene systems // Acc Chem Res. – 2015. – Vol. 48. – P. 111–118. https://doi.org/10.1021/ar500384p

14. Kavan L., Dunsch L. Spectroelectrochemistry of carbon nanostructures // ChemPhysChem. – 2007. – Vol. 8. – P. 974–998. https://doi.org/10.1002/cphc.200700081

15. Ferrari A.C., Meyer J.C., Scardaci V., Casiraghi C., Lazzeri M., Mauri F., Piscanec S., Jiang D., Novoselov K.S., Roth S., Geim A.K. Raman spectrum of graphene and graphene layers // Phys Rev Lett. – 2006. – Vol. 97. – Art. 187401. https://doi.org/10.1103/PhysRevLett.97.187401

16. Thomsen C., Reich S. Double resonant Raman scattering in graphite // Phys Rev Lett. – 2000. – Vol. 85. – P. 5214–5217. https://doi.org/10.1103/PhysRevLett.85.5214

17. Malard L.M., Pimenta M.A., Dresselhaus G., Dresselhaus M.S. Raman spectroscopy in graphene // Phys Rep. – 2009. – Vol. 473. – P. 51–87. https://doi.org/10.1016/j.physrep.2009.02.003

18. Ferrari A.C., Basko D.M. Raman spectroscopy as a versatile tool for studying the properties of graphene // Nat Nanotechnol. – 2013. – Vol. 8. – P. 235–246. https://doi.org/10.1038/nnano.2013.46

19. Ott A., Verzhbitskiy I.A., Clough J., Eckmann A., Georgiou T., Casiraghi C. Tunable D peak in gated graphene // Nano Res. – 2014. – Vol. 7. – P. 338–344. https://doi.org/10.1007/s12274-013-0399-2

20. Choi M., Son J., Choi H., Shin H., Lee S., Kim S., Lee S., Kim S., Lee K., Kim S.J., Hong B.H., Hong J., Yang I. *In-situ* Raman spectroscopy of current-carrying graphene microbridge // Journal of Raman Spectroscopy. – 2014. – Vol. 45. – P. 168–172. https://doi.org/10.1002/jrs.4442

21. Binder J., Urban J.M., Stepniewski R., Strupinski W., Wysmolek A. *In situ* Raman spectroscopy of the graphene/water interface of a solution-gated field-effect transistor: electron–phonon coupling and spectroelectrochemistry // Nanotechnology. – 2016. – Vol. 27. – Art. 045704. https://doi.org/10.1088/0957-4484/27/4/045704

22. Hiramatsu M., Hori M. Carbon nanowalls: Synthesis and emerging applications // Springer Vienna. – 2010. https://doi.org/10.1007/978-3-211-99718-5

23. Bohlooli F., Yamatogi A., Mori S. Manganese oxides/carbon nanowall nanocomposite electrode as an efficient non-enzymatic electrochemical sensor for hydrogen peroxide // Sens Biosensing Res. – 2021. – Vol. 31. – Art. 100392. https://doi.org/10.1016/j.sbsr.2020.100392

24. Tomatsu M., Hiramatsu M., Foord J.S., Kondo H., Ishikawa K., Sekine M., Takeda K., Hori M. Hydrogen peroxide sensor based on carbon nanowalls grown by plasma-enhanced chemical vapor deposition // Jpn J Appl Phys. – 2017. – Vol. 56. – Art. 06HF03. https://doi.org/10.7567/JJAP.56.06HF03

25. Bohlooli F., Anagri A., Mori S. Development of carbon-based metal free electrochemical sensor for hydrogen peroxide by surface modification of carbon nanowalls // Carbon N Y. – 2022. – Vol. 196. – P. 327–336. https://doi.org/10.1016/j.carbon.2022.05.002

26. Zhumadilov R.Ye., Yerlanuly Y., Kondo H., Nemkayeva R.R., Ramazanov T.S., Hori M., Gabdullin M.T. Hydrogen peroxide sensing with nitrogen-doped carbon nanowalls // Sens Biosensing Res. – 2024. – Vol. 43. – Art. 100614. https://doi.org/10.1016/j.sbsr.2023.100614

27. Markhabayeva A., Dupre R. ., Nemkayeva R. ., Nuraje N. Synthesis of hierarchical WO_3 microspheres for photoelectrochemical water splitting application // Physical Sciences and Technology. – 2023. – Vol. 10. – P. 33–39. https://doi.org/10.26577/phst.2023.v10.i2.04

28. Yerlanuly Y., Nemkayeva R. R., Zhumadilov R. Y., Gabdullin M. T. Investigation and evaluation of the morphology properties of carbon nanowalls based on fractal analysis and Minkowski functionals // Physical Sciences and Technology. – 2022. – Vol. 9. – P. 4–10. https://doi.org/10.26577/phst.2022.v9.i2.01

29. Myrzabekova M., Sarkar S., Baigarinova G., Guseinov N., Ilyin A. Obtaining and research of new composite materials polymer-graphene // Physical Sciences and Technology. – 2015. – Vol. 1. – P. 4–9. https://doi.org/10.26577/phst-2014-1-21

30. Yerlanuly Y., Christy D., Van Nong N., Kondo H., Alpysbayeva B., Nemkayeva R., Kadyr M., Ramazanov T., Gabdullin M., Batryshev D., Hori M. Synthesis of carbon nanowalls on the surface of nanoporous alumina membranes by RI-PECVD method // Appl Surf Sci. – 2020. – Vol. 523. – Art. 146533. https://doi.org/10.1016/j.apsusc.2020.146533

31. Xie Y., Huang Y., Zhang Y., Wu T., Liu S., Sun M., Lee B., Lin Z., Chen H., Dai P., Huang Z., Yang J., Shi C., Wu D., Huang L., Hua Y., Wang C., Sun S. Surface modification using heptafluorobutyric acid to produce highly stable Li metal anodes // Nat Commun. – 2023. – Vol. 14. – Art. 2883. https://doi.org/10.1038/s41467-023-38724-x

32. Fu Q., Wang X., Han J., Zhong J., Zhang T., Yao T., Xu C., Gao T., Xi S., Liang C., Xu L., Xu P., Song B. Phase-junction electrocatalysts towards enhanced hydrogen evolution reaction in alkaline media // Angewandte Chemie International Edition. – 2021. – Vol. 60. – P. 259–267. https://doi.org/10.1002/anie.202011318

33. Wang D., Liu C., Zhang Y., Wang Y., Wang Z., Ding D., Cui Y., Zhu X., Pan C., Lou Y., Li F., Zhu Y., Zhang Y. CO_2 electroreduction to formate at a partial current density up to 590 mA mg^{-1} via micrometer-scale lateral structuring of bismuth nanosheets // Small. – 2021. – Vol. 17. https://doi.org/10.1002/smll.202100602

34. Kurita S., Yoshimura A., Kawamoto H., Uchida T., Kojima K., Tachibana M., Molina-Morales P., Nakai H. Raman spectra of carbon nanowalls grown by plasma-enhanced chemical vapor deposition // J Appl Phys. – 2005. https://doi.org/10.1063/1.1900297

35. Davami K., Shaygan M., Kheirabi N., Zhao J., Kovalenko D.A., Rümmeli M.H., Opitz J., Cuniberti G., Lee J.-S., Meyyappan M. Synthesis and characterization of carbon nanowalls on different substrates by radio frequency plasma enhanced chemical vapor deposition // Carbon N Y. – 2014. – Vol. 72. – P. 372–380. https://doi.org/10.1016/j.carbon.2014.02.025

36. Liu R., Chi Y., Fang L., Tang Z., Yi X. Synthesis of carbon nanowall by plasma-enhanced chemical vapor deposition method // Journal of Nanoscience and Nanotechnology – 2014. – Vol. 14. – P. 1647-1657. https://doi.org/10.1166/jnn.2014.8905

37. Sun J., Sadd M., Edenborg P., Grönbeck H., Thiesen P.H., Xia Z., Quintano V., Qiu R., Matic A., Palermo V. Real-time imaging of Na + reversible intercalation in "Janus" graphene stacks for battery applications // Sci Adv. – 2021. – Vol. 7. https://doi.org/10.1126/sciadv.abf0812

38. Das A., Chakraborty B., Piscanec S., Pisana S., Sood A.K., Ferrari A.C. Phonon renormalization in doped bilayer graphene // Phys Rev B. – 2009. – Vol. 79. – Art. 155417. https://doi.org/10.1103/PhysRevB.79.155417

39. Das A., Pisana S., Chakraborty B., Piscanec S., Saha S.K., Waghmare U. V., Novoselov K.S., Krishnamurthy H.R., Geim A.K., Ferrari A.C., Sood A.K. Monitoring dopants by Raman scattering in an electrochemically top-gated graphene transistor // Nat Nanotechnol. – 2008. – Vol. 3. – P. 210–215. https://doi.org/10.1038/nnano.2008.67

40. Johra F.T., Lee J.-W., Jung W.-G. Facile and safe graphene preparation on solution based platform // Journal of Industrial and Engineering Chemistry. – 2014. – Vol. – 20. – P. 2883–2887. https://doi.org/10.1016/j.jiec.2013.11.022

41. Quezada-Renteria J.A., Ania C.O., Chazaro-Ruiz L.F., Rangel-Mendez J.R. Influence of protons on reduction degree and defect formation in electrochemically reduced graphene oxide // Carbon N Y. – 2019. – Vol. 149. – P. 722–732. https://doi.org/10.1016/j. carbon.2019.04.109

42. Ahn G., Ryu S. Reversible sulfuric acid doping of graphene probed by in-situ multi-wavelength Raman spectroscopy // Carbon N Y. – 2018. – Vol. 138. – P. 257–263. https://doi.org/10.1016/j.carbon.2018.05.065

43. Pinilla-Sánchez A., Chávez-Angel E., Murcia-López S., Carretero N.M., Palardonio S.M., Xiao P., Rueda-García D., Sotomayor Torres C.M., Gómez-Romero P., Martorell J., Ros, C. Controlling the electrochemical hydrogen generation and storage in graphene oxide by in-situ Raman spectroscopy // Carbon N Y. – 2022. – Vol. 200. – P. 227–235. https://doi.org/10.1016/j.carbon.2022.08.055

44. Hallam P.M., Banks C.E. Quantifying the electron transfer sites of graphene // Electrochem commun. – 2011. – Vol. 13. – P. 8–11. https://doi.org/10.1016/j.elecom.2010.10.030

45. Ambrosi A., Chua C.K., Bonanni A., Pumera M. Electrochemistry of Graphene and Related Materials // Chem Rev. – 2014. – Vol. 114. – P. 7150–7188. https://doi.org/10.1021/cr500023c

46. Kumar S., Baruah B., Kumar A. Tunable degree of oxidation through variation of H2O2 concentration and its effect on structural, optical and supercapacitive properties of graphene oxide powders synthesized using improved method // Mater Today Commun. – 2017. – Vol. 13. – P. 26–35. https://doi.org/10.1016/j.mtcomm.2017.08.007

47. Vimalanathan K., Scott J., Pan X., Luo X., Rahpeima S., Sun Q., Zou J., Bansal N., Prabawati E., Zhang W., Darwish N., Andersson M.R., Li Q., Raston C.L. Continuous flow fabrication of green graphene oxide in aqueous hydrogen peroxide // Nanoscale Adv. – 2022. – Vol. 4. – P. 3121–3130. https://doi.org/10.1039/D2NA00310D

48. Angizi S., Hong L., Huang X., Selvaganapathy P.R., Kruse P. Graphene versus concentrated aqueous electrolytes: the role of the electrochemical double layer in determining the screening length of an electrolyte // NPJ 2D Mater Appl. – 2023. – Vol. 7. – Art. 67. https://doi.org/10.1038/s41699-023-00431-y

49. Eigler S., Dotzer C., Hirsch A. Visualization of defect densities in reduced graphene oxide // Carbon N Y. – 2012. – Vol. 50. – P. 3666–3673. https://doi.org/10.1016/j.carbon.2012.03.039

Information about authors:

*Zhumadilov Rakhymzhan, PhD **is** a Senior researcher at the Kazakh-British Technical University (Almaty, Kazakhstan), e-mail: rakimzhan@gmail.com*

Zhumadilov Rakhymzhan, PhD is a Senior researcher at the Kazakh-British Technical University (Almaty, Kazakhstan), e-mail: rakimzhan@gmail.com

Nemkayeva Renata is a Researcher at the Kazakh-British Technical University (Almaty, Kazakhstan), e-mail: quasisensus@mail.ru

Kondo Hiroki, PhD is a Professor at the Kyushu University (Fukuoka, Japan), e-mail: hkondo@ed.kyushu-u.ac.jp

Markhabayeva Aiymkul, PhD is a Senior researcher at the Kazakh-British Technical University (Almaty, Kazakhstan), e-mail: aiko_marx@mail.ru

Yerlanuly Yerassyl, PhD is a Senior researcher at the Kazakh-British Technical University (Almaty, Kazakhstan), e-mail: yerlanuly@ physics.kz

Gabdullin Maratbek., PhD is a Rector (Chairman of the Board) of the Kazakh-British Technical University (Almaty, Kazakhstan), e-mail: gabdullin@physics.kz

Hori Masaru, PhD is a Professor at the Nagoya University (Nagoya, Japan) e-mail: hori.masaru.g1@f.mail.nagoya-u.ac.jp

Supporting Information

In-situ Raman analysis of carbon nanowalls
during electrochqmical measurement

Rakhymzhan Ye. Zhumadilov[1,2,3*] , Bauyrzhan Ye. Zhumadilov[1,2] , Renata R. Nemkayeva[1,2] ,

Hiroki Kondo[4] , Aiymkul A. Markhabayeva[1,2] , Yerassyl Yerlanuly[1,2,3*] ,

Maratbek T. Gabdullin[1,2,3] and Masaru Hori[5]

[1] Kazakh-British Technical University, Almaty, Kazakhstan
[2] Al-Farabi Kazakh National University, Almaty, Kazakhstan
[3] Institute of Applied Science and Information Technologies, Almaty, Kazakhstan
[4] Kyushu University, Fukuoka, Japan
[5] Center for Low-temperature Plasma Sciences, Nagoya University, Nagoya, Japan
*e-mail: rakimzhan@gmail.com, yerlanuly@physics.kz
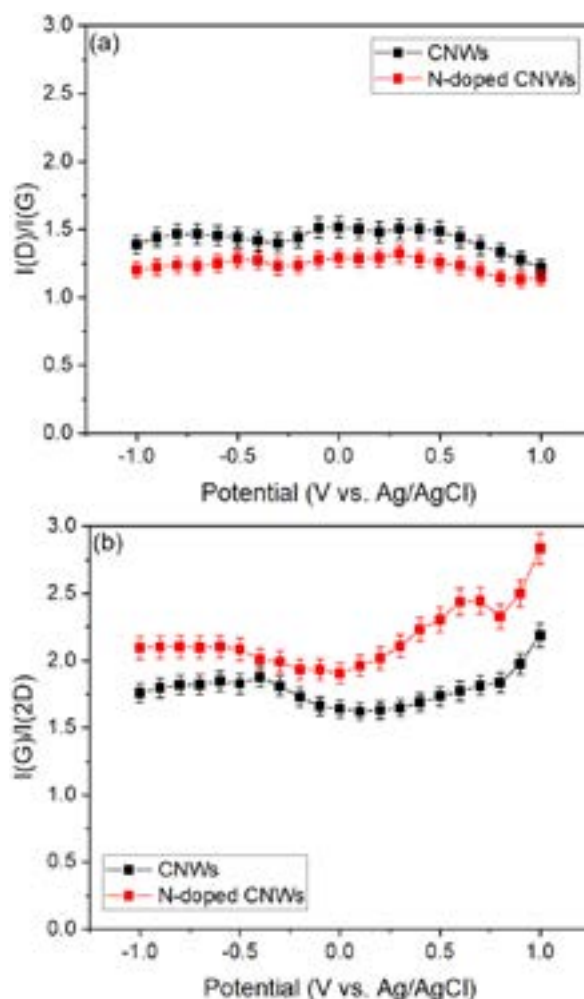
Figure S1 – (a) Dependences of the intensity ratio of the D and G peaks,
and (b) dependence of the intensity ratio of the G and 2D peaks on the applied potential vs. Ag/AgCl.
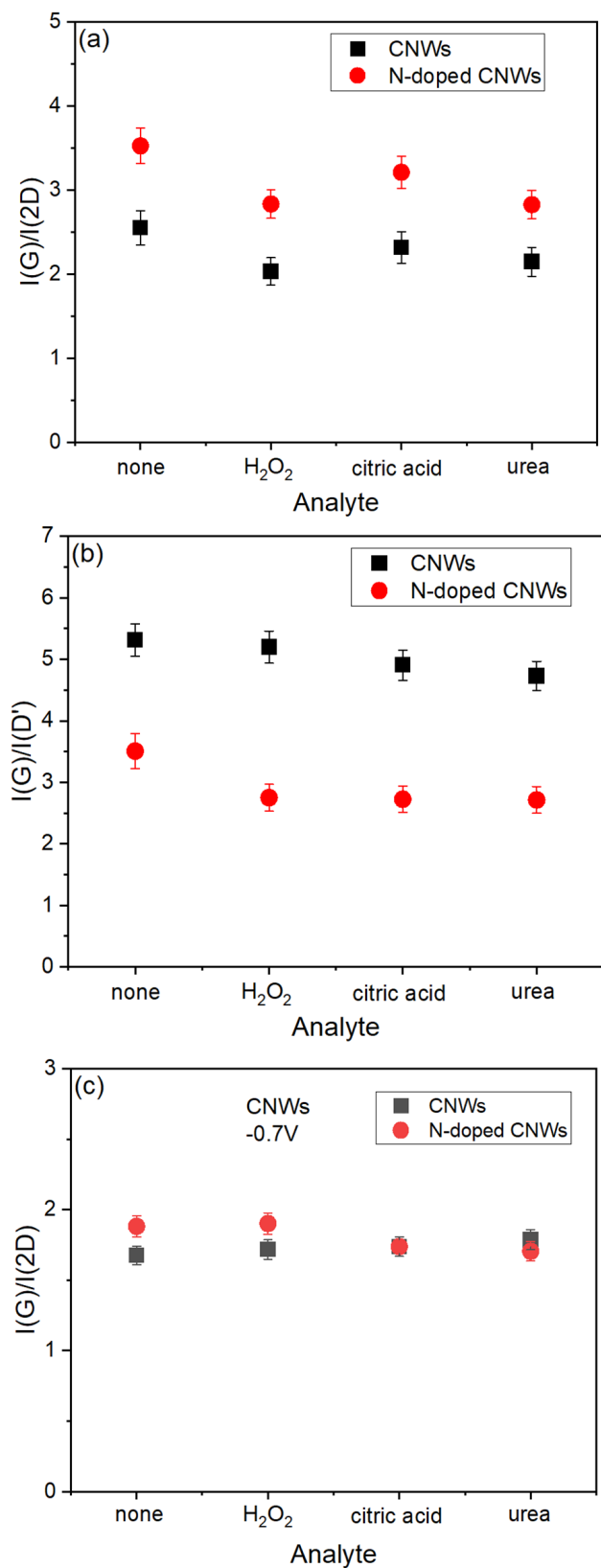
Figure S2 – (a) Dependences of the intensity ratio of the G and 2D peaks, (b) dependence of the intensity ratio of the G and Dˋ peaks, and (c) dependence of the intensity ratio of the G and 2D peaks at -0.7V on the different analytes.

Synthesis and characterization of carbon nanomaterials obtained using electric discharge

M.K. Kazankapova[1,2,3] [iD] , B.T. Yermagambet[1,2,3] [iD] , B.K. Kasenov[4] [iD] ,

Zh.M. Kassenova[1,2,3] [iD] , A.B. Malgazhdarova[1,2*] [iD] , G.K. Mendaliyev [1,2] [iD] ,

A.S. Akshekina[1] [iD] and U.M. Kozhamuratova[1,2] [iD]

[1]«Institute of Coal Chemistry and Technology» LLP, Astana, Kazakhstan
[2]L.N. Gumilyov Eurasian National University, Astana, Kazakhstan
[3]Kazakh university of technology and business named after K. Kulazhanov, Astana, Kazakhstan
[4]«Chemical and Metallurgical Institute named after Zh.Abisheva», Karagandy, Kazakhstan
*e-mail: coaltech@bk.ru

In recent years, carbon nanomaterials have been studied for their applications in important areas of engineering and technology due to their unique physical, chemical, and biological properties. The high demand for developing carbon nanomaterials through environmentally friendly and low-cost synthesis strategies has resulted in significant efforts being undertaken worldwide. This study presents the synthesis and characterization of carbon nanomaterials (CNMs) using the electric arc discharge method under conditions of 75 V and 100 A. A copper substrate was employed to promote material deposition. Structural and morphological properties were examined using SEM and Raman spectroscopy. The results revealed the formation of multilayer carbon nanostructures with a high degree of graphitization (up to 88.98%) and particle sizes ranging from 38 to 53.5 nm. Electrophysical measurements demonstrated high dielectric constants and semiconducting behavior over the temperature range of 293–483 K, indicating the material's potential for electronic applications. The synthesis method offers a scalable, cost-effective, and environmentally friendly approach to producing high-quality carbon nanomaterials.

Key words: carbon nanotubes (CNTs), graphitization, temperature dependence, nanostructured materials, graphitic structures.
PACS number(s): 82.33;.Pt 82.80.− d.

1 Introduction

The use of carbon nanomaterials, including CNTs and fullerenes, is currently of great importance in various modern areas of nanotechnology, new technological processes, and the creation of new high-performance and high-quality materials in biological engineering [1].

Carbon materials are materials with high strength, thermal and electrical conductivity, and chemical stability. They are widely used in many industries. In recent years, novel carbon nanostructures and so-called carbon-carbon nanocomposites have been theoretically predicted and successfully synthesized. These materials exhibit distinct atomic structures, well-defined dimensions, and diverse morphologies, leading to a broad spectrum of unique physical and chemical

properties [2,3]. The electro-discharge technique is extensively utilized for synthesizing superior-quality carbon nanotubes (CNTs) as it operates at exceptionally elevated temperatures [4]. An overview of various classes of carbon nanomaterials synthesized from coal is presented in Figure 1.

The chemical bonding in carbon nanotubes (CNTs) is entirely composed of sp²-hybridized bonds, which are significantly stronger than the sp³ bonds found in alkanes, thereby imparting exceptional mechanical strength to CNTs [5]. Notably, CNTs exhibit an extraordinarily high length-to-diameter ratio, reaching up to 132,000,000:1, which surpasses that of any other known material [6].

Thanks to their distinctive hexagonal carbon framework, CNTs exhibit exceptional electrical, mechanical, and thermal characteristics, rendering

them highly adaptable for numerous applications in diverse scientific and industrial domains [7,8]. As members of the fullerene family, CNTs derive their name from their elongated, hollow, hexagonal cylindrical structure, characterized by single-atom-thick walls composed of carbon sheets known as graphene. These graphene layers are rolled up at specific chiral angles, which ultimately determine the electronic and mechanical properties of the resulting CNTs. The ends of CNTs are typically capped with a fullerene-like molecular structure [9].

Structurally, CNTs are divided into two primary categories: single-walled carbon nanotubes (SW-CNTs) and multi-walled carbon nanotubes (MW-CNTs). Each of these structures arranges itself into bundles, held together by van der Waals forces, forming rope-like assemblies with enhanced mechanical stability [10].

The primary application areas of carbon nanotubes (CNTs) include electronics, medicine, chemistry, pharmaceuticals, and biology. However, the selection of an appropriate CNT synthesis method is a critical factor when considering their potential for various applications. The assessment of different synthesis techniques is typically based on key criteria such as cost-effectiveness, raw material conversion efficiency, and process controllability [11].

After comparing many international and domestic literature data, the electric arc discharge method was selected as one of the most effective methods for producing carbon nanomaterials. This method is based on connecting two graphite electrodes with a high current in an inert gas atmosphere, creating a stable arc discharge between them, which ensures the evaporation of graphite at high temperatures and the formation of carbon nanostructures. These methods ensure scalable and effective CNT production while allowing precise control over their structural features [12].

Currently, there are several common methods for synthesizing CNTs, namely thermal plasma [13], chemical vapor deposition (CVD) [14], and arc discharge [15] methods. Several researchers, based on their research results [16], first developed a thermal plasma method for obtaining multi-walled CNTs from carbon, and secondly, a method based on the thermal decomposition of carbon-containing gases (chemical vapor deposition) accompanied by gas-phase chemical deposition of crystalline nanocarbons on metal. Accordingly, the most effective of these methods was found to be the electric arc discharge method.
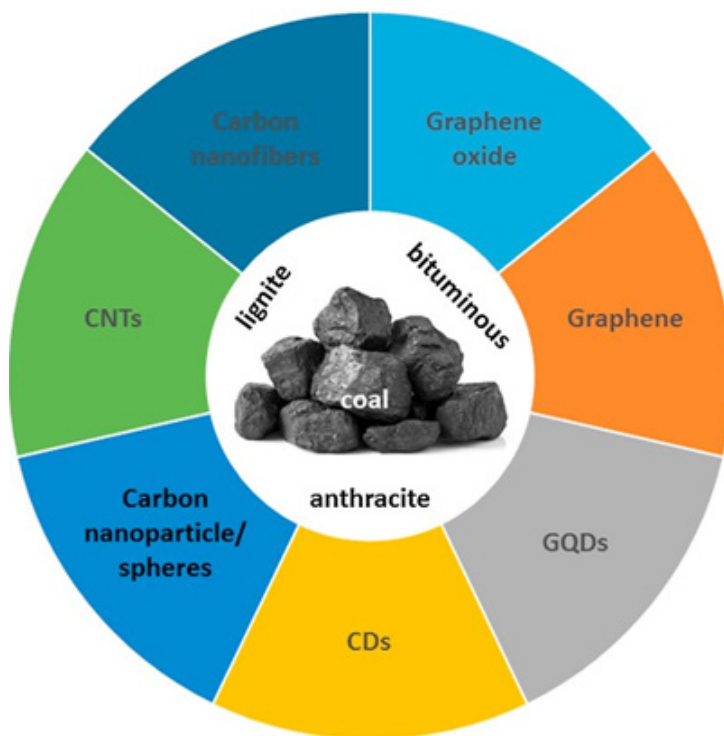

Figure 1 – Types of carbon nanomaterials obtained from different types of coal.

One of the first to synthesize nano-materials using the electric arc discharge method was the Japanese scientist Sumio Iijima [17]. He studied and characterized the structure of the an-ode formed by generating an electric arc discharge using a microscope. The electric arc discharge is caused by high current and very high temperature (fig. 2).
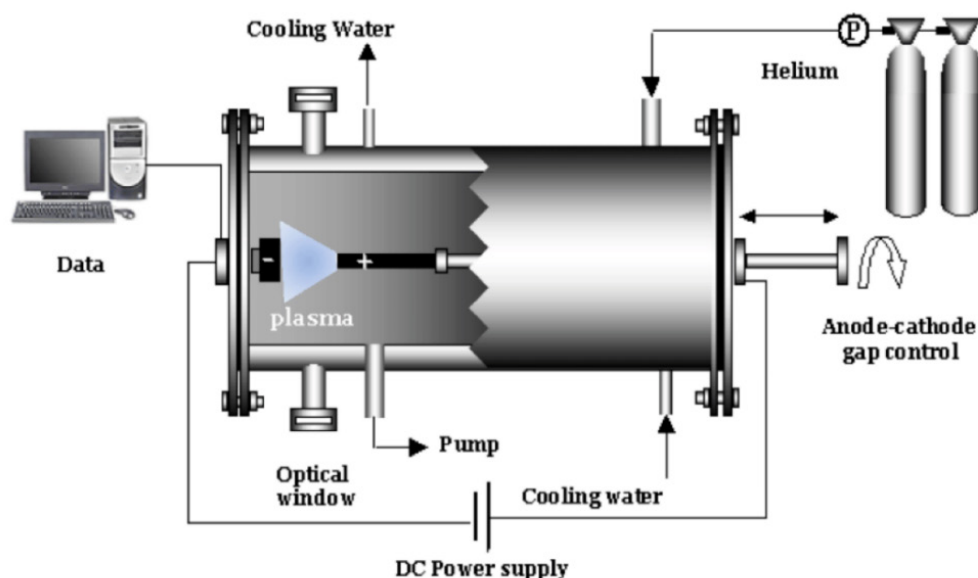

Figure 2 – Production of carbon nanotubes using the electric arc discharge method.

Summarizing the reviewed literature, the electric arc discharge method can be considered as the most optimal method for synthesizing carbon nanotubes, which uses plasma-chemical and thermodynamic processes to generate carbon nanostructures from carbon-based plasma. This method is widely recognized for its cost efficiency, high raw material conversion rate, and controllability of the synthesis process, making it highly suitable for large-scale CNT production [19].

During the electric discharge process, a high-current arc is established between graphite electrodes in an atmosphere of inert gas, resulting in the evaporation of carbon, which subsequently condenses into nanotubular structures. The controlled parameters of this method, including arc current, voltage, gas composition, and pressure, enable precise tailoring of CNT properties, such as diameter, length, and defect density. Due to these advantages, the electric discharge method remains a promising approach for synthesizing high-purity CNTs with well-defined structural characteristics, facilitating their integration into applications in electronics, medicine, chemistry, pharmaceuticals, and biotechnology [20].

The electric arc discharge method remains one of the most efficient and scalable techniques for the synthesis of various carbon nanomaterials (CNMs), including fullerenes, carbon nanotubes (CNTs), graphene, carbon nanohorns, and core–shell nanoparticles. In recent years, significant progress has been made in understanding the mechanisms governing the formation and structural evolution of these materials under arc plasma conditions.

Roslan et al. (2018) studied the transformation of fullerenes into multi-walled carbon nanotubes (MW-CNTs) using arc discharge plasma, revealing insights into the gradual structural reorganization of carbon species during the synthesis process [21]. Complementarily, Raniszewski (2018) demonstrated that the application of an external electromagnetic field during arc discharge leads to a noticeable improvement in CNT yield and crystallinity, opening new avenues for controlled synthesis [22].

Further development in the control of product morphology was achieved by Zhang et al. (2019), who showed that varying the buffer gas type and pressure enables selective synthesis of different nanocarbon structures, including fullerenes, graphene, and nanohorns, within the same arc reactor [23]. Another noteworthy study by Zaikovskii et al. (2019) reported the formation of tin–carbon core–shell nanoparticles during arc discharge in helium, providing insight into

metal-carbon interaction and encapsulation mechanisms in plasma conditions [24].

In addition to arc systems operating in noble gases, the synthesis of carbon nanosheets has been successfully conducted in gliding arc reactors. Ma et al. (2021) compared chemical vapor dissociation of toluene with graphite exfoliation, demonstrating that process parameters significantly affect the morphology and surface structure of the resulting nanosheets [25].

A deeper understanding of nanoparticle formation dynamics in carbon arc plasma was provided by Yatom et al. (2018), who combined experimental diagnostics with numerical modeling. Their findings revealed that carbon nanoparticles predominantly nucleate in the peripheral regions of the arc, where temperature and carbon vapor gradients are optimal for nucleation and growth [26].

Arc discharge techniques have also been adapted for the synthesis of carbon nanomaterials from coal-derived precursors. A 2021 study reported the fabrication of graphene-containing nanostructures using electric arc treatment of coke derived from Shubarkol brown coal. These materials exhibited promising structural characteristics suitable for applications in energy storage and catalysis [27].

Overall, the arc discharge technique continues to be a powerful and versatile tool for producing high-quality carbon nanomaterials. The ability to control synthesis parameters—such as gas type, pressure, electrode composition, and external fields—provides wide tunability in nanomaterial structure and functionality. Future work will likely focus on process scaling, hybrid nanomaterials, and integration into device applications.

Carbon nanomaterials, particularly carbon nanotubes (CNTs), have been widely investigated due to their exceptional mechanical, thermal, and electrical properties. Numerous synthesis techniques have been developed, with the electric arc discharge method recognized for its high purity and crystallinity of produced CNTs. However, despite extensive research, limited attention has been paid to the use of copper substrates in arc discharge synthesis, and the resulting structural, morphological, and electrophysical properties of the synthesized CNMs remain insufficiently explored. In this study, we introduce a novel approach using a copper substrate in the electric arc discharge method (100 A, 75 V) to synthesize carbon nanomaterials. We characterize the resulting nanostructures using SEM and Raman spectroscopy and evaluate their electrophysical properties over a wide temperature range. This work provides new in-

sights into scalable production of CNMs with high dielectric constants and tunable electrical behavior, highlighting their potential for advanced electronic applications [28].

2 Materials and methods

The electric arc discharge method (100 A, 75 V) was employed to obtain nanomaterials. Pyrolysis gas acted as the carbon source, while graphite was used for the electrode and a copper plate as the substrate. The synthesis of carbon nanomaterials was carried out using the electric arc discharge method under the following conditions: a DC power source provided a stable discharge current of 100 A at a voltage of 75 V between two high-purity graphite electrodes. The discharge was conducted in a sealed stainless-steel chamber filled with argon gas (99.999% purity) at a pressure of 400 Torr (approximately 53 kPa). A continuous argon flow rate of 1.5 L/min was maintained throughout the process to ensure an inert atmosphere and remove reaction by-products. The inter-electrode gap was set at approximately 2 mm, and the arc discharge was sustained for 10 minutes per synthesis run. The copper substrate was positioned below the electrode assembly to collect deposited carbon material, while additional deposition occurred on the reactor wall and electrode surface. The analysis was performed using a laboratory carbonization furnace, gas chromatograph, scanning electron microscope, and Raman spectroscopy

The chemical analysis and surface morphology of the samples were studied using energy dispersive X-ray spectroscopy on an SEM (Quanta 3D 200i) with an EDAX energy dispersive analyzer. SEM images were obtained with the Quanta 3D 200i field-emission gun (FEG) at magnifications of ×2000, ×10000, and ×50000. A 5 nm conductive gold coating was applied to the samples using a Q150T ES sputter coater (Quorum Technologies, UK) to prevent charging effects during imaging.

The SEM system was operated under high-vacuum mode, with an accelerating voltage of 5–15 kV, depending on the sample's conductivity and required resolution. Energy-dispersive X-ray spectroscopy (EDS) was performed using an EDAX Apollo X detector integrated into the SEM system to analyze the elemental composition of the samples.

Raman spectroscopy analysis was performed using an NT-MDT NTEGRA Spectra system, which provides high spatial and spectral resolution for carbon nanomaterial characterization. A 532 nm solid-state laser was used as the excitation source, with an

output power of 5 mW to prevent sample degradation. The spectral range was set from 500 to 3500 cm⁻¹, with a spectral resolution of 1 cm⁻¹. Measurements were carried out using a 100× objective lens (NA = 0.95), providing a spatial resolution of approximately 300 nm. The system was calibrated prior to each measurement using the 520.7 cm⁻¹ silicon peak as a reference. The acquisition time for each spectrum varied between 10 and 30 seconds, depending on the fluorescence level of the sample. The intensity ratios ID/IG and I2D/IG were calculated to evaluate the degree of graphitization, defect density, and multilayer nature of the synthesized carbon nanomaterials. Data processing and spectral deconvolution were conducted using Nova PX software, ensuring precise background correction and peak fitting.

Measurement of electrical properties (dielectric constant ε, electrical resistance R) was carried out by measuring the electrical capacitance C of samples on a serial LCR-800 device (L, C, R meter) at an operating frequency of 1, 5, 10 kHz with a base error of 0.05-0.1%.

Plane-parallel samples were pre-fabricated in the form of disks with a diameter of 10 mm and a thickness of 1-6 mm with a binder additive (~1.5%). The pressing process was performed under a pressure of 20 kg/cm². The resulting discs were then fired in a silit furnace at 200°C for 6 hours. Afterward, they were carefully polished on both sides.

The dielectric constant was determined from the electrical capacitance of the sample at known values of the sample thickness and the surface area of the electrodes. To obtain the relationship between electrical induction D and electric field strength E, the Sawyer-Tower circuit was used. Visual observation of D (E of the hysteresis loop) was carried out on an S1-83 oscilloscope with a voltage divider consisting of a resistance of 6 mOhm and 700 kOhm, and a reference capacitor of 0.15 μF. Generator frequency 300 Hz. In all temperature studies, samples were placed in an oven, the temperature was measured with a chromel-alumel thermocouple connected to a B2-34 voltmeter with an error of ± 0.1 mV. Temperature change rate 5 K/min. The dielectric constant at each temperature was determined by the formula:

$$\varepsilon = \frac{C}{C_0} \qquad (1)$$

where $C_0 = \frac{\varepsilon_0 \cdot S}{d}$ is the capacitance of the capacitor without the test substance (air).

The band gap (ΔE) of the test substance was calculated using the following formula:

$$\Delta E = \frac{2kT_1T_2}{0.43(T_2 - T_1)} \lg \frac{R_1}{R_2}, \qquad (2)$$

The calculation of the band gap (ΔE) was performed using the formula, where k denotes the Boltzmann constant (8.6173303×10^{-5} eV·K⁻¹), R1 is the resistance at temperature T_1, and R_2 is the resistance at temperature T_2.

To confirm the reliability of the results, the dielectric constant of the standard substance barium titanate ($BaTiO_3$) was measured at 1 kHz, 5 kHz, and 10 kHz frequencies.

To ensure clarity in sample identification throughout the study, the synthesized carbon nanomaterials were categorized based on their collection location and assigned the following labels: S1 refers to the sample collected from the reactor wall, S2 corresponds to the material deposited on the copper substrate, E1 designates the sample obtained from the graphite electrode under gas-phase deposition conditions, and E2 represents the electrode-derived sample formed under solid-state conditions without the involvement of gas. These designations are consistently used in the subsequent sections to distinguish between the different sample types.

3 Results

Scanning electron microscopy (SEM) analysis of nanomaterials obtained from the reactor wall indicates the formation of flakes and finely dispersed agglomerates with different particle sizes 104-116 nm. In the Raman spectra of the sample, two typical peaks are observed at 1361 cm⁻¹ and 1590 cm⁻¹, corresponding to the D and G band. They are associated with the disordered structure, defects and ordered graphitic carbon structure of carbon materials. The material possesses a limited degree of graphitization (Gf = 36.08%). A key indicator of carbon material quality, the ID/IG intensity ratio, was determined, while the I2D/IG value of 0.247 (notably lower than the >1.6 observed in monolayer graphene) and the IG/I2D ratio of 4.04 support the presence of a multilayer CNT structure. The ID/IG ratio of 1.05 suggests a considerable number of defects within the material. (Fig. 3,4).
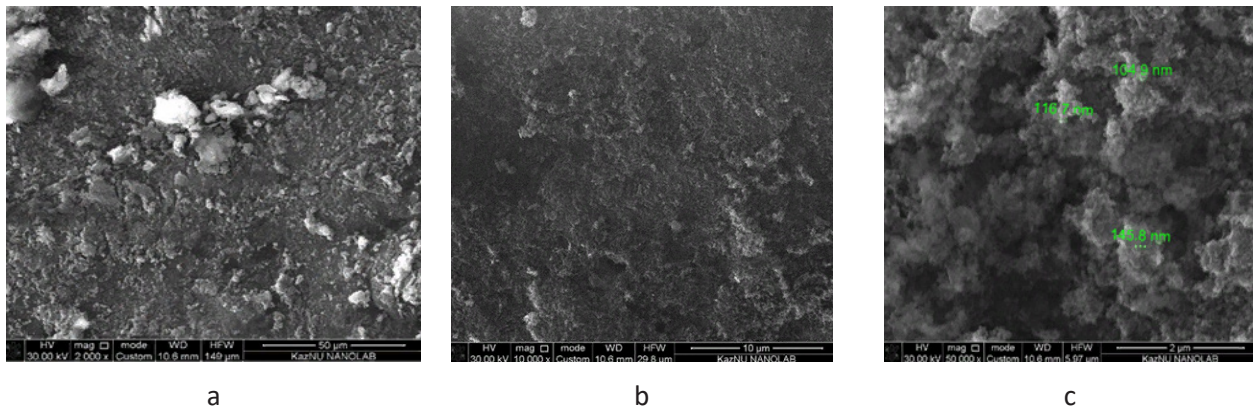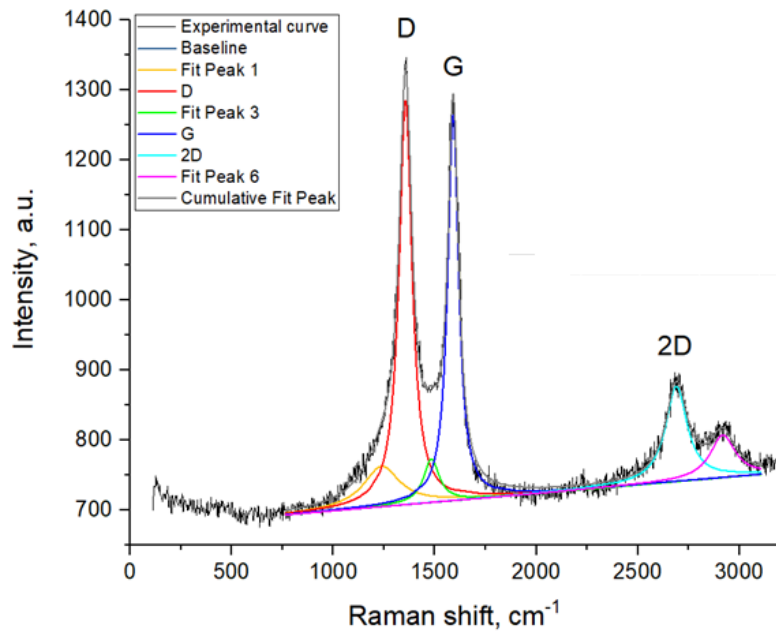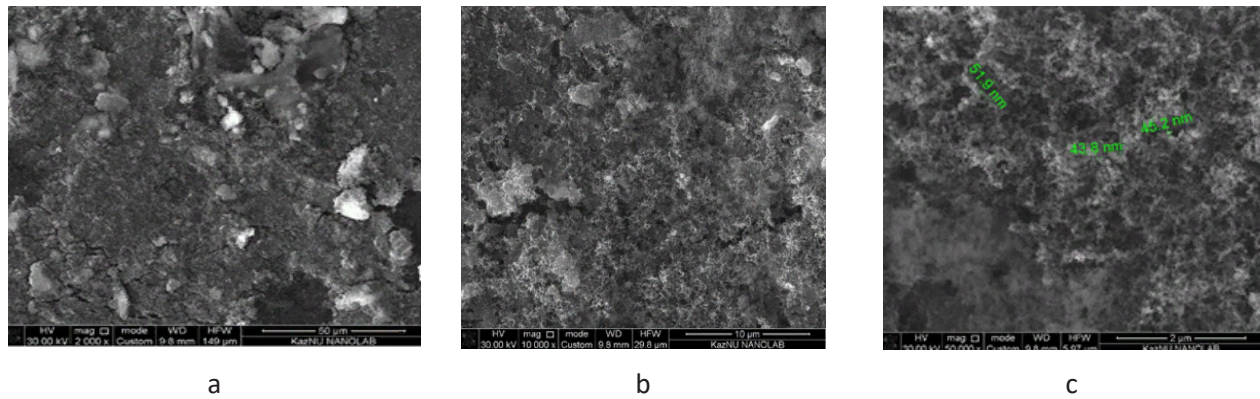
Figure 3 – SEM images of sample S1 (100 A, 75 V). a – x2000, b – x10000, c – x50000.

G_f=36.08%, I(D)/I(G)=1.05, I(G)/I(D)=0.95, I(G)/I(2D)=4.04 (Lorentz) I(2D)/I(G)=0.247
D = 1361 cm^{-1}; G = 1590 cm^{-1}; 2D = 2693 cm^{-1}
Figure 4 – Raman spectrum of sample S1 (100 A, 75 V).

The SEM images of the sample obtained from the substrate exhibit a graphite-like signal with visible flake-shaped particles measuring between 43 nm and 51 nm. Raman spectroscopy shows characteristic peaks at D (1354; 1341 cm^{-1}) and G (1579; 1588 cm^{-1}). The ID/IG intensity ratio, commonly used to assess carbon material quality, suggests a graphitization degree of 38.08%. The measured I2D/IG values (0.217 and 0.11) are much lower than the typical value for single-layer graphene (>1.6), while IG/I2D ratios (4.6 and 8.99) indicate a multilayer structure. The ID/IG ratios (0.64 and 1.025) reveal a significant number of defects in the material (Fig. 5,6).

a   b   c

Figure 5 – SEM images of sample S2 (100 A, 75 V). a – x2000, b – x10000, c – x50000.
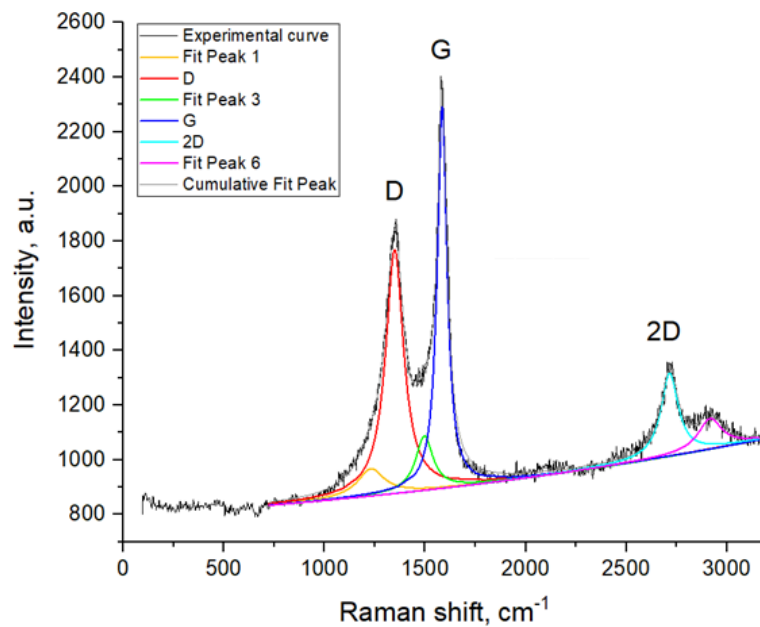
G_f=38.08%, I(D)/I(G)=0.64, I(G)/I(D)=1.56, I(G)/I(2D)=4.6 (Lorentz) I(2D)/I(G)=0.217

D = 1354 cm^{-1}; G = 1579 cm^{-1}; 2D = 2716 cm^{-1}

Figure 6 – Raman spectrum of sample S2 (100 A, 75 V).

Nanomaterials obtained from the electrode, as observed in SEM images, consist of flakes and small spherical agglomerates with particle sizes of 38–53.5 nm. Raman analysis confirms the formation of few-layer graphene or CNM, with characteristic peaks at 1360 cm^{-1} (D band) and 1575 cm^{-1} (G band). The graphitization degree was determined to be 88.98%, and the ID/IG intensity ratio, which assesses carbon material quality, was examined. The I2D/IG ratio (0.39) is significantly lower than that of monolayer graphene (>1.6), while the IG/I2D ratio (2.54) supports the presence of a low-layered carbon nanomaterial. The ID/IG ratio of 0.86 suggests minimal structural defects in the analyzed sample (fig. 7,8).

a   b   c
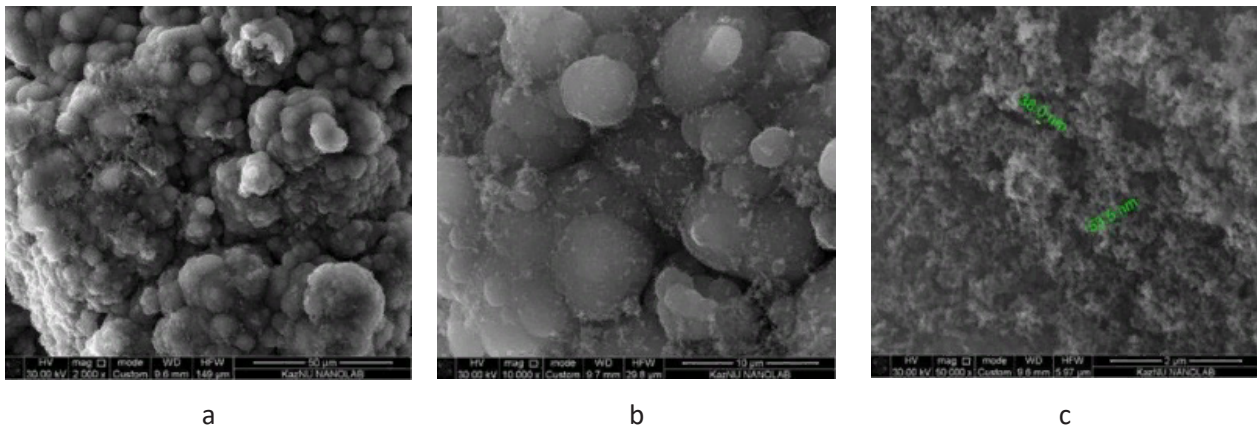
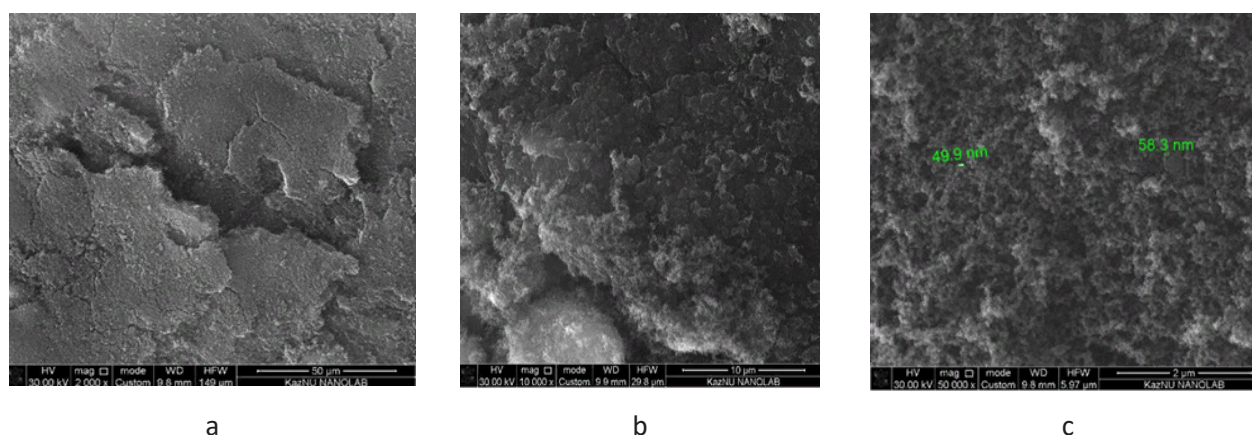**Figure 7** – SEM images of sample E1 (100 A, 75 V). a – x2000, b – x10000, c – x50000.
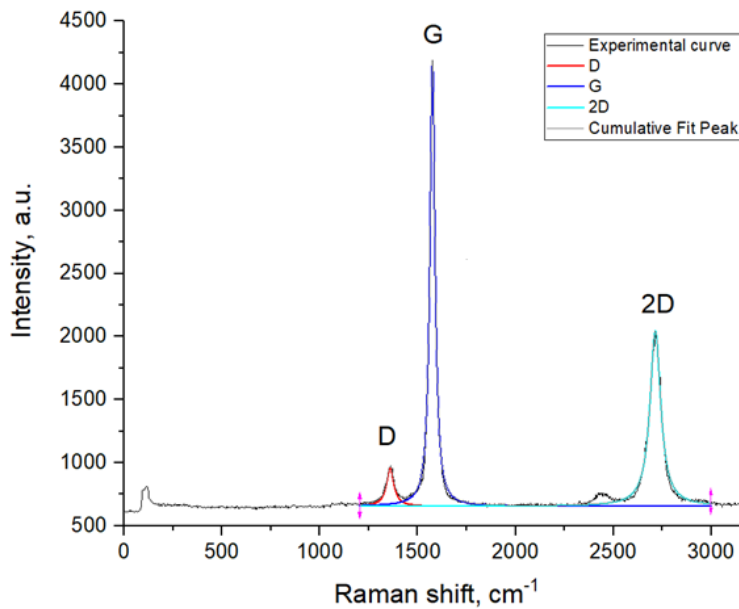
G_f=88.98%, I(D)/I(G)=0.085, I(G)/I(D)=11.72, I(G)/I(2D)=2.54 (Lorentz) I(2D)/I(G)=0.39

D = 1360 cm^{-1}; G = 1575 cm^{-1}; 2D = 2716 cm^{-1}

Figure 8 – Raman spectrum of sample E1 (100 A, 75 V).

SEM analysis of the nanomaterials obtained from the electrode shows the presence of flakes and large agglomerates, with particle sizes between 49 and 56 nm. The Raman spectra from the sample reveal a graphite structure, marked by the D bands at 1346 and 1356 cm^{-1} and the G band at 1580 cm^{-1}. The broad D-peak indicates that the sample has a low graphitization degree, with high disorder and numerous defects. The sample displays a heterogeneous nature. The graphitization degree is 53.7%, and the ID/IG ratio provides insight into the material's quality. The I2D/IG ratio (0.35 and 0.24) is much lower than the typical value for single-layer graphene (>1.6), while the IG/I2D ratio values of 2.87 and 4.13 suggest a low-layered nanomaterial. The ID/IG ratios of 0.97 and 0.59 imply a minimal presence of defects in the material (fig. 9,10).
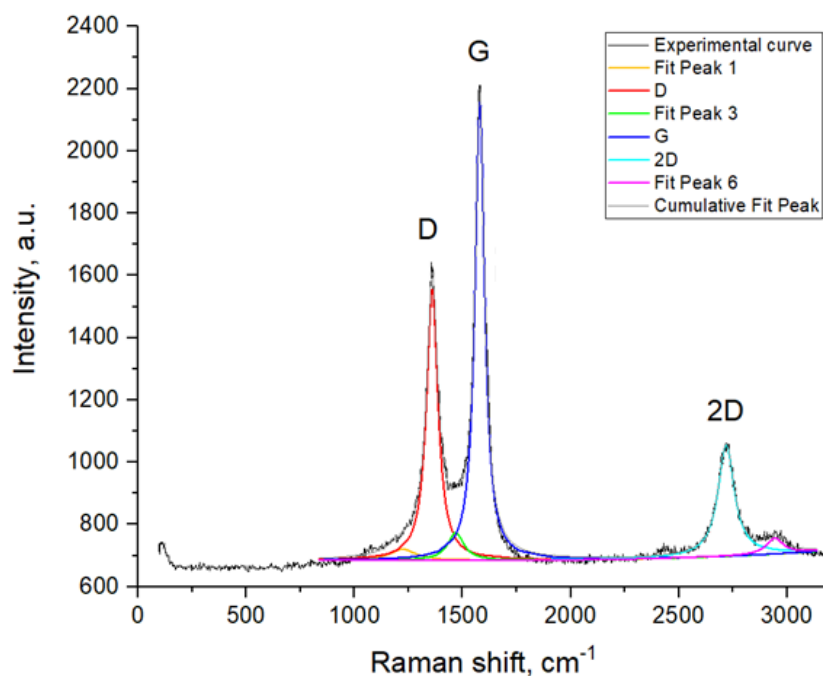
Figure 9 – SEM images of sample E2 (100 A, 75 V). a – x2000, b – x10000, c – x50000.

G_f=53.7%, I(D)/I(G)=0.59, I(G)/I(D)=1.69, I(G)/I(2D)=4.13 (Lorentz) I(2D)/I(G)=0.24
D = 1356 cm^{-1}; G = 1580 cm^{-1}; 2D = 2717 cm^{-1}
Figure 10 – Raman spectrum of sample E2 (100 A, 75 V).

Among the four samples studied, sample E1 (electrode-derived material, gas-phase deposition) demonstrated the highest degree of graphitization (88.98%) and the lowest defect density, as indicated by its low ID/IG ratio and prominent 2D peak in the Raman spectrum. This superior structural order can be attributed to the localized high-temperature plasma environment near the electrode, which promotes more complete carbon rearrangement and crystallization into graphitic domains. In contrast, sample S1 (reactor wall deposit) exhibited a lower graphitization degree (36.08%) and higher defect density. This is likely due to the cooler, less controlled deposition environment along the reactor wall, which results in rapid quenching and disordered carbon structures. Samples S2 and E2 showed intermediate behavior, reflecting the influence of both deposition surface and gas-phase versus solid-state formation conditions.

These differences highlight the critical role of deposition location and temperature gradient in deter-

mining the structural quality of the resulting carbon nanomaterials. The electrode surface, being directly exposed to the arc core, provides the most favorable conditions for forming high-quality, low-defect CNTs and graphene-like layers.

The formation of flakes and spherical agglomerates observed in SEM images may result from two competing mechanisms: (1) layered growth from carbon atoms adsorbed on a substrate surface, and (2) volumetric nucleation in the gas phase, followed by aggregation during cooling. Overall, the nanostructure formation is primarily governed by carbon vapor concentration, local temperature, deposition rate, and surface properties of the collection zones – all of which vary significantly across the different sample types.

The study focused on the electrophysical properties of carbon materials formed by the electric arc discharge method at 100 A, where a high graphitization degree was noted. Electrophysical measurements of carbon nanomaterials synthesized by the electric arc discharge method were carried out at a temperature of 293-483 K in the frequency ranges of 1, 5, and 10 kHz. Figure 11 shows how the dielectric constant (a) and electrical resistivity (b) of a carbon nanomaterial vary with temperature at frequencies of 1 kHz (I), 5 kHz (II), and 10 kHz (III).

Comparative data on the electrical properties of the resulting carbon materials are shown in Table 1.
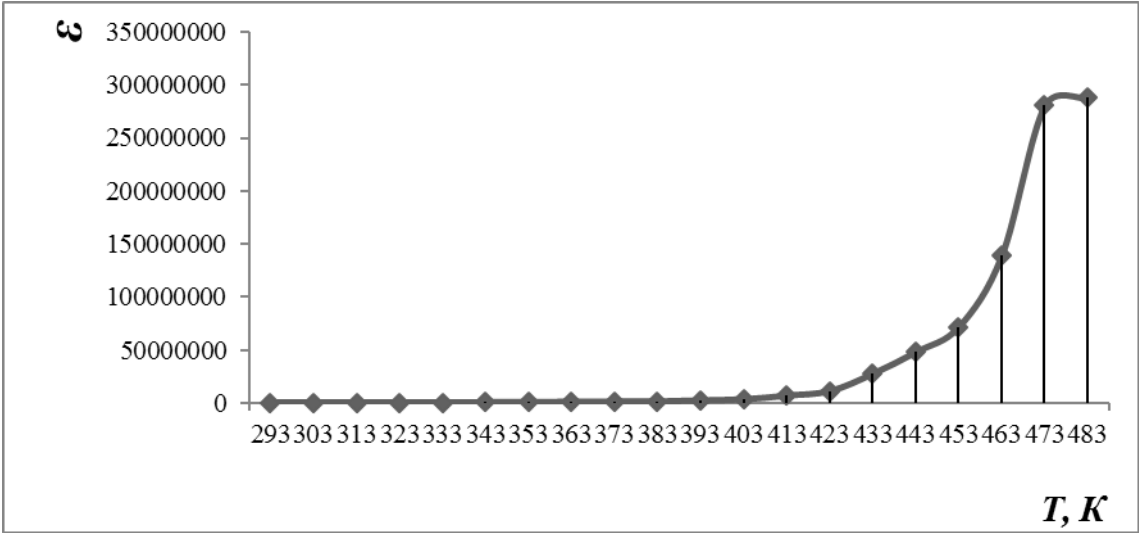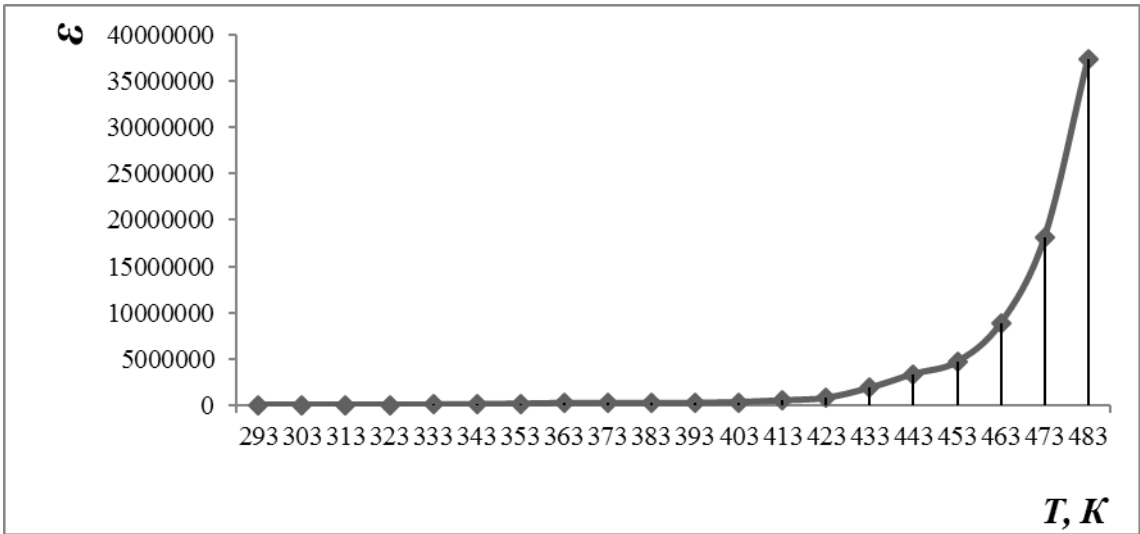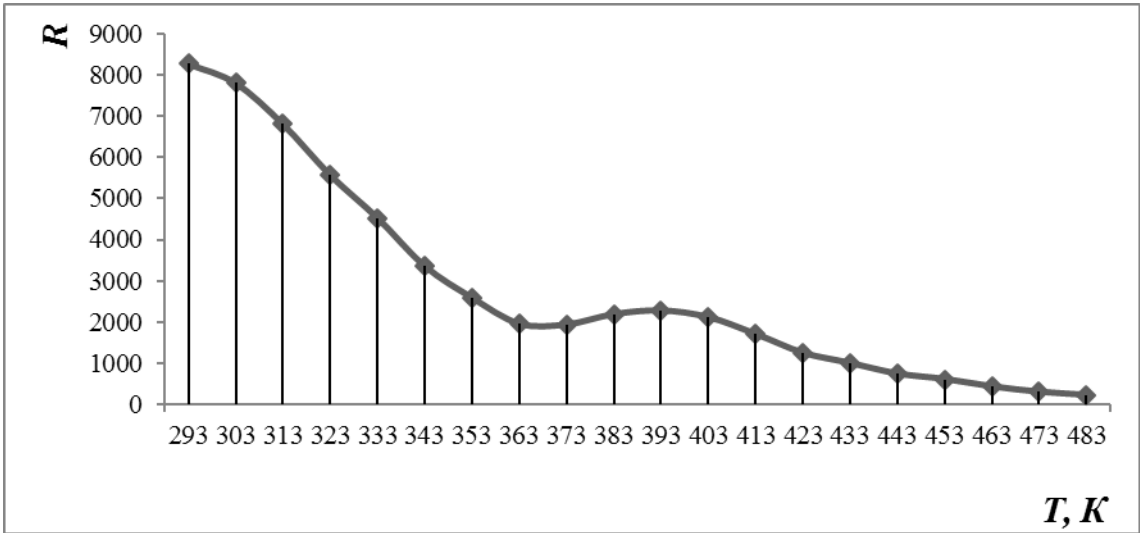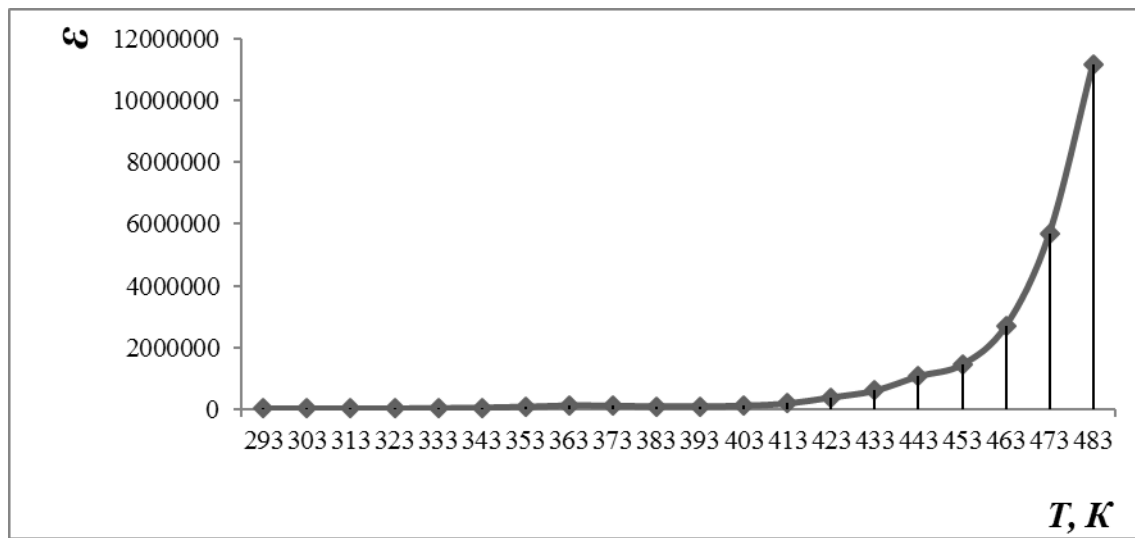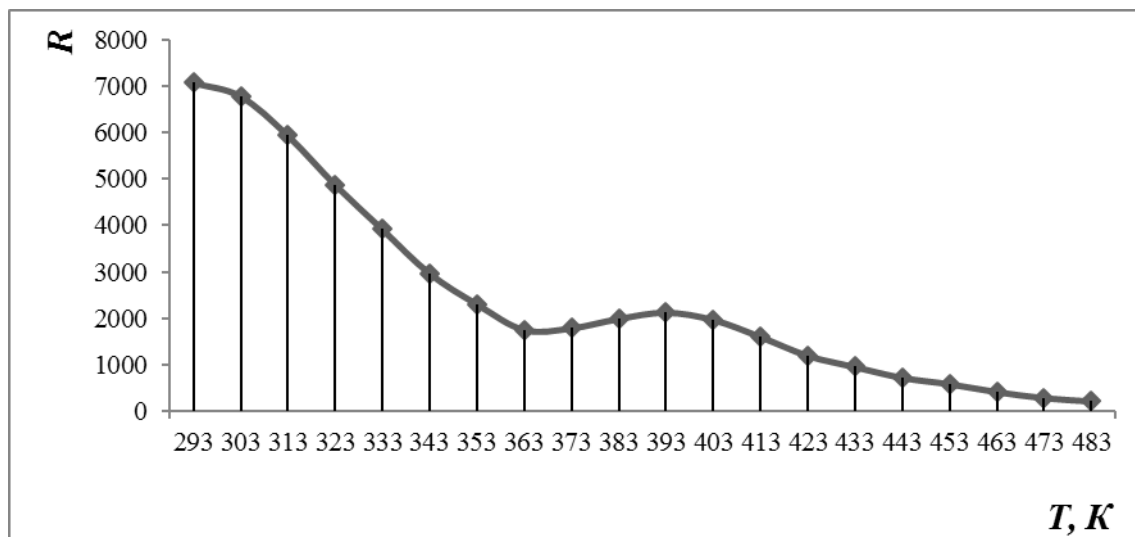

a)
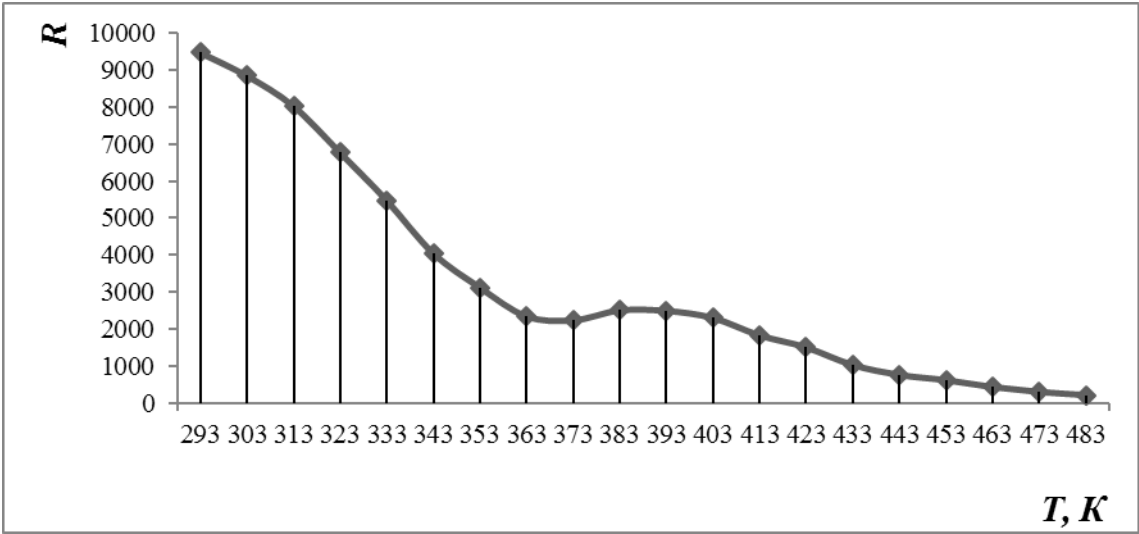
b)

I

a)

b)

II

a)

b)

III

Figure 11 – Variation of dielectric constant (a) and electrical resistivity (b) of carbon nanomaterial
at different temperatures at frequencies of 1 kHz (I), 5 kHz (II) and 10 kHz (III).

Table 1 – Temperature dependence of electrical resistance (R), capacitance (C), and dielectric constant (ε)

Name of material	Dielectric constant (ε)					
	at 1 kHz		at 5 kHz		at 10 kHz	
	293 K	483 K	293 K	483 K	293 K	483 K
BaTiO₃	1296	2159	1220	2102	561	2100
Nanomaterial	525877	287880816<	51819	37393213	24336	11181691
	Electrical resistance (lg*R*)					
BaTiO₃	4.13	3.67	4.47	3.58	5.18	3.37
Nanomaterial	3.98	2.35	3.92	2.35	3.85	2.34

The findings from investigations into the temperature dependence of the dielectric constant (ε) of a nanomaterial obtained at 100 A, 75 V show high ε values at all frequencies and in the range of 293-483 K. Thus, the ε values of this material at 293 K exceed ε of the reference BaTiO3 by 406 times at 1 kHz, 42 times at 5 kHz and 43 times at 10 kHz. This material holds promise for microcapacitor technology. The temperature dependence of its electrical resistance (R) reveals semiconductor conductivity from 293-363 K, metallic conductivity between 363-393 K, and again semiconductor conductivity from 393-483 K (at 10 kHz). According to the research, the band gap of this material is 0.72 eV within the 293-363 K range:

$$\Delta E = \frac{2 \times 0,000086173 \times 293 \times 363}{0,43(363-293)} \lg \frac{3,85}{3,24} = 0,72 \text{eV}$$ (3)

In the temperature range of 493-483 K, the band gap of the material is 1.2 eV, which classifies it as a narrow-bandgap semiconductor.

$$\Delta E = \frac{2 \times 0,000086173 \times 393 \times 483}{0,43(483-393)} \lg \frac{3,33}{2,34} = 1,2 \text{eV}$$ (4)

It is important to highlight that the dielectric constant of the carbon materials produced is competitive with that of the new $La_{15/8}Sr_{1/8}NiO_4$, which has a remarkably high dielectric constant in the range of 10^5-10^6.

During the experiment, carbon materials containing graphene were synthesized using the electric arc discharge method, which is considered one of the most promising methods for producing nanomaterials, allowing for the production of products of relatively high purity and with few defects.

The nanomaterials synthesized, particularly sample E1, exhibited extremely high dielectric constants (ε), reaching up to 2.88×10^8 at 1 kHz and 483 K, significantly exceeding those of conventional dielectrics such as barium titanate (BaTiO₃), which typically ranges from 10^3 to 10^4 under similar conditions.

Compared to other carbon-based nanomaterials such as reduced graphene oxide or CNT–polymer composites, which generally exhibit ε values in the range of 10^2–10^4, the results obtained in this study suggest a remarkably high capacity for charge storage. Additionally, the observed semiconductor-to-metal transition with temperature and narrow band gap (0.72–1.2 eV) are comparable to or better than many reported CNT-based and graphene-based systems. These features suggest strong potential for application in microcapacitor technologies, temperature-sensitive electronic switches, and semiconducting layers in nanoelectronic devices, especially where high dielectric response and thermal stability are required.

The temperature range of 293–483 K selected for measuring the electrophysical properties refers to the post-synthesis characterization phase, not the

synthesis plasma itself. However, water cooling was implemented to control the local temperature of the sample collection surfaces (e.g., electrode and substrate) during and immediately after discharge, minimizing thermal damage and improving measurement repeatability.

Regarding plasma temperature control, water cooling does not significantly reduce the central arc plasma temperature (typically several thousand K), but it plays a crucial role in moderating the surrounding reactor wall and electrode temperatures, which directly affect deposition morphology, particle agglomeration, and cooling rates of the carbon nanomaterials. This indirectly influences crystallinity and defect formation.

A direct comparative analysis of synthesis outcomes with and without cooling was not the primary focus of this study, but will be considered in future work.

4 Conclusion

In this study, carbon nanomaterials were successfully synthesized using an electric arc discharge method with a copper substrate and characterized through SEM, Raman spectroscopy, and electrical measurements. A key novelty lies in the use of a copper substrate and controlled collection zones (electrode, substrate, wall), which revealed strong spatial effects on graphitization quality, defect density, and morphology. Among the four samples, the electrode-derived nanomaterial (E1) showed the highest graphitization degree (88.98%) and the lowest defect content, highlighting the importance of deposition environment and thermal gradients in tailoring nanomaterial properties.

Importantly, the synthesized materials exhibited ultra-high dielectric constants and a tunable semiconducting-to-metallic transition, positioning them as promising candidates for next-generation microcapacitors, sensors, and thermally responsive nanoelectronic devices.

Future work should explore scaling the process for industrial production, optimizing substrate materials, and integrating these nanomaterials into functional electronic or energy storage systems. Additionally, a deeper investigation into long-term stability, conductivity under varying environments, and mechanical properties will be valuable for broadening application potential.

References

1. Il'in, A. M., Messerle, V. E., & Ustimenko, A. B. The formation of carbon nanotubes on copper electrodes under the arc discharge conditions // High Energy Chemistry. – 2010. – Vol. 44. – P. 326-331. https://doi.org/10.1134/S0018143910040120

2. Lozano-Castelló, D., Suárez-García, F., Alcañiz-Monge, J., Cazorla-Amorós, D., Linares-Solano, A. Gas-Adsorbing Nanoporous Carbons. – CRC Press: In Carbon Nanomaterials Sourcebook. – 2018. – P. 465-486.

3. Bardhan, N. M. 30 years of advances in functionalization of carbon nanomaterials for biomedical applications: a practical review // Journal of Materials Research. – 2017. – Vol. 32. –Is. 1. – P. 107-127. https://doi.org/10.1557/jmr.2016.449

4. Khamdohov, E. Z., Teshev, R. S., Khamdohov, Z. M., Khamdohov, A. Z., Kalajokov, Z. H., Kalajokov, H. H. Production of carbon films by the electric arc sputtering of graphite in a magnetic field // Journal of Surface Investigation. X-ray, Synchrotron and Neutron Techniques. – 2014. – Vol. 8. – P. 1306-1310. https://doi.org/10.1134/S1027451014060317

5. Wang, X., Li, Q., Xie, J., Jin, Z., Wang, J., Li, Y., Fan, S. Fabrication of ultralong and electrically uniform single-walled carbon nanotubes on clean substrates // Nano letters. – 2009. – Vol. 9. –Is. 9. – P. 3137-3141. https://doi.org/10.1021/nl901260b

6. Mittal, G., Dhand, V., Rhee, K. Y., Park, S. J., Lee, W. R. A review on carbon nanotubes and graphene as fillers in reinforced polymer nanocomposites // Journal of industrial and engineering chemistry. – 2015. – Vol. 21. – P. 11-25. https://doi.org/10.1016/j.jiec.2014.03.022

7. Abbas, A., Al-Amer, A. M., Laoui, T., Al-Marri, M. J., Nasser, M. S., Khraisheh, M., Atieh, M. A. Heavy metal removal from aqueous solution by advanced carbon nanotubes: critical review of adsorption applications // Separation and Purification Technology. – 2016. – Vol. 157. – P. 141-161. https://doi.org/10.1016/j.seppur.2015.11.039

8. Das, R., Ali, M. E., Abd Hamid, S. B., Ramakrishna, S., Chowdhury, Z. Z. Carbon nanotube membranes for water purification: A bright future in water desalination // Desalination. – 2014. – Vol. 336. – P. 97-109. https://doi.org/10.1016/j.desal.2013.12.026

9. Liu, X., Wang, M., Zhang, S., Pan, B. Application potential of carbon nanotubes in water treatment: a review //Journal of Environmental Sciences. – 2013. – Vol. 25. –Is. 7. – P. 1263-1280. https://doi.org/10.1016/S1001-0742(12)60161-2

10. Ng K. W., Lam W. H., Pichiah S. A review on potential applications of carbon nanotubes in marine current turbines // Renewable and Sustainable Energy Reviews. – 2013. – Vol. 28. – P. 331-339. https://doi.org/10.1016/j.rser.2013.08.018

11. Liu, W. W., Chai, S. P., Mohamed, A. R., & Hashim, U. Synthesis and characterization of graphene and carbon nanotubes: A review on the past and recent developments // Journal of Industrial and Engineering Chemistry. – 2014. – Vol. 20. –Is. 4. – P. 1171-1185. https://doi.org/10.1016/j.jiec.2013.08.028

12. Ying, L. S., bin Mohd Salleh, M. A., Rashid, S. B. A. Continuous production of carbon nanotubes–A review // Journal of Industrial and Engineering Chemistry. – 2011. – Vol. 17. – Is. 3. – P. 367-376. https://doi.org/10.1016/j.jiec.2011.05.007

13. Marsh H., Reinoso F. R. Activated carbon. Amsterdam: Elsevier. – 2006.

14. Dresselhaus, M. S., Dresselhaus, G., Eklund, P. C., Saito, R. Electrons and phonons in fullerenes. Optical and Electronic Properties of Fullerenes and Fullerene-Based Materials. – 1999. – P. 217.

15. Tian, Y., Zhang, Y., Wang, B., Ji, W., Zhang, Y., Xie, K. Coal-derived carbon nanotubes by thermal plasma jet // Carbon. – 2004. – Vol. 42. – Is. 12-13. – P. 2597-2601. https://doi.org/10.1016/j.apmt.2018.06.007

16. Yermagambet, B. T., Kazankapova, M. K., Borisenko, A. V., Nurgaliyev, N. U., Kasenova, Zh. M., Sayranbek, A., Kanagatov, K. G., Nauryzbaeva. A.T. Synthesis of carbon nanotubes by the method of CVD on the surface of the hydrophobic zone of the oil shale // News of the Academy of Sciences of the Republic of Kazakhstan . Series of Geology and Technical Sciences. – 2019. – Vol. 5. – Is. – 437. – P. 177-188. https://doi.org/10.32014/2019.2518-170X.140

17. Mohammad, M. I., Moosa, A. A., Potgieter, J. H., Ismael, M. K. Carbon nanotubes synthesis via arc discharge with a yttria catalyst // International Scholarly Research Notices. – 2013. – Vol. 1. – P. 785160. https://doi.org/10.1155/2013/785160

18. Rud, A. D., Kuskova, N. I., Ivaschuk, L. I., Boguslavskii, L. Z., Perekos, A. E. Synthesis of carbon nanomaterials using high-voltage electric discharge techniques by MM Rahman. InTech.–Rijeka. – 2011. – P. 99-116.

19. Perez-Cabero, M., Rodrıguez-Ramos, I., & Guerrero-Ruız, A. Characterization of carbon nanotubes and carbon nanofibers prepared by catalytic decomposition of acetylene in a fluidized bed reactor // Journal of catalysis. – 2003. – Vol. 215. – Is. 2. – P. 305-316. https://doi.org/10.1016/S0021-9517(03)00026-5

20. Yang, Z., Zhang, Q., Luo, G., Huang, J. Q., Zhao, M. Q., Wei, F. Coupled process of plastics pyrolysis and chemical vapor deposition for controllable synthesis of vertically aligned carbon nanotube arrays // Applied Physics A. – 2010. – Vol. 100. – P. 533-540. https://doi.org/10.1007/s00339-010-5868-9

21. Roslan, M. S., Abd Rahman, M. M., Jofri, M. H., Chaudary, K. T., Mohamad, A., Ali, J. Fullerene-to-MWCNT structural evolution synthesized by arc discharge plasma // Journal of Carbon Research. – 2018. – Vol. 4. – Is. 4. – P. 58. https://doi.org/10.3390/c4040058

22. Raniszewski, G. Optimization of the carbon nanotubes synthesis in arc discharge systems // COMPEL-The international journal for computation and mathematics in electrical and electronic engineering. – 2018. – Vol. 37. – Is. 5. – P. 1618-1625. https://doi.org/10.1108/COMPEL-01-2018-0019

23. Zhang, D., Ye, K., Yao, Y., Liang, F., Qu, T., Ma, W., Watanabe, T. Controllable synthesis of carbon nanomaterials by direct current arc discharge from the inner wall of the chamber // Carbon. – 2019. – Vol. 142. – P. 278-284. https://doi.org/10.1016/j.carbon.2018.10.062

24. Zaikovskii, A., Novopashin, S., Maltsev, V., Kardash, T., Shundrina, I. Tin–carbon nanomaterial formation in a helium atmosphere during arc-discharge // RSC advances. – 2019. – Vol. 9. – Is. 63. – P. 36621-36630. https://doi.org/10.1039/C9RA05485E

25. Ma, X., Li, S., Chaudhary, R., Hessel, V., Gallucci, F. Carbon nanosheets synthesis in a gliding arc reactor: on the reaction routes and process parameters // Plasma Chemistry and Plasma Processing. – 2021. – Vol. 41. – P. 191-209. https://doi.org/10.1007/s11090-020-10120-z

26. Yatom, S., Khrabry, A., Mitrani, J., Khodak, A., Kaganovich, I., Vekselman, V., Raitses, Y. Synthesis of nanoparticles in carbon arc: measurements and modeling // MRS communications. – 2018. – Vol. 8. – Is. 3. – P. 842-849. https://doi.org/10.1557/mrc.2018.91

27. Yermagambet, B. T., Kazankapova, M. K., Kasenov, B. K., Aitmagambetova, A. Z., Kuanyshbekov, E. E. Synthesis of graphene-containing nanomaterials based on a carbon product using electric arc discharge // Solid Fuel Chemistry. – 2021. – Vol. 55. – P. 380-390. https://doi.org/10.3103/S0361521921060057

28. Komokhov, P. G., Svatovskaya, L. B., Solovyova, V. Y., Sychev, A. M. High-strength concrete based on elements of nanotechnology using the sol-gel method, Achievements, problems and perspective directions of development of theory and practice of building materials science, Tenth Academic Readings of the RAASN. – 2006.

Information about authors:

Kazankapova Maira, PhD, Associate Professor, Corresponding Member of KazNANS, Leading Researcher, Head of Laboratory of LLP "Institute of Coal Chemistry and Technology" (Astana, Kazakhstan), e-mail: maira_1986@mail.ru

Yermagambet Bolat, Doctor of Chemical Sciences, Professor, Academician of KazNANS, Project Manager, Chief Researcher, Director of LLP "Institute of Coal Chemistry and Technology" (Astana, Kazakhstan), e-mail: bake.yer@mail.ru

Kasenov Bulat, Doctor of Chemical Sciences, Professor. Head Laboratory of the Chemical-Metallurgical Institute named after. Zh.Abisheva (Karaganda, Kazakhstan), e-mail: kasenov1946@mail.ru

Kassenova Zhanar, Candidate of Chemical Sciences (PhD), Member of KazNANS, Leading Researcher is a Deputy Director of LLP "Institute of Coal Chemistry and Technology" (Astana, Kazakhstan), e-mail: zhanar_k_68@mail.ru

Malgazhdarova Ainagul is a Junior Researcher at the «Institute of Coal Chemistry and Technology», master student *at the Eurasian National University of L.N. Gumilyov (Astana, Kazakhstan), e-mail: malgazhdarova.ab@mail.ru*

Mendaliyev Gani is a Junior Researcher at the «Institute of Coal Chemistry and Technology», master student at the Eurasian National University of L.N. Gumilyov (Astana, Kazakhstan), e-mail: ganimen02@mail.ru

Akshekina Assel is a Senior Lab Assistant at the «Institute of Coal Chemistry and Technology», master student at the Eurasian National University of L.N. Gumilyov (Astana, Kazakhstan), e-mail: akshekina11@gmail.com

Kozhamuratova Ultugan is a Junior Researcher at the «Institute of Coal Chemistry and Technology», master student *at the Eurasian National University of L.N. Gumilyov (Astana, Kazakhstan), e-mail: kozhamuratova.u@mail.ru*

Development of biocompatible coatings for orthopedic joint implants

A.B. Kengesbekov [1,2] , A. Serikbaykyzy [1] , M.B. Bayandinova [2,3*] ,

E.E. Batanov [1] , N.E. Bazarov [4] and A.N. Askhatov [1]

[1]Daulet Serikbayev East Kazakhstan Technical University, Ust-Kamenogorsk, Kazakhstan
[2]Institute of Composite Materials, Ust-Kamenogorsk, Kazakhstan
[3]Sarsen Amanzholov East Kazakhstan University, Ust-Kamenogorsk, Kazakhstan
[4]"PlasmaScience" LLP, Ust-Kamenogorsk, Kazakhstan
*e-mail: shohmanovamb@gmail.com
(*Received April 2, 2025; received in revised form May 7, 2025; accepted May 20, 2025*)

This article presents both theoretical and experimental approaches to the development of biocompatible coatings based on hydroxyapatite modified with titanium dioxide for orthopedic implants made from Ti-13Nb-13Zr titanium alloy. The primary objective was to enhance the adhesion, mechanical strength and antibacterial properties of the coatings by employing a combined technique: micro-arc oxidation followed by gas-thermal spraying. The influence of electrolyte composition and micro-arc oxidation parameters on the coating's morphology, surface roughness and adhesion strength were systematically investigated. The highest values of hardness and adhesion were achieved using electrolyte containing Na_2SiO_3, NaOH and $Na_2S_2O_3$ in conjunction with detonation sputtering method. Morphological and elemental analyses confirmed the density, uniform elemental distribution and minimal porosity of these coatings. Mechanical stability was verified through Rockwell B scale and Martens tests. The proposed dual-step surface treatment strategy offers a promising route for tailoring implant surfaces with multifunctional properties. The obtained results demonstrate that the proposed method can significantly improve the durability and performance of orthopedic implants by producing biocompatible, corrosion-resistant, and mechanically robust coatings.

Key words: Biocompatible coatings, micro-arc oxidation, surface modification, mechanical properties, surface roughness, coating adhesion.
PACS number(s): 62.20.-x; 62.20. Мк.

1 Introduction

Total knee and hip arthroplasty are some of the most successful and common surgical procedures. Implants are made of polyetheretherketone, UHM-WPE, cobalt and titanium alloys, and ceramics that mimic the natural joint and are biocompatible [1,2]. Titanium alloys are widely used [3-8], but their implants do not always provide effective osseointegration. To improve bioactivity, a porous layer is created or porous structures are developed [9].

The application of hydroxyapatite (HAp) coating was a solution to this problem; however, due to the brittleness of HAp, the coating can peel off, leading to metal ion release, infections, bleeding, and bacterial growth [10-12]. In mobile implants (e.g., hip implants), HAp particles cause fretting corrosion.

Another problem is bacterial infection leading to implant failure [13]. Pure HAp does not prevent bacterial adhesion because organic substances are easily absorbed by its surface, creating favourable conditions for their growth [14].

Thus, reinforcing nanoparticles such as Al_2O_2, TiO_2, etc. can be added to HAp to solve this problem. The development of HAp-based composites with TiO_2, yttrium-stabilized zirconium dioxide, Al_2O_2, nanodiamond, magnesium or natural fiber is actively investigated to improve the mechanical properties of HAp [15-18]. Several methods for antibacterial coatings have been proposed [19, 20], including the addition of Ag ions [21], antibiotic peptides [22] and organic compounds [23]. In [24], the concept of a multifunctional coating with both the necessary functionality and biocompatibility was proposed.

From the literature analysis, it can be seen that among the various enhancers, TiO_2 has been most widely used to improve the adhesion and cohesive strength, anti-wear properties, hardness and biological performance of the coating [25, 26]. Moreover, it has been reported that TiO_2 reinforcement in HA significantly improved the corrosion resistance [27, 28].

HA-TiO_2 based coatings are usually produced by plasma spraying (PS). In fact, PS is the most conventional commercial method and is approved for the fabrication of hydroxyapatite coatings by the US Food and Drug Administration (FDA) [29]. However, plasma spraying of HAp is very sensitive to crystalline conditions. Excessive heating of the plasma leads to low crystallinity of HAp and disintegration into more soluble phases (β-TCP) [30,31]. An amorphous phase is also observed in plasma spraying of HAp. This can lead to a decrease in coating strength and jeopardizes the long-term stability of the coating [32].

In the last decade, various authors have proposed to fabricate HAp coatings using alternative methods. Currently, methods that are free of the disadvantages of plasma spraying, such as vacuum plasma spraying [33], cold spraying [34], micro-arc oxidation (MAO) [35], high-velocity oxygen-fuel (HVOF) spraying [36], detonation spraying [37, 38], etc., are being intensively studied.

Thus, HVOF, detonation spraying and MAO methods represent a good prospect for obtaining HA-TiO_2 based coatings on titanium alloy. The above methods are further developed by scientists by optimizing the deposition parameters of the coatings and by combining several methods, etc. Thus, the properties of the coatings are related to the deposition parameters, which need to be optimized to control and analyze the effect of deposition parameters on the coating characteristics.

The role of pretreatment in enhancing the performance characteristics of biocomposite coatings was identified in this phase of work. HAp-TiO_2 biocomposite coatings were obtained using a combined technique of MAO and subsequent gas-thermal spraying detonation spraying, HVOF and cold spraying of calcium-phosphate ceramics based on hydroxyapatite. Comprehensive studies of theoretical and practical aspects of the formation of biocomposite coatings based on various combinations of nonmetallic structures have been carried out.

Based on the above, our aim is to study theoretical and practical aspects of formation of biocomposite coatings based on hydroxyapatite with TiO_2 addition, as well as to analyse methods of their deposition. Special attention is paid to combined technologies, including micro-arc oxidation and subsequent gas-thermal spraying, in order to optimise deposition parameters and improve the performance characteristics of the coatings.

2 Materials and methods

In accordance with the set objectives, Ti-13Nb-13Zr alloys were chosen as the object of the study. The choice of the research material is justified by the fact that Ti-13Nb-13Zr alloys are used for the manufacture of medical implants, such as joints and bone fixators, due to their biocompatibility and corrosion resistance, operating in temperature ranges from -50°C to 300°C.

The influence of microarc oxidation on the formation of calcium-phosphate coatings during gas-thermal spraying has been investigated. Samples from titanium alloy Ti13Nb13Zr (⌀ 25 mm) underwent mechanical treatment, cleaning and ultrasonic treatment (20-80 kHz) in distilled water or cleaning solution, providing effective removal of contaminants without damage to the material.

Electrolyte compositions were individually selected for each of the material samples prior to MAO coating:

1) 20 g/L Na_2SiO_3, 10 g/L KOH;
2) 20 g/L H_3BO_3, 10 g/L KOH;
3) 20 g/L Na_2SiO_3, 10 g/L NaOH,10 g/L $Na_2S_2O_3$.

The parameters of the microarc oxidation process were set within the following limits: pulse duration – 100-500 μs, pulse frequency – 50-100 Hz, current density – 0.13-0.35 A/cm², process duration – 5-20 minutes, electrical voltage – 50-100 V. These parameters, as well as electrolyte compositions and process mode were specially developed for the formation of calcium-phosphate coating with optimal properties. The MAO device includes a programmable AC source Guintek "APS-77300", a galvanic cooling bath, a set of electrodes, software for controlling and monitoring the electrophysical parameters of the process, as well as a digital oscilloscope that provides registration of kinetic dependencies during treatment. The formation of calcium-phosphate coating was carried out in alternating mode.

The schematic diagram of the device for carrying out MAO is presented in Figure 1.
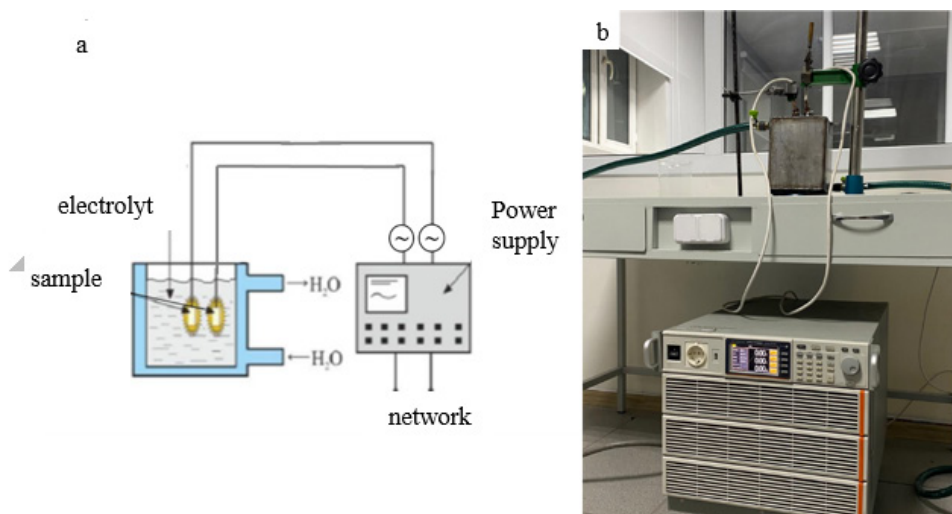
Figure 1 – Schematic diagram of the device (a) and experimental
setup with power supply (b) for microarc oxidation.

The surface microstructure and cross-sectional morphology of the coatings were studied by scanning electron microscopy (SEM) on a Vega 4 (Tescan, Czech Republic). A tungsten filament was used as a cathode. To study the elemental composition of the obtained coatings, the Xplore 30 energy dispersive analysis SEM attachment (Oxford Instruments) was used.

Rockwell B hardness (HRB) measurements were made using a 1/16 inch (1.5875 mm) diameter steel ball under a 100 kgf (980.7 N) load. A preload of 10 kgf ensured stable contact with the specimen surface. The depth of the indentation was recorded automatically by the device TR 5006M, and the results were determined according to GOST 9013. The method was used to evaluate soft metals and titanium alloys [39] .

Hardness and modulus of elasticity of the samples were measured according to the Martens method (ASTM E 2546) on a hardness tester FISCHER-SCOPE HM2000S ("Fischerscope", Germany), at indenter load F = 245.2mN and dwell time 20s. Surface roughness was determined according to GOST 25142-82 using a profilometer model 130.

Adhesion was measured using a tensile testing machine according to ASTM C633 standard specification. A two-component epoxy system (Adhesive 2214) was used as adhesive and the pulley diameter was 25 mm. After bonding, the pulleys were incubated at 24 °C and 50% relative humidity for 24 hours until the adhesive was fully cured.

To improve adhesion, a preliminary sandblasting with dry corundum was carried out (at air pressure of 0.3-0.6 MPa, the distance from the nozzle shear of the jet-abrasive gun to the treated surface is 80-200 mm).

3 Results and discussion

Surface analysis of the samples revealed differences in the morphology and porosity of the coatings depending on the electrolyte composition (Figure 2). The obtained coatings have rounded porosity, which indicates favorable conditions for osteointegration. The average pore size of MAO coatings of titanium alloy Ti13Nb13Zr samples is 12-23 μm, and the coating thickness varies within 3-8 μm.

Hydroxyapatite powder with a dispersity of 20-60 μm was used as the spraying material (Figure 3).

Figure 4 shows the values of surface roughness R_a depending on the modes of microarc oxidation (MAO) and the applied spraying method: detonation, cold and HVOF spraying. The first mode of MAO shows moderate roughness (R_a 1.8-2.0 μm) for all spraying methods. In the second mode, a maximum increase in roughness is observed, reaching R_a 2.8 μm when HVOF is used, which is due to the enhancement of the porous surface structure that promotes coating adhesion. In the third mode, the roughness decreases, especially in cold spraying (R_a about 1.8 μm), which may be related to the densification effect of the coating.
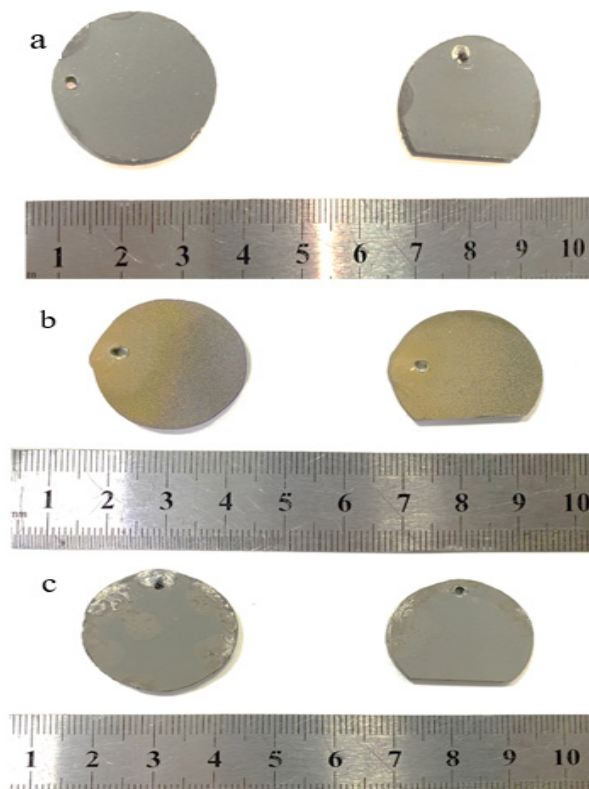
Figure 2 – Samples of titanium alloys after microarc oxidation:
Electrolyte 1: 20 g/L Na_2SiO_3, 10 g/L KOH; b) Electrolyte 2: 20 g/L H_3BO_3, 10 g/L KOH;
c) Electrolyte 3: 20 g/L Na_2SiO_3, 10 g/L NaOH, 10 g/L $Na_2S_2O_3$.
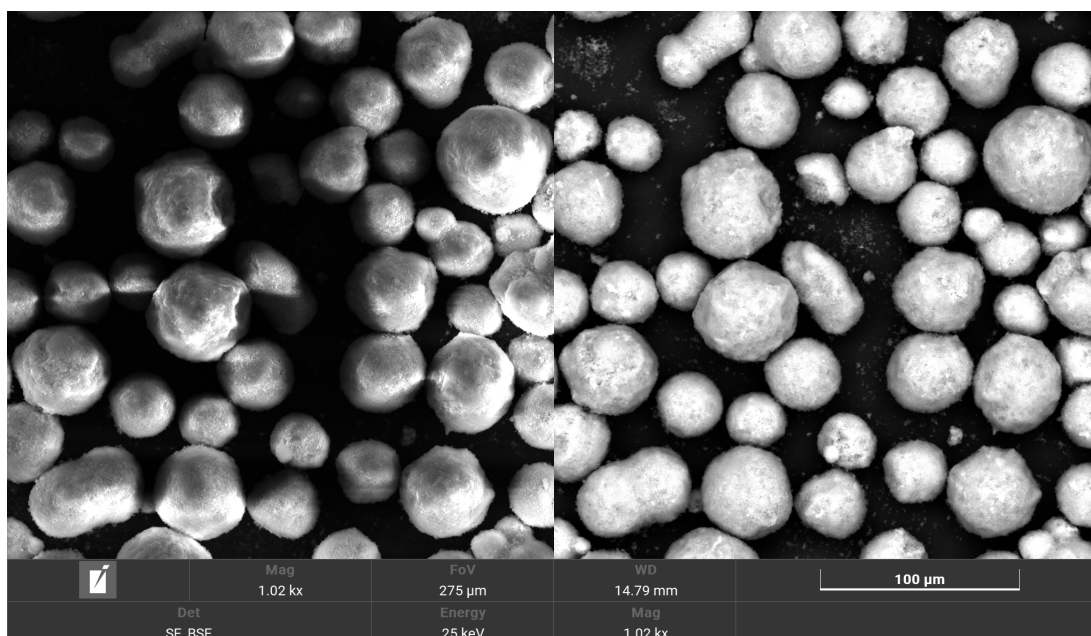

Figure 3 – SEM images of hydroxyapatite powder
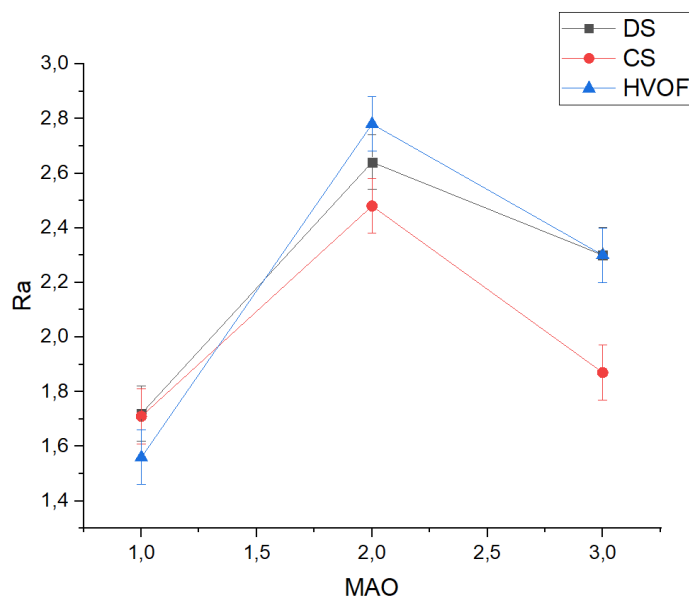with particle sizes in the range of 20-60 μm.

Figure 4 – Dependence of surface roughness parameter on microarc oxidation modes
for different spraying methods: detonation (DS), cold (CS) and HVOF spraying.

Based on the presented data, the second electrolyte (20 g/L H_3BO_3, 10 g/L KOH) provides the highest surface roughness (R_a) after microarc oxidation, which is attributed to the synergistic effect of boric acid and potassium hydroxide. Boric acid (H_3BO_3) promotes active pore formation and microstructural rough texture, whereas potassium hydroxide (KOH) accelerates the oxide layer formation process by increasing the ionic conductivity of the electrolyte. Compared to the other compositions, the first electrolyte (Na_2SiO_3, KOH) exhibits lower roughness due to the formation of a dense structure, while the third electrolyte (Na_2SiO_3, NaOH, $Na_2S_2O_3$) creates a layered surface with less porosity.

Adhesion strength plays a key role in evaluating the performance of coatings, as it determines their resistance to mechanical loads and durability under service conditions. The results of adhesion tests for these samples are presented in Figure 5. The analysis has shown that the choice of electrolyte composition and micro arc oxidation (MAO) modes has a significant influence on the substrate surface characteristics and adhesion of coatings applied by different spraying methods. Electrolytes based on sodium silicate (Na_2SiO_3) in combination with potassium hydroxide (KOH) or sodium hydroxide (NaOH) provide the formation of porous and rough layers that are optimal for adhesion in high velocity HVOF and detonation spraying. Boric acid electrolytes (H_3BO_3) promote smooth and dense layers, which improves adhesion

in cold spraying, where mechanical bonding is limited by low process temperatures. Maximum adhesion of the coatings is observed at an optimal combination of high porosity and surface roughness, which is achieved by using electrolytes with $Na_2S_2S_2O_3$ addition and MAO modes that promote active growth of the oxide layer.

Figure 6 shows the results of analysis of coatings deposited by different methods on a substrate treated with a solution of Na_2SiO_3 (10 g/L) and KOH. Figure 6a of the presented micrograph of the coating obtained by high-speed gas thermal spraying method shows the structure, the zone ($\sim$0-16 μm) calcium (Ca) and phosphorus (P) concentration reaches a maximum at a depth of $\sim$12-16 μm, indicating the formation of calcium-phosphate compounds. In Figure 6b, it can be seen that the coating is virtually absent, as evidenced by the following facts: the distribution of elements such as calcium (Ca) and silicon (Si) remains almost unchanged and uniform, indicating their association with the substrate material rather than the spraying layer (Figure 6c). The hydroxyapatite coating obtained by the detonation method has a thickness of $\sim$30 μm and is characterized by a stable structure and good adhesion to the substrate. The presence of key elements (Ca, P, O) confirms the successful formation of the functional layer, although porosity may affect the mechanical properties of the coating.
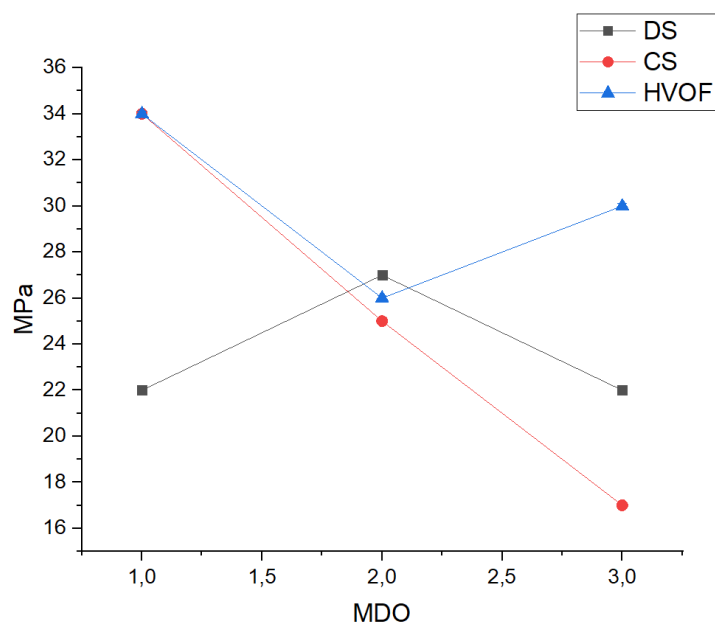
Figure 5 – Dependence of coating adhesion strength on microarc oxidation modes
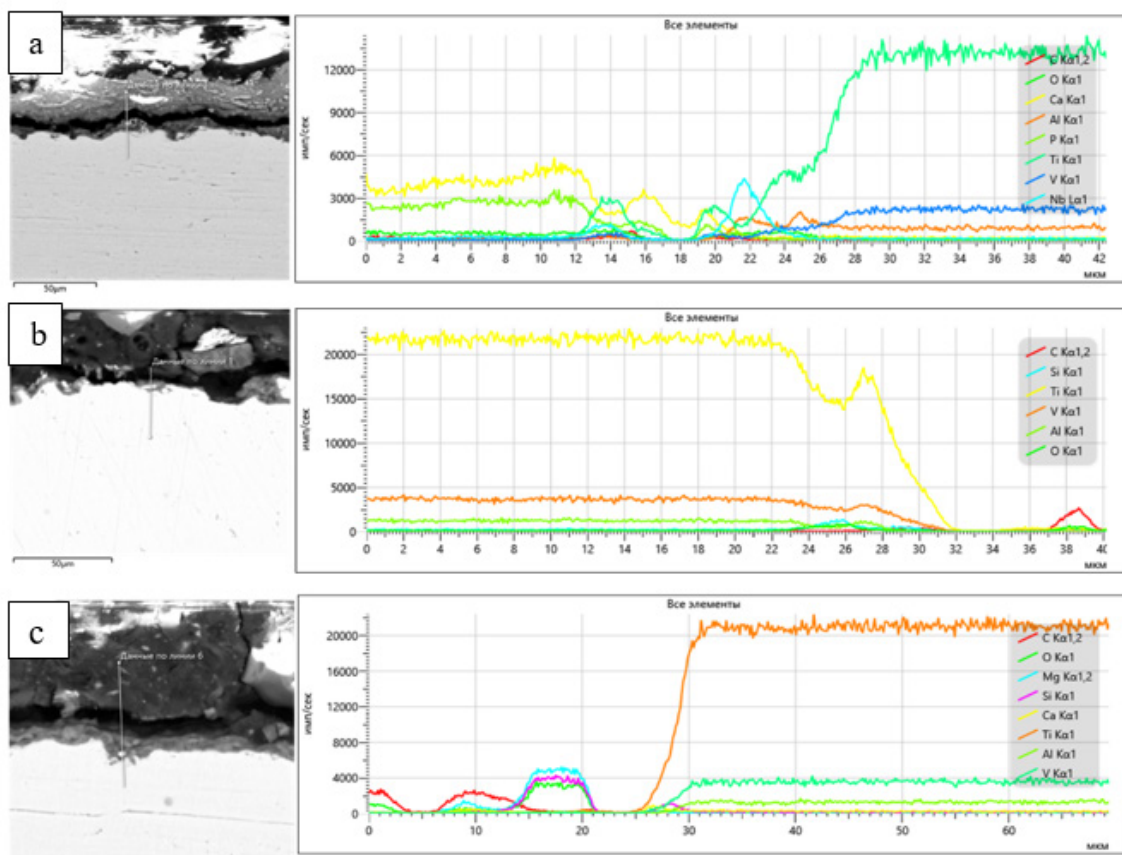for different spraying methods: detonation (DS), cold (CS) and HVOF spraying.

Figure 6 – Morphology and distribution of elements in coatings obtained
by different methods: (a) HVOF, (b) cold spraying, (c) detonation spraying.

Figure 7 shows the analysis results of coatings deposited on a substrate with a pre-formed MAO layer in a solution of 20 g/L H_3BO_3 and 10 g/L KOH using three methods: (a) high-speed gas-thermal spraying, (b) cold spraying, and (c) detonation spraying

High-speed gas-thermal spraying formed a dense coating ~18 μm thick with a uniform distribution of calcium and phosphorus (Figure 7a), and a high oxygen content indicating a protective oxide layer. In Figure 7b, it can be seen that the distribution of hydroxyapatite is heterogeneous as evidenced by a peak of calcium (Ca) at ~18-22 μm depth and a rapid decrease in its concentration indicating localized deposition of material. The coating has a porous structure and a maximum thickness of about ~18 μm, beyond which the titanium (Ti) substrate begins, indicating an insufficient thickness of the functional layer. The low oxygen (O) concentration and the absence of significant phosphorus (P)

content indicate poor formation of the hydroxyapatite layer.

Figure 7c shows that the coating is characterized by a dense structure and thickness up to ~30 μm, after which the titanium substrate begins, confirmed by a sharp increase in the concentration of titanium (Ti). The main component of hydroxyapatite, calcium (Ca), is uniformly distributed in the working layer (~10-30 μm), but the concentration of phosphorus (P), characteristic of hydroxyapatite, is either too low or not detected in the spectrum. Oxygen (O) is detected in significant amounts, indicating the presence of oxide phases, while magnesium (Mg) and silicon (Si) are present in trace amounts. Despite the high density and minimal porosity of the coating, the insufficiently uniform distribution of hydroxyapatite may limit the biocompatibility and protective properties of the coating, requiring further optimization of the spraying process.
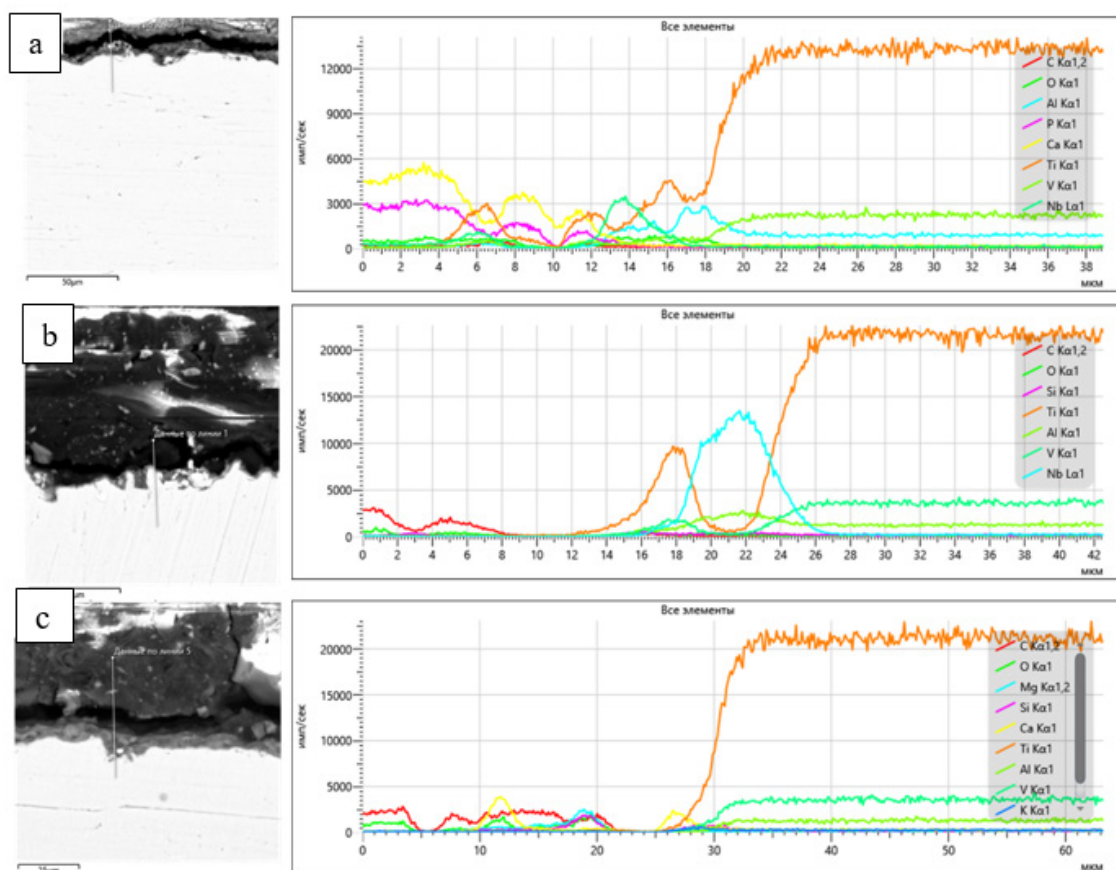

Figure 7 – Morphology and distribution of elements in coatings obtained by different methods: (a) HVOF, (b) cold spraying, (c) detonation spraying.

Figure 8 shows the microstructures and elemental analysis results of coatings deposited on substrates with pre-formed MAO layer in a solution of 20 g/L Na₂SiO₃, 10 g/L NaOH and 10 g/L Na₂S₂O₃, using three methods: high-speed gas-thermal spraying (a), cold spraying (b) and detonation spraying (c). The coating obtained by high-speed gas-thermal spraying method has a thickness up to ~12-16 μm, a dense structure and a high concentration of oxygen (O) and silicon (Si), which provides its protective properties. Cold spraying forms a coating up to ~28 μm thick, but its structure is porous and the distribution of calcium (Ca) and silicon (Si) is non-uniform, which reduces the effectiveness of the coating. Detonation spraying produces a ~30μm thick coating with a uniform distribution of calcium (Ca), magnesium (Mg) and oxygen (O), providing density and minimal porosity, making this method the most effective for creating protective layers.
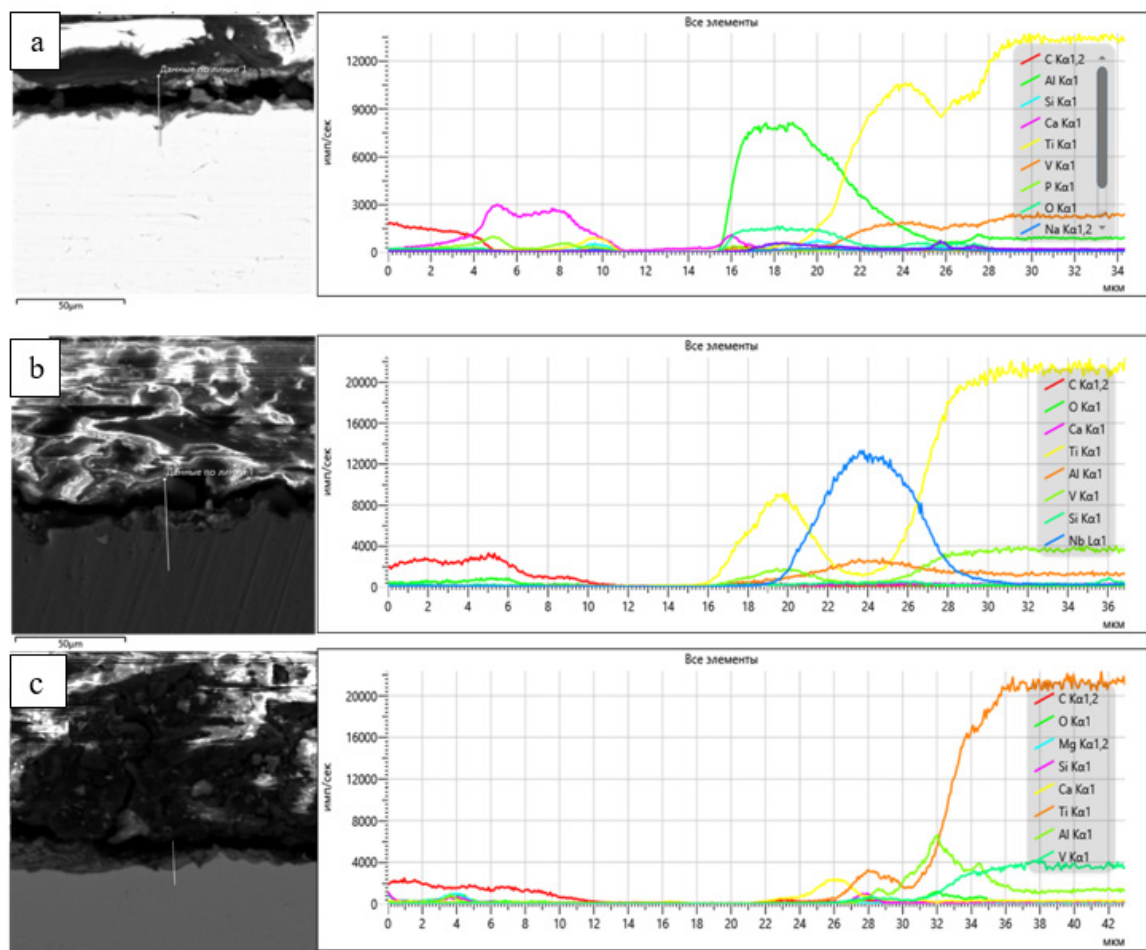
Figure 8 – Morphology and distribution of elements in coatings obtained
by different methods: (a) HVOF, (b) cold spraying, (c) detonation spraying.

The study was complemented by measurements of the hardness of the top layer of the coatings on the Rockwell B scale (HRB). The results in Figure 9 show that the detonation sprayed coatings have the highest HRB values due to the dense structure and minimal porosity of the top layer. High-speed gas-thermal spraying shows average HRB hardness values, confirming the balance of mechanical characteristics and uniformity of the coating structure. Cold sprayed coatings have minimal HRB hardness due to high porosity and insufficient layer density. Thus, detonation spraying provides the highest hardness and strength values among the studied methods.

Figure 9 – Results of microhardness study of biocomposite coatings:
detonation (DS), cold (CS) and HVOF spraying.
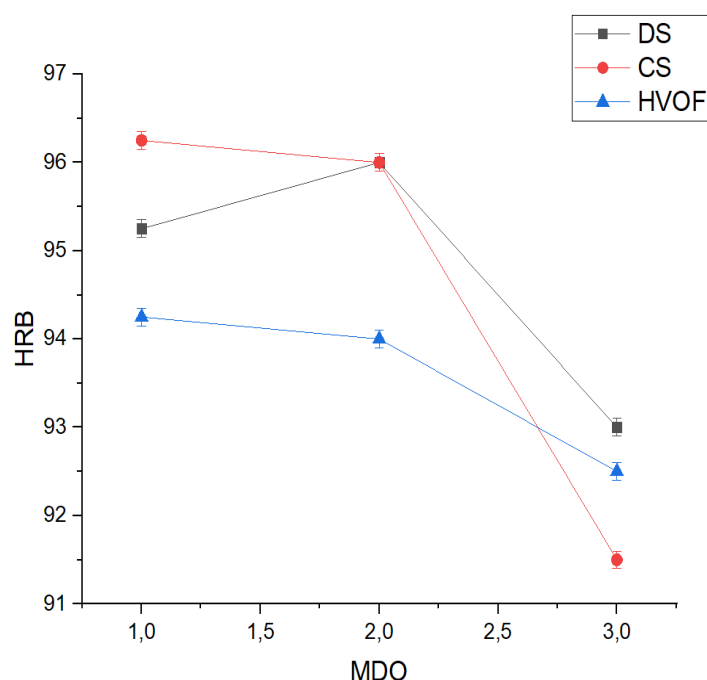
4 Conclusion

An effective technology for forming biocompatible coatings based on hydroxyapatite modified with titanium dioxide (HAp-TiO$_2$) for orthopaedic implants made of titanium alloy Ti-13Nb-13Zr has been developed and experimentally validated. The combined approach including micro-arc oxidation and subsequent gas-thermal spraying (HVOF, detonation and cold spraying) significantly improved adhesion, density and mechanical characteristics of the coatings.

It was found that both the parameters of micro-arc oxidation and the composition of the electrolyte exert a strong influence on the substrate's morphology and roughness, creating favorable conditions for robust adhesion of the coating layer. The highest values of roughness (up to R$_a$ 2.8 μm) and adhesion strength are achieved using a boron-containing electrolyte and the method of high-speed gas-thermal spraying. The best mechanical characteristics, including maximum hardness and minimum porosity, were recorded for the coatings obtained by detonation spraying.

Overall, the optimal combination of the parameters of micro-arc oxidation and coating method allows to form strong, uniform and functional biocompatible layers capable to increase the reliability and service life of orthopaedic implants.

References

1. Abitha H., Kavitha V., Gomathi B., Ramachandran B. A recent investigation on shape memory alloys and polymers-based materials on bio artificial implants-hip and knee joint // Materials Today: Proceedings. – 2020. – T. 33. – C. 4458-4466. https://doi.org/10.1016/j.matpr.2020.07.711

2. Shriya P., Pankaj D. Recent developments and advancements in knee implants materials, manufacturing: A review // Materials Today: Proceedings. – 2021. – T. 46. – C. 756-762. https://doi.org/10.1016/j.matpr.2020.12.465

3. Prakash S., Singh S., Pruncu C., Pramanik A., Krolczyk G. Investigation of machining characteristics of hard-to-machine Ti-6Al-4V-ELI alloy for biomedical applications // Journal of Materials Research and Technology. – 2019. – T. 8. – №. 5. – C. 4849-4862. https://doi.org/10.1016/j.jmrt.2019.08.033

4. Mussabek G., Baktygerey S., Taurbayev Y., Yermukhamed D., Zhylkybayeva N., Zaderko A.N., Diyuk V.E., Afonin S., Grishchenko L.M., Lisnyak V.V. Gas-phase approach to the modification of carbon surfaces by F-, Cl-and Br-containing groups and their selective substitution for catalytic sulfo groups // Applied Surface Science. – 2025. – Art. 162285. https://doi.org/10.1016/j.apsusc.2024.162285

5. Prakash C., Singh S., Le C.H., Krolczyk G., Ramakrishna S. Microwave sintering of porous Ti–Nb-HA composite with high strength and enhanced bioactivity for implant applications //Journal of Alloys and Compounds. – 2020. – Vol. 824. – Art. 153774. https://doi.org/10.1016/j.jallcom.2020.153774

6. Yar-Mukhamedova G.Sh., Muradov A.D., Mukashev K., Umarov F., Imanbayeva A.K., Mussabek G. Belisarova F. Impact of polyethylene terephthalate on the mechanical properties of polyimide films // Eurasian Physical Technical Journal. – 2025. – Vol. 22(1). –P. 28-36. https://doi.org/10.31489/2025N1/28-36

7. Pramanik A., Islam N., Basak A.K., Dong Yu, Littlefair G., Prakash C. Optimizing dimensional accuracy of titanium alloy features produced by wire electrical discharge machining // Materials and Manufacturing Processes. – 2019. – Vol. 34. – No. 10. – P. 1083-1090. https://doi.org/10.1080/10426914.2019.1628259

8. Pramanik A., Basak A. K., Prakash C. Understanding the wire electrical discharge machining of Ti6Al4V alloy // Heliyon. – 2019. – Vol. 5. – No. 4. https://doi.org/10.1016/j.heliyon.2019.e01473

9. Malik A., Manna A., Prakash C., Singh S. Laser-assisted jet electrochemical machining of titanium-based biomedical alloy // Biomanufacturing. – 2019. – P. 185-203. https://doi.org/10.1007/978-3-030-13951-3_9

10. Prakash C., Singh S., Ramakrishna S., Królczyk G., Le C. H. Microwave sintering of porous Ti-Nb-HA composite with high strength and enhanced bioactivity for implant applications // Journal of Alloys and Compounds. -2020. -Vol. 828. -Art. 153774. https://doi.org/10.1016/j.jallcom.2020.153774

11. Skakov M., Bayandinova M., Kozhakhmetov Y., Tuyakbaev B. Microstructure and corrosion resistance of composite based on ultra-high molecular weight polyethylene in acidic media // Coatings. – 2025. – Vol. 15. – No. 1. – P. 89. https://doi.org/10.3390/coatings15010089

12. He Z., Sun S. Deng C. Effect of hydroxyapatite coating surface morphology on adsorption behavior of differently charged proteins // Journal of Bionic Engineering. – 2020. – Vol. 17. – P. 345-356. https://doi.org/10.1007/s42235-020-0028-1

13. Kenzhina I., Kozlovskiy A., Blynskiy P., Tolenova A. Effect of dislocation density-associated strengthening factors on the thermal stability of composite ceramics // Physical Sciences and Technology. – 2024. – Vol. 11. – No. 1-2. – P. 23-31. https://doi.org/10.26577/phst2024v11i1a3

14. Ntsoane T.P., Topić M., Härting M., Heimann R.B., Theron C.C. Spatial and depth-resolved studies of air plasma-sprayed hydroxyapatite coatings by means of diffraction techniques: Part I // Surface and Coatings Technology. – 2016. – Vol. 294. – P. 153-163. https://doi.org/10.1016/j.surfcoat.2016.03.045

15. Khatoon Z., McTiernan C., Suuronen E., Mah T., Alarcon E. Bacterial biofilm formation on implantable devices and approaches to its treatment and prevention // Heliyon. – 2018. – Vol. 4. – No. 12. https://doi.org/10.1016/j.heliyon.2018.e01067

16. Mocanu A., Furtos G., Rapuntean S., Horovitz O., Flore Ch., Garbo C., Danisteanu A., Rapuntean G., Prejmerean C. Synthesis; characterization and antimicrobial effects of composites based on multi-substituted hydroxyapatite and silver nanoparticles // Applied Surface Science. – 2014. – Vol. 298. – P. 225-235. https://doi.org/10.1016/j.apsusc.2014.01.166

17. Chen X., Zhang B., Yongfeng G., Zhou P., Li H. Mechanical properties of nanodiamond-reinforced hydroxyapatite composite coatings deposited by suspension plasma spraying // Applied Surface Science. – 2018. – Vol. 439. – P. 60-65. https://doi.org/10.1016/j.apsusc.2018.01.014

18. Rutkuniene Z., Balandyte M., Karbauskyte G. Formation of diamond like carbon films on materials for medical application // Physical Sciences and Technology. – 2021. – Vol. 8. – No. 1-2. – P. 35-40. https://doi.org/10.26577/phst.2021.v8.i1.04

19. Kenesbekov A., Rakhadilov B., Kozhanova R., Stepanova O. Structural and phase changes in tin coatings subjected to thermal treatment // Key Engineering Materials. – 2020. – Vol. 839. – P. 131-136. https://doi.org/10.4028/www.scientific.net/KEM.839.131

20. Khazeni D., Saremi M.M., Soltani R. Development of HA-CNTs composite coating on AZ31 magnesium alloy by cathodic electrodeposition. Part 1: Microstructural and mechanical characterization // Ceramics International. – 2019. – Vol. 45. – No. 9. – P. 11174-11185. https://doi.org/10.1016/j.ceramint.2019.01.105

21. Heimann, R. B., & Lehmann, H. D. Bioceramic coatings for medical implants: trends and techniques. – John Wiley & Sons, 2015. 496 p.

22. Surmenev R. A., Surmeneva M. A., Ivanova A. A. Significance of calcium phosphate coatings for the enhancement of new bone osteogenesis–a review // Acta biomaterialia. – 2014. – Vol. 10. – No. 2. – C. 557-579. https://doi.org/10.1016/j.actbio.2013.10.036

23. Chen W., Liu Y., Courtney H., Bettenga M., Agrawal C. In vitro anti-bacterial and biological properties of magnetron co-sputtered silver-containing hydroxyapatite coating // Biomaterials. – 2006. – Vol. 27. – No. 32. – P. 5512-5517. https://doi.org/10.1016/j.biomaterials.2006.07.003

24. Kazemzadeh-Narbat M., Lai B.F., Ding C., Kizhakkedathu J.N., Hancock R.E., Wang R. Multilayered coating on titanium for controlled release of antimicrobial peptides for the prevention of implant-associated infections // Biomaterials. – 2013. – Vol. 34. – No 24. – P. 5969-5977. https://doi.org/10.1016/j.biomaterials.2013.04.036.

25. Shen J., Jin B., Qi Y., Jiang Q., Gao, X. Carboxylated chitosan/silver-hydroxyapatite hybrid microspheres with improved antibacterial activity and cytocompatibility // Materials Science and Engineering: C. – 2017. – Vol. 78. – P. 589-597. https://doi.org/10.1016/j.msec.2017.03.100

26. Raphel J., Holodsniy M., Goodman S.B., Heilshorn S.C. Multifunctional coatings to simultaneously promote osseointegration and prevent infection of orthopaedic implants // Biomaterials. – 2016. – Vol. 84. – P. 301-314. https://doi.org/10.1016/j.biomaterials.2016.01.016

27. Ren J., Zhao D., Qi F., Liu W., Chen Y. Heat and hydrothermal treatments on the microstructure evolution and mechanical properties of plasma sprayed hydroxyapatite coatings reinforced with graphene nanoplatelets // Journal of the Mechanical Behavior of Biomedical Materials. – 2020. – Vol. 101. – Art. 103418. https://doi.org/10.1016/j.jmbbm.2019.103418

28. Fu L., Khor K. A., Lim J. P. Yttria stabilized zirconia reinforced hydroxyapatite coatings //Surface and coatings Technology. – 2000. – Vol. 127. – No. 1. – P. 66-75. https://doi.org/10.1016/S0257-8972(00)00559-4

29. Kuroda D., Niinomi M., Morinaga M., Kato Y., Yashiro T. Design and mechanical properties of new β type titanium alloys for implant materials // Materials Science and Engineering: A. – 1998. – Vol. 243. – No. 1-2. – P. 244-249.3 https://doi.org/10.1016/S0921-5093(97)00808-3

30. Prakash C., Kansal H. K., Pabla B. S., Puri S. On the influence of nanoporous layer fabricated by PMEDM on β-Ti implant: biological and computational evaluation of bone-implant interface // Materials Today: Proceedings. – 2017. – Vol. 4. – No. 2. – P. 2298-2307. https://doi.org/10.1016/j.matpr.2017.02.078

31. Ratha I., Datta P., Balla V. K., Nandi S. K., Kundu, B. Effect of doping in hydroxyapatite as coating material on biomedical implants by plasma spraying method: A review // Ceramics International. – 2021. – Vol. 47. – No. 4. – P. 4426-4445. https://doi. org/10.1016/j.ceramint.2020.10.112

32. Hameed P., Gopal V., Bjorklund S., Ganvir A., Sen D., Markocsan N., Manivasagam G. Axial suspension plasma spraying: An ultimate technique to tailor Ti6Al4V surface with HAp for orthopaedic applications // Colloids and Surfaces B: Biointerfaces. – 2019. – Vol. 173. – P. 806-815. https://doi.org/10.1016/j.colsurfb.2018.10.071

33. Heimann, R. B. Thermal spraying of biomaterials // Surface and Coatings Technology. – 2006. – Vol. 201. – No. 5. – P. 2012-2019. https://doi.org/10.1016/j.surfcoat.2006.04.052

34. Rakhadilov B., Bayandinova M., Kussainov R., Maulit A. Electrolyte-plasma surface hardening of hollow steel applicator needles for point injection of liquid mineral fertilizers // AIMS Materials Science. – 2024. – Vol. 11. – №. 2. -P. 295-308. https://doi.org/10.3934/matersci.2024016

35. Yugeswaran S., Yoganand C. P., Kobayashi A., Paraskevopoulos K. M., Subramanian B. Mechanical properties, electrochemical corrosion and in-vitro bioactivity of yttria stabilized zirconia reinforced hydroxyapatite coatings prepared by gas tunnel type plasma spraying // Journal of the mechanical behavior of biomedical materials. – 2012. – Vol. 9. – P. 22-33. https://doi.org/10.1016/j.jmbbm.2011.11.002

36. Skakov M.K., Ocheredko I. A., Bayandinova M. B., Tuyakbaev B.T. The impact of technological parameters of the torch to physical and chemical properties of a gas-thermal burner for spraying ultra-high molecular weight polyethylene // Physical Sciences and Technology. – 2022. – Vol. 9. – No. 3-4. – P. 59-68. https://doi.org/10.26577/phst.2022.v9.i2.08

37. Tang J., Zhao Z., Liu H., Cui X., Wang J., Xiong T. A novel bioactive Ta/hydroxyapatite composite coating fabricated by cold spraying // Materials Letters. – 2019. – Vol. 250. – P. 197-201. https://doi.org/10.1016/j.matlet.2019.04.123

38. Kengesbekov, A. Influence of plasma arc current and gas flow on the structural and tribological properties of TiN coatings obtained by plasma spraying // Coatings. – 2024. – Vol. 14. – No. 11. – Art. 1404. https://doi.org/10.3390/coatings14111404

39. Kengesbekov A. B., Rakhadilov B. K., Tyurin Y. N., Magazov N. M., Kylyshkanov M. K., Sagdoldina Z. B. (2021). The influence of pulse-plasma treatment on the phase composition and hardness of Fe-TiB$_2$-CrB$_2$ coatings // Eurasian Journal of Physics and Functional Materials. – 2021. – Vol. 5. – No. 2. – P. 155-162. https://doi.org/10.32523/ejpfm.2021050209

Information about authors:

Kengesbekov Aidar Bakytbekuly, PhD is a Leading Researcher at the Scientific Center "Protective and Functional Coatings" at the D.Serikbaev East State Technical University (Ust-Kamenogorsk, Kazakhstan),e-mail: kenesbekovaidar@gmail.com

Serikbaikyzy Ainur is a PhD student of the educational program 8D05301 – "Technical Physics" at the D. Serikbayev East Kazakhstan Technical University, Junior researcher at the Scientific Center "Protective and Functional Coatings" (Ust-Kamenogorsk, Kazakhstan), e-mail: ainura.serikbaikyzy@gmail.com

Bayandinova Moldir Boleukhanovna is a Senior Researcher at the "Institute of Composite Materials" LLP, Senior Lecturer of the Department of Physics and Technology, Sarsen Amanzholov University of East Kazakhstan (Ust-Kamenogorsk, Kazakhstan), e-mail: shohmanovamb@gmail.com

Batanov Elaman is a Master's student of the educational program "7M05301 – Technical Physics", Junior researcher at the Scientific Center "Protective and Functional Coatings" at the D.Serikbaev East State Technical University, (Ust-Kamenogorsk, Kazakhstan), e-mail: batanovelman1234@gmail.com

Bazarov Nuraly Erkinuly is a Researcher at the «PlasmaScience» LLP (Ust-Kamenogorsk, Kazakhstan), e-mail: bazarov.nuraly@ gmail.com

Askhatov Arnur is Technician of the Scientific Centre "Protective and Functional Coatings" at the D. Serikbayev East Kazakhstan Technical University, (Ust-Kamenogorsk, Kazakhstan), e-mail: ashatovarnur@gmail.com

Effect of copper in silver coatings on the corrosion behavior of NZ30K–0.1 wt.% ag alloy in Ringer–Locke solution

V. Greshta

Zaporizhzhia Polytechnic National University, Zaporizhzhia, Ukraine
e-mail: greshtaviktor@gmail.com
(*Received April 21, 2025; received in revised form May 30, 2025; accepted June 02, 2025*)

This study investigates the corrosion behavior of NZ30K + 0.1 wt.% Ag alloy coated with a silver layer containing copper impurities introduced unintentionally during plasma spraying. X-ray spectral analysis revealed the coating composition as 60.1 wt.% Ag and 39.9 wt.% Cu, which significantly influenced the corrosion performance in Ringer–Locke solution. Intense contact corrosion occurred at coating defects, initiating crevice corrosion and delamination at the transition between cylindrical and flat surfaces. A rapid negative shift in corrosion potential (E_{cor}) at 29.9 mV/s was observed–1.67 times faster than in samples with a 1200 nm thick pure silver coating. Subsequently, the shift rate decreased to 0.008 mV/s and stabilized at −1.356 V. Localized corrosion developed into pitting and deep ulcers due to selective anodic dissolution, resembling damage typical of stainless steels in chloride environments. The results indicate that copper contamination in silver coatings on NZ30K-based biodegradable implants is detrimental, as it accelerates local corrosion and hydrogen evolution, potentially contributing to muscle necrosis during bone healing.

Key words: Biodegradable magnesium alloy, NZ30K-Ag composite, corrosion in Ringer-Locke solution, copper-contaminated silver coatings, localized and crevice corrosion.
PACS number(s): 81.40.Np.

1 Introduction

Recently, biodegradable implants made of magnesium alloys have been used in traumatology [1]. Magnesium is not capable of forming self-protective oxide films [2], so its alloys with Al, Ca, Cu, Fe, Li, Mn, Ni, Sr, Zn [3-6], often modified with rare earth elements, are used to produce biodegradable implants for a controlled rate of their dissolution in the osteosynthesis process [7]. In addition, polymer coatings on the surface of biodegradable implants [8-12] and silver metallization [13] are often used to address these issues. In paper [14], NZ30K alloy additionally alloyed with 0.1 wt.% Ag was proposed for the production of biodegradable implants. It has high mechanical properties [15] and specific shock absorption capacity [16], which are required for such products [17], does not contain toxic chemical elements and does not contribute to biological complications, such as Alzheimer's disease, muscle destruction, and does not reduce osteoclast activity [18,19]. Zinc, Zr, and Nd in NZ30K alloy significantly reduce the rate of general corrosion (~50%) during osteosynthesis [20], but they

form inclusions, intermetallic and other secondary phases, which in chloride-containing media, such as Ringer Locke solution, create microgalvanic pairs with a solid magnesium solution [21], which is the cause of pitting in the vicinity of these inclusions [22]. This is also inherent in stainless steels and alloys that are passivated [23-26]. In paper [27], it has been found that point and linear microdefects in the silver coating on the surface of the NZ30K alloy + 0.1 wt.% Ag were the focus of the nucleation of contact and crevice corrosion in the Ringer-Locke solution. They contributed to the local delamination of the coating from the alloy and the development of pitting and crevice corrosion, which proceeded according to the mechanisms established in [28-30]. At the same time, when silver is applied to the surface of the NZ30K+0.1 wt.% Ag alloy, it is possible that copper from the base on which the silver target is located may accidentally enter the coating. Under such conditions, copper can selectively dissolve in the silver coating. Therefore, the paper investigated the effect of copper in a silver coating on the surface of NZ30K+ 0.1 wt.% Ag alloy on its local corrosion destruction.

2 Materials and methods

We studied samples of silver-alloyed magnesium alloy NZ30K, which were smelted in an induction crucible furnace and subjected to aging [14]. The diameter of the samples was 12 and the length was 30 mm. Their chemical composition by the X-ray spectral method using the INKA ENERGY 350 has been determined (Table 1).

The samples of the alloy under study were clad with a 1300 nm thick layer of silver using a DC magnetron sputtering system equipped with a circular source and an Ag target (50 mm in diameter) in a gas discharge. The vacuum chamber of the system was a cylinder with an internal diameter and height of 500 mm. Cylindrical samples made of silver-alloyed

NZ30K alloy + 0,1 mass. % (Table 1) were chemically degreased and cleaned by ultrasonication in a hot ethanol bath for 10 minutes and dried in warm air. Then they were mounted on a rotating (9 Hz) fixture located 90 mm from the sputtering source. Before deposition of the silver coating, air was pumped out of the chamber by a diffusion oil pump to a residual pressure of $1 \cdot 10^{-3}$ Pa. The samples were ion-etched at a bias potential of 1000 V for 15 minutes at a pressure of 1.5 Pa. An unbalanced magnetron was used in a 600 mA DC mode at 400 V. The silver coating was applied at a constant magnetron power of 240 W and a base bias voltage of 100 V. The argon pressure in the deposition chamber was 1.0 Pa. The time of silver deposition on the surface of the studied magnesium alloy was 25 minutes for a coating thickness of 1300 nm.

Table 1 – Chemical composition of silver alloy NZ30K + 0,1 mass. % Ag.

Alloy	Content of chemical elements, wt. %				
NZ30K+Ag	Mg	Zn	Zr	Nd	Ag
	95.57	0.69	0.86	2.76	0.09

The chemical composition of the coating on the surface of the NZ30K alloy + 0.1 wt.% Ag was determined by X-ray spectroscopy using the INKA ENERGY 35, in particular, it has been determined that the silver content was 60.1 and copper was 39.9 wt. %.

Corrosion tests of silver clad samples with copper impurities have been carried out in a Ringer-Locke solution (an aqueous solution of undistilled water with the following chemical reagents, in mg/l NaCl – 9; $NaHCO_3$; $CaCl_3$; KCl 0.2; $C_6H_{12}O_6$ – 1) at a temperature of 20±1°C.

The establishment of the steady-state value of the corrosion potential E_{cor} on the tested samples on the PN-2MK-10A potentiostat in automatic mode has been recorded. The surface of the corrosion damage on the samples after their testing in the Ringer-Locke solution using an optical microscope MMR-2P and a scanning electron microscope JSM6360 with an energy dispersive microanalyzer JED-2300 has been examined.

3 Research results and discussion

According to the results of metallographic analysis of the surface of a sample made of NZ30K alloy + 0.1 wt.% Ag (Table 1) clad with a layer of silver and

copper, last one accidentally got into it from a copper base for a silver target during plasma spraying, it has found that it has an ordered microstructure with micropores up to 0.1 μm in size (Fig. 1).
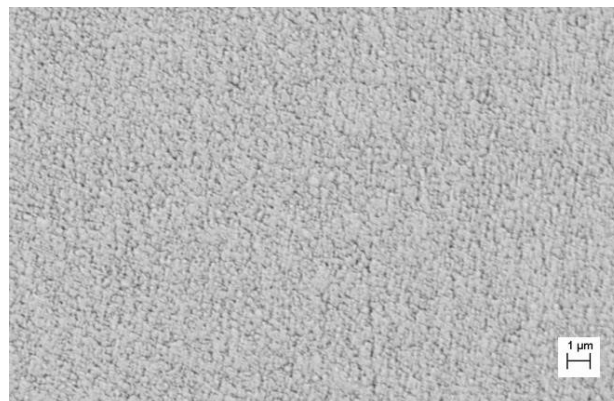

Figure 1 – Microstructure of a 1300 nm thick silver and copper clad layer on the surface of a NZ30K+0.1 wt.% Ag alloy sample (×1000).

It has been found that through these micropores in the coating, the NZ30K alloy + 0.1 wt.% Ag came into contact with the Ringer-Locke solution in which the sample has been tested. This caused contact corrosion on the end surface of the

V. Greshta

Phys. Sci. Technol., Vol. 12 (No. 1-2), 2025: 95-102

sample (Fig. 2), which developed into crevice corrosion at the transition points of the end surface of the sample to the cylindrical surface and led to

the formation of cracks in the coating and its delamination from the alloy (upper right corner of the sample, Fig. 2).

Figure 2 – End surface of a sample made of NZ30K alloy + 0.1 wt.% Ag clad with a layer of silver with copper impurities with a thickness of 1300 nm after corrosion tests in Ringer-Locke solution.

It should be noted that the cylindrical surface of the sample underwent more intense localized corrosion damage than the end surface (Fig. 3). Most likely, this is due to the technological features of coating on different surfaces of the sample and the state of their surfaces formed after casting and mechanical cutting of the end surface.

Figure 3 – Cylindrical surface of a sample made of NZ30K alloy + 0.1 wt.% Ag clad with a layer of silver with copper impurities with a thickness of 1300 nm after corrosion tests in Ringer-Locke solution.

Scanning electron microscopy of the surfaces of local corrosion damage of the studied sample (Figs. 2, 3) showed that they have a characteristic developed microrelief (Fig. 4) inherent in the selective dissolution of steels and alloys at the anode areas in corrosive media. This is consistent with the data of [31, 32].

Pores (~25 μm) and corrosion tunnels on the surface of the local corrosion damage of the test sample have been found (Fig. 4). According to [33], they can be formed as a result of the ionization of an electronegative chemical element on the surface of the alloy (Mg), which contributes to the formation of unbalanced vacancies that diffuse into its volume, where they coagulate and form pores. This tendency can be supported only by the solid-phase diffusion of magnesium atoms to the surface of local corrosion damage, as the chemical element with the most negative value of the standard electrode potential in the NZ30K alloy + 0.1 wt.% Ag, and Zn, Zr, Nd, and Ag in the opposite direction, since they are thermodynamically more stable than Mg [34, 35]. The observed (Figs. 2-4) local corrosion damage of the studied sample is characterized by critical potentials

(Table 2) at which its corrosion behavior has changed significantly, since (Fig. 4) shows the reorganization of the surface layers of the alloy with the formation of pores from corrosion tunnels that turned into cor- rosion ulcers. It should be noted that such mecha- nisms of formation of localized corrosion damage on the surface of samples of stainless steels and alloys were revealed in [28-30, 31, 36].
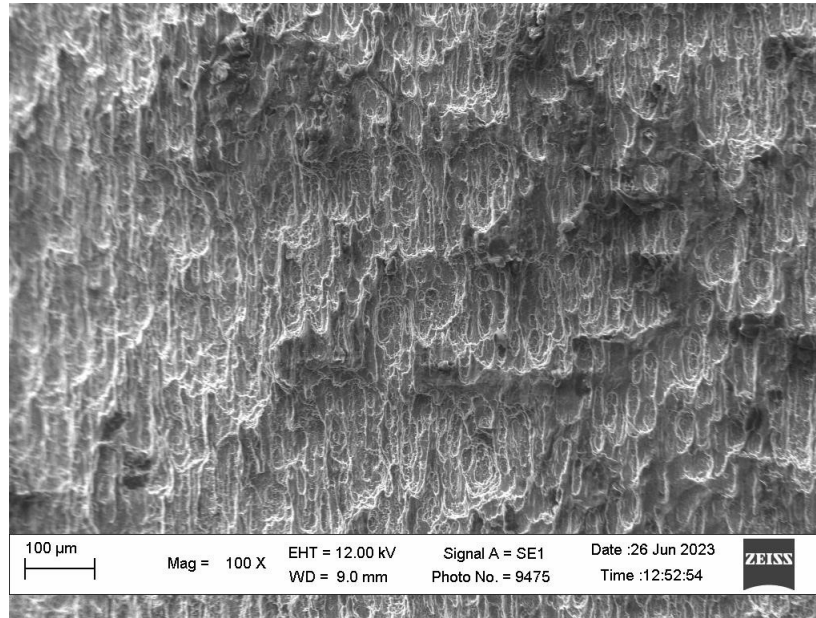

Figure 4 – Characteristic microrelief of the surface of local corrosion damage of a sample
of NZ30K alloy + 0.1 wt.% Ag clad with a layer of silver with copper impurities
with a thickness of 1300 nm after corrosion tests in Ringer-Locke solution.

Table 2 – Corrosion potentials E_{cor} of NZ30K alloy + 0.1 wt.% Ag clad with a layer of silver and copper 1300 nm thick depending on the time of exposure of samples in Ringer-Locke solution.

No. of points	τ, s	E_{cor}, V	No. of points	τ, s	E_{cor}, V	No. of points	τ, s	E_{cor}, V
1	4	-1.30944	21	300	-1.34432	41	1012	-1,3472
2	12	-1.31008	22	332	-1.34368	42	1044	-1,34912
3	20	-1.3104	23	364	-1.34432	43	1076	-1,34976
4	28	-1.31008	24	396	-1.34336	44	1140	-1,35328
5	36	-1.31136	25	428	-1.34368	45	1172	-1,35168
6	44	-1.31232	26	460	-1.344	46	1204	-1,35264
7	52	-1.31296	27	492	-1.344	47	1236	-1,35424
8	60	-1.31456	28	524	-1.34624	48	1268	-1.3536
9	68	-1.31488	29	556	-1.34528	49	1300	-1.35424
10	76	-1.31456	30	620	-1.3472	50	1364	-1.35328
11	84	-1.31456	31	652	-1.34784	51	1396	-1.35264
12	92	-1.31424	32	684	-1.3472	52	1428	-1.35296
13	100	-1.3152	33	716	-1.3456	53	1492	-1.35232
14	108	-1.31584	34	748	-1.3472	54	1524	-1.35264
15	116	-1.31648	35	780	-1.3472	55	1556	-1.35296

V. Greshta

Phys. Sci. Technol., Vol. 12 (No. 1-2), 2025: 95-102

Continuation of the table

No. of points	τ, s	E_{cor}, V	No. of points	τ, s	E_{cor}, V	No. of points	τ, s	E_{cor}, V
16	124	-1.31584	36	812	-1.34784	56	1588	-1.35296
17	140	-1.3168	37	876	-1.34752	57	1652	-1.35488
18	148	-1.31744	38	908	-1.34624	58	1684	-1.35648
19	156	-1.31776	39	940	-1.3472	59	1748	-1.35616
20	172	-1.31808	40	972	-1.34912	60	1796	-1.35552

According to the results of the analysis (Fig. 5) and (Table 2), it has been found that after the first 156 seconds of testing, the potential of the sample under study shifted to the negative side at a rate of 0.1 mV/s. This is 1.67 times more intense than for a sample of the same alloy clad with a 1200 nm thick silver layer.
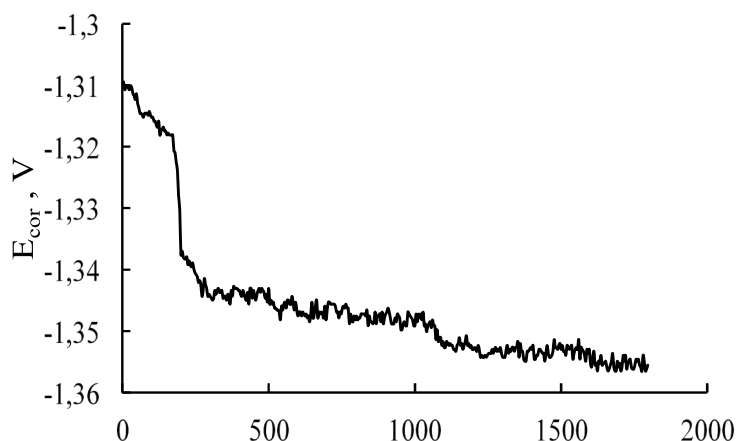

Figure 5 – Dependence between the corrosion potential E_{cor} of NZ30K alloy + 0.1 wt.% Ag clad with a layer of silver with copper impurities 1300 nm thick and the time of corrosion tests (τ) of the sample in Ringer-Locke solution.

Further, it has been recorded that the potential E_{cor} of the test sample abruptly shifted to the negative side from -1.31808 (point 20 after 172 seconds of testing (Table 2) to -1.344 V (points 26, 28 after 460 and 492 seconds of testing (Table 2) (Fig. 5). Thus, it has been found that the rate of shift of the potential E_{cor} of the sample to the negative side was 29.9 mV/s. This is due to the sudden detachment of a significant portion of the Ag+Cu clad layer from the alloy surface and a rapid increase in its contact area with the Ringer-Locke solution (Figs. 2, 3, 5). It should be noted that after that, a slow shift of the potential E_{cor} towards the negative side has been observed (Fig. 5). In particular, it shifted to the negative side from -1.34624 (point 28 after 524 seconds of testing (Table 2) to -1.35648 and -1.35616 V (points 58, 59 (Table 2). Thus, it turns out that the rate of this process was 0.008 mV/s and remained constant until the steady-state value of the corrosion potential E_{cor} of the sample has been established. A similar trend was observed for the sample of the NZ30K alloy + 0.1 wt. % Ag clad with a 1200-nm-thick silver layer. This shows that the copper in the silver coating intensifies contact corrosion between it and the alloy only at the first stage of testing, which accelerates its delamination and increases the area of contact between the alloy and the Ringer-Locke solution, which contributes to a rapid shift in the potential E_{cor} in the negative direction (Fig. 5). Further, the processes of corrosion dissolution of the sample proceeded according to the mechanisms inherent in the selective dissolution of steels and alloys at the anode areas [24, 32, 34, 36]. They determine the mechanisms of local anodic processes in alloys [28-30, 36], which depend on their

specific magnetic susceptibility, which determines the atomic state of the solid solution [37].

It should be noted that after immersion of the test sample in the Ringer-Locke solution, its potential E_{cor} was 62, 113, 124, and 109 mV higher than that of samples with coating thicknesses of 1200, 900, 500, and 200...300 nm, respectively. In addition, the difference between the steady-state values of corrosion potentials and those established after immersion of samples with a coating thickness of 1300 (Ag+Cu), 1200, 900, 500, and 200...300 nm (Ag) in the solution was 47, 55, 48, 32, and 27 mV, respectively. This may indicate that the intensity and duration of contact and crevice corrosion, which was accompanied by delamination of the coating from the alloy, was the lowest in samples with a coating thickness of 200...300 and 500 nm. At the same time, it should be noted that the potential difference found when establishing the steady-state values of corrosion potentials E_{cor}, for the sample with a coating thickness of 1300 nm (Ag+Cu) was even less than for the samples with 1200 and 900 nm, but the depth of local corrosion damage was the greatest. This is due to a decrease in cathodic depolarization under the influence of copper and an increase in the potential difference between the alloy and the coating. Thus, it can be noted that the presence of copper in the silver coating on the surface of implants is not permissible.

Summarizing the above, it can be noted that the sample of NZ30K+0.1 wt. % Ag clad with a 1300 nm thick layer of silver with copper impurities from the base on which the silver target for plasma spraying was placed, underwent intense contact and crevice corrosion with delamination of the coating at the intersection of cylindrical and flat surfaces. This contributed to the development of pitting and crevice corrosion of the sample under the influence of a chloride-containing media by mechanisms inherent in stainless steels and alloys. In addition, they were accelerated by the selective dissolution of copper in the silver coating.

4 Conclusion

According to the results of corrosion tests of a sample of NZ30K alloy + 0.1 wt. % Ag clad with layer of silver with copper impurities, it has been found that it was subjected to intense contact and crevice corrosion. It was accompanied by delamination of the coating from the alloy at the intersection of the cylindrical and end surfaces. In these places, pitting and ulcerative corrosion under the influence of a chloride-containing media was observed by mechanisms inherent in stainless steels and alloys. It is shown that the surfaces of corrosion pits on the studied sample have a characteristic microrelief inherent in the selective dissolution of metals on the anode areas of steels and alloys with pores (up to ~25 μm) formed as a result of the coagulation of nonequilibrium vacancies in the process of solid-phase diffusion of alloy components in their vicinity. It was found that the E_{cor} corrosion potential of the sample shifted to the negative side at a rate of 29.9 mV/s for 320 seconds, which is associated with localized coating delamination. Further, a slow negative shift of E_{cor} was observed at a rate of 0.008 mV/s until it reached a steady-state value of -1.356 V. It is proved that the presence of copper in the silver coating on the surface of implants is unacceptable.

References

1. Li H., Zheng Y., Qin L. Progress of biodegradable metals // Progress in natural science: Materials International. – 2014. – Vol. 24. – No. 5. – P. 414–422. https://doi.org/10.1016/j.pnsc.2014.08.014

2. Pilling N., Bedworth R.J. The oxidation of metals at high temperatures // Inst. Metals. – 1993. – Vol. 29. – P. 529–593.

3. Müller W.D., Nascimento M.L., Zeddies M., Córsico M., Gassa L.M., Mele M.A.F.L.D. Magnesium and its alloys as degradable biomaterials: corrosion studies using potentiodynamic and EIS electrochemical techniques // Materials Research. – 2007. – Vol. 10. – P. 5–10. https://doi.org/10.1590/S1516-14392007000100003

4. Witte F., Ulrich H., Rudert M., Willbold E. Biodegradable magnesium scaffolds: Part 1: Appropriate inflammatory response // Journal of Biomedical Materials Research Part A. – 2007. – Vol. 81. – P. 748–756. https://doi.org/10.1002/jbm.a.31170

5. Xu L., Yu G., Zhang E., Pan F., Yang K. In vivo corrosion behavior of Mg–Mn–Zn alloy for bone implant application // Journal of Biomedical Materials Research Part A. – 2007. – Vol. 83, No. 3. – P. 703–711. https://doi.org/10.1002/jbm.a.31273

6. Zhang G.D., Huang J.J., Yang K., Zhang B.C., Ai H.J. Experimental study of in vivo implantation of a magnesium alloy at early stage // Acta Metallurgica Sinica. – 2007. – Vol. 43. – P. 1186–1190.

7. Mueller W.-D., Nascimento M.L., Zeddies M., Corsico M., Gassa L.M., de Mele M.F.L. Magnesium and its alloys as degradable biomaterials: corrosion studies using potentiodynamic and EIS electrochemical techniques // Materials Research. – 2007. – Vol. 10, No. 1. – P. 5–10. http://dx.doi.org/10.1590/S1516-14392007000100003

8. Komarov F.F., Ismailova G.A., Mil'chanin O.V., et al. Effect of thermal processing on the structure and optical properties of crystalline silicon with GaSb nanocrystals formed with the aid of high-dose ion implantation // Technical Physics. – 2019. – Vol. 60. – P. 1348–1352. http://dx.doi.org/10.1134/S1063784215090078

9. Muradov A.D., Mukashev K.M., Korobova N.E., et al. Influence of γ-Irradiation on the Optical Properties of the Polyimide–YBa$_2$Cu$_3$O$_{6.7}$ System // Journal of Applied Spectroscopy. – 2018. – Vol. 85. – P. 260–266. http://dx.doi.org/10.1007/s10812-018-0642-4

10. Sagyndykov A.B., Kalkozova Z.K., et al. Fabrication of nanostructured silicon surface using selective chemical etching // Technical Physics. – 2017. – Vol. 62. – P. 1675–1678. http://dx.doi.org/10.1134/S106378421711024X

11. Muradov A., Mukashev K., Ismailova G., et al. Chemical co-precipitation synthesis and characterization of polyethylene glycol coated iron oxide nanoparticles for biomedical applications // Int. Multidisc. Sc. GeoConf. SGEM. – 2017. – Vol. 17. – P. 201–208. http://dx.doi.org/10.5593/sgem2017/61/S24.027

12. Yar-Mukhamedova G.S., Darisheva A.M., Yar-Mukhamedov E.S. Adsorption of the components of a chrome-plating electrolyte on dispersed corundum particles // Materials Science. – 2019. – Vol. 54. – P. 907–912.

13. Muradov A.D., Mukashev K.M., Korobova N.E. Impact of silver metallization and electron irradiation on the mechanical deformation of polyimide films // Technical Physics. – 2017. – Vol. 62, No. 11. – P. 1692–1697. http://dx.doi.org/10.1134/S1063784217110226

14. Greshta V.L., Shalomeev V.A., Dzhus A.V., Mityaev O.A. Study of the effect of silver alloying on the microstructure and properties of magnesium alloy NZ30K for implants in osteosynthesis // New Materials and Technologies in Metallurgy and Engineering. – 2023. – Vol. 2. – P. 14–19. https://doi.org/10.15588/1607-6885-2023-2-2

15. Zhou H., Hou R., Yang J., Sheng Y., Li Z., Chen L., Li W., Chen L., Li W., Wang X. Influence of Zirconium (Zr) on the microstructure, mechanical properties and corrosion behavior of biodegradable zinc-magnesium alloys // Journal of Alloys and Compounds. – 2020. – Vol. 840. – P. 155792. https://doi.org/10.1016/j.jallcom.2020.155792

16. Sun M., Yang D., Zhang Y., Mao L., Li X., Pang S. Recent advances in the grain refinement effects of Zr on Mg alloys: a review // Metals. – 2022. – Vol. 12, No. 8. – P. 1388. https://doi.org/10.3390/met12081388

17. Wang J., Zou Y., Dang C., Wan Z., Wang J., Pan P. Research progress and the prospect of damping magnesium alloys // Materials. – 2024. – Vol. 17, No. 6. – P. 1285. https://doi.org/10.3390/ma17061285

18. Ferreira P.C., Piai K.D.A., Takayanagui A.M.M., Segura-Muñoz S.I. Aluminum as a risk factor for Alzheimer's disease // Revista Latino-Americana de Enfermagem. – 2008. – Vol. 16. – P. 151–157. https://doi.org/10.1590/S0104-11692008000100023

19. Bach F.W., Schaper M., Jaschik C. Influence of lithium on hcp magnesium alloys // Materials Science Forum. – 2003. – Vol. 419. – P. 1037–1042.

20. Sun M., Wu G., Wang W., Ding W. Effect of Zr on the microstructure, mechanical properties and corrosion resistance of Mg-10Gd-3Y magnesium alloy // Materials Science and Engineering: A. – 2009. – Vol. 523, No. 1–2. – P. 145–151. https://doi.org/10.1016/j.msea.2009.06.002

21. Zeng R.-C., Zhang J., Huang W.-J. et al. (2016) Review of studies on corrosion of magnesium alloys // Transactions of Nonferrous Metals Society of China. – Vol. 16, No. 2. – P. 763–771. https://doi.org/10.1016/S1003-6326(06)60297-5

22. Ghali E. Properties, use and performance of magnesium and its alloys // Corrosion Resistance of Aluminum and Magnesium Alloys: Understanding, Performance and Testing. –2020. – P. 319–347. https://doi.org/10.1002/9780470531778

23. Narivs'kyi O.E. Corrosion fracture of platelike heat exchangers // Fiziko-Khimichna Mekhanika Materialiv. – 2005. -Vol. 41, No. 1. – P. 104–108. https://www.scopus.com/record/display.uri?eid=2-s2.0-27744440620

24. Narivs'kyi O. The influence of heterogeneity of AISI321 steel on its pitting resistance in chloride-containing media // Materials Science. – 2007. -Vol. 43, No. 2. – P. 256–264. https://doi.org/10.1007/s11003-007-0029-9

25. Narivskiy A., Yar-Mukhamedova G., Temirgaliyeva E. et al. Corrosion losses of alloy 06KhN28MDT in chloride-containing commercial waters // Int. Multidisc. Sc. GeoConf. SGEM. – 2016. -P. 63–70.

26. Mishchenko V.G., Snizhnoi G.V., Narivs'kyy O.E. Magnetometric investigations of corrosion behavior of AISI 304 steel in chloride-containing environment // Metallofizika i Noveishie Tekhnologii. – 2011. -Vol. 33, No. 6. – P. 769–774.

27. Greshta V., Narivskyi O., Dzhus A. et al. Corrosion dissolution of an implant made of NZ30K alloy alloyed with Ag and coated with a layer of silver in a model solution of the osteosynthesis process // Int. Multidisc. Sc. GeoConf. SGEM. -2024. -P. 1.

28. Narivskyi O.E., Subbotin S.O., Pulina T.V. et al. Modeling of pitting of heat exchangers made of 18/10 type steel in circulating waters // Materials Science. – 2023. -Vol. 58, No. 5. – P. 1–7. https://doi.org/10.1007/s11003-023-00725-y

29. Narivskyi O.E., Subbotin S.O., Pulina T.V. et al. Mechanism of pitting corrosion of austenitic steels of heat exchangers in circulating waters and its prediction // Materials Science. –2023. -Vol. 59, No. 5. – P. 275–282. https://doi.org/10.1007/s11003-024-00773-y

30. Narivskyi O., Subbotin S., Pulina T. Corrosion behavior of austenitic steels in chloride-containing media during the operation of plate-like heat exchangers // Physical Sciences and Technology. – 2023. -Vol. 10, No. 3–4. – P. 48–56. https://doi.org/10.26577/phst.2023.v10.i2.06

31. Narivs'kyi O.E. Micromechanism of corrosion fracture of the plates of heat exchangers // Materials Science. – 2007. -Vol. 43, No. 1. – P. 124–132. https://doi.org/10.1007/s11003-007-0014-3

32. Narivs'kyi O.E. Corrosion fracture of platelike heat exchangers // Materials Science. – 2005. -Vol. 41, No. 1. – P. 122–128. https://doi.org/10.1007/s11003005-0140-8

33. Pickering H.W. Characteristic features of alloy polarization curves // Corrosion Science. – 1983. -Vol. 23, No. 10. – P. 1107–1120. https://doi.org/10.1016/0010-938X(83)90092-6

34. Poutbaix M., De Zoubov N. Atlas of electrochemical equilibrium in aqueous solutions. – Pergamon Press. -1966. https://doi.org/10.1016/0022-0728(67)80059-7

35. Moffat T.P., Fan F.-R.F., Bord A.J. Electrochemical and scanning tunneling microscopic study of dealloying of Cu_3Au // Electrochemical Society. – 1991. -Vol. 11. – P. 3224–3235.

36. Narivs'kyi O.E., Belikov S.B. Pitting resistance of 06KhN28MDT alloy in chloride-containing media // Materials Science. – 2008. -Vol. 44. – P. 573–580. https://doi.org/10.1007/s11003-009-9107-5

37. Narivs'kyi O.E., Snizhnoi G.V., Pulina T.V. et al. Effect of specific magnetic susceptibility of AISI 304 and 08Kh18N10 steels on their limiting potentials in chloride-containing environments // Materials Science. – 2024. -Vol. 59, No. 3. – P. 649–657. https://doi. org/10.1007/s11003-024-00824-4

38. Dzhus A., Subbotin S., Pulina T., Snizhnoi G. Modeling the resistance of plate-like heat exchangers made of 06KhN28MDT alloy (analogous to AISI 904L steel) to crevice corrosion in recycled water enterprises // Physical Sciences and Technology. – 2024. -Vol. 11, No. 3–4. – P. 58–66. https://doi.org/10.26577/phst2024v11i2b07

39. Zellele D.M., Yar-Mukhamedova G.Sh., Rutkowska-Gorczyca M.A. A review on properties of electrodeposited nickel composite coatings: $Ni-Al_2O_3$, Ni-SiC, $Ni-ZrO_2$, $Ni-TiO_2$ and Ni-WC // Materials. –2024. -Vol. 17, No. 23. – P. 5715. https://doi. org/10.3390/ma17235715

40. Imanbayeva A.K., Syzdykova R.N., Temirbayev A.A. Concept formulation and university teaching methodology for dynamic chaos // Journal of Physics: Conference Series. – Vol. 1136, No. 1. – P. 012029. https://doi.org/10.1088/1742-6596/1136/1/012029

41. Prikhodko O., Maltekbasov M., Almasov N. et al. Structure and electronic properties of amorphous $As_{40}Se_{30}S_{30}$ films prepared by ion-plasma sputtering method // Physical Sciences and Technology. –2016. – Vol. 2, No. 1. https://doi.org/10.26577/2409-6121-2015-2-1-24-29

42. Zelele D.M., Rutkowska-Gorczyca M. Electrochemical synthesis and functional properties of metal and alloy-based composition coatings // Recent Contributions to Physics. –2024. -Vol. 1, No. 88. – P. 41–48.

43. Greshta V., Narivskyi O., Dzhus A. et al. Corrosion behaviour of magnesium alloys NZ30K and NZ30K alloyed with silver in the model solution of the osteosynthesis process // Eurasian Physical Technical Journal. –2024. -Vol. 21, No. 3. – P. 29–36. https://doi.org/10.31489/2024No3/29-36

44. Mussabek G.K., Yermukhamed D., Dikhanbayev K.K. et al. Self-organization growth of Ge-nanocolumns // Materials Research Express. –2017. -Vol. 4. – P. 035003. https://doi.org/10.1088/2053-1591/aa5ed6

45. Sakhnenko N., Ved M., Koziar M. Ternary cobalt-molybdenum-zirconium coatings: electrolytic deposition and functional properties // Physical Sciences and Technology. –2018. – Vol. 3, No. 2. – P. 65–75. https://doi.org/10.26577/phst-2016-2-108

46. Imanbayeva A., Tursynbek Y., Syzdykova R., Mukhamedova A. Evaluating the effectiveness of information security based on the calculation of information entropy // Journal of Physics: Conference Series. -2021. -Vol. 1783(1). -Art. 012042. https://doi.org/10.1088/1742-6596/1783/1/012042

47. Mussabek G., Zhylkybayeva N., Lysenko I., Lishchuk P.O., Baktygerey S., Yermukhamed D., Taurbayev Ye., Sadykov G., Zaderko A.N., Skryshevsky V.A., Lisnyak V.V., Lysenko V. Photo- and radiofrequency-induced heating of photoluminescent colloidal carbon dots // Nanomaterials. -2022. -Vol.12. – Art. 2426. https://doi.org/10.3390/nano12142426

48. Yar-Mukhamedova G., Muradov A., Mukashev K., Umarov F., Imanbayeva A., Mussabek G., Belisarova F. Impact of polyethylene terephthalate on the mechanical properties of polyimide films // Eurasian Physical Technical Journal. -2025. -Vol. 22, 28–36. https://doi.org/10.31489/2025N1/28-36

49. Nenastina T., Sakhnenko M., Oksak S., Yar-Mukhamedova G., Zellele D., Mussabek G., Imanbayeva A. Study of complexation patterns in the system Ni^{2+}, MoO_4^{2-}, $P_2O_7^{4-}$, Cit^{3-} for the development of poly-ligand electrolytes // Eurasian Chemico-Technological Journal. -2024. -Vol. 26. -P. 155–160. https://doi.org/10.18321/ectj1638

50. Muradov A., Młyniec A., Mukashev K., Yar-Mukhamedova G., Sandybaev Y. Simulation of mechanical strain of metallic electron-irradiated polyimide films // Physical Sciences and Technology. -2018. -Vol. 4(2). -P. 95–100. https://doi.org/10.26577/phst-2017-2-139

Information about author:

Greshta Victor L., Candidate of Technical Sciences, Professor at the Zaporizhzhia Polytechnic National University, Zaporizhzhia, Ukraine; email: greshtaviktor@gmail.com.

X-RAY fluorescence analysis of mineral composition in Khaudak and Uchkizil groundwaters, Uzbekistan

N.B. Uralov* , Kh.Kh. Turayev , B.A. Normurodov ,

I.A. Umbarov , F.B. Kurbonov and Y.Sh. Bozorov

Termez State University, Termez, Uzbekistan
* e-mail: uralovnuriddin0091@gmail.com

This study focuses on the analysis of underground waters from Khaudak and Uchkizil, located in the southern region of Uzbekistan. These waters are characterized by the presence of various mineral salts, including iodine-containing compounds. The research examines the similarities between these waters, as well as their compositional changes over time under the influence of external environmental factors. Water samples collected at different intervals were analyzed to monitor variations in composition. The elemental content of the samples was determined using X-ray fluorescence (XRF) analysis, which revealed that iron compounds present in the water tend to precipitate over time. The initial iron content of the water was approximately 0.130%, with subsequent sedimentation resulting in iron-rich deposits containing up to 65% iron. In addition, a freshly collected water sample was treated with specific oxidizing agents for iodine and stored for one month. This process led to the formation of a reddish-brown precipitate primarily composed of iron and chlorine, with minor components including iodine and similar elements. The precipitate was found to contain 1.317% iodine, corresponding to 7.66% (21.32 mg/L) of the total iodine content in the Haudak water. Furthermore, exposure of the water to ultraviolet light under open-air conditions resulted in the oxidation and volatilization of iodine, indicating its sensitivity to photochemical degradation.

Key words: Khaudak, Uchkizil, iron (III)-chloride, X-ray fluorescence.
PACS number(s): 78.55.−m; 92.20.cn; 92.40.K.

1 Introduction

In recent years, iodine-related health issues have become increasingly prominent worldwide. A growing number of iodine deficiency disorders are being reported, both in terms of incidence and variety. One of the urgent tasks in addressing these concerns is the study and analysis of iodine-bearing surface and groundwater sources. This includes detailed examination of physical and chemical characteristics such as temperature, color, mineral composition, and density. Among these sources, Khaudak and Uchkizil groundwaters in southern Uzbekistan are of particular interest due to their high mineralization and significant iodine content.

Studies conducted in South China have shown that iodine concentrations in groundwater often exceed the World Health Organization's recommended range of 5–300 μg/l. The enrichment of iodide is especially pronounced under mildly acidic (pH ≈ 6.6) and reducing conditions (Eh ≈ 198.4 mV) [1]. Based on the results of iodine analysis in seven geo-ecological zones across China, 4 levels were recognized in groundwater with concentrations of less than 10 μg/l and greater than 300 μg/l [2]. It has been determined that iodine in water exists primarily as molecular iodine (85.6%), followed by iodide ions (3.2%), iodate (9.1%), and iodine chloride (2.1%) [3]. Microorganisms are known to play a critical role in the iodine biogeochemical cycle by mediating oxidation, reduction, volatilization, and deiodination processes. Comparative metagenomic analyses of deep groundwater in the North China Plain revealed the presence of idrABP1P2 gene clusters involved in the reduction of iodine species. Additionally, iron- and sulfur-reducing bacteria may contribute to iodide formation via reductive dissolution of iron minerals and abiotic iodate reduction [4]. In addition, the water of the Datong Basin was analyzed. According to it, the range of iodine in the groundwater of the Datong Basin was 4-2175 μg/l, and it was determined that the enrichment of iodine in the groundwater was due to the ac-

tion of microorganisms. [5]. In Danish groundwater, iodine concentrations were observed in 23 groundwater wells between 2011 and 2021. The study found that iodine concentrations fluctuate over time. [6]. Concentrations of iodide (I-), iodate (IO3 -), and total iodine (TI) from natural iodine species were studied at four Danish research sites. TI concentrations in groundwater ranged from 5 to 14,500 μg/l. High TI concentrations in the four iodine specification areas were characterized by three main causes: atmospheric deposition and leaching from iodine-enriched soil due to proximity to the sea, desorption of aquifer sediments from marine organic matter and iodine-enriched soil, and the effect of iodine from minerals and residual brines leading to upward diffusion of iodine. [7]. In addition, iodide, iodine, and common iodine in the main drinking water samples were analyzed in this country. 6 regions with an average of 15 μg/l and close to 12 μg/l were identified [8]. Within the Commonwealth of Independent States (CIS), iodine-rich groundwaters have been investigated in Russia, Azerbaijan, Turkmenistan, Uzbekistan, and Ukraine. Among total proven reserves, Turkmenistan holds approximately 40% of iodine-rich groundwater, followed by Russia (34%), Azerbaijan (22%), Ukraine (3%), and Uzbekistan (1%) [9]. In most cases, high-iodine waters were drawn from wells 75–120 m deep. The combination of high pH and a reducing environment facilitates iodine enrichment, accounting for 63.2–99.3% of the total iodine content. Sediment samples from such wells contain 0.18–1.46 mg/kg of iodine, moderately correlated with total organic carbon (TOC) [10].

External factors also influence changes in the amount of iodine in natural waters. For example, when studying the effects of ozone on iodine on the sea surface for a certain period of time, a decrease in iodine emission was detected [11]. Iodine concentrations in the solution were measured at different temperatures and at different time intervals. According to the results of the study, which contained iodine, when frozen samples were stored for a long time, it was found that the amount of iodine changed little. [12]. In some studies, however, iodide detection is achieved by oxidizing iodide to hypoiodic acid using monochloramine [13]. And the detection of iodine and total iodine in seawater by the method of differential pulse polarography brings some convenience. For example, it is convenient to determine the amount of iodine after oxidation of iodide to iodine by exposure to ultraviolet light by very low chemical processing [14]. More than a dozen chemical reagents have

been applied to identify iodine and Bromine species in marine sediments. As a result, iodine was found to exist mainly in the electro-positive state in the form of N-iodoamides, while bromine was found to exist in a variety of chemical forms [15]. The effect of ultraviolet rays on iodine present in marine waters was studied based on the spectrophotometric method, and iodide was then analyzed by difference [16].

The conversion of iodide into elemental iodine is favored in acidic environments and can be enhanced by pre-acidification using hydrochloric or sulfuric acids, followed by oxidative treatment to release free iodine into the air [17, 18]. In practical applications, electrodialysis is employed to concentrate iodized sodium chloride from brines, a process used in Japan to produce various types of iodized table salt [19]. The synthesis of polyaniline nitrocellulose (PANS) was carried out using aniline (AN) and nitrocellulose (NS). This substance was used as the main product for ion exchange membranes. As a result, research is ongoing on the use of PANS as a new ion exchange membrane for the separation of iodine from saline waters. [20], The crystal structure and Hirshfeld surface analysis results of the newly synthesized complex compound $[Cd(OPD)_3SO_4]$ H_2O derived from o-phenylenediamine (OPD) are being studied, and the sorption properties are being analyzed. [21].

Currently, the composition of sorbents obtained as a result of numerous syntheses is carried out using analyzers operating on the basis of luminescence properties. For example, the interaction of charged particles – protons, nitrogen, oxygen and carbon ions – with LiF single crystals was studied using the luminescence method. [22]. The properties of the thermally stimulated luminescence (TSL) peak in the phase transition temperature region were also studied through the spectral-luminescent properties of ammonium halide crystals. [23].

This study focuses on the Khaudak and Uchkizil underground waters located in the Surkhandarya region of Uzbekistan, which are known to contain elevated concentrations of iodine alongside other mineral salts. These waters offer a unique opportunity to explore the physicochemical mechanisms underlying iodine retention and mobilization under natural and induced conditions. To this end, water samples were collected and analyzed for baseline parameters, including temperature, color, mineral composition, and density. The effects of environmental exposure and oxidative treatments on the chemical composition of the waters were examined using X-ray fluorescence (XRF) spectroscopy.

2 Materials and methods

Polyethylene containers with a capacity of 5 liters and 1 liter for storing brine samples and forming sediment; 100 ml beakers and flasks for separating the formed sediment; Büchner funnel, filter paper and vacuum pump for filtering the sediment; Glass beaker, drying cabinet for drying the separated sediment; Thermometer with a range of 0-100 °C for monitoring the temperature of the initial water sample and the conditions during sediment formation; Areometer for determining the density of brine; 30% solution of iron (III) chloride for oxidizing the iodide compound contained in brine; X-ray fluorescence analyzer for analyzing the composition of water and sediment; When iron (III) chloride is used as an oxidant to separate iodine from brine, a selective oxidation process for iodine occurs, since most iodine-containing groundwater sources also contain bromine along with iodine, and iron (III) chloride cannot oxidize bromine, and iodine can be separated separately. After determining the amount of ions in brine, it is possible to draw clear conclusions about the method by which iodine can be separated.

The X-ray fluorescence analysis. EDX-8100P Energy Dispersive X-Ray Fluorescence Spectrometer (SHIMADZU). This spectrometer with ranges of detectable elements from C to U. The X-ray tube consists of a Rh-anode and operates at a voltage of 4-50 kV. The given range of concentrations is from ppm to 100%.

3 Experimental part

Khaudak water is extracted from the ground from a depth of about 3,000 meters, and Uchkizilwater from a depth of about 400 meters. They are mainly present at temperatures of 70-80 °C and 25-30 °C, respectively, at the time they are mined underground. A solution of a brown-reddish suspension is formed when the water of the tank drops from its initial temperature to room temperature (15-25 °C) and gradually forms a precipitate for 5-6 days. The Uchkizil water will not be significantly hot when mined, and the color of the solution will also be clear and close to transparency. Therefore, brown-reddish sediment from it falls less often. Below, a brown-reddish sediment obtained over 30 days from Uchkizil water was separated and dried, and the spectra obtained from the X-ray fluorescent analyzer (Figure 1) and images in a scanning electron microscope (Figure 2) obtained at a particle size of 10 μm were given (Table 1).
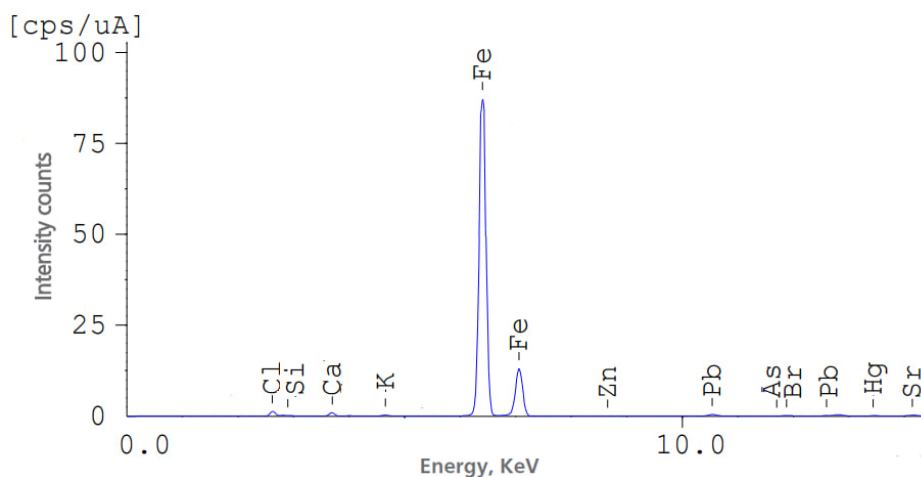

Figure 1 – X-ray fluorescence analyzer spectrum of sediment taken from Uchkizil water.
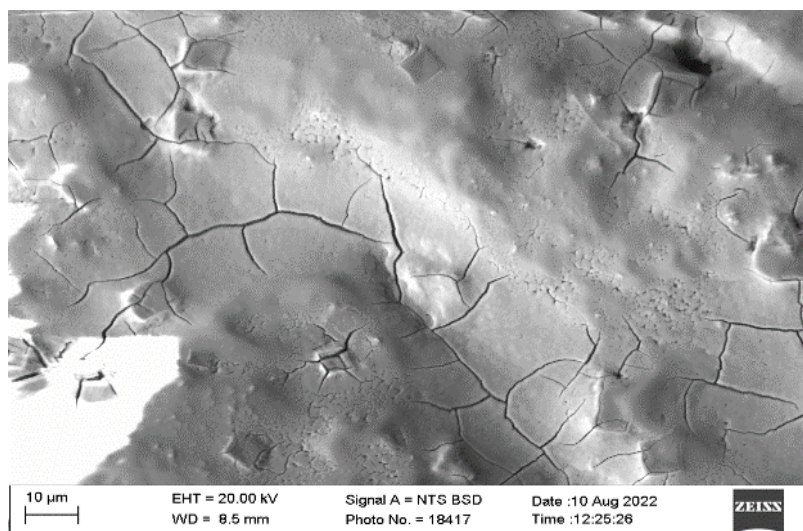
Figure 2 – SEM image of the sediment taken from Uchkizil water.

Table 1 – Quantitative result of the X-ray fluorescence analyzer of the sediment obtained from Uchkizil water.

Analyte	Result	[3-sigma]	Proc.-Calc.	Line	Int.(cps/uA)
Fe	77.398 %	[0.193]	Quan-FP	FeKa	320.6805
Cl	14.894 %	[0.369]	Quan-FP	ClKa	0.6529
Ca	3.336 %	[0.097]	Quan-FP	CaKa	1.8473
Si	3.227 %	[0.369]	Quan-FP	SiKa	0.1098
Pb	0.332 %	[0.012]	Quan-FP	PbLb1	0.1781
As	0.197 %	[0.071]	Quan-FP	AsKb	0.3581
K	0.197 %	[0.034]	Quan-FP	K Ka	0.0250
Sr	0.183 %	[0.010]	Quan-FP	SrKa	2.5602
Br	0.121 %	[0.005]	Quan-FP	BrKa	0.1427
Zn	0.096 %	[0.009]	Quan-FP	ZnKa	0.0305
Hg	0.020 %	[0.006]	Quan-FP	HgLa	0.0061

It can be seen from this table that there is no iodine in the precipitate, and iron, chlorine, and calcium can be mentioned as the main elements. It was observed that certain water-soluble compounds of iron precipitate when brought from 70-80 °C to room temperature (15-25 °C) or hydrolyze and form water-insoluble compounds and sink to the bottom of the solution. The solution left after the separation of the brown-reddish sediment that fell under the water of the Khaudak is clear, it was dried at a temperature of 20-30 °C under the influence of sunlight and examined in an X-ray fluorescent analyzer (Figure 3, Table 2).

Below, Uchkizil water was left in the open air, under the influence of sunlight, for 1 week after it was taken from the ground. Then it was analyzed in an X-ray fluorescence analyzer (Fig. 4, Table 3).

This table lists chlorine as the main constituent and calcium as the main mass.

After extracting the water from the underground, it was left in the open air for 2 weeks under the influence of sunlight. Sample 2. Then it was analyzed in an X-ray fluorescence analyzer (Fig. 5, Table 4).
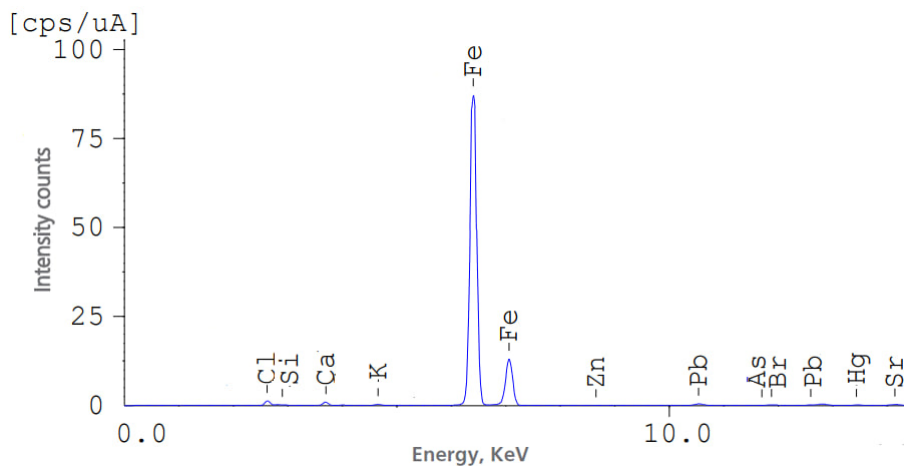
Figure 3 – X-ray fluorescence analyzer spectrum of salt obtained as
a result of evaporation of Khaudak water.

Table 2 – Quantitative result of X-ray fluorescence analyzer of the salt obtained as a result of the evaporation of water from in Khaudak.

Analyte	Result	[3-sigma]	Proc.-Calc.	Line	Int.(cps/uA)
Cl	70.093 %	[0.833]	Quan-FP	ClKa	2.2786
Ca	26.982 %	[0.429]	Quan-FP	CaKa	3.5882
K	1.273 %	[0.101	Quan-FP	K Ka	0.0399
Sr	0.703 %	[0.009]	Quan-FP	SrKa	10.1298
Br	0.514 %	[0.011]	Quan-FP	BrKa	0.6417
S	0.235 %	[0.054]	Quan-FP	SKa	0.0980
Fe	0.130 %	[0.006]	Quan-FP	FeKa	0.1543
Zn	0.070 %	[0.008]	Quan-FP	ZnKa	0.0229
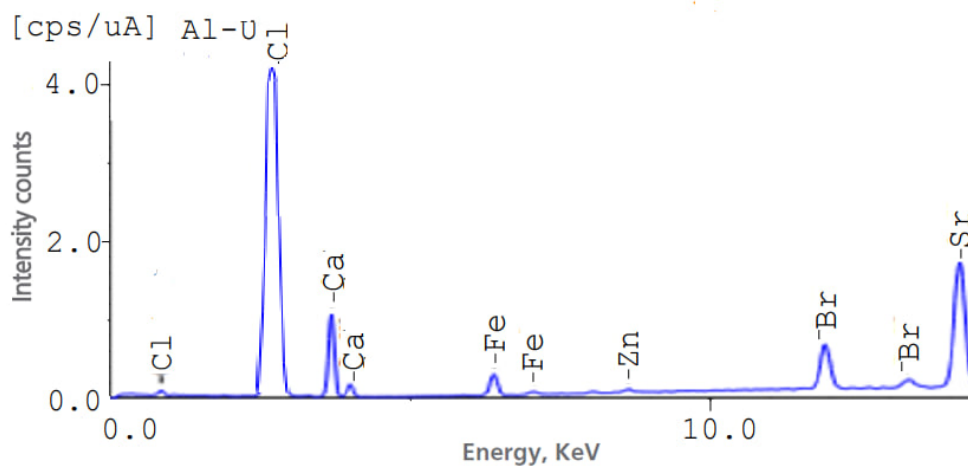
Figure 4 – X-ray fluorescence analyzer spectrum of 1-week-old water of Uchkizil water, sample 1.

Table 3 – Quantitative X-ray fluorescence analyzer result of Uchkizil water, sample 1.

Analyte	Result	[3-sigma]	Proc.-Calc.	Line	Int.(cps/uA)
Cl	11.715 %	[0.155]	Quan-FP	ClKa	1.8506
Ca	2.110 %	[0.039]	Quan-FP	CaKa	2.6479
Fe	0.073 %	[0.002]	Quan-FP	FeKa	1.0001
Sr	0.125 %	[0.002]	Quan-FP	SrKa	20.0853
K	0.064 %	[0.007]	Quan-FP	K Ka	0.0176
Br	0.047 %	[0.001]	Quan-FP	BrKa	0.6858
Zn	0.006 %	[0.001]	Quan-FP	ZnKa	0.0221
H_2O	85.860 %	[------]	Balance	--------	--------
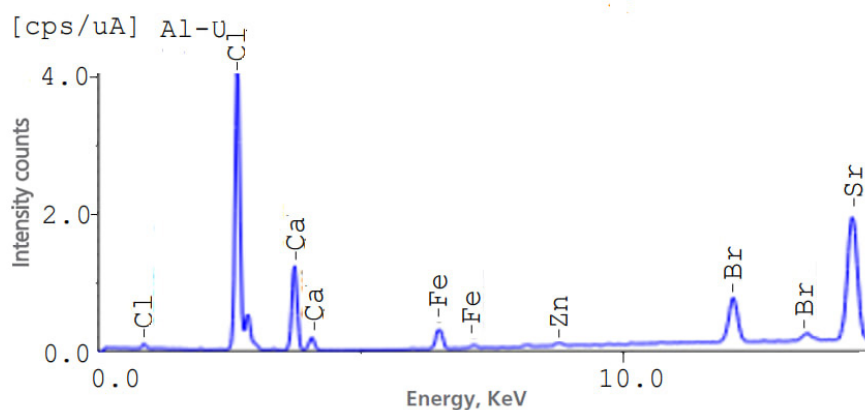
Figure 5 – The X-ray fluorescence analyzer spectrum of 2-week-old water of Uchkizil water, sample 2.

Table 4 – Quantitative X-ray fluorescence analyzer result of Uchkizil water, sample 2.

Analyte	Result	[3-sigma]	Proc.-Calc.	Line	Int.(cps/uA)
Cl	11.754 %	[0.155]	Quan-FP	ClKa	1.8559
Ca	2.120 %	[0.039]	Quan-FP	CaKa	2.6555
Sr	0.125 %	[0.002]	Quan-FP	SrKa	20.0113
Fe	0.071 %	[0.002]	Quan-FP	FeKa	0.9690
K	0.062 %	[0.007]	Quan-FP	K Ka	0.0170
Br	0.048 %	[0.001]	Quan-FP	BrKa	0.7012
Zn	0.005 %	[0.001]	Quan-FP	ZnKa	0.0202
H_2O	85.815 %	[------]	Balance	--------	--------

As can be seen from this table, little change has occurred compared to the value of iron in the previous table.

Uchkizil water was left in the open air for 6 weeks after being extracted from the ground, under the influence of sunlight. Sample 3. Then it was analyzed in an X-ray fluorescence analyzer (Fig. 6, Table 5).

The underground water of Khaudak was kept for 4 weeks in an open environment under the influence of light, then the analysis of the analyzer was carried out (Fig. 7, Table 6).
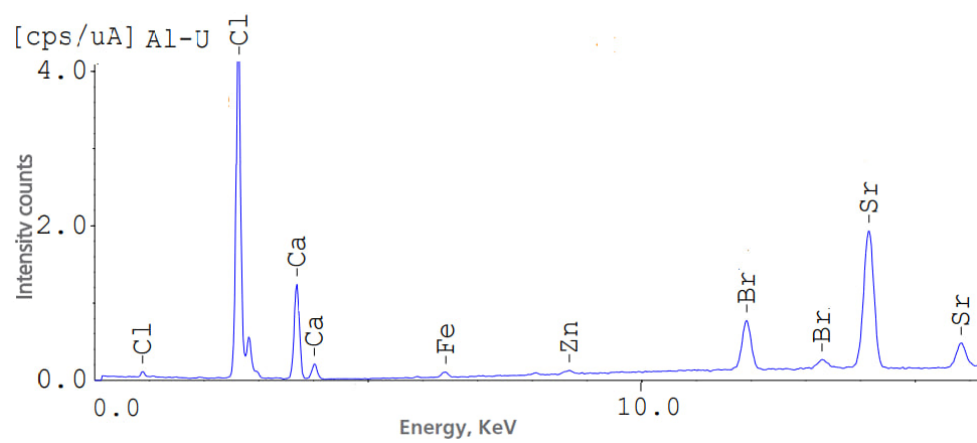
Figure 6 – The spectrum of Uchkizil water 2 weeks in an X-ray fluorescent analyzer, sample 3.

Table 5 – Uchkizil water, quantitative result of sample 3 from X-ray fluorescent analyzer.

Analyte	Result	[3-sigma]	Proc.-Calc.	Line	Int.(cps/uA)
Cl	12.099 %	[0.157]	Quan-FP	ClKa	1.9070
Ca	2.171 %	[0.040]	Quan-FP	CaKa	2.6739
Sr	0.124 %	[0.002]	Quan-FP	SrKa	19.7715
K	0.056 %	[0.006]	Quan-FP	K Ka	0.0151
Br	0.048 %	[0.001]	Quan-FP	BrKa	0.6904
Fe	0.016 %	[0.001]	Quan-FP	FeKa	0.2160
Zn	0.006 %	[0.001]	Quan-FP	ZnKa	0.0214
H_2O	85.481 %	[------]	Balance	--------	--------
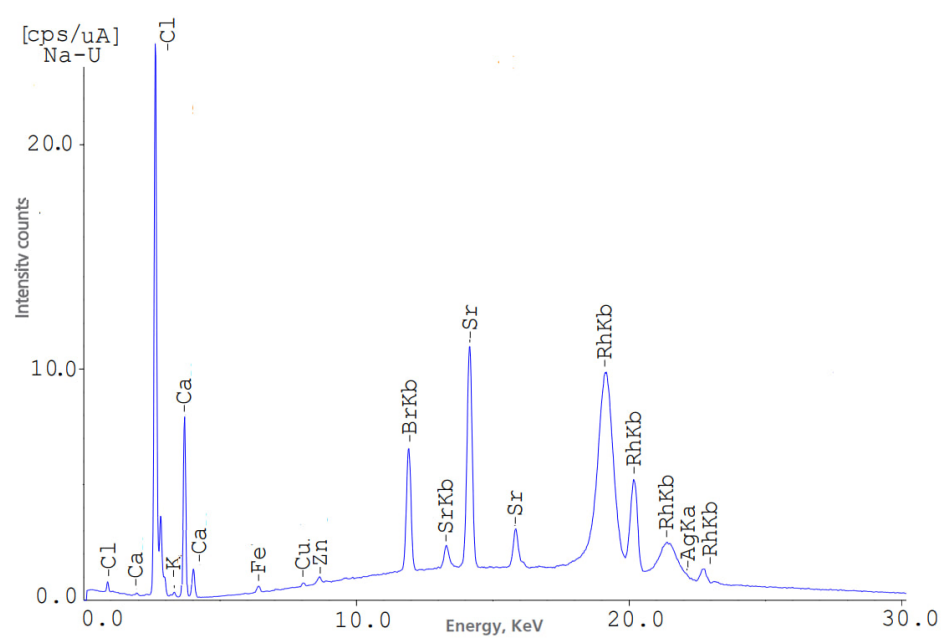
Figure 7 – X-ray fluorescence analyzer spectrum of Khaudak 1-month-old water.

Table 6 – Quantitative result of X-ray fluorescence analyzer of Khaudak 1 month water.

Analyte	Result (ppm)	Result (%)	[3-sigma]	Proc.-Calc.	Line	Int.(cps/uA)
Cl	133682.9 ppm	13.368	[823.663]	Quan-FP	ClKa	128.4750
Ca	17710.98 ppm	1.771	[184.954]	Quan-FP	CaKa	47.1744
K	829.649 ppm	0.083	[94.152]	Quan-FP	K Ka	1.1207
Sr	662.721 ppm	0.066	[4.040]	Quan-FP	SrKa	106.8234
Br	426.566 ppm	0.043	[3.461	Quan-FP	BrKa	53.5927
Fe	71.311 ppm	0.0071	[6.599]	Quan-FP	FeKa	2.0086
Ag	52.328 ppm	0.0052	[10.472]	Quan-FP	AgKa	2.1917
Zn	41.250 ppm	0.0041	[4.122]	Quan-FP	ZnKa	2.6987
Cu	18.408 ppm	0.0018	[4.054]	Quan-FP	CuKa	1.0050
H_2O	84.650 %	84.650	[------]	Balance	--------	--------

It can be seen that the values in this table are very close to the elements and their amounts in the above Uchkizil water.

There is an oil production area around Khaudak water, and the following indicators were obtained when analyzing the composition of the water separated from this oil (Figure 8, Table 7).
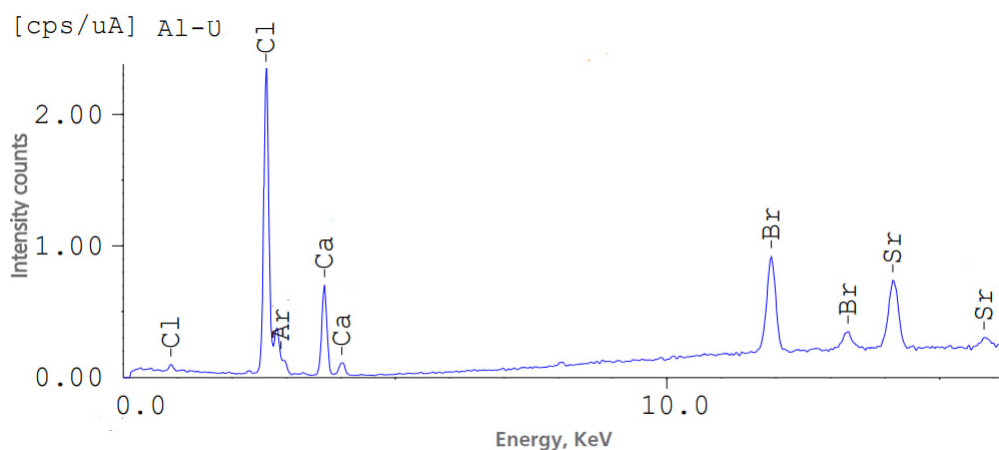
Figure 8 – Spectrum of oil water in X-ray fluorescence analyzer.

Table 7 – Quantitative result of oil water from X-ray fluorescence analyzer.

Analyte	Result	[3-sigma]	Proc.-Calc.	Line	Int.(cps/uA)
Cl	5.189 %	[0.092]	Quan-FP	ClKa	1.0113
Ca	0.695 %	[0.017]	Quan-FP	CaKa	1.5505
K	0.031 %	[0.003]	Quan-FP	K Ka	0.0148
Br	0.030 %	[0.001]	Quan-FP	BrKa	0.7932
Sr	0.021 %	[0.001]	Quan-FP	SrKa	5.6960
P	0.004 %	[0.011]	Quan-FP	P Ka	0.0014
H_2O	94.030 %	[------]	Balance	--------	--------

N.B. Uralov *et al.*

Phys. Sci. Technol., Vol. 12 (No. 1-2), 2025: 103-114

4 Results and discussion

The contents of Uchkizil, Khaudak underground waters, which are rich in various mineral salts, and water separated from Khaudak oil were studied. According to it, the change and stability indicators of the amount of Ca, Fe, Br and Sr in Uchkyzil water based on 3 samples are shown in Fig. 9.
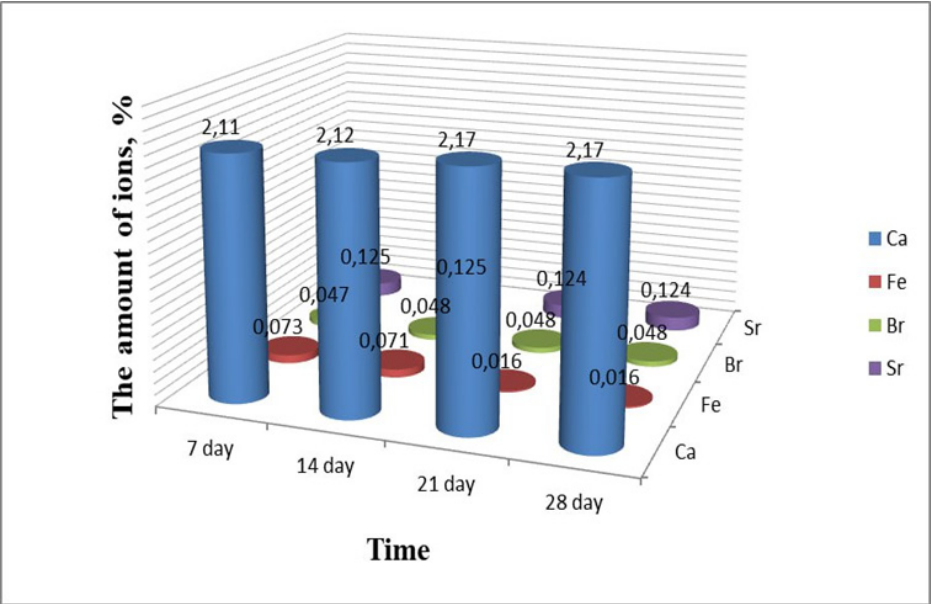

Figure 9 – Quantitative diagram of elements Ca, Fe, Br and Sr in the water of Uchkizil.

In this diagram, it can be seen that the concentration of Br and Sr compounds in the waters presented based on 3 samples has not changed for different periods. If we explain that strontium salts dissolve well in water and do not form precipitates, we can see that Br is stable to the effects of external environmental factors, such as the sun, ultraviolet rays, and air. It can be seen that the amount of Fe has decreased by a small amount.

A sample of 5 l of Haudak water was taken and a 30% Fe (III) chloride solution was added to it, shaken for 5 minutes, and kept for 1 month. As a result, a brown-red precipitate was formed, the main part of which consists of iron and chlorine, and a smaller part of compounds with iodine and similar elements. The composition of this precipitate was imaged in an X-ray fluorescence analyzer (Fig. 10, Table 8).
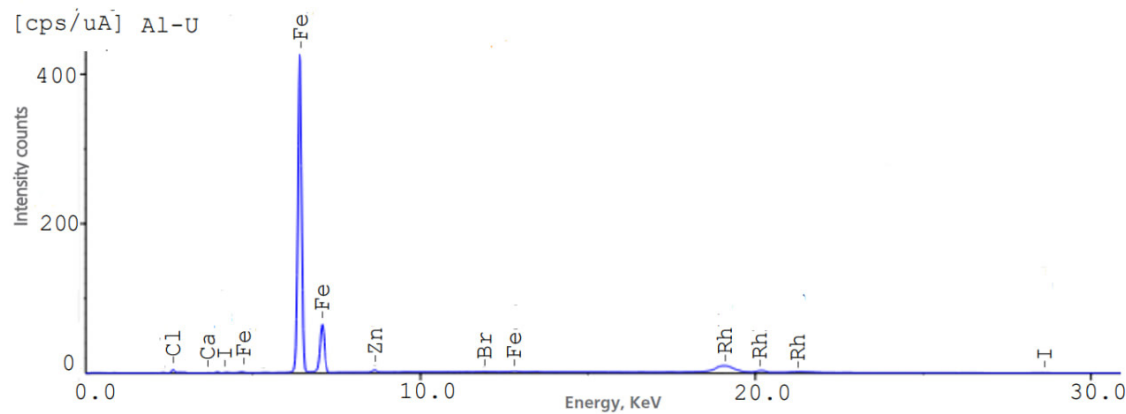
**Figure 10** – The spectrum of the sediment in the X-ray fluorescence analyzer.

Table 8 – Quantitative result of precipitation obtained from X-ray fluorescence analyzer.

Analyte	Result	[3-sigma]	Proc.-Calc.	Line	Int.(cps/uA)
Fe	84.717 %	[0.243	Quan-FP	FeKa	3046.5512
Cl	10.196 %	[0.160]	Quan-FP	ClKa	11.9197
S	1.614 %	[0.066]	Quan-FP	SKa	1.5363
I	1.317 %	[0.047]	Quan-FP	I Ka	7.3613
Zn	0.977 %	[0.037]	Quan-FP	ZnKa	23.7076
P	0.701 %	[0.104]	Quan-FP	P Ka	0.2426
Ca	0.211 %	[0.027]	Quan-FP	CaKa	0.5385
Br	0.135 %	[0.026]	Quan-FP	BrKa	5.9278
Cs	0.131 %	[0.086]	Quan-FP	CsLa	0.7456

The precipitated part is 1.24 g and we can see that it consists of 1.317% I iodine. This value is 7.66% of the total iodine in water (21.32 mg/l).

Based on the analytical analysis presented above, the quantitative ratios of certain elements in Uchkizil, Khaudak and Khaudak oil waters oxidized based on $FeCl_3$ salt of Khaudak water are presented in the diagram in Fig. 11.

In this picture, it can be seen that the amount of iodine in various water samples containing iodine has decreased or completely disappeared due to the passage of time due to external factors. Only if the obtained water sample is oxidized in a short time or separated using special sorbents, it becomes important for practice.
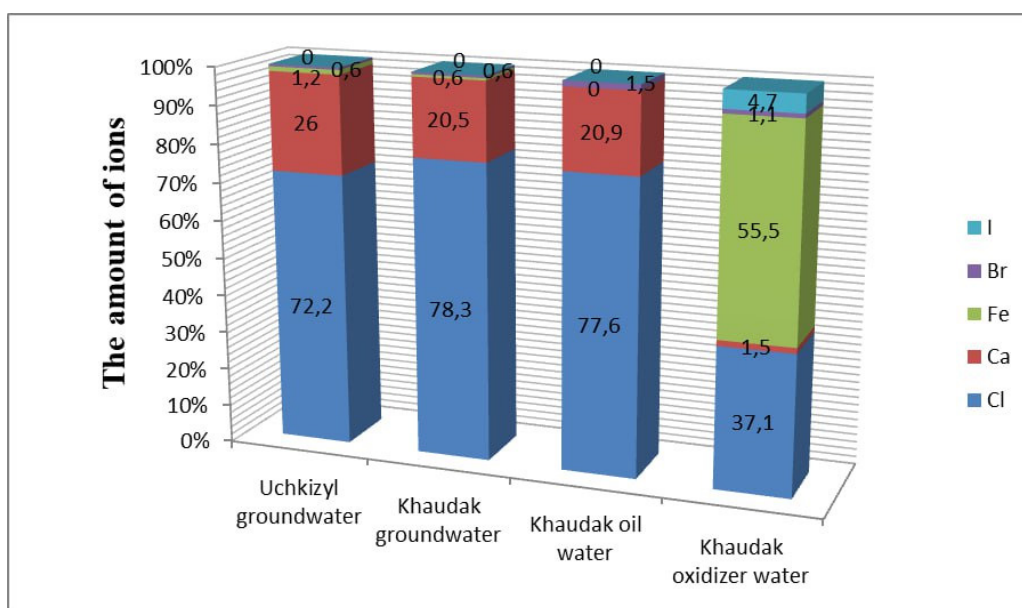
Figure 11 – Quantitative description of water samples and sediment content obtained from them.

5 Conclusion

In this study, several groundwater samples containing iodine were studied by X-ray fluorescence analysis. It has been proven that certain salts in water form precipitates due to the decrease in solubility as a result of lowering the temperature to room temperature, and they form precipitates as a result of hydrolysis. In this case, it was determined that iron salts have a high precipitation forming ability. It has been proven that iodine contained in waters with high mineral content is oxidized and released into the air under the influence of ultraviolet rays contained in sunlight and air oxygen. It was found that iron compounds in salt water settle over time.

As a result of adding special oxidants for iodine to the water of the newly obtained sample, it was observed that iodine precipitated over a certain period of time. The reasons for the relatively high amount of iodine in the mud at the bottom of the water, given in the above literature, have been confirmed. 7.66% of the iodine in the water containing 21.32 mg/l was precipitated by oxidation.

References

1. Zhou F., Xu Q., Chen Y., Zhang W., Qiu R. Iodine enrichment in the groundwater in South China and its hydrogeochemical control // Journal of Environmental Sciences. – 2024. -Vol. 142. -P. 226–235. https://doi.org/10.1016/j.jes.2023.07.017

2. Ma R., Yan M., et al. Deficiency and excess of groundwater iodine and their health associations. Nature Communications. -2022. -Vol. 13. -Art. 7354. https://doi.org/10.1038/s41467-022-35042-6

3. Umbarov I., Turayev K., Uralov N., Abduraxmonov S., Musayev Ch., Tursunov Kh., Eshonqulov Kh., Kadirova N. (2024). Investigating the processes and rate of iodide ion and compound oxidation in subterranean hydrothermal waters. BIO Web of Conferences. -2024. -Vol. 105. -Art. 05019. https://doi.org/10.1051/bioconf/202410505019

4. Jiang Z., Huang M., Jiang Y., Dong Y., Shi L., Li J., Wang Y. Microbial contributions to iodide enrichment in deep groundwater in the North China Plain // Environmental Science & Technology. -2023. -Vol. 57(6). -P. 2625–2635. https://doi.org/10.1021/acs.est.2c06657

5. Li J., Jiang Z., Xie X., Wang Y. Mechanisms of iodine enrichment in the pore-water of fluvial/lacustrine aquifer systems: Insight from stable carbon isotopes and batch experiments // Journal of Hydrology. -2022. -Vol. 613. -Art. 128334. https://doi.org/10.1016/j.jhydrol.2022.128334

6. Voutchkova D.D. Temporal variation of iodine in Danish groundwater // Geological Survey of Denmark and Greenland (GEUS). -2023. -Vol. 53. – Art. 8352. https://doi.org/10.34194/geusb.v53.8352

7. Voutchkova D.D., Ernstsen V., Kristiansen S.M., Hansen B. Iodine in major Danish aquifers // Environmental Earth Sciences. -2017. -Vol. 76. -Art. 447. https://doi.org/10.1007/s12665-017-6775-6

8. Voutchkova D.D., Ernstsen V., Hansen B., Sørensen B.L., Zhang Ch., Kristiansen S.M. Assessment of spatial variation in drinking water iodine and its implications for dietary intake: A new conceptual model for Denmark // Science of the Total Environment. -2014. -Vol. 493. -P. 432–444. https://doi.org/10.1016/j.scitotenv.2014.06.008

9. Review of the iodine market in the CIS. 5th edition, supplemented and revised. Moscow. 2010. -P.10–13. (In Russian)

10. Li J., Wang Y., Xie X., Zhang L., Guo W. Hydrogeochemistry of high iodine groundwater: A case study at the Datong Basin, northern China // Environmental Science: Processes & Impacts. -2013. -Vol. 15(4). -P. 848–859. https://doi.org/10.1039/c3em30841c

11. Tinel L., Adams T.J., et al. Influence of the sea surface microlayer on oceanic iodine emissions // Environmental Science & Technology. -2020. -Vol. 20. -P. 13228–13237. https://doi.org/10.1021/acs.est.0c02736

12. Lusiya M., Kampos A.M. New approach to evaluating dissolved iodine speciation in natural waters using cathodic stripping voltammetry and a storage study for preserving iodine species // Marine Chemistry. -1997. -Vol. 57. -P. 107–117. https://doi.org/10.1016/S0304-4203(96)00093-X

13. Gong T., Zhang X. Determination of iodide, iodate and organo-iodine in waters with a new total organic iodine measurement approach // Water Research. -2013. -Vol. 47. -P. 6660–6669. https://doi.org/10.1016/j.watres.2013.08.039

14. Selyodka J.R., Liss P.S. A new method for the determination of iodine species in seawater // Deep Sea Research and Oceanographic Abstracts. -1974. -Vol. 21. -P. 777–783. https://doi.org/10.1016/0011-7471(74)90085-0

15. Harvey G.R. A study of the chemistry of iodine and bromine in marine sediments // Marine Chemistry. -1980. -Vol. 8. – P. 327–332. https://doi.org/10.1016/0304-4203(80)90021-3

16. Jickells T.D., Boyd S.S., Knap A.H. Iodine cycling in the Sargasso Sea and the Bermuda inshore waters // Marine Chemistry. -1988. -Vol. 24. -P. 61–82. https://doi.org/10.1016/0304-4203(88)90006-0

17. Brix T., Reynolds J.E. Iodine recovery systems and methods. U.S. Patent No. 8496815. 2010.

18. Tikhonov S., Neumann L. Technology of iodine extracting from formation and associated water of oil and gas fields. U.S. Patent No. 11040879. 2021.

19. Doya M., Tsukagoshi T. Method for co-producing iodine and salt. Patent No. 0069167. 2023.

20. Bozorov Y.Sh., Turaev Kh.Kh., Djalilov A.T., Aliqulov R.V., Umbarov I.A., Haitov B.T., Akhatov J.K., Uralov N.B. Synthesis of a new ion exchange membrane and its surface morphology // Recent Contributions to Physics. -2024. -Vol. 4(91). -P. 2663–2276. https://doi.org/10.26577/RCPh.2024.v91.i4.a6

21. Akhatov A., Turaev K., Ashurov J., Umbarov I., Tillaev Kh., Nomozov A., Uralov N., Eshdavlatov E. Synthesis, structure and Hirschfeld surface analysis of a complex compound based on Cd(II) salt and o-phenylenediamine // Bulletin. Physical Series (VKF).-2024. -Vol. 91(4). -P. 77–85. https://doi.org/10.26577/RCPh.2024.v91.i4.a8 (In Russian)

22. Lescinskis Br., Kizane G., Supe A., Gzibovskis E., Tiliks J., Lescinskis A., Grishmanov V., Tanaka S. Dosimetry of charged particles using lyoluminescence method // Physical Sciences and Technology. -2017. -Vol. 4(1). https://doi.org/10.26577/phst-2017-1-121

23. Koketayev T.A., Tussupbekova A.K. Polymorphic phase transitions and recombination luminescence in ammonium halide crystals // Physical Sciences and Technology. -2019. -Vol. 6(3–4). https://doi.org/10.26577/phst-2019-2-p10

Information about authors:

Uralov Nuriddin Bekmuradovich is a PhD doctorate at the Faculty of Chemistry, Termez State University, (Termez, Uzbekistan), e-mail: uralovnuriddin1991@gmail.com

Turaev Khayit Khudaynazarovich, Doctor of Chemical Sciences is a Professor at the Faculty of Chemistry, Termez State University, (Termez, Uzbekistan), e-mail: hhturayev@rambler.ru

Normurodov Bakhtiyor Abdullayevich, DSc is an Associate professor at the Faculty of Chemistry, Termez State University, (Termez, Uzbekistan), e-mail: normurodovbakhtiyor@gmail.com

Umbarov Ibragim Amanovich, Doctor of technical sciences is a Professor at the Faculty of Chemistry, Termez State University, (Termez, Uzbekistan), e-mail: umbarov@mail.ru

Kurbonov Fakhriddin Bobomurotovich is a Lecturer at the Faculty of Chemistry of Termez State University, (Termez, Uzbekistan), e-mail: bekzur22@gmail.com

Modeling of thermal distribution
on cryosurface for low temperatures

O.D. Vorobyova [1,2*] , D.Yu. Sokolov [1,2] and Ye.S. Korshikov [1]

[1]Al-Farabi Kazakh National University, Almaty, Kazakhstan
[2]Almaty Technological University, Almaty, Kazakhstan
*e-mail: olga.vorobyova842@gmail.com

In this work, the temperature distribution on a cryosurface operating at low temperatures (in the range from 300 K to 80 K) was thoroughly studied. This type of cryogenic cooling surface is specifically designed for experimental processes that involve the controlled deposition and subsequent cooling of various inorganic compounds. Such processes are essential for conducting detailed investigations into the physicochemical properties, morphology, and structure of these materials under cryogenic conditions. The temperature distribution was analyzed through numerical simulation, which included modeling the cooling process of the cryopanel surface down to cryogenic temperatures using the finite element method. Liquid nitrogen was selected as the working coolant due to its availability, low boiling point, and high efficiency in achieving the required cooling rate. The simulation results revealed the temperature gradient both within the volume and on the surface of the cryopanel. Additionally, the influence of the thermal conductivity of different structural materials–aluminum and stainless steel–on the cooling efficiency was examined. The desired cryosurface temperature range (80–90 K) was successfully reached within 1800 seconds, using a nitrogen flow through a coiled pipe of 6 mm in diameter.

Key words: cryosurface, computer modelling, thermal distribution, low temperatures, thermal conductivity.
PACS number(s): 64.60.−i; 78.20.Bh

1 Introduction

Cryosurfaces play an important role for cooling and further work with samples in the low temperature range. Computer simulation is one of the most modern and relevant methods for studying the heat transfer processes of cryopanels when interacting with the environment and materials of various compositions applied to the surface of the substrate. This will solve several problems related to:

1) the development of an effective heat exchanger and the study of its heat transfer properties;

2) creating an autonomous system for maintaining temperatures of varying accuracy under conditions of thermal energy balance on the surface of the cryopanel.

In this regard, it is relevant to study the influence of heat transfer processes before achieving optimal temperature operating conditions on the surface of the cryopanel.

Cooling of the coil to cryogenic temperatures is achieved by supplying a cryogenic liquid (in this case, liquid nitrogen with a temperature of 77 K is considered). The use of cryogenic liquids is widespread in modern scientific, medical and food industries [1].

Another challenge in cryogenic cooling is to define and understand the cooling process and the thermal characteristics that affect it with subsequent heat transfer. Therefore, research continues on this topic [2-3].

Rapid progress has been made in the past two decades. In 2007, the authors of [4] analyzed experimental data on the cooling of a horizontal pipe and the heat flux formed in it. They were able to show the transitional regimes from creep to cooling, including visualization of the data obtained during the analysis [4]. In 2012, a similar study was conducted in [5], but in a vertical pipe. They determined the heat flux and heat transfer features with separation of boiling zones and transition flows of the cryogenic liquid flow. Further research in the field of cryogenic liquid cooling contributed more data and investigated the influence of various flow parameters on the cooling process.

These data allowed more accurate modeling of both the cooling process itself and the flow pattern. In 2015, experiments were conducted on cooling lines with liquid nitrogen (LN_2) in horizontal and inclined pipes. The influence of pipe length and mass flow on cooling time and heat flux was investigated [6]. In 2015, Darr et al. conducted in-line cooling experiments with LN_2 in a vertical tube of approximately 0.5 m length and simulated the cooling process using a one-dimensional homogeneous model [7].

In 2016, they further expanded the mass flow range of the experiments and improved the film boiling correlations by taking into account the flow directions [8]. Darr's research has provided many important updates to the investigation of cryogenic line cooling. However, the applicability of the proposed correlations needs to be investigated, especially for a tube that is much longer than the studied one.

This leads to the following issues for calculating temperature using computer modeling:

1) There is always high ambiguity and uncertainty in the data when using cryogenic characteristics in the study.

2) These high uncertainties will lead to significant scatter of results when attempting to develop a cryogenic model that describes the relationship with the experimental data.

For two-phase flows, experimental data and analytical models can be related using computational fluid dynamics (CFD) models.

Such studies for two-phase flow have successfully developed both analytical models [9-11] and CFD models [12-14]. This formed the basis for the experimental validation of models for predicting the behavior of two-phase flow of cryogenic liquids and flow visualization methods [16-17].

Considering that the main attention is paid to the research of heat exchangers at high temperature [18-20], a model of a cooling heat exchanger was developed in this work. This study presents a the temperature distribution of a cryosurface at low temperatures from 80 to 300 K. Determining the thermal efficiency of the cryosurface will improve the design of cryopanels. The model was developed using the finite element method; temperature-time dependencies were obtained when the surface was cooled to cryotemperatures.

2 Methodology

2.1 Methods
In this work, the finite element method (FEM) was used, which can be a minimization function or described by partial differential equations in the form of a set of finite volumes (Fig. 1).

Features of FEM:

1) Using simple approximating elements, one can achieve any accuracy of piecewise approximation of physical fields on finite elements.

2) Locality of approximation leads to systems of sparse equations for the discretized problem. This helps to solve problems with a very large number of nodal unknowns.

The main stages of the finite element method are described below.

The modeling program (in this work, the COMSOL Multiphysics software package) generates a finite element mesh based on the geometry. The mesh description consists of several arrays of system equation solvers, the main ones being the nodal coordinates and the connections between the elements.

2.2 Equations.

To solve the global system of equations for the entire solution domain, it is necessary to combine the equations of local elements. Element connections are used for the assembly process. Before solving, boundary conditions (which are not taken into account in the element equations) must be entered. Before solving a system of equations, boundary conditions must be specified.

Heat removal from the surface of the cryopane is ensured by convection of the gaseous coolant flow and is described by the general heat conduction equation and the Navier-Stokes equation.

The general equation of thermal conductivity for any solid [21]:

$$\rho C_p \frac{\partial T}{\partial t} + \nabla \cdot q = Q \qquad (1)$$

The general equation of thermal conductivity for a liquid (in this case, liquid nitrogen) [21]:

$$\rho C_p \frac{\partial T}{\partial t} + \rho C_p \cdot u \cdot \nabla T + (\nabla \cdot q) = 0 \qquad (2)$$

where
ρ – density,
u – velocity vector,
p – pressure,
τ – viscous stress tensor,
C_p – specific heat capacity,
T – absolute temperature,
q – heat flux vector,

Accordingly, the principle of energy conservation is the equation of heat transfer in continuous media from the first law of thermodynamics. These

equations in integral and local forms at the nodes of the model grid are applicable to various heat transfer equations that can be solved in COMSOL Multiphysics software package [21-22].

3 Results and discussion

This study presents computer modeling of a cryopanel (300x300x20 mm) with a channel of 6 mm in diameter. Liquid nitrogen enters the cryopanel channel at a speed of 50 mm/s and a temperature of 80 K. In this configuration, we consider the flow to be laminar. We consider the walls of the heat exchanger to be insulated and their initial temperature is set to room temperature.

Figure 2 shows the simulation results for the first 800 seconds of liquid nitrogen flow. As can be seen from the figure, the temperature distribution on the surface is uneven. After 800 seconds, only the channel is cooled, but not the surface. Then the temperature equalizes and the difference between the ends of the cryopanel becomes no more than 0.16 K.
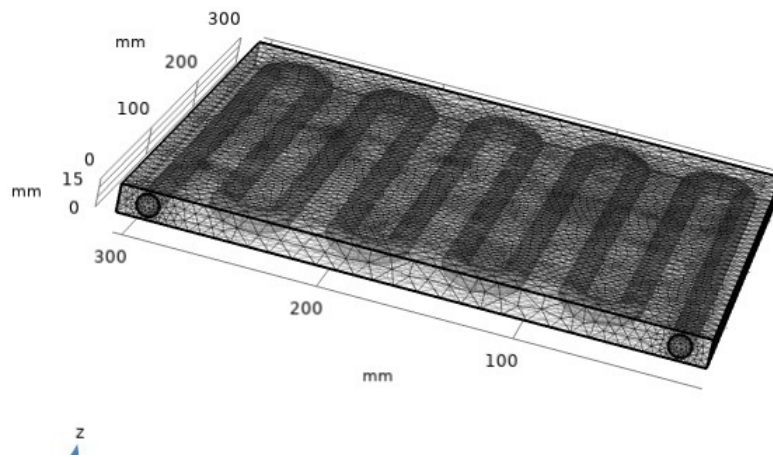
Figure 1 – Image of the calculation grid for the cryopanel volume.
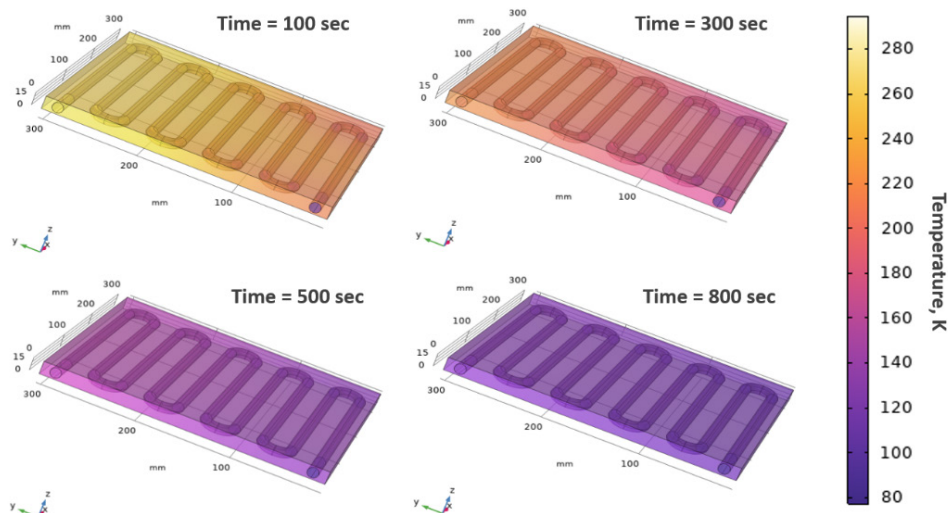
Figure 2 – Time distribution of volumetric temperature in a cryopanel.

Comparing aluminum and steel cryopanels, the results showed that the temperature distribution cannot be compared between two panels if one does not define the same time schedule. When one considers aluminum and steel, where the thermal conductivity coefficient is 235 W/(m·K) for aluminum and 45 W/(m·K) for steel, it is almost obvious that the relative cooling efficiency will be much different (Fig. 3). After 800 seconds, the average temperature difference between the ends of the steel cryopanel was more than 100 K (Fig. 3a), and for the aluminum cryopanel it was 14 K (Fig. 3b). Thus, in this case, based on the modeling results, preference is given to the aluminum cryopanel in terms of thermal conductivity.
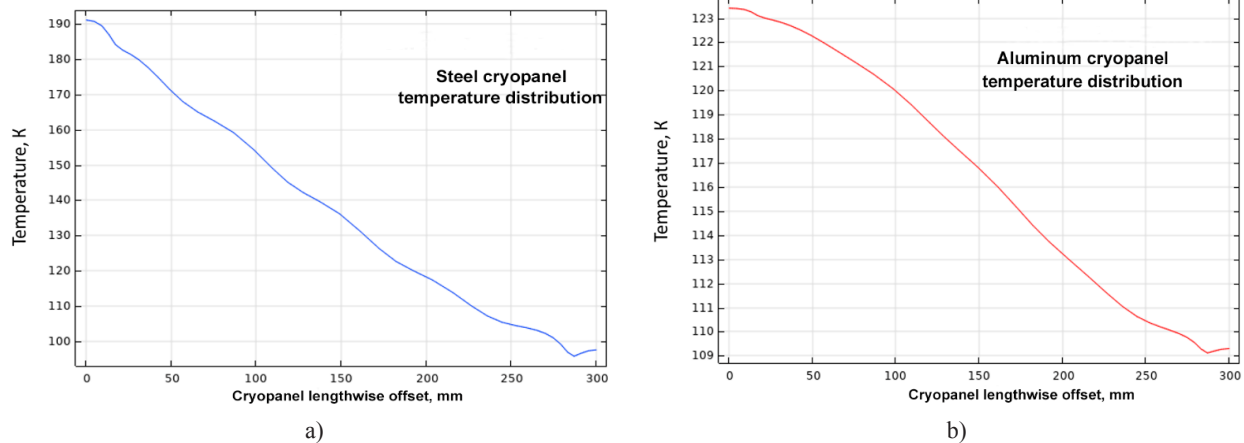
Figure 3 – An average temperature distribution along the cryopanel surface 800 second later:
a) aluminum cryopanel; b) steel cryopanel.

Next, Figure 4 shows the total time spent on cooling the cryopanel. To reach the optimum operating temperature (around 80 K), the aluminum panel took 1850 seconds. The steel panel cooled down more slowly, taking 3000 seconds. Comparing the cooling rate of the entire cryopanel it's shown that the aluminum panel is 43% more efficient due to its high thermal conductivity.
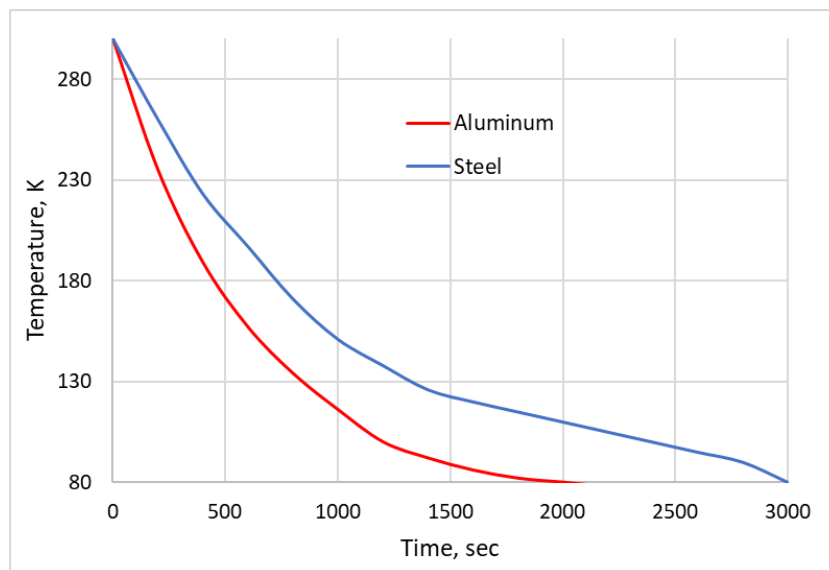

Figure 4 – Comparison of the average temperature of the cryosurface made
of steel and aluminum for the 3000 seconds.

4 Conclusions

This work presents a variant of computer modeling of cryogenic surfaces. These surfaces are used in scientific research and food industries. Such types of heat exchangers as cryopanels require preliminary assessments of their efficiency to ensure optimal operating conditions. In this study it's demonstrated that the aluminum cryopanel is 43% more efficient than the steel one, that is in respect of the whole cryopanel surface. When one considers the aluminum and steel, where the thermal conductivity coefficient is 4 times to other it is almost obvious that the relative cooling efficiency will be much different

During the work, the process of cryosurface cooling from room temperature to 80 K was studied. After analyzing the distribution of the average temperature over the volume of the cryosurface, it was found that the coil through which liquid nitrogen flows cools the surface unevenly. This requires additional time to complete cooling of the working surface of the cryo-panel. Only 800 seconds after the start of cooling, the temperature of 80 K is reached only along the inner surface of the channel. At the same time, the temperature of the cryosurface equalizes to values of about 80 K only 1850 seconds after the start of cooling. Thus, the configuration of coils throughout the volume that conduct liquid nitrogen affects the achievement of optimal working low temperatures. To improve the indicators for the cooling time, it is recommended to change the coil configuration, and an assessment of the optimal channel diameter is required.

The model allowed us to evaluate the efficiency of materials and the geometry of the pipeline tubes during the design of universal cryogenic surfaces. The results of this study can contribute to the further development of cryogenic technologies in this area.

References

1. Sokolov D.Y., Yerezhep D., Vorobyova O., Ramos M.A., Shinbayeva A. Optical studies of thin films of cryocondensed mixtures of water and admixture of nitrogen and argon // Materials. – 2022. – Vol. 15. – P. 7441-7459. https://doi.org/10.3390/ma15217441

2. Wang B. et al. Potential applications of cryogenic technologies to plant genetic improvement and pathogen eradication // Biotechnology advances. – 2014. – Vol 32. Is.3. – P. 583-595. https://doi.org/10.1016/j.biotechadv.2014.03.003

3. Rutkuniene Z. LES modeling gas particle dispersion and thermal characteristics in a reacting turbulent low // Phys. Sci. Technol. – 2024. – Vol. 11. Is. 1-2. – P. 76-84. https://doi.org/10.26577/phst2024v11i1a9

4. Yuan K., Ji Y., Chung J.N. Cryogenic chilldown process under low flow rates // Int. J. Heat Mass Transf. – 2007. – Vol. 50. Is.19–20. – P. 4011–4022. https://doi.org/10.1016/j.ijheatmasstransfer.2007.01.034

5. Hu H., Chung J.N., Amber S.H. An experimental study on flow patterns and heat transfer characteristics during cryogenic chilldown in a vertical pipe // Cryogenics (Guildf). – 2012. – Vol. 52. Is. 4–6. –P. 268–275. https://doi.org/10.1016/j.cryogenics.2012.01.033

6. Johnson J., Shine S.R. Transient cryogenic chill down process in horizontal and inclined pipes // Cryogenics (Guildf), – 2015. – Vol. 71. – P. 7–17. https://doi.org/10.1016/j.cryogenics.2015.05.003

7. Darr S.R. et al. An experimental study on terrestrial cryogenic tube chilldown II. Effect of flow direction with respect to gravity and new correlation set // Int. J. Heat Mass Transf.– 2016. – Vol. 103. – P. 1243–1260. https://doi.org/10.1016/j.ijheatmasstransfer.2016.05.019

8. Yang J. et al. Numerical study of transient conjugate heat transfer of the cryosupersonic air-quenching based on a Mach-weighted pressure-based method // International Journal of Heat and Mass Transfer. – 2019. – Vol. 134. – P. 586-599. https://doi.org/10.1016/j.ijheatmasstransfer.2019.01.064

9. Ganesan V. et al. Universal critical heat flux (CHF) correlations for cryogenic flow boiling in uniformly heated tubes // Int. J. Heat Mass Transf.– 2021.– Vol. 166. – P. 120678. https://doi.org/10.1016/j.ijheatmasstransfer.2020.120678

10. Devahdhanush V.S., Mudawar I. Review of critical heat flux (CHF) in jet impingement boiling // Int. J. Heat Mass Transf. –2021. – Vol. 169. – P. 120893. https://doi.org/10.1016/j.ijheatmasstransfer.2020.120893

11. Cai C. et al. Assessment of void fraction models and correlations for subcooled boiling in vertical upflow in a circular tube // Int. J. Heat Mass Transf. 2021.– Vol. 171. – P. 121060. https://doi.org/10.1016/j.ijheatmasstransfer.2021.121060

12. Devahdhanush V.S. et al. Assessing advantages and disadvantages of macro- and micro-channel flow boiling for high-heat-flux thermal management using computational and theoretical/empirical methods // Int. J. Heat Mass Transf. – 2021. – Vol. 169. – P. 120787. https://doi.org/10.1016/j.ijheatmasstransfer.2020.120787

13. Ferreira J., Kaviany M. Geometric-confinement suppression of flow-boiling instability using perforated wick: Part I CHF and conductance enhancement //Int. J. Heat Mass Transf.– 2020. – Vol. 159. –P. 120080. https://doi.org/10.1016/j.ijheatmasstransfer.2020.120080

14. O'Neill L.E., Mudawar I. Review of two-phase flow instabilities in macro- and micro-channel systems // Int. J. Heat Mass Transf.– 2020. – Vol. 157. – P. 119738. https://doi.org/10.1016/j.ijheatmasstransfer.2020.119738

15. Kim Y.J. et al. Flow boiling CHF experiment with sudden expansion tubes // Int. Commun. Heat Mass Transf. – 2020. – Vol. 114.– P. 104557. https://doi.org/10.1016/j.icheatmasstransfer.2020.104557

16. Lee H.et al. Experimental and computational investigation of vertical downflow condensation // Int. J. Heat Mass Transf. – 2015. – Vol. 85. – P. 865–879. https://doi.org/10.1016/j.ijheatmasstransfer.2015.02.037

17. Lee J., O'Neill L.E., Mudawar I. 3D computational investigation and experimental validation of effect of shear-lift on twophase flow and heat transfer characteristics of highly subcooled flow boiling in vertical upflow // Int. J. Heat Mass Transf. – 2020. – Vol. 150. – P. 119291. https://doi.org/10.1016/j.ijheatmasstransfer.2019.119291

18. Dzhus A.V., Subbotin S.O., Pulina T.V. and Snizhnoi G.V. Modeling the resistance of plate-like heat exchangers made of 06khn28mdt alloy (analogous to aisi904l steel) to crevice corrosion in recycled water enterprises // Phys. Sci. Technol. – 2024. – Vol. 11. Is. 3-4. – P. 58-66 https://doi.org/10.26577/phst2024v11i2b07

19. Abdullayev J. Sh., Sapaev I. B. Modeling and calibration of electrical features of p-n junctions based on Si and GaAs // Phys. Sci. Technol. – 2024. – Vol. 11. Is. 3-4 – P. 39-48. https://doi.org/10.26577/phst2024v11i2b05

20. Dzhus A., Snizhnoi G. Prediction the durability of heat exchangers made of 06KhN28MDT alloy (analogous to AISI904L steel) to crevice corrosion during their operation in recycled water // Phys. Sci. Technol. – 2023. – Vol. 10. Is. 3-4. – P. 57-67. https://doi.org/10.26577/phst.2023.v10.i2.07

21. Hodzhaeva M., Golikov O., Sokolov D., Yerezhep D. Research of the temperature dynamics change of a universal cryogenic surface using the finite element method // Recent Contributions to Physics. – 2022. – Vol. 1. Is. 80. – P. 66–74. https://doi. org/ 10.26577/rcph.2022.v80.i1.08 (In Russian)

22. Tazhenova M.S., Sultan R.R., Katpayeva K.A. Numerical study of thermophysical characteristics of a cryogenic surface // Phys. Sci. Technol. –2023. – Vol. 10. Is. 1-2. – P. 4-12. https://doi.org/10.26577/phst.2023.v10.i1.01

Information about authors:

Vorobyova Olga is a 3rd year PhD student at al-Farabi Kazakh National University (Almaty, Kazakhstan), Research Fellow of the scientific project at Almaty Technological University (Almaty, Kazakhstan), e-mail: olga.vorobyova842@gmail.com

Sokolov Dmitriy, PhD is an Associate Professor at al-Farabi Kazakh National University (Almaty, Kazakhstan), Head of the scientific project at Almaty Technological University (Almaty, Kazakhstan), e-mail: yasnyisokol@gmail.com

Korshikov Yevgeniy, PhD is a Senior lecturer at al-Farabi Kazakh National University (Almaty, Kazakhstan), e-mail: e.s.korshikov@ physics.kz

Quantitive assessment of the use of Kazakhstan montmorillonite clays as sorbent carriers for pharmaceutical substances

D.K. Bolatkan[1] , A.Zh. Kerimkulova[2]* , M.M. Beisebekov[3] ,

K. Akatan[1] , N. Kantay[1] , E. Shaimardan[3] , A Kukhareva[2,3] ,

A. Bukunova[4] and S.K. Kabdrakhmanova[2]

[1]S.Amanzholov East Kazakhstan University, Ust-Kamenogorsk, Kazakhstan
[2]Satbayev University, Almaty, Kazakhstan
[3]Scientific Center of Composite Materials, Almaty, Kazakhstan
[4]D.Serikbayev East KazakhstanTechnical University, Ust-Kamenogorsk, Kazakhstan
*e-mail:kerimkulova07@mail.ru, s.kabdrakhmanova@gmail.com

Bentonite materials are widely utilized across various industries due to their unique physicochemical properties. This study presents a qualitative and comparative analysis of mineral substances derived from bentonite clay deposits in East Kazakhstan. The montmorillonite content in the samples ranges from 75.5% to 88%, with adsorption capacity (determined by the methylene blue method) varying between 119 and 204 mg/g. The pH of the samples lies within the range of 7 to 10. FTIR and XRF analyses confirmed the presence of major components such as silicon and aluminum oxides, while X-ray diffraction identified montmorillonite as the dominant crystalline phase. Textural characterization revealed specific surface areas of 94–104 m²/g, pore volumes of 0.03–0.05 cm³/g, and pore sizes between 0.8 and 1.04 nm. SEM analysis demonstrated a flaky, layered, and porous morphology typical of bentonite. Based on these properties, the bentonite samples exhibit strong potential for industrial use. They are applicable in oil production (as components of drilling fluids) and construction (as insulating and sealing agents). Additionally, their high sorption capacity makes them promising candidates for pharmaceutical applications, particularly as carriers in topical formulations such as ointments and pastes for wound healing and inflammatory skin conditions.

Keywords: bentonite clays, montmorillonite, mineral composition, surface area, physico-chemical properties.
PACS number(s): 82.70.Dd; 72.80.Tm; 82.80.−d.

1 Introduction

Currently, the development of the chemical industry, environmental degradation, the depletion of natural resources, and the increase in synthetic products have posed new challenges for scientists. One of the key objectives is to develop products derived from economically viable and accessible raw materials that do not have adverse effects on human health [1]. In this context, the study of the properties of natural clays, which belong to the category of mineral raw materials, and the identification of their potential applications in industry and everyday life, is of particular relevance.

Bentonites are natural mineral clays composed mainly of various metal oxides. Due to their chemical composition, they are widely used in the production of construction materials [2], porcelain [3], as additives in animal feed [4], and in such fields as medicine, pharmaceuticals [5], and cosmetology [6], which contributes to the growing demand for these materials.

Approximately 30% of the global bentonite reserves are located in China, 15% in the United States, and 7% in Turkey [7]. Other countries with significant bentonite resources include Greece, Russia, France, India, Turkey, Azerbaijan, Georgia, and Armenia. In Kazakhstan, large bentonite reserves are

concentrated in the southern and eastern regions [8]. In South Kazakhstan, the Dzherzhinskoye, Ildersay, and Andreevskoye deposits are estimated to contain around 100 million tons of bentonite, while the Darbaza and Keles deposits hold approximately 58 million tons [9]. In Eastern Kazakhstan, the group of deposits known as the Manyrak bentonite clays is estimated to contain up to 50 million tons [10].

The distribution of bentonites across different geographical regions, along with factors such as climate, geological structure, and local environmental conditions, contributes to the variation in their physico-chemical properties [11]. Since the formation of mineral clays is a prolonged and complex process, significant differences can also be observed in the properties of bentonites extracted from different depths within a single deposit [12]. These differences, in turn, are key factors determining the quality and potential applications of bentonitic clay. Therefore, identifying the chemical composition, phase structure, and qualitative characteristics of natural clays is of critical importance.

During geological exploration activities conducted in the 1960s, mineral clays from the Tagan deposit in Eastern Kazakhstan began to be extensively studied [9]. According to X-ray phase analysis, the bentonites of the Tagan deposit are predominantly composed of montmorillonite minerals, with quartz, feldspar, and calcite as secondary components [13].

In recent years, due to the rapid growth in oil and gas production, special attention in the exploration sector has been given to high-quality drilling fluids based on bentonite powders, which are used for well cementing. These materials are particularly relevant for exploratory offshore oil drilling. Chemically unmodified bentonite powders must possess high viscosity and relatively high static shear stress. Such properties are characteristic of the bentonites from the 14th horizon of the Tagan deposit. Furthermore, these bentonites are also used in the production of cracking catalysts for crude oil processing. The bentonite from the 12th horizon of the Tagan deposit is notable for its high content of montmorillonite in alkaline form, which serves as the base material for the pharmaceutical product Tagansorbent. This drug is designed for the removal of heavy metal ions and is used in cases of poisoning, diarrhea, and intoxication [14].

In the 1990s, the physico-chemical properties of bentonites from the Tagan deposit were studied, leading to an expansion in their fields of application [14]. According to studies [14, 15], the montmorillonite content in Tagan deposit bentonites was reported to

be 90–92%, which directly contributes to their high binding capacity, as well as their adsorption and catalytic activity [16].

The potential use of sulfuric acid-modified bentonite from the 14th horizon of the Tagan deposit for the removal of Cu^{2+}, Pb^{2+}, Cd^{2+}, and Zn^{2+} heavy metal ions from mining wastewater has been investigated in studies [17, 18]. These studies revealed that the degree of sorption of heavy metal ions reached 90–98%. Furthermore, in the study [19], to increase the surface area and enhance the sorption capacity of Tagan bentonites, thermal activation at 120 °C for 4 hours followed by treatment with sulfuric acid for 2 hours increased the specific surface area up to 85 m²/g.

In addition, the abundance of micro- and macroelements in Tagan bentonites has enabled the use of clay from the 12th horizon for pharmaceutical purposes [20]. At present, bentonite is used as an enterosorbent in the form of a ready-made product to remove accumulated toxins and radionuclides from the human body. It can also be applied as an antacid to neutralize excess stomach acid [21]. Furthermore, studies [22, 23] have shown the high potential for using this clay horizon as a feed additive.

In conclusion, based on the results of the conducted literature review, it has been determined that further research aimed at expanding the application areas of bentonite clay remains highly relevant due to its unique properties. Accordingly, this study presents a comparative analysis of the physico-chemical properties of bentonites distributed in the East Kazakhstan region, with a particular focus on their potential application in medicine.

2 Experimental section

2.1 Materials

Chrysoidin 6 W, Rhodamine ($C_{21}H_{16}N_2O_3 \cdot HCl$ ≥85% (HPLC)), Trilon B, Methylene blue, sodium pyrophosphate, ethanol (96%,C_2H_5OH), sulfuric acid (98%, H_2SO_4), sodium hydroxide (≥99%, NaOH), potassium bichromate (≥99%,$K_2Cr_2O_7$),sodium thiosulfate (99%,$Na_2S_2O_3$), potassium iodide(≥99%, KI) obtained from Sigma-Aldrich (Bangalore, India). All other reagents were of analytical grade a- were used without additional purification.

2.2 Methods
2.2.1 Raw materials

Three different bentonite samples were collected for the study from clay deposits in the East Kazakhstan region, which are known to contain re-

serves of alkali and alkaline earth metal bentonites. Sampling of bentonite clay was carried out at three discrete and representative points of the Tagan deposit at a depth of 1.5 meters, selected in advance based on geological exploration data and clay stratum mapping. To ensure the reliability of the analysis and reflect the spatial heterogeneity of the raw material, each sample was manually extracted using the trenching method. The sampling sites were located within a single clay bed, evenly distributed to avoid areas of intensive weathering or anthropogenic impact.The collected samples, each with a volume of 50 mL and a diameter of 10 mm, were ground using a FRITSCH-6 (GERMANY) planetary ball mill at a temperature of 25 ± 2 °C, with a rotation speed of 300 rpm for 15 minutes. The ground material was then sieved through a 0.01 mm mesh. The bentonite samples used in the study were conditionally labeled as B_1, B_2, and B_3.

2.2.2 Quality indicators bentonites

The moisture content of the bentonite samples was determined in accordance with ASTM D2216 "Standard Test Methods for Laboratory Determination of Water (Moisture) Content of Soil and Rock by Mass". The ash content was measured following ASTM D2974 "Standard Test Methods for Determining the Water (Moisture) Content, Ash Content, and Organic Material of Peat and Other Organic Soils". The mass fraction of montmorillonite in the bentonite was determined according to GOST 28177-89.

The sorption capacity based on methylene blue and the pH level were determined in accordance with pharmacopoeial standard [18]. The adsorption capacity of bentonite clays was determined in accordance with the methodology outlined in the State Pharmacopoeia of the Russian Federation, based on the sorption of methylene blue from aqueous solution. A pre-weighed amount of air-dried clay sample was mixed with a methylene blue solution of known concentration and allowed to interact under controlled conditions. The mixture was stirred and maintained at room temperature for a contact time of 60 minutes. After equilibration, the suspension was filtered, and the residual concentration of methylene blue was measured spectrophotometrically at 667 nm. The adsorption capacity was calculated from the difference between the initial and final dye concentrations, expressed in mg/g of dry sorbent. Experimental parameters such as contact time, pH (maintained near neutral), and solution concentration were standardized in accordance with pharmacopoeial guidelines to ensure reproducibility and accuracy.

2.2.3 XRF analysis

To determine the main oxide composition of the bentonite clay, energy-dispersive X-ray fluorescence spectroscopy (EDXRF) was employed. The analysis was performed using the NEX CG II instrument (Rigaku, Japan). This device is based on a fully dispersive optical system and features a highly sensitive detector utilizing anisotropic X-ray radiation.

2.2.4 X-ray diffraction analysis

The structural and phase composition of the samples was investigated using X-ray diffraction (XRD) on an X'Pert PRO diffractometer (Malvern Panalytical Empyrean, Netherlands) with monochromatized copper radiation (CuKα, K-Alpha1 [Å] = 0.1542) and a scanning step of 0.02°. During the analysis, the measurement angle ranged from 10° to 80°, with an X-ray tube voltage of 45 kV and a current of 30 mA. The measurement time per step was 0.5 seconds, and a universal aluminum sample holder (PW1172/01) was used. The obtained XRD patterns were analyzed using the ICDD PDF-4/AXIOM XRD database.

The formula for calculating the interplanar spacing ddd in X-ray diffraction analysis is based on Bragg's Law:

$$2dsin \; = n\lambda \longrightarrow d = \lambda/(2sin \;) \qquad (1)$$

2.2.5 FTIR analysis

The chemical structure of the bentonite samples was analyzed using FTIR (FT-801 IR Spectrometer, Simex, Russia) in the wavelength range of 500–4000 cm^{-1} with a resolution of 1 cm^{-1} at a temperature of 25 ± 2°C and 100 scans. During the analysis, the clay powder was mixed with potassium bromide in a 1:9 ratio and ground in an agate mortar until a fully homogeneous mixture was achieved. Subsequently, a tablet was prepared using a press in a die at 200 MPa pressure, and water vapor was drawn using a vacuum pump for 5 minutes to form the tablet.

2.2.6 SEM analysis

The surface morphology of the mineral clays was investigated using a 3D-SEM instrument, Quanta 200 (FEI, Netherlands). Measurements were conducted in high vacuum mode using a secondary electron detector with an accelerating voltage of 5 kV. The surface of the mineral clays was coated with gold nanoparticles to enhance electron transfer.

2.2.7 BET analysis

The specific surface area and pore characteristics of the clay were investigated using the BSD-660S A3

Physical Adsorption Analyzer based on low-temperature adsorption of liquid nitrogen. The analysis was conducted at a temperature of 30°C for a duration of 120 minutes. The specific surface area of the samples was determined using the BET method, while the pore characteristics were analyzed using the BJH (Barrett-Joyner-Halenda) method.

2.2.8 Thermogravimetric analysis

The thermal characteristics were studied with a LabSysevo differential thermogravimetric analyzer (Setaram, France), in an argon atmosphere. The temperature range was $30\pm5 – 700\pm5$°C, with a heating rate of 10 ± 1°C/min. The mass of the samples was approximately 25 ± 2 mg.

2.2.9 Average partical size and Zeta potential

The zeta potential was measured using a Malvern Zetasizer Nano ZS90 instrument (UK). The Zetasizer systems utilize electrophoretic light scattering (ELS) and dynamic light scattering (DLS) methods, which provide information on the mobility, charge, and size of particles in dispersive systems ranging from nanometers to micrometers. For each sample, 12 scans were performed per run, with a total of 3 runs conducted. The entire experiment was repeated at least three times. The particle charge (zeta potential) was determined by performing 12 scans, with a minimum of 3 runs recorded. Error bars were obtained using the standard zeta potential software.

3 Results and discussion

3.1 Preparation of raw materials

The colors of mineral clays vary widely depending on the types and quantities of chemical elements they contain [24]. The colors of the samples selected for the study ranged from light to dark brown, as shown in Figure 1.

The B_1 bentonite (Figure 1a) has a light color. The light color of the B1 sample likely results from its montmorillonite content and its classification as an alkaline and alkaline earth type bentonite, as identified in the study [25]. Clays of this type are known to exhibit high adsorptive properties, swelling in water, and high plasticity [26].

On the other hand, the B_2 and B_3 samples are brownish-red in color (Figure 1b, 1c). This indicates the presence of iron oxides and other metal oxides in the clay composition [6]. Such mineral clays are known to be thermally stable, possess high strength, and exhibit good adsorptive properties [27]. According to [28], colored bentonite clays can be used for the production of ceramic glazes, porcelain dishes, and construction materials.

Figure 1 – Bentonite samples: a – B_1; b – B_2; c – B_3.

3.2 Quality indicators of bentonites

The results of the qualitative analysis of the bentonite clays are shown in Table 1. Determining the qualitative composition of bentonites allows for a better understanding of their potential applications. The quality of bentonite clays depends on the content and ionic form of montmorillonite [29]. In the B_1 bentonite, the mass fraction of montmorillonite was 88%, with a pH value of 8.9. In B_2 bentonite, the montmorillonite content was 75.5%, and the pH value was 8.1, while in B_3 bentonite, the montmorillonite content was 83%, and the pH value was 7.1. According to the pharmacopeial article, the pH of bentonite clays should range from 7 to 10, and their methylene blue adsorption capacity should be no less than 150 mg per gram for their high potential in pharmaceutical applications [30]. Based on this pharmacopeial guideline, it can be concluded that the B_1 and B_2 samples have a higher potential for use in pharmaceuticals. Moreover, the closer the pH of the

bentonites is to a basic medium, the higher their ion exchange properties [31].

The methylene blue adsorption capacity reached its highest value of 204.4 mg/g in the B_1 sample. In the B_2 sample, the capacity was 119.88 mg/g, while in the B_3 sample, it was 150 mg/g.

Additionally, the moisture content of the bentonite clays ranged from 7.3% to 7.8%, which is consistent with the norm of 8% indicated in the pharmacopeial article (Table 1). This confirms the potential of the bentonite clays studied for use in pharmaceutical production.

Table 1 – Qualitative properties of bentonites.

Quality indicators			
	B_1	B_2	B_3
Mass fraction of montmorillonite, %	88.0±0.02	75.5±0.21	83.0±0.5
Mass fraction of moisture, %	7.8±0.02	7.2±0.05	7.3±0.31
Mass fraction of ash content, %	14.04±0.41	15.1±0.14	14.17±0,21
Sorption capacity, mg/g	204.4±1	119.88±5	182.02±6
pH	8.9±0.5	8.1±0.3	7.1±0.4

3.3 XRF analysis

The comparative elemental composition of the bentonite clays is presented in Table 2. The main constituents of the bentonite are silicon and aluminum oxides. According to the obtained results, in sample B_1, SiO_2 was found to be 71.5%, Al_2O_3 – 21.0%, MgO – 3.67%, CaO – 1.98%, Fe_2O_3 – 1.43%, TiO_2 – 0.135%, K_2O – 0.0240%, and As_2O_3 – 0.0004%. In sample B_2, the composition was SiO_2 – 70.1%, Al_2O_3 – 17.2%, Fe_2O_3 – 6.62%, MgO – 2.85%, CaO – 1.78%, TiO_2 – 0.799%, K_2O – 0.0220%, and As_2O_3 – 0.0010%. In sample B_3, the composition was SiO_2 – 69.4%, Al_2O_3 – 16.7%, Fe_2O_3 – 8.58%, MgO – 2.44%, CaO – 0.965%, TiO_2 – 0.95%, K_2O – 0.0297%, and As_2O_3 – 0.013%.

From these values, it can be observed that the content of aluminum and silicon oxides is significantly higher, as these oxides are rock-forming oxides and are part of the main composition of the

bentonite crystal lattice [32], which is confirmed by the results where spectra corresponding to the bonds of these compounds were identified. Furthermore, the reddish-brown coloration in the samples B_2 and B_3 indicates an increased iron content, 6.62% and 8.58%, respectively. Bentonites B_1 has a relatively low iron oxide content (1.43%).

In addition, the concentrations of trace metal oxides were determined as follows: in sample B_1, Cr_2O_3 – 0.0021%, PbO – 0.0003%, and As_2O_3 – 0.0004%; in sample B_2, Cr_2O_3 – 0.175%, PbO – 0.0025%, and As_2O_3 – 0.0010%; in sample B_3, Cr_2O_3 – 0.0199%, PbO – 0.0035%, and As_2O_3 – 0.0013%. Among these, only sample B_1 meets the maximum permissible concentrations specified by the relevant pharmacopeial standards. Therefore, this sample can be considered safe in terms of toxic heavy metal content and is deemed suitable for medical use.

Table 2 – XRF analysis results of bentonites.

Composition	B_1	B_2	B_3	Composition	B_1	B_2	B_3
MgO, %	3.67	2.85	2.44	GeO_2, %	0.0002	-	0.0006
Al_2O_3, %	21.0	17.2	16.7	As_2O_3, %	0.0004	0.0010	0.0013
SiO_2, %	71.5	70.1	69.4	SeO_2, %	0.0002	0.0009	0.0010
P_2O_5, %	-	0.0826	0.0997	Br, %	-	0.0001	0.0002
SO_3, %	0.0387	0.192	0.494	Rb_2O, %	0.0004	0.0005	0.0004
Cl, %	0.0043	0.0046	0.0159	SrO, %	0.358	0.0380	0.0332
K_2O, %	0.0240	0.0220	0.0297	Y_2O_3, %	0.0008	0.0023	0.0026

Continuation of the table

Composition	B_1	B_2	B_3	Composition	B_1	B_2	B_3
CaO, %	1.98	1.78	0.965	Nb_2O_5, %	-	0.0028	0.0034
TiO_2, %	0.135	0.799	0.952	Ag_2O, %	0.0008	-	0.0007
$V2O_5$, %	0.0037	0.0259	0.0343	SnO_2, %	0.0076	0.0079	0.0074
Cr_2O_3, %	0.0021	0.175	0.0199	Sb_2O_3, %	0.0010	0.0011	0.0010
MnO, %	0.105	0.129	0.148	TeO_2, %	0.0039	0.0036	0.0034
Fe_2O_3, %	1.43	6.62	8.58	I, %	-	-	-
Co_2O_3, %	0.0158	0.0294	0.0333	BaO, %	-	0.0572	0.0311
NiO, %	0.0162	0.0112	0.0102	HfO_2, %	0.0095	0.0111	0.0110
CuO, %	0.0040	0.0058	0.0056	Ta_2O_3, %	-	-	(0.0007)
ZnO, %	0.0021	0.0026	0.0028	WO_3, %	-	0.0020	-
PbO, %	0.0003	0.0025	0.0035	U_3O_8, %	0.0006	0.0008	0.0010
Ga_2O_3, %	0.0008	0.0038	0.0048	Ir_2O_3, %	0.0004	0.0007	-

3.4 Average particle size and zeta potencial

One of the important parameters that describe the colloidal properties of bentonite is the average particle size and zeta potential. These parameters allow for the evaluation of the stability of suspensions and the degree of particle aggregation.

The charge of the bentonite samples studied (B_1, B_2, and B_3) was found to be -13.6 mV, -16.6 mV, and -16.2 mV, respectively (Table 3). These negative values are due to uncompensated charges in the crystal lattice resulting from isomorphic substitution, where trivalent cations replace tetravalent silicon atoms in the tetrahedral structure and aluminum in the octahedral sites, leading to a negative zeta potential [33]. The negative zeta potential is significant for drug delivery systems, as it facilitates the transport of positively charged drug molecules, allowing for controlled release and sustained dosing [34, 35].

Table 3 – Average particle size and zeta potencial of bentonite clay.

Sample	B_1	B_2	B_3
Size. nm	1614±50	1534±35	1409±15
Zeta potencial	−13.6±1	−16.6±2	−16.2±2

The negative charge of bentonite clays significantly expands their potential applications. The negatively charged bentonite particles repel each other due to electrostatic repulsion forces. This interaction influences the stability of colloidal suspensions and their rheological properties, preventing aggregation and sedimentation [36].

This property is crucial in fields like drilling fluid formulation, where viscosity control is essential for efficient oil well drilling and the prevention of wellbore collapse [37]. Moreover, negatively charged bentonite clays attract heavy metal ions and organic pollutants to their surface, exhibiting strong adsorptive properties. They can also interact with polyelectrolytes, forming stable complexes [38]. These interactions can enhance the mechanical properties and adhesion of composite materials used in coatings.

Most importantly, the combination of nonionic or negatively charged polymers with positively charged pharmaceutical substances allows for the creation of various composites for the production of extended-release drug formulations [39].

3.5 FTIR analysis

The comparative FTIR spectra of the bentonite samples used in the study are shown in Figure 2. The analysis of these spectra reveals two key regions that provide information about the chemical structure and composition of the bentonite.

The analysis of the spectra demonstrates a clear visual similarity between the samples. The first re-

gion of the spectrum, in the range of 3700–3400 cm^{-1}, is associated with the valence vibrations of hydroxyl groups coordinated with cations in Al-OH [40]. These hydroxyl groups play a critical role in the interlayer interactions and determine properties of the clay, such as swelling and adsorptive characteristics [41]. In this region, all the samples exhibit a sharp absorption band at 3620–3600 cm^{-1} due to the presence of water molecules, which are associated with the clay matrix through hydrogen bonds [42]. Water absorbed in the crystalline lattice also contributes to the hydration and swelling of the clay.

Additionally, all the samples show an absorption band in the range of 1635–1615 cm^{-1}, which corresponds to asymmetric OH-stretching of water and is a structural element of the clay [43].

The second region of the spectrum, in the range of 1150–500 cm^{-1}, contains information about the silicate structure of the clays. In this region, absorption bands characteristic of the Si-O bond vibrations in the tetrahedral layers of the clay are observed [44].

The presence of these bands confirms the presence of silicate layers, which form the main structure of the clays.

In the B$_1$ sample, peaks are present in the areas of 1028–1008 cm^{-1}, corresponding to stretching vibrations and characteristic of layered silicate minerals. These peaks are associated with the threefold degenerate Si-O stretching vibrations [45]. All the samples exhibit a sharp peak in the region of 986–968 cm^{-1}, corresponding to OH-deformation modes of Al-Al-OH or Al-OH-Al [46]. A band observed in the B$_1$ sample at 902–895 cm^{-1} corresponds to the OH-deformation mode of Al-Al-OH or Al-OH-Al [37]. Additionally, the absorption band at 797 cm^{-1} in the B$_2$ sample is characteristic of the symmetric valence stretching vibrations of Si-O-Si in tetrahedral SiO$_4$ units [47].

The XRF analysis results confirm that the main composition of the bentonite clays consists of aluminosilicates (Table 2). The FTIR analysis results align with the XRF findings.
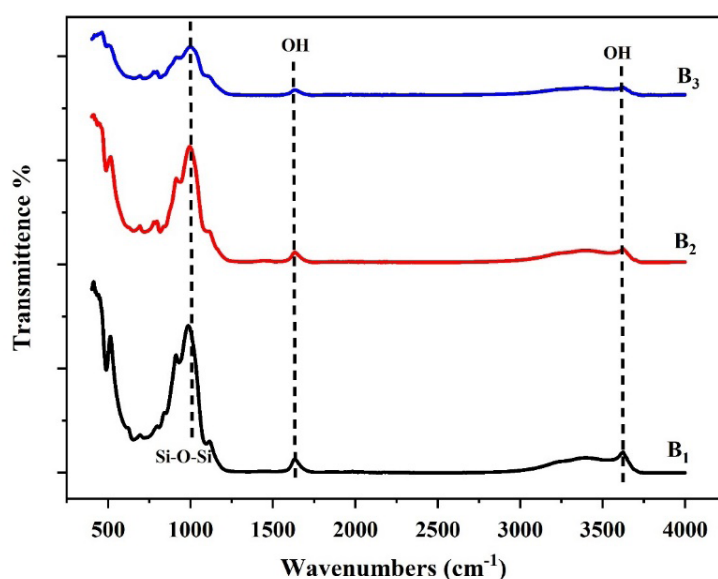

Figure 2 – FTIR Spectra of bentonite samples.

3.6 X-ray diffraction analysis

The crystallinity of mineral clays and the form of metal ions are very important indicators that determine their thermal and mechanical properties. Figure 3 shows the comparative X-ray diffractograms of the samples under investigation.

The analysis of the X-ray diffraction patterns of all the investigated samples revealed a significant similarity in the nature of the diffraction peaks. The

main diffraction reflections, presented in Table 4, are observed at 2θ angles of 19.72° (003), 25.10° (020), 35.85° (200), and 61.91° (130).

The diffractogram of sample B$_1$ revealed phases corresponding to the hexagonal lattice of silicon dioxide, the tetragonal modification of aluminum oxide, the cubic lattice of magnesium oxide, and a complex compound containing Al, Si, and Fe elements, which corresponds to the findings of the IR spectros-

copy. These characteristics indicate that the sample belongs to the mineral phase of montmorillonite. In the B_1 sample, peaks corresponding to montmorillonite dominate, with characteristic 2θ values at $19.72°$ (003), $25.10°$ (020), $35.85°$ (200), and $61.91°$ (130). Quartz peaks, including the main peak at $26.62°$ (101), are weakly expressed.

In samples B_2 and B_3, phases with a hexagonal structure of silicon dioxide, an orthorhombic modification of aluminum oxide, a hexagonal lattice of sodium oxide, and cubic-centered magnesium oxide elements were identified. Signs of monoclinic modification of montmorillonite were also observed. The intensity of the peak corresponding to quartz is more pronounced at 2θ $26.62°$ (101), where the interplanar distance is 3.35 Å.

Montmorillonite demonstrates a broad, diffuse, and asymmetric basal reflection, indicating high dispersion and low crystallinity of this mineral. The main minerals in the composition of bentonite are montmorillonite (M) and quartz (Q). This corresponds to the findings that the main composition of the bentonite samples, as shown in Table 1, consists of montmorillonite.

X-ray diffraction analysis of the bentonite clay samples revealed interplanar spacings characteristic of their mineralogical composition. Reflections observed at $d = 4.91$ Å and $d = 2.50$ Å correspond to the (003)/(020) and (130) planes of montmorillonite, respectively. These peaks are indicative of a well-ordered layered structure and confirm the presence of crystalline montmorillonite in the samples. In particular, the (130) reflection at 2.50 Å is often used as a diagnostic feature of crystallinity and may reflect the distribution of cations within the octahedral sheets. The interlayer spaces oriented perpendicular to these planes typically host exchangeable cations such as Na^+ and Ca^{2+}, which are electrostatically bound and contribute significantly to the clay's sorptive and ion-exchange properties. Additionally, diffraction peaks at $d = 4.28$ Å and 3.35 Å correspond to quartz, indicating the presence of crystalline silica as an accessory phase. The presence of quartz may reduce the overall sorption capacity of the clay by diluting the montmorillonite content and decreasing the specific surface area available for adsorption.

Table 4 – Values of d-spacing, diffraction angles (2θ), and hkl.

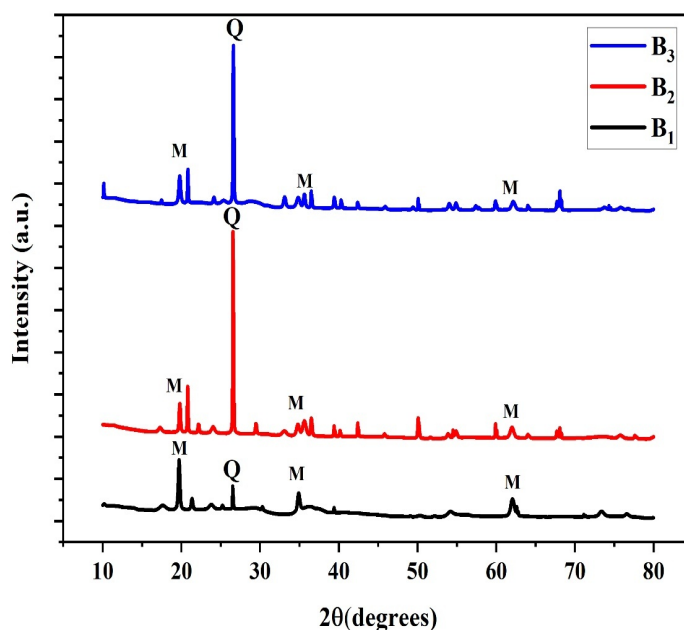| Mineral	$2\theta(°)$	d-spacing (Å)	hkl
Montmorillonite	19.72	4.91	003
	25.10	4.50	020
	35.85	2.55	200
	61.91	2.50	130
Quartz	20.73	4.28	100
	26.62	3.35	101
	39.39	2.29	102
	42.49	2.12	200
	50.14	1.82	112

Figure 3 – B_1; B_2; B_3 XRD Spectra of bentonites.

3.7 SEM analysis

The morphological characteristics of the bentonites studied are shown in Figure 4. The results indicate that the shapes and sizes of the bentonite samples vary. Bentonitic particles are found in rhombohedral, elliptical, and square shapes. The particle sizes range from approximately 170 nm to 70 μm.

Sample B_1 has a scaly structure with an irregular shape. Additionally, the smaller particles have undergone agglomeration, and the size of the agglomerates ranges from 11.53 μm to 34 μm.

Sample B_2 consists of lamellar, plate-like, scaly particles that have formed larger particles due to agglomeration. Their sizes vary up to 203.2 nm. The B_2

sample, compared to the others, shows a plate-like, flaky, and porous structure. The flaky-porous structure is often typical for montmorillonite clays, as identified in previous studies [47].

Sample B_3 consists of solid particles with a rough surface, and their sizes range from 170.1 nm to 297.6 nm. This structure indicates a large surface area of the material, which, in turn, contributes to the high adsorption properties of the bentonites [12].

The high adsorption values of the bentonites for methylene blue, as shown in Table 1, correspond to their surface structure, as identified in the SEM analysis. This suggests that the bentonites studied have high potential for use as adsorbents.
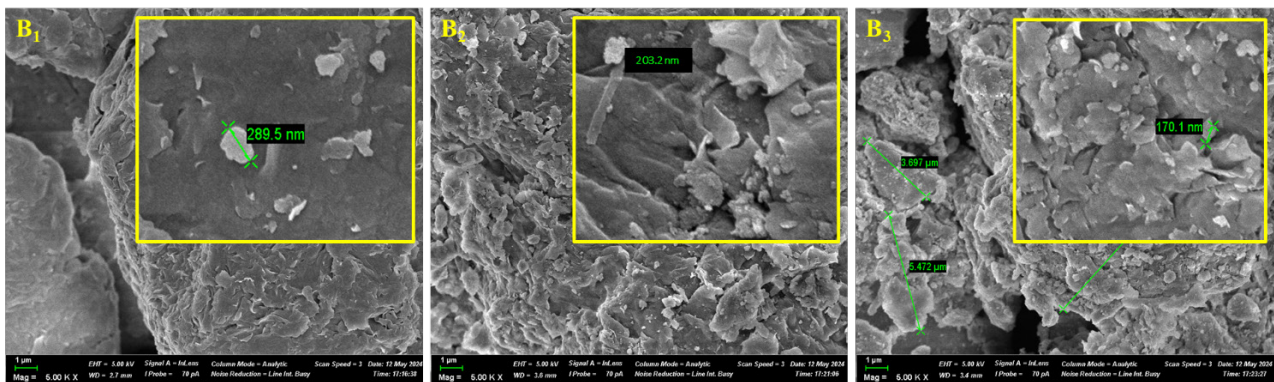
Figure 4 – The morphology of B_1, B_2 and B_3 bentonites.

3.8 BET analysis

The BET method was used to determine the specific surface area, average pore size, and volume of the bentonite samples. The specific surface area determined by the BET method describes the adsorptive capacity of the samples. On the other hand, pore volume and size reflect the diversity of their internal structure. The nitrogen adsorption-desorption isotherms of all the samples are shown in Figure 5 and Table 5.

The specific surface area and pore volume and size of bentonites are among the most important parameters that characterize their adsorptive properties. Based on the research results, it was observed that the isotherms of all the samples correspond to type 4 in the Brunauer classification and exhibit hysteresis loops typical of type 2. This indicates that the sorption process starts in mesopores and ends in micropores [43].

According to the obtained results, the specific surface area of the bentonite clays, depending on

their adsorptive properties, was as follows: for sample B_1, 104.39 m²/g; for B_2, 96.55 m²/g; and for B3, 102.87 m²/g. For B_1, the pore volume and size were 0.05 cm³/g and 0.65 nm, indicating that it is microporous. This also correlates with the highest adsorption capacity for methylene blue, which was found to be 204.4 mg/g for B_1 bentonite (Table 1) [48]. The pore volume of sample B_2 was 0.03 cm³/g with an average pore size of 0.83 nm, while for B_3, these values were 0.04 cm³/g and 1.04 nm, respectively, indicating a higher proportion of mesopores. Based on the specific surface area and pore volume, the optimal parameters were found to belong to sample B_1. According to a study [49], the surface area of the bentonites analyzed ranged from 103 to 130 m²/g, making them highly suitable for use as adsorbents. Consequently, it can be seen that the B_1, B_2, and B_3 samples from this study also have great potential for use in the preparation of biomedical products.

Table 5 – BET Analysis of bentonites.

	B_1	B_2	B_3
S (mL/g)	104.39±5	96.55±3	102.87±5
Pore volume (cm³/g)	0.05±5	0.03±4	0.04±3
Pore size (nm)	0.83±6	0.83±4	1.04±3
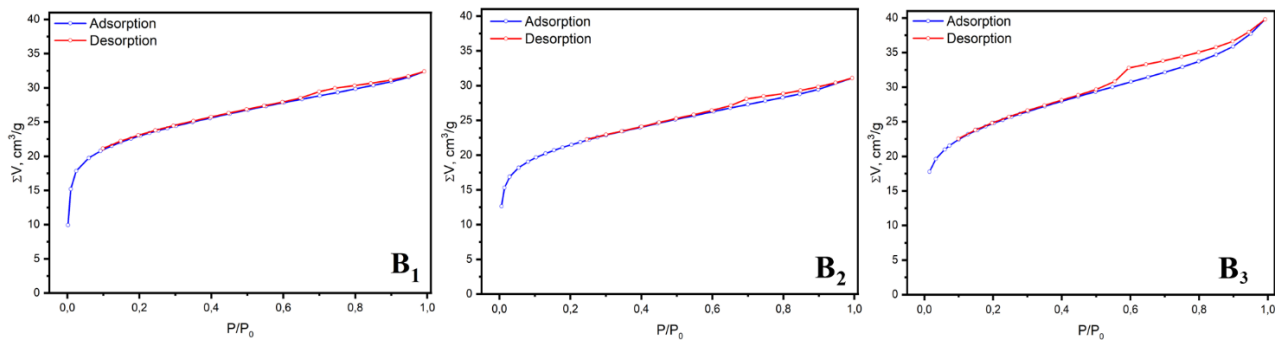
**Figure 5** – Adsorption-desorption isotherms of bentonites.

3.9 Thermogravimetric analysis

The relative TGA (Thermogravimetric Analysis) and DTA (Differential Thermal Analysis) thermograms of the bentonites are shown in Figure 6. The thermodegradation of all samples can be divided into three stages. The B_1 sample differs from the other samples in that it loses 3% of its mass at 360°C, which confirms the higher moisture content of the B_1 bentonite, as indicated in Table 1. Additionally, compared to the other two samples, B_1 loses more mass in each stage. When the temperature rises to 240°C, the weight of B_1 and B_2 samples decreases by 11%, while the B_3 sample decreases by 10%. This change cor-responds to the amount of absorbed moisture on the bentonite surface and in the interlayer spaces [50].

The second change occurs in the temperature range of 250°C-500°C, where the mass of all samples decreases by approximately 2.5%. This may be related to the dehydration of crystallized water that is tightly bound to the montmorillonite mineral in the bentonite [51].

The third change occurs in the temperature range of 500°C-700°C, when the crystalline structure of the mineral in the bentonite begins to undergo destruction. This is accompanied by structural changes and the loss of the original mineralogical structure.
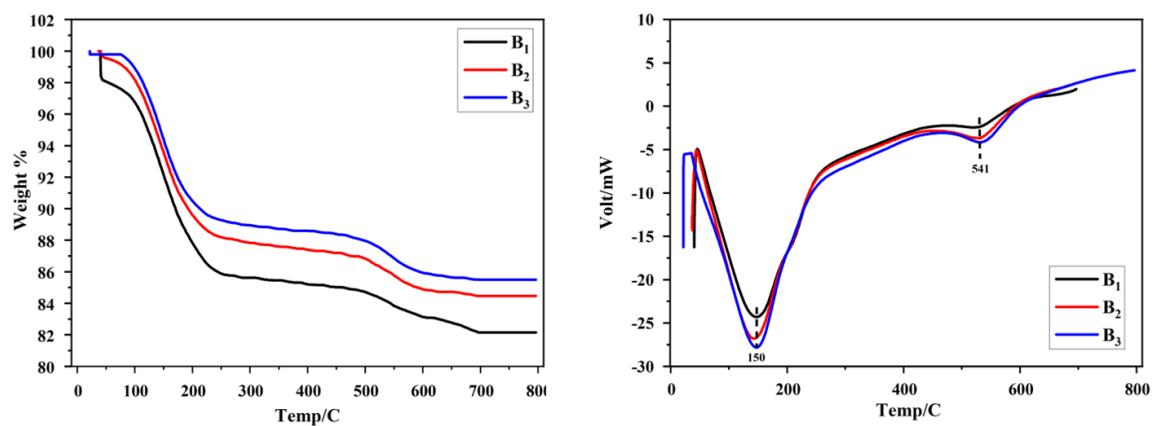
Figure 6 – The TGA-DTA graphs of bentonites.

The analysis of the DTA curves for all three samples (B_1, B_2, B_3) revealed two distinct endothermic effects. The first, intense endothermic peak is observed around 150°C, and is likely associated with the removal of physically adsorbed and interlayer water. This thermal effect is recorded in all samples with slight variations in intensity. The most pronounced effect is observed in the B_1 sample, which may indicate an increased moisture content in the structure of this sample.

The second endothermic peak is recorded around 541°C and is interpreted as the result of dehydration, accompanied by the destruction of the crystalline structure of montmorillonite and the removal of structurally bound hydroxyl groups.

4 Conclusion

The results of the conducted research showed that the physicochemical properties of the obtained bentonite samples were thoroughly studied. The mineralogical composition, determined using X-ray phase analysis and IR spectroscopy methods, revealed that the main mineral component of all samples is aluminosilicates. Additionally, it was shown that the primary mineral constituting bentonite corresponds to montmorillonite. The elemental composition, analyzed using the XRF method, confirmed the presence of elements characteristic of the montmorillonite mineral in the bentonite, including SiO_2, Al_2O_3, Fe_2O_3, MgO, and CaO. According to the obtained results, the montmorillonite content was 88% in the B_1 sample, 75.5% in the B_2 sample, and 83% in the B_3 sample. The methylene blue adsorption capacities were 204.4 mg/g for B_1, 119.88 mg/g for B_2, and 182.02 mg/g for B_3. The pH values of the medium were 8.9 for B_1, 8.1 for B_2, and 7.1 for B_3.

In terms of texture parameters, the specific surface area for the B_1 sample was 104.39 m²/g, the pore volume and size were 0.05 cm³/g and 0.83 nm, respectively, and the zeta potential was -13.6. For the B_2 sample, the surface area was 96.55 m²/g, the pore volume and size were 0.03 cm³/g and 0.83 nm, respectively, and the zeta potential was -16.6. For the B_3 sample, the surface area was 102.87 m²/g, the pore volume and size were 0.04 cm³/g and 1.04 nm, respectively, and the zeta potential was -16.2.

The results demonstrate that bentonite clays possess strong potential for use as adsorbents and as drug carriers in biomedical applications. Additionally, further research is needed to explore their application as a main component in composite materials.

References

1. Bangar, S. P., Ilyas R., Chowdhury A., Navaf M., Sunooj K. V., Siroha A. K. Bentonite clay as a nanofiller for food packaging applications // Trends in Food Science & Technology. – 2023. – Vol. 142. -Is. 15. -P.104-242. https://doi.org/10.1016/j.tifs.2023.104242
2. Thakkar K., Sre M., Ballari S. O., Yadav M. K. D., Bansode M. S. S., Shukla M. S. Application of bentonite clay as a binding material // Design Engineering. – 2021. – Vol. 3.- Is. 9. -P. 9111-9131.
3. Boussak H., Chemani H., Serier A. Characterization of porcelain tableware formulation containing bentonite clay // International Journal of Physical Sciences. – 2015. – Vol. 10. – Is. 1. – P. 38-45. https://doi.org/10.5897/IJPS2014.4218
4. Rychen G., et. al. Safety and efficacy of bentonite as a feed additive for all animal species // EFSA Journal. – 2017. – Vol. 15. – Is. 12. -Art. e05096. https://doi.org/10.2903/j.efsa.2017.5096
5. Todorovic B.Z., Stojiljković S. T., Stojiljković M. S., Pertovic S.M., Takic L.M., Stojiljković D.T. Removal of As³⁺ cations from water by activated charcoal, bentonite and zeolite in a batch system at different pH*1 // Journal of Elementology. – 2017. – Vol. 22.-Is. 2. – P.713-723. https://doi.org/10.5601/jelem.2016.21.3.1247
6. Sarruf F. D., Contreras V. J. P., Martinez R. M., Velasco M. V. R., Baby A. R. The scenario of clays and clay minerals use in cosmetics/dermocosmetics // Cosmetics. – 2024. – Vol. 11. – Is. 7. https://doi.org/10.3390/cosmetics11010007
7. Khamroyev J., Akmalaiuly K., Fayzullayev N. Mechanical activation of navbahorsk bentonite and its textural and adsorption characteristics // News of the National Academy of Sciences of the Republic of Kazakhstan, Series of Geology and Technical Sciences. – 2022. – Vol. 1.-Is. 451. – P.167-174. https://doi.org/10.32014/2022.2518-170X.154
8. Starý J., Jirasek J., Pticen F., Zahradnik J., Sivek M. Review of production, reserves, and processing of clays (including bentonite) in the Czech Republic // Applied Clay Science. – 2021. – Vol. 205. https://doi.org/10.1016/j.clay.2021.106049
9. Belousov P., Krupskaya V. Bentonitovye gliny Rossii i stran blizhnego zarubezh'ya // Georesursy. – 2019. – Vol. 21. – P.79-90. (In Russian)
10. Orudzheva D.S., Obukhov A.N. Zaysan Depression. Petroleum Geology // A Digest of Russian Literature on Petroleum Geology. – 1991. – Vol. 25.-Is. 7/8. – P.1278-280.

11. Sapargaliyev Y., Sapargaliyeva L., Dolgopolova A., Azelkhanov A., Suyekpayev E. Applications Of montmorillonite from the Tagan Deposit, Kazakhstan // Global Advanced Research Journal of Engineering, Technology and Innovation. – 2015. – Vol. 4. -P. 041-050.

12. Pan T., Chen J., He M.Y., Ding C., Ma Y., Liang H., Zhang T., Du X. Characterization and resource potential of Li in the clay minerals of Mahai Salt Lake in the Qaidam Basin, China // Sustainability. – 2023. – Vol. 15. -Art. 14067. https://doi.org/10.3390/su151914067

13. Krupskaya V., Zakusin S., Tyupina E., Dorzhieva O., Chernov M., Bychkova Y.V. Transformation of the montmorillonite structure and its adsorption properties due to the thermochemical treatment // Geochemistry. – 2019. – Vol. 64. – P.300-319. (In Russian).

14. Sapargaliyev E.M. Genesis features of the Tagansky field of bentonites in the Zaysan depression // Messenger of Ore Deposits. – 2007. – Vol. 3. – P.40-46.

15. Izosimova Y., Gurova I., Tolpeshta I., Karpukhin M., Zakusin S., Zakusina O., Samburskiy A., Krupskaya V. Adsorption of Cs (I) and Sr (II) on bentonites with different compositions at different pH // Minerals. – 2022. – Vol. 12. – Art. 862. https://doi.org/10.3390/min12070862

16. Suiekpayev Y., Sapargaliyev Y., Dolgopolova A., Seltmann R., Raspopov A., Bekenova G. Predictive estimate of Ti-Zr placer deposits in mesozoic and cenozoic sediments at nw margins of the Zaysan basin, East Kazakhstan // NEWS of National Academy of Sciences of the Republic of Kazakhstan. Series of geology and technical sciences. – 2019. – Vol. 2.-Is. 434. – P.6-14. https://doi.org/10.32014/2019.2518-170X.32

17. Muzdybayeva S., Musabekov K., Muzdybayev N., Askarova G., Nurbaeva N., Taybaeva P. Effectiveness of use of nano-structure minerals "Bentonite of Taganskiy Deposit for waste water clearing in metallurgy industry // European Journal of Sustainable Development. – 2014. – Vol. 3. – P.195-195. https://doi.org/10.14207/ejsd.2014.v3n3p195

18. Federacii G. F. R. State Pharmacopoeia of the Russian Federation. Part 1. – 2010.

19. Chernyakova R., Zh J.U., Sh S.G., Kaiynbayeva R., Kozhabekova N. Sorption of manganese (II) and vanadium (IV) cations by Tagan bentonite in an aqueous medium // Izvestiya NAN RK. Series of Chemistry and Technology. – 2021. – Vol. 3. – P. 68–74. https://doi.org/10.32014/2021.2518-1491.69

20. Rozhkova O.V., Muzdybaeva Sh.A., Bukeeva A.B., Kudajbergenova S.Zh., Rozhkov V.I., Ermekov M.T., Nurtaj Zh.T. Efficiency of using bentonite clay for treatment of mine water in the mining industry // Vestnik KazUTB. – 2024. – Vol. 2. – P. 460.

21. Sapargaliyev Y.M., S.A., Samatov I.B. Structural characteristics of the medicinal preparations Tagansorbent // Geology of Kazakhstan. – 1997. – Vol. 5. – P. 87–97.

22. Liu R., Mei X., Zhang J., Zhao D.-b. Characteristics of clay minerals in sediments of Hemudu area, Zhejiang, China in Holocene and their environmental significance // China Geology. – 2019. – Vol. 2. – P. 8–15. https://doi.org/10.31035/cg2018069

23. Daumova G.K., Abdulina S.A., Kokayeva G.A., Adilkanova M.A. Experimental studies on wastewater sorption treatment with subsequent disposal of used sorbents // Chemical Engineering Transactions. – 2018. – Vol. 70. – P. 2125–2130. https://doi.org/10.3303/CET1870355

24. Belousov P.E., Belousov P.B., Zakusin S.V., Krupskaya V.V. Quantitative methods for determining montmorillonite content in bentonite clays // Georesursy. – 2020. – Vol. 22. – P. 38–47. https://doi.org/10.18599/grs.2020.3.38-47

25. Kumari N., Mohan C. Basics of clay minerals and their characteristic properties // Clay and Clay Minerals. – 2021. – Vol. 24. – P.1–29. https://doi.org/0.5772/intechopen.97672

26. Rautureau M., Figueiredo Gomes C., Liewig N., Katouzian-Safadi M. Clays and health: Properties and therapeutic uses. Springer Nature. – 2017, 217p. https://doi.org/10.1007/978-3-319-42884-0

27. Nadziakiewicz M., Kehoe S., Micek P. Physico-chemical properties of clay minerals and their use as a health promoting feed additive // Animals. – 2019. – Vol. 9. –.Is. 10. – P.714. https://doi.org/10.3390/ani9100714

28. Devapriya A., Thyagaraj T. Evaluation of red soil–bentonite mixtures for compacted clay liners // Journal of Rock Mechanics and Geotechnical Engineering. – 2024. – Vol. 16. – P. 697–710. https://doi.org/10.1016/j.jrmge.2023.04.006

29. Maged A., Kharbish S., Ismael I.S., Bhatnagar A. Characterization of activated bentonite clay mineral and the mechanisms underlying its sorption for ciprofloxacin from aqueous solution // Environmental Science and Pollution Research. – 2020. – Vol. 27. – P. 32980–32997. https://doi.org/10.1007/s11356-020-09267-1

30. Martsouka F., Papagiannopoulos K., Hatziantoniou S., Barlog M., Lagiopoulos G., Tatoulis T., Tekerlekopoulou A.G., Lampropoulou P., Papoulis D. The antimicrobial properties of modified pharmaceutical bentonite with zinc and copper // Pharmaceutics. – 2021. – Vol. 13. – Art.1190. https://doi.org/10.3390/pharmaceutics13081190

31. Kabdrakhmanova S., Joshy K., Sathian A., Aryp K., Akatan K., Shaimardan E., Beisebekov M., Gulden T., Kabdrakhmanova A., Maussumbayeva A. Anti-bacterial activity of Kalzhat clay functionalized with Ag and Cu nanoparticles // Engineered Science. – 2023. – Vol. 26. – Art. 972. https://dx.doi.org/10.30919/es972

32. Widi R., Trisulo D., Budhyantoro A., Chrisnasari R. Preparation of immobilized glucose oxidase wafer enzyme on calcium-bentonite modified by surfactant // IOP Conference Series: Materials Science and Engineering. – 2017. – Vol. 223. – Article 012050. https://doi.org/10.1088/1757-899X/223/1/012050

33. Selvasudha N., Dhanalekshmi U.-M., Krishnaraj S., et al. Multifunctional clay in pharmaceuticals // Clay Science and Technology. IntechOpen. – 2021. Available at: http://dx.doi.org/10.5772/intechopen.92408

34. Srasra E., Bekri-Abbes I. Bentonite clays for therapeutic purposes and biomaterial design // Current Pharmaceutical Design. – 2020. – Vol. 26, -No. 6. – P. 642–649. https://doi.org/10.2174/1381612826662200203144034

35. Akichoh H., Berraaouan D., Salhi S., Abdesselam T., El Miz M. Chemical and physical characterization of Moroccan bentonite taken from Nador (North of Morocco) // American Journal of Chemistry. – 2017. – Vol. 7, No. 4. – P. 105–112. https://doi.org/10.5923/j.chemistry.20170704.01

36. Elgamouz A., Tijani N., Shehadi I., Hasan K., Qawam M. Characterization of the firing behaviour of an illite–kaolinite clay mineral and its potential use as membrane support // Heliyon. – 2019. – Vol. 5. – Article e02281. https://doi.org/10.1016/j.heliyon.2019.e02281

37. Moosavi M. Bentonite clay as a natural remedy: A brief review // Iranian Journal of Public Health. – 2017. – Vol. 46, No. 9. – P. 1176–1183.

38. De Segonzac G.D. The transformation of clay minerals during diagenesis and low-grade metamorphism: a review // Sedimentology. – 1970. – Vol. 15. – P. 281–346.

39. Theng B. Negatively charged polymers (polyanions) // Developments in Clay Science. – 2012. – Vol. 4. – P. 111–127.

40. Kabdrakhmanova S., Aryp K., Shaimardan E., Kanat E., Selenova B., Nurgamit K., Kerimkulova A., Amitova A., Maussumbayeva A. Acid modification of clays from the Kalzhat, Orta Tentek deposits and study of their physical-chemical properties // Materials Today: Proceedings. – 2023. https://doi.org/10.1016/j.matpr.2023.04.427.

41. Ravindra R.T., Kaneko S., Endo T., Lakshmi R.S. Spectroscopic characterization of bentonite // Journal of Lasers, Optics & Photonics. – 2017. – Vol. 4.

42. Hayati-Ashtiani M. Characterization of nano-porous bentonite (montmorillonite) particles using FTIR and BET-BJH analyses // Particle & Particle Systems Characterization. – 2011. – Vol. 28. – P. 71–76.

43. Widjaya R., Juwono A., Rinaldi N. Bentonite modification with pillarization method using metal stannum // AIP Conference Proceedings. – 2017. – Vol. 1904. – Article 020010. https://doi.org/10.1063/1.5011867

44. Mekhamer W. Stability changes of Saudi bentonite suspension due to mechanical grinding // Journal of Saudi Chemical Society. – 2011. – Vol. 15. – P. 361–366.

45. González J.A., Ruiz M. del C. Bleaching of kaolins and clays by chlorination of iron and titanium // Applied Clay Science. – 2006. – Vol. 33, Iss. 3–4. – P. 219–229. https://doi.org/10.1016/j.clay.2006.05.001

46. Shafiq M., Alazba A.A., Amin M.T. Functionalized bentonite clay composite with NiAl-layered double hydroxide for the effective removal of Cd(II) from contaminated water // Sustainability. – 2022. – Vol. 14, No. 22. – P. 15462. https://doi.org/10.3390/su142215462

47. Tabak A., Yilmaz N., Eren E., Caglar B., Afsin B., Sarihan A. Structural analysis of naproxen-intercalated bentonite (Unye) // Chemical Engineering Journal. – 2011. – Vol. 174. – P. 281–288. https://doi.org/10.1016/j.cej.2011.09.027

48. Banik N., Jahan S., Mostofa S., Kabir H., Sharmin N., Rahman M., Ahmed S. Synthesis and characterization of organoclay modified with cetylpyridinium chloride // Bangladesh Journal of Scientific and Industrial Research. – 2015. – Vol. 50. – Iss. 1. – P. 65–70. https://doi.org/10.3329/bjsir.v50i1.23812

49. Ouhaddouch H., Cheikh A., Idrissi M.O.B., Draoui M., Bouatia M. FT-IR Spectroscopy applied for identification of a mineral drug substance in drug products: Application to bentonite // Journal of Spectroscopy. – 2019. – Vol. 2019. – Art. 2960845. https://doi.org/10.1155/2019/2960845

50. Viseras C., Carazo E., Borrego-Sánchez A., García-Villén F., Sánchez-Espejo R., Cerezo P., Aguzzi C. Clay minerals in skin drug delivery // Clays and Clay Minerals. – 2019. – Vol. 67. – P. 59–71. https://doi.org/10.1007/s42860-018-0003-7

51. Rostami-Vartooni A., Alizadeh M., Bagherzadeh M. Green synthesis, characterization and catalytic activity of natural bentonite-supported copper nanoparticles for the solvent-free synthesis of 1-substituted 1H-1,2,3,4-tetrazoles and reduction of 4-nitrophenol // Beilstein Journal of Nanotechnology. – 2015. – Vol. 6. – P. 2300–2309. https://doi.org/10.3762/bjnano.6.236

Information about authors:

Bolatkan Dana Kairatkyzy is a 2nd year PhD student at the S. Amanzholov East Kazakhstan University, (Oskemen, Kazakhstan), email: chilibayeva@mail.ru

Kerimkulova Aigul Zhadraevna, PhD is an Associate professor at Satbayev University (Almaty, Kazakhstan), e-mail: kerimkulova07@ mail.ru

Beisebekov Madiyar, PhD is a Researcher at the Scientific Center of Composite Materials (Almaty, Kazakhstan), e-mail: make1987@ mail.ru

Akatan Kydyrmolla, PhD is a Head of the National Scientific Laboratory for Collective Use, S.Amanzholov East Kazakhstan University (Almaty, Kazakhstan) e-mail: ahnur.hj@mail.ru

Kantai Nurgamit, PhD is a Researcher at the National Scientific Laboratory for Collective Use, S.Amanzholov East Kazakhstan University (Oskemen, Kazakhstan) e-mail: nurgan85@mail.ru

Shaimardan Yesbol, PhD is a Senior researcher at Scientific Center of Composite Materials (Almaty, Kazakhstan) e-mail: esbol_ shay@mail.ru

Kukhareva Anastassiya Dmitrievna is a 2nd year master student at Satpaev university (Almaty, Kazakhstan) e-mail: kad1311@mail.ru

Bukunova Al'mira, candidate of chemical sciences is an Associate professor at School of Earth Sciences, D. Serikbayev East Kazakh stan technical university (Oskemen, Kazakhstan) e-mail: ABukunova@edu.ektu.kz

Kabdrakhmanova Sana Kanatbekovna, candidate of technical sciences is an Associate professor at the Department of Chemical and Biochemical Engineering, Satbayev University (Almaty, Kazakhstan) e-mail: sanaly33@mail.ru

Study of elastic scattering of protons
on ^{7}Li in the energy range of 3–5.3 MeV

Sh.M. Kazhykenov[1*] (ID), D.M. Janseitov[2] (ID) and G.U. Yerbolatova[1] (ID)

^{1}D. Serikbayev East-Kazakhstan Technical University, Oskemen, Kazakhstan
^{2}Institute of Nuclear Physics of the Republic of Kazakhstan, Almaty, Kazakhstan
*e-mail: nuclearshalkar@gmail.com

This study explores the elastic scattering of protons on the ^{7}Li nucleus within the framework of the optical model using the Full-Wave Method (FWM). The approach is based on a high-precision numerical solution of the radial Schrödinger equation, incorporating a microscopic folding potential derived from the M3Y nucleon–nucleon interaction and the nuclear matter density distribution. An imaginary component of the optical potential, parameterized in Woods–Saxon form, is included to simulate absorption effects due to open inelastic channels. Numerical simulations are implemented in Python using a 6 to 8 order Runge–Kutta method to ensure computational accuracy and stability. The resulting phase shifts, scattering amplitudes, and differential cross sections are calculated for proton energies in the range of 3.0 to 5.5 MeV and compared with experimental data measured at the Van de Graaff accelerator. The analysis reveals systematic overestimations of the differential cross section at both forward and backward angles and emphasizes the necessity of including the imaginary part of the potential and increasing the number of partial waves to improve agreement with observations.

The results demonstrate that the Full-Wave Method provides a physically consistent description of the elastic scattering process and offers a solid foundation for further theoretical refinement and experimental validation in light nuclear systems.

Key words: light nuclei, elastic scattering, microscopic potential, optical model, FWM, Runge-Kutta method.

PACS number(s): 25.40.Cm, 24.10.-i, 27.20.+n

1 Introduction

The elastic scattering of protons on the ^{7}Li nucleus represents a key process for investigating the structure of light nuclei and understanding the underlying mechanisms of nuclear interaction. Light nuclei such as ^{7}Li serve as ideal systems for testing nuclear models due to their relatively simple structure and the availability of precise experimental data. In this context, studying scattering processes involving protons provides valuable information on the spatial distribution of nuclear matter, phase shifts, and interaction potentials [1, 2].

A critical aspect of nuclear reaction analysis lies in the application of microscopic methods that connect observable scattering parameters to the fundamental nucleon–nucleon interaction. One such approach is the Full-Wave Method (FWM), which is based on the numerical solution of the radial Schrödinger equation for the proton–nucleus system.

This method employs a microscopic folding potential, such as the M3Y interaction [3], derived from realistic effective nucleon–nucleon forces and nuclear density distributions [4, 5]. The use of such models enables detailed calculation of phase shifts, scattering amplitudes, and differential cross sections [6, 7].

The motivation for this study arises from the need to produce more accurate theoretical predictions that can be reliably compared with experimental data. In particular, the ^{7}Li nucleus has been extensively studied [8, 9], but several aspects of its structure and reaction dynamics remain insufficiently understood. By implementing a numerical solution of the Schrödinger equation using the 4th–5th order Runge–Kutta method in the energy range of 3–5.3 MeV, this study aims to obtain improved theoretical cross sections. Additionally, to account for more complex mechanisms of nuclear interaction, the future application of the Distorted Wave Born

Approximation (DWBA) is proposed [10, 11]. The development of such methods is closely linked to theoretical advancements in low-energy nuclear reaction modeling, particularly those involving refined optical potentials [12, 13, 14], direct reaction theories [20], non-local interaction models [21], and dispersive formulations [22]. Optimization techniques, such as χ^2-minimization implemented using Python solvers like *solve_ivp*, are also considered [23].

The main objective of this study is to refine the parameters of the nuclear optical potential and to investigate the structure of the ^{7}Li nucleus by comparing theoretical predictions with experimental results. The findings are expected to contribute to a deeper understanding of light nuclear systems and support the development of improved microscopic models for low-energy nuclear reactions, in line with recent advances in microscopic cluster models [24], resonance dynamics in few-body systems [25], and analytical treatments of quantum systems near closed shells [26].

2 Theoretical method

The study of nuclear reactions requires the use of various methods to describe the interactions between particles and the nucleus. The following methods were used in this study:

2.1 Full-Wave Method.
The full wave method uses the full Schrödinger equation for nuclear interactions and is applied to multi-channel reactions. The basic equation is:

$$\left[\frac{2\mu}{\hbar^2}(\nabla^2 + k^2) - V(r)\right]\Psi(r) = 0 \qquad (1)$$

2.3 Potentials used in the full wave method (FWM)
2.3.1 Microscopic potential M3Y.
The microscopic folding potential M3Y is an effective nucleon-nucleon interaction derived from the matrix elements of the Goldstone method and developed to describe nuclear reactions including elastic scattering, nuclear fusion, and dissociation of cluster structures.

1. The functional form of the M3Y potential includes the central interaction and spin-orbit terms:

$$V_{M3Y}(r) = t_M e^{-\mu r} + t_E e^{-\lambda r} \qquad (2)$$

where: t_M, t_E – interaction amplitude parameters (MeV), μ и λ – interaction ranges (fm), $t_M = 7999$ MeV $\mu = 4.0$ fm^{-1} represent the medium-range attraction, $t_E = -2134$ MeV , $\lambda = 2.5$ fm^{-1} correspond to the short-range repulsion [3].

2. Effective folding potential:

$$V_{\text{fold}}(r) =$$
$$= \int \rho_A(r')\rho_B(r'')V_{M3Y}(|r - r'|)\, d^{3r'} d^{3r''} \qquad (3)$$

where: ρ_A и ρ_B – densities of interacting nuclei, values taken from [4]. $V_{M3Y}(|\boldsymbol{r} - \boldsymbol{r}'|)$ – basic NN-interaction. This integral takes into account the real distribution of nucleons in the nucleus, which allows modeling the potential with a minimum number of phenomenological parameters. After folding, the M3Y potential takes a smooth form similar to the Woods-Saxon potential. The paper [3] provides typical parameters for light nuclei that we used:

$$V(r) = \frac{V_0}{1 + \exp\left(\frac{r - R_V}{a_V}\right)} \qquad (4)$$

2.3.2 Optical potential and its relationship with microscopic potential
The microscopic potential gives us only the real part of the interaction, but to describe the real data it is necessary to take into account the inelastic processes that are responsible for the absorption of the wave (transitions to excited states, reactions with nuclear breakup, etc.).

Therefore, we wrote the optical potential as:

$$V(r) = V_{M3Y}(r) + iW(r) \qquad (5)$$

where the real part V_{M3Y}(r) was taken from the work [3]:

Depth of potential: V_0= 55 MeV, potential well radius: $R_V = 1.25A^{1/3}$ fm where A=7 (mass number of the nucleus ^{7}Li), Substituting this into the formula gives: $R_V \approx 2.0$ fm, diffusion parameter: $a_V = 0.65$ fm, and the values for the imaginary part W(r) in the form of a Woods-Saxon potential, which is parameterized by the absorption effects, taken from

the work [2]. Thus, our final form of the optical potential is:

$$V(r) = V_{\text{M3Y}}(r) + i\,\frac{W_0}{1 + \exp\left(\dfrac{r - R_W}{a_W}\right)} \qquad (6)$$

where: $W_0 = -5$ MeV (absorption intensity), $R_W = 2.0$ fm (radius), $W = 0.5$ fm (diffuseness).

Scattering amplitude in FWM

$$f(\theta) = \sum_{l=0}^{\infty} (2l + 1) e^{i\delta_l} \sin \delta_l \; P_l(\cos\theta) \qquad (7)$$

where: $f(\theta)$ is the complex scattering amplitude as a function of the scattering angle θ, δ_l are the phase shifts for each partial wave l, calculated from the numerical solution of the radial Schrödinger equation with the optical potential $V(r)$, $P_l(\cos\theta)$ are the Legendre polynomials, $(2l +1)$ is the statistical weight of the l-th partial wave. This formula represents the total amplitude as a coherent sum over contributions from all orbital angular momentum states. Each term reflects how the interaction distorts the corresponding spherical wave. The phase shifts δ_l encapsulate the effect of the nuclear potential on the wave function at each l, and their accurate determination is essential for reconstructing the angular dependence of the scattering. Once the amplitude $f(\theta)$ is known, the differential cross section is obtained via: $\frac{d\sigma}{d\Omega} = |f(\theta)|^2$.

2.3 Connection between theory and experimental data

Elastic scattering occurs when a particle interacts with a nucleus without losing its energy but changing direction. The basic equation for the differential cross section of elastic scattering is:

$$\frac{d\sigma}{d\Omega} = |f(\theta)|^2 \qquad (8)$$

where $f(\theta)$ – scattering amplitude, and θ – angle of scattering.

$$f(\theta) = \frac{1}{k}\sum_{l=0}^{\infty} (2l + 1) e^{i\delta_l} \sin \delta_l \; P_l(\cos\theta) \qquad (9)$$

where δ_l – phase shifts of the proton wave function.

2.4 Experimental data

The experimental data on elastic proton scattering on the ⁷Li nucleus were obtained from Fasoli et al. [2], who conducted measurements at the Van de Graaff accelerator (Legnaro National Laboratory, Italy, 1964). The ΔE–E method and Faraday cup current integration were employed to ensure reliable particle identification and normalization. Differential cross sections were measured in the angular range 70^0-180^0 (lab system) and are used in this study as a reference for validating the theoretical results.

Table 1 – Dependence of the differential cross section of protons on the ⁷Li nucleus on the proton energy. Data taken from [2].

Proton energy (MeV)	3.0023	3.2011	3.4065	3.5979	3.8033	4.2074	4.4138	4.6146	4.8020	4.9893	5.1964	5.3960
Differential cross-section (barn)	0.93525	0.95693	1.0182	1.0977	1.1589	1.2510	1.2027	1.0235	0.81085	0.61340	0.49207	0.44071

3. Results and discussion

Theoretical calculations of the differential cross section, scattering amplitudes, and phase shifts were performed for the nuclear reaction ⁷Li(p,p)⁷Li. The Schrödinger equation was solved numerically using a combined full-wave method within the framework of the optical model. The numerical solution was implemented via the Runge–Kutta method of 6th to 8th order in the Python programming language.

Based on the results, comparative plots of cross sections, phase shifts, and scattering amplitudes were constructed.

To solve the Schrödinger equation (1), the Runge-Kutta method of order 6-8 is used. The main steps of the algorithm are:

1. The boundary conditions for the wave function $\Psi(r)$ are specified. 2. The coordinate space r is divided into a grid. 3. Numerical integration is used by the Runge-Kutta method. 4. The system of

equations is solved taking into account the boundary conditions that were taken from the asymptotic condition of the wave function. 5. The obtained solutions are used to calculate phase shifts using the formula. 6. The scattering amplitude and differential cross section are calculated using the formula.

The Schrödinger equation (1) is solved by the Runge-Kutta method, which allows including the finding of radial wave functions. Different interaction potentials are used: microscopic M3Y

potential (2) from [3,6], Folding potential (3), phenomenological optical potential (4) based on systematics [1,5]. Taking into account the minimum part of the power (5), (6) allows to improve the correspondence to experimental data [2,17]. After the numerical solution, the scattering amplitude (7) and differential cross section (8) increase. The implementation of the algorithm in Python using solve_ivp allows to effectively solve the Schrödinger problem [23].
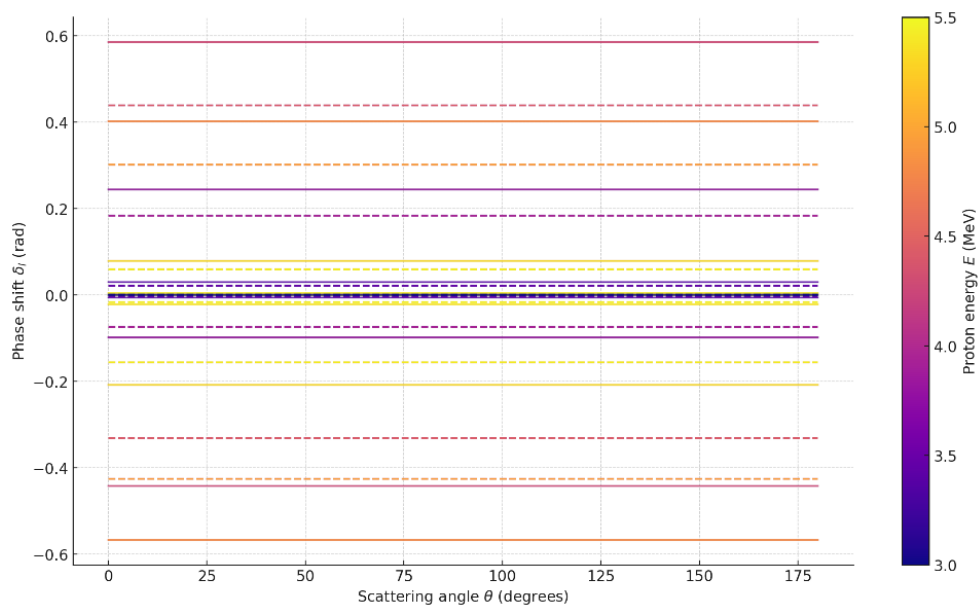
Figure 1 – Phase shifts δ*l* in the full-wave method with the M3Y potential depending
on the proton scattering angle. Solid line – without the imaginary part of the optical potential.
Dashed line – with the imaginary part of the optical potential included.

Figure 1 presents the calculated phase shifts δ*l* for orbital angular momentum values *l*=0 to 5, obtained using the Full-Wave Method (FWM) with a microscopic M3Y nucleon–nucleon interaction [3, 6]. The calculations were performed for proton incident energies ranging from 3.0 to 5.5 MeV.

Each curve corresponds to a fixed energy and angular momentum value. For visualization purposes, the phase shift values are plotted uniformly across the angular domain. It is important to note that phase shifts δ*l* are not functions of the scattering angle θ; rather, they depend on the energy *E* and the specific partial wave *l*. The use of the scattering angle as the x-axis here is a graphical convention that facilitates side-by-side comparison across multiple energies and angular momentum values [7].

Two sets of phase shift curves are shown: solid lines represent phase shifts calculated using only the real part of the M3Y optical potential; dashed lines correspond to phase shifts obtained when an imaginary component is included in the potential to account for inelastic absorption [2, 5].

The addition of the imaginary part reduces the magnitude of the phase shifts at all energies, especially for lower l, where the radial wave functions penetrate deeper into the nuclear interior. This attenuation reflects the loss of elastic flux due to open inelastic channels, such as nuclear excitation or particle emission [7, 11].

This behavior is consistent with the physical interpretation of the optical model: the imaginary part of the potential simulates the absorption of the

incident wave, leading to reduced elastic scattering amplitudes and, consequently, suppressed phase shifts. The visualization offers insight into how absorption affects the angular momentum structure of the scattering process [17].

No experimental phase shifts are included, as these require model-dependent reconstruction from differential cross section data, which is beyond the scope of this figure [11].

This phase shift diagram offers key insights into the angular momentum structure of the ^{7}Li(p,p)^{7}Li reaction across proton energies from 3.0 to 5.5 MeV. It reveals how partial waves evolve with energy,

showing that significant contributions come from $l=0$ to 4, while higher-order shifts remain negligible. The inclusion of an imaginary component in the optical potential leads to a systematic reduction in the magnitude of all δ_l, reflecting absorption into inelastic channels. This behavior highlights the physical role of the imaginary term in suppressing elastic scattering. Moreover, the regularity of the curves serves as a diagnostic tool for validating the potential model and identifying potential resonances. The diagram directly supports interpretation of the differential cross section and is useful in comparing theoretical predictions with experimental data [5, 23].
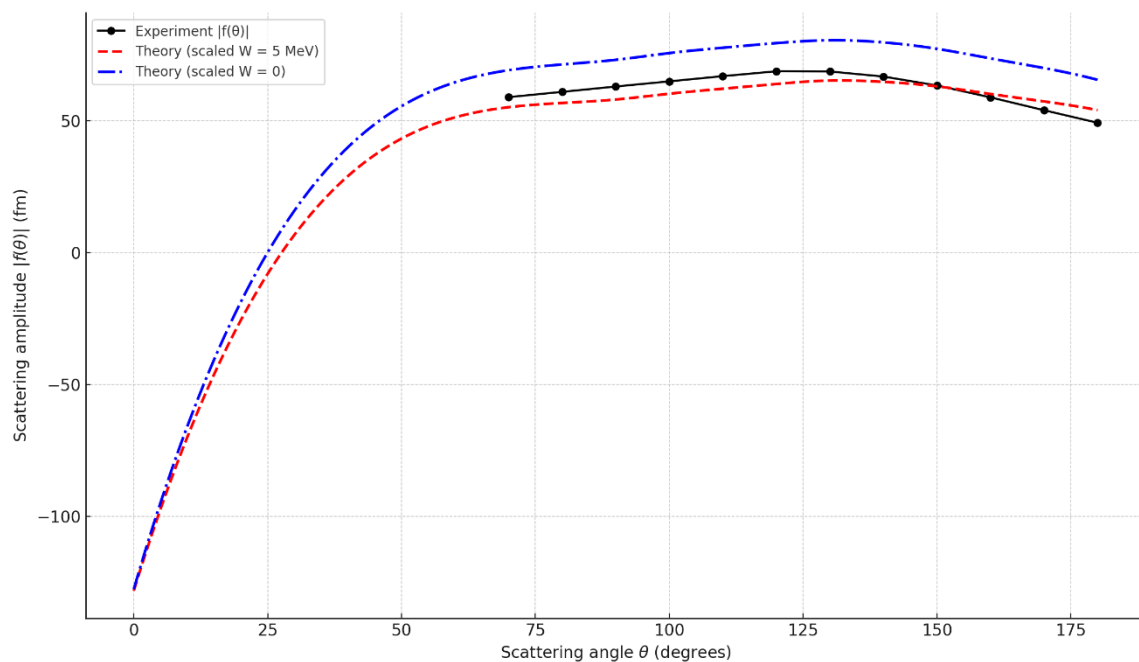
Figure 2 – Angular dependence of the elastic scattering amplitude |f(θ)|(fm) calculated using the Full-Wave Method (FWM) with the microscopic M3Y folding potential. The blue dash-dotted line corresponds to the theoretical amplitude computed using only the real part of the optical potential. The red dashed line includes an imaginary component W=5 MeV. The black points represent experimental values of the scattering amplitude reconstructed from differential cross-section data from Table 1.

Figure 2 illustrates the angular dependence of the elastic proton scattering amplitude |f(θ)|, calculated using the Full-Wave Method (FWM) with a microscopic M3Y folding potential [3, 6]. The graph shows results for a fixed proton energy of 4.41 MeV. Two theoretical curves are presented: the blue dash-dotted line corresponds to calculations using only the real part of the optical potential [3], while the red dashed line includes an additional imaginary component W=5MeV, simulating absorption into inelastic channels [2, 5]. The black points represent

experimental values of the scattering amplitude, reconstructed from differential cross section data [2].

The amplitude demonstrates clear angular dependence, with a maximum around θ≈130⁰, followed by a gradual decline toward backward angles. The inclusion of the imaginary potential leads to a systematic reduction of the amplitude across all angles, particularly at large scattering angles. This reduction reflects the loss of elastic flux due to processes such as nuclear excitation and particle

emission [7, 17]. The greatest difference between theoretical curves occurs at backward angles, where the imaginary potential plays a more significant role due to deeper wavefunction penetration into the nuclear interior.

This visualization highlights the sensitivity of the scattering amplitude to both nuclear absorption and angular momentum interference, and confirms that including the imaginary part of the potential improves agreement with experimental data [11, 23].
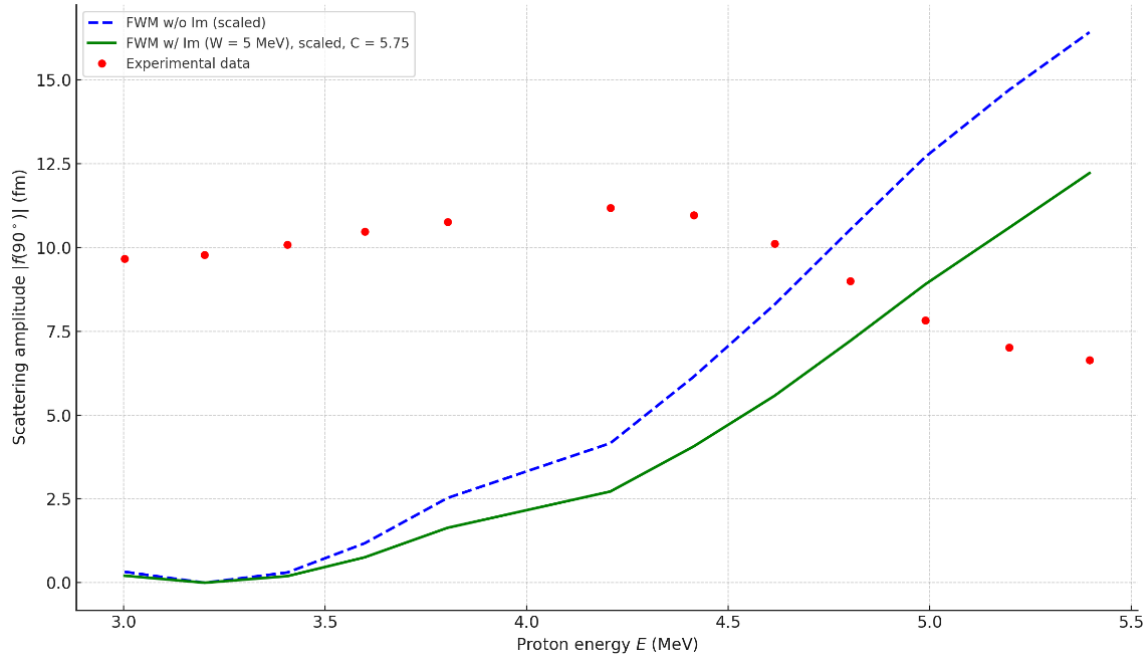

Figure 3 – Scattering amplitude |f(θ=90∘)| as a function of proton energy. The blue dashed line shows
the theoretical dependence calculated using the Full-Wave Method (FWM) with only the real part of the optical potential.
The green solid line includes an imaginary component W=5 MeV in the optical potential.
The red dots represent experimental data, extracted from differential cross-section measurements at θ=90[0], taken from Table 1.

This figure presents the elastic scattering amplitude |f(θ)| as a function of proton incident energy, calculated using the Full-Wave Method (FWM) with and without the inclusion of an imaginary component in the optical potential. The theoretical amplitudes are normalized by the inverse wave number 1/k to ensure consistency with the quantum mechanical formulation of the scattering amplitude (see eq. 9) [7]. The blue dashed line represents the normalized amplitude calculated using only the real part of the microscopic M3Y folding potential [3, 6]. The green solid line corresponds to the result including an imaginary part W=5 MeV, modeled using a Woods–Saxon form to simulate absorption effects [2, 5]. Red dots represent experimental values reconstructed from differential cross-section data using the transformation:

$$|f(\theta)|_{\text{exp}} = \sqrt{\frac{d\sigma}{d\Omega}} \qquad (10)$$

with unit conversion from barns to fm^2. Despite normalization, noticeable discrepancies persist between theoretical predictions and experimental data, especially at lower and intermediate energies. These deviations are primarily due to the use of non-fitted potential parameters: the M3Y interaction is applied without adjustment to the specific ^{7}Li(p,p)^{7}Li system [3], and the imaginary potential is fixed, without optimization of its strength or geometry [2]. Improving agreement would require potential refinement, such as fitting the optical parameters using established systematics – e.g., the Burtebaev et al. parameter set for light nuclei [1], or the global

Koning-Delaroche optical potential [5]. Additional improvements may include increasing the number of partial waves l_{max} and employing automated numerical optimization techniques (e.g., χ^2 minimization) to better match experimental data [23].

Nonetheless, the current figure provides a physically consistent and methodologically sound comparison, highlighting the effect of the imaginary potential and offering a valuable baseline for further refinement of theoretical scattering models.

4. Conclusion

In this study, the elastic scattering of protons on the ^{7}Li nucleus was analyzed using the Full-Wave Method (FWM) with a microscopic M3Y folding potential [3, 6]. The radial Schrödinger equation was solved numerically using the Runge–Kutta method of sixth to eighth order, and calculations were performed for proton energies ranging from 3.0 to 5.5 MeV.

The results show that the theoretical differential cross section systematically overestimates the experimental values at both forward ($\theta \approx 20^0$) and backward ($\theta \approx 160^0 - 180^0$) angles, by up to 35% in some cases [2]. The scattering amplitude |f(θ)| exhibits a pronounced peak near $\theta = 130^0$, consistent with the experimental diffraction maximum. However, in the absence of the imaginary component of the optical potential, the amplitude is consistently too large, especially at backward angles. The inclusion of a phenomenological imaginary term with W=5MeV improves the shape and suppresses the amplitude, bringing theoretical predictions closer to experimental data, particularly in the angular range $\theta = 100^0 - 150^0$.

Nevertheless, the overall agreement remains qualitative. Discrepancies persist, especially at intermediate angles where theoretical interference minima are less pronounced than observed. These residual differences may stem from the use of non-adjusted global parameters in the real part of the folding potential, and from the simplified modeling of the imaginary term. Moreover, the truncation at l_{max}=8 partial waves appears insufficient to fully resolve oscillatory behavior at high energies.

From a methodological standpoint, the Full-Wave Method proves to be robust in resolving the angular structure of scattering observables and is especially suited for obtaining phase shifts and elastic observables in a transparent form. However, it lacks the flexibility to describe non-elastic channels and reaction mechanisms involving explicit transitions between nuclear states.

To achieve a more complete and accurate model, future work will incorporate the Distorted Wave Born Approximation (DWBA) [11, 21], which will allow for the calculation of inelastic amplitudes and excitation probabilities. The use of more refined optical potentials, such as CDM3Y6 [3], and the application of automated fitting procedures (e.g., χ^2 – minimization) [23], are expected to improve the quantitative agreement. Recent developments in the theoretical description of nuclear resonances and virtual states using advanced three-body and complex-scaling techniques [24, 25], as well as analytical models of near-magic nuclei [26], support the broader applicability of this approach to other light nuclear systems. Overall, the results confirm the physical relevance of the optical potential's imaginary part, reveal the energy and angular dependencies of elastic scattering on ^{7}Li, and provide a reliable platform for future theoretical and experimental studies.

References

1. Burtebaev N., Lukyanov K.V., Zagrebaev V.I., Kadyrov Sh.A. Phenomenological and semi-microscopic study of the p, d, ^{3}He and ^{4}He elastic scattering on ^{6}Li // Recent Contributions to Physics. – 2011. – Vol. 36, No. 1. – P. 5–15.

2. Fasoli U., Toniolo D., Zago G. Elastic and inelastic scattering of protons by ^{7}Li in the energy interval (3.0–5.5) MeV // Nuovo Cimento. – 1964. – Vol. 34, No. 3. – P. 542. https://doi.org/10.1007/BF02749997

3. Khoa D.T., et al. Microscopic optical model potential for nuclear reactions // Physical Review C. – 2000. – Vol. 63, No. 3. – P. 034007. https://doi.org/10.1103/PhysRevC.63.034007

4. Chapel E., Bauge E., Delaroche J.P., Girod M., Gogny D. Microscopic optical potential derived from mean-field theory // Physical Review C. – 1998. – Vol. 57, No. 1. – P. 513. https://doi.org/10.1103/PhysRevC.57.513

5. Koning A.J., Delaroche J.P. Local and global nucleon optical models from 1 keV to 200 MeV // Nuclear Physics A. – 2003. – Vol. 713, No. 3–4. – P. 231–310. https://doi.org/10.1016/S0375-9474(02)01321-0

6. Khoa D.T., Satchler G.R., von Oertzen W. Folding model analysis of elastic and inelastic alpha-nucleus scattering // Physical Review C. – 1997. – Vol. 56, No. 2. – P. 954. https://doi.org/10.1103/PhysRevC.56.954

7. Feshbach H. Unified theory of nuclear reactions // Annals of Physics. – 1958. – Vol. 5, No. 4. – P. 357–390; 1962. – Vol. 19, No. 2. – P. 287–333. https://doi.org/10.1016/0003-4916(58)90007-1

8. De Vries H., De Jager C.W., De Vries C. Nuclear charge-density-distribution parameters from elastic electron scattering // Atomic Data and Nuclear Data Tables. – 1987. – Vol. 36, No. 3. – P. 495–536. https://doi.org/10.1016/0092-640X(87)90013-1

9. EXFOR Database (Experimental Nuclear Reaction Data) – IAEA. Available at: https://www-nds.iaea.org/exfor/

10. IAEA Optical Model Library – IAEA. Available at: https://www-nds.iaea.org/omlib/

11. Satchler G.R. Direct nuclear reactions. Chapter 1 in *Direct Nuclear Reactions*. – Oxford: Oxford University Press, 1983. – P.1–45.

12. Gales S., Stoyanov Ch., Trzaska W. Theoretical approaches to nuclear structure. Chapter 2 in *Nuclear Structure Far from Stability: New Physics and New Technology*. – Bristol: Institute of Physics Publishing, 1999. – P. 23–54.

13. Bertulani C.A. Thermonuclear reaction rates. Chapter 4 in *Nuclear Reactions in Astrophysics*. – Weinheim: Wiley-VCH, 2007. – P. 97–156.

14. Tamura T. The optical model in nuclear physics. Chapter 3 in *Nuclear Optical Model*. – Amsterdam: North-Holland, 1971. – P. 65–110.

15. Mahaux C., Sartor R. Single-particle motion in nuclei // Advances in Nuclear Physics. – 1991. – Vol. 20. – P. 1–223. https://doi.org/10.1007/0-306-47086-6_1

16. Jeukenne J.P., Lejeune A., Mahaux C. Microscopic calculation of the optical-model potential // Physical Review C. – 1977. – Vol. 16, No. 1. – P. 80–96. https://doi.org/10.1103/PhysRevC.16.80

17. Varner R.L., et al. A global nucleon optical model potential // Physics Reports. – 1991. – Vol. 201, No. 2–3. – P. 57–119. https://doi.org/10.1016/0370-1573(91)90039-O

18. Soukhovitskii E.Sh., et al. Dispersive coupled-channel optical model for actinide nuclei // Physical Review C. – 2004. – Vol. 69, No. 4. – P. 044605. https://doi.org/10.1103/PhysRevC.69.044605

19. Amos K., Canton L., Pisent G., Svenne J.P., van der Knijff D. Nucleon-nucleus scattering: A microscopic nonlocal optical potential // Nuclear Physics A. – 2000. – Vol. 728, No. 1. – P. 65–95. https://doi.org/10.1016/j.nuclphysa.2003.08.005

20. Rauscher T., Thielemann F.-K. Astrophysical reaction rates from statistical model calculations // Atomic Data and Nuclear Data Tables. – 2000. – Vol. 75, No. 1–2. – P. 1–351. https://doi.org/10.1006/adnd.2000.0834

21. Austern N. Direct Nuclear Reaction Theories. – New York: Wiley-Interscience, 1970.

22. Mukhamedzhanov A.M., Tribble R.E. Asymptotic normalization coefficients and direct radiative capture rates // Physical Review C. – 1999. – Vol. 59, No. 6. – P. 3418–3423. https://doi.org/10.1103/PhysRevC.59.3418

23. Thompson I.J., Nunes F.M. Nuclear Reactions for Astrophysics: Principles, Calculation and Applications of Low-Energy Reactions. – Cambridge: Cambridge University Press, 2009. https://doi.org/10.1017/CBO9780511627195

24. Kato K., Odsuren M., Kikuchi Y., Myo T., Vasilevsky V.S., Takibayev N. Photodisintegration and virtual state in the complex scaling method // Physical Sciences and Technology. – 2016. – Vol. 3, No. 1. – P. 6–11. https://doi.org/10.26577/phst-2016-1-87

25. Vasilevsky V.S., Kato K., Takibayev N.Zh. Formation and decay of resonance state in ^{9}Be and ^{9}B nuclei. Microscopic three-cluster model investigations // Physical Sciences and Technology. – 2016. – Vol. 3, No. 1. – P. 30–35. https://doi.org/10.26577/phst-2016-1-91

26. Thompson E.A., Inyang E.P., William E.S. Analytical determination of the non-relativistic quantum mechanical properties of near doubly magic nuclei // Physical Sciences and Technology. – 2021. – Vol. 8, No. 3–4. – P. 10–21. https://doi.org/10.26577/phst.2021.v8.i2.02

Information about authors:

Kazhykenov Shalkar is a Senior lecturer at the D. Serilbayev East Kazakhstan Technical University (Oskemen, Kazakhstan),
email: nuclearshalkar@gmail.com

Janseitov Daniyar, PhD is a Researcher at the Institute of Nuclear Physics (Almaty, Kazakhstan) e-mail: d.janseitov@inp.kz
Yerbolatova Gulnar is a Senior lecturer at the D. Serilbayev East Kazakhstan Technical University (Oskemen, Kazakhstan)
e-mail: .gulnara_77@mail.ru

Real-time small object detection with YOLOv8n/8s and YOLOv11n/11s models in complex natural landscapes

D.M. Zhexebay , A.A. Skabylov , D.A. Turlykozhayeva ,

A. Bolysbay , U.K. Turmaganbet* ,

T. Namazbayev and M. Tao

School of Electronics and Information, Northwestern Polytechnical University, Xi'an, China
*e-mail: uturmaganbet@gmail.com

Unmanned Aerial Vehicles (UAVs) are increasingly employed for real-time object detection in critical applications such as security surveillance, disaster response, and environmental monitoring. However, accurate detection in UAV imagery remains challenging due to small target sizes, cluttered backgrounds, and varying environmental conditions. This study evaluates the performance of YOLOv8n/v8s and YOLOv11n/11s models for human detection in UAV-captured imagery across diverse natural landscapes. To ensure practical deployment in resource-constrained environments, the models were implemented on a Raspberry Pi 5 using the OpenVINO framework. Experimental results show that both YOLO series achieve comparable detection accuracy in the range of 80–82%, with YOLOv8n and YOLOv11n demonstrating the highest processing speeds of 10.50 and 11.04 frames per second (FPS), respectively. These findings confirm the feasibility of using lightweight YOLO models for real-time human detection on embedded systems. The results highlight the potential of integrating edge AI and UAVs for autonomous, on-site monitoring in remote or complex terrains, offering scalable solutions for intelligent aerial surveillance.

Key words: UAV, object detection, accuracy, YOLO models.
PACS number(s): 01.30.−y, 07.05.Pj.

1 Introduction

Unmanned Aerial Vehicles (UAVs), commonly known as drones, are aircraft that operate without direct human control, relying on remote radio signals or autonomous programming. In recent years, they have been widely adopted in both civilian and military sectors, with applications in agriculture, aerial photography, public safety, ecological protection, and military operations. Their increasing popularity stems from key advantages such as compact size, versatility, and cost-effectiveness [1-3].

Despite these advancements, detecting small objects using UAVs in complex natural environments remains a major challenge. High-altitude perspectives reduce objects to a few pixels, making feature extraction difficult for YOLO models. Scale variations, background clutter, and occlusion further complicate detection, as small objects are often obscured by vegetation, shadows, or other elements. Additionally, dynamic conditions like lighting changes, motion blur,

and atmospheric disturbances impact image clarity, further degrading detection performance [3-9].

To solve the above-mentioned problems authors [1] for small object detection proposed UAV-YOLOv8 model with Wise-IoUv3, BiFormer attention, and the Focal FasterNet Block, resulting in high detection accuracy. In [2] authors, optimized YOLOv8 variant achieving good mAP@0.5 while reducing computational complexity. For structured environments, WeiSun et.al introduced the RSOD algorithms[3] an improved YOLOv3-based model for UAV traffic monitoring with VisDrone-Det2018 and UAVDT datasets. To expand object detection beyond the visible spectrum, Jiang et.al. proposed a thermal infrared (TIR) detection framework [4] using YOLO models for FLIR cameras. The YOLOv5s model reached great mAP at 50 FPS, proving effective under low-visibility conditions. Chang et.al. explored enhancements for high-altitude small object detection [5], where SPD-convolution, coordinate attention, transposed convolution, and Alpha-IoU

D.M. Zhexebay *et al.*

Phys. Sci. Technol., Vol. 12 (No. 1-2), 2025: 142-153

loss were incorporated, improving precision, accuracy, and recall in YOLOv5s. Han et.al. designed, the Senselite model [6] with GSConv, SlimNeck, and a squeeze-and-excitation mechanism, reaching to high mAP@0.5, surpassing YOLOv5 in computational efficiency. For urban road monitoring, Wang et.al. optimized YOLOv9-based model [7], which developed with SCRCONV, SPPELANBRA, and Inner-MP-DIOU loss, achieving state-of-the-art results on the CICVAC dataset. Zhang et.al. introduced, RTS-NET a real-time detection network [8] for UAV patrols, achieving superior mAP and 163.9 FPS, prioritizing real-time efficiency. Zheng et al. analyzed YOLO-based deep learning models [9] across multiple applications, including agriculture, fire detection, ecology, marine science, and UAV navigation. Muzammul et.al. presented, a quantum-inspired multi-scale detection model [10] for ultra-small object detection, incorporating sub-pixel convolution, adversarial training, and self-supervised learning. These above discussed articles exhibited relatively good efficiency in small object detection, however these results can be further improved in terms of speed and accuracy.

In this article, we propose an advanced real-time object detection model for UAV-based surveillance using the latest YOLOv8n/v8s and YOLO 11n/11s, integrated with the OpenVINO framework on Raspberry Pi 5 to optimize speed, accuracy, and efficiency across diverse environments. The latest YOLO versions [11] provide significant advancements in precision, processing speed, and adaptability for various detection tasks, and we believe that the proposed integrated model can further enhance computational efficiency.

The article is structured as follows: Section 2 introduces the YOLO models and their architecture, highlighting key improvements and design choices. Section 3 describes the datasets and processing methods, including data collection, and preprocessing techniques. Section 4 discusses the detection model, detailing training strategies and optimization techniques. Finally, Section 5 presents the results, analyzing model performance in terms of accuracy, efficiency, and real-time applicability in UAV-based object detection.

2 Background

2.1. YOLO series
This section presents an overview of the most widely used YOLO object detection models − YOLOv8n/s, YOLOv11n/s − developed in recent years [11,12].

YOLOv8 represents the latest and most advanced iteration in the YOLO series, offering five different models optimized for various scales: YOLOv8n, YOLOv8s, YOLOv8m, YOLOv8l, and YOLOv8x. As depicted in Figure 1, the architecture of YOLOv8 is composed of three core layers: the backbone, the neck, and the detection head [11,12].

The Backbone Layer is built on CSPDarknet53 [12], leveraging five down sampling stages to extract multi-scale features. Unlike previous YOLO versions, YOLOv8 replaces the conventional Cross Stage Partial (CSP) module with the C2f module, which incorporates both dense and residual connections, improving gradient flow and feature representation. Additionally, it integrates the Spatial Pyramid Pooling Fast (SPPF) module, enabling enhanced multi-scale feature extraction while reducing computational complexity and inference latency. This combination ensures a lightweight yet powerful backbone capable of detecting small and large objects efficiently.

The Neck Layer utilizes a fusion of Feature Pyramid Network (FPN) [13,14] and Path Aggregation Networks (PANet) to enhance feature propagation and multi-scale detection. FPN's top-down structure improves the transmission of high-level semantic features to lower layers, aiding small object detection. PANet strengthens feature reuse with a bottom-up pathway, enriching the spatial information flow. Though PANet increases computational cost, its integration with C2f modules balances efficiency and performance, allowing YOLOv8 to capture objects of varying scales with high precision.

The Detection Head Layer adopts a decoupled head structure, separating classification and regression tasks for better optimization. YOLOv8 moves away from traditional anchor-based methods, implementing the Task-Aligned Assigner [15], which dynamically assigns positive and negative samples during training, improving detection accuracy. Classification is handled using binary cross-entropy loss (BCE Loss), while bounding box regression benefits from distribution focal loss (DFL) [16] and Complete Intersection over Union (CIoU) [17] loss. These loss functions refine object localization by penalizing misaligned bounding boxes and improving convergence speed.

One of the features of YOLOv8 is the C2f module, which enhances the gradient flow throughout the backbone and neck. This is achieved by incorporating more skip connections and removing convolutions in its branches, taking inspiration from the C3 module and ELAN design in YOLOv5. Further-

more, YOLOv8 introduces a decoupled head that separately processes the extraction of target position and category information, significantly improving detection accuracy. Another important innovation is the shift from conventional anchor-based design to anchor-free architecture. For classification, YOLOv8 utilizes VFL loss, while DFL loss and CIOU loss are employed for regression tasks [18]. To enhance bounding box regression, YOLOv8 employs IoU-based loss functions [19], which evaluate the overlap between predicted and ground truth bounding boxes. While standard IoU Loss struggles in cases of non-overlapping boxes, CIoU mitigates this issue by minimizing the normalized distance between box centers and incorporating an aspect ratio penalty. This leads to faster convergence, superior localization accuracy, and improved performance in detecting small and fast-moving objects [18,19].
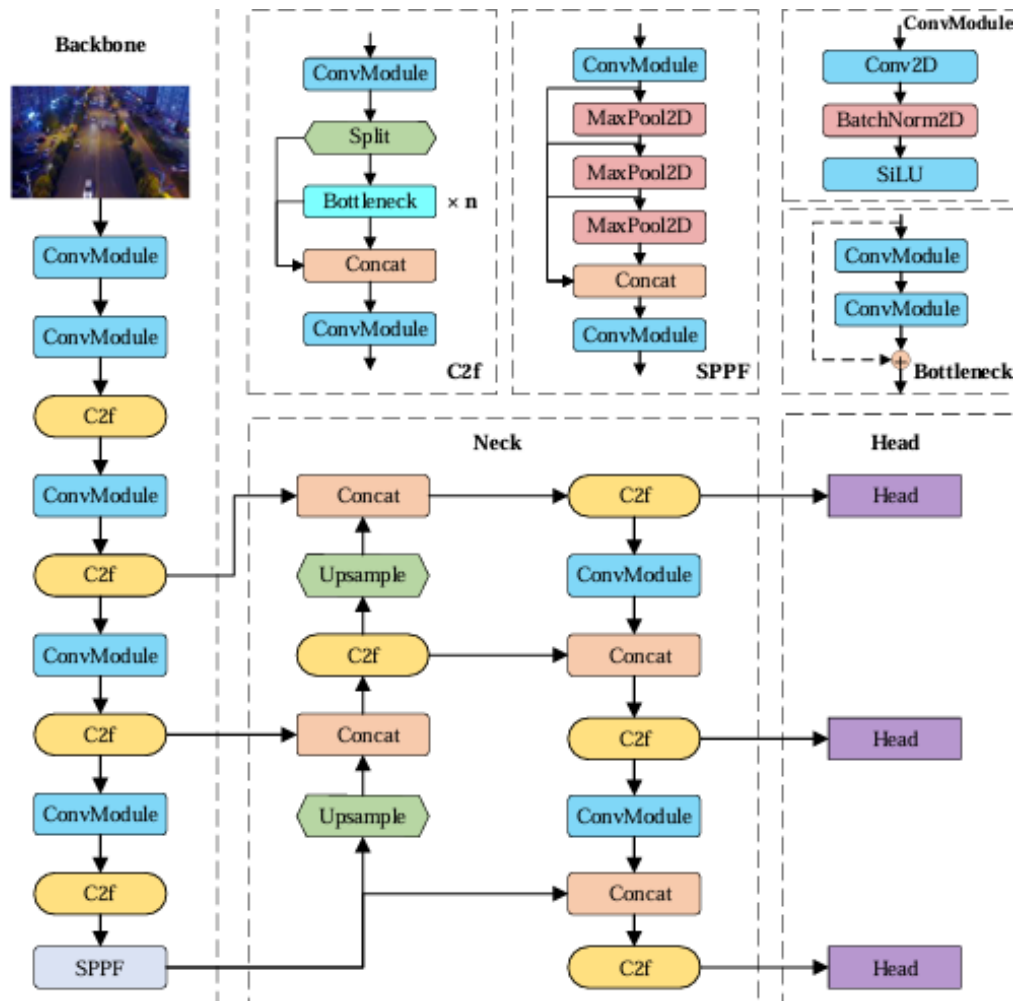
Figure 1 – Structure of YOLOv8 [18].

YOLOv11, the latest version in the YOLO series, brings notable advancements in speed, accuracy, and feature extraction. Like YOLOv8, the architecture of YOLOv11, as depicted in Figure 2, consists of three main components: the backbone, the neck, and the head.

The backbone is the initial and crucial component of YOLOv11, tasked with extracting key features from the input image at various scales. YOLOv11 incorporates C3K2 blocks, which replace the C2f blocks found in YOLOv8 [13]. The C3K2 blocks provide a more computationally efficient implementation of Cross-Stage Partial (CSP) [14]. Additionally, the last two blocks of the backbone are the Spatial Pyramid Pooling Fast (SPPF) and Cross-Stage Partial with Spatial Attention (C2PSA) [16, 19]. The SPPF

block uses multiple max-pooling layers to efficiently capture multi-scale features, while the C2PSA block integrates an attention mechanism to improve the model's accuracy.

The neck is the second major component of YOLOv11. As shown in Figure 2, it includes several Conv layers, C3K2 blocks, Concat operations, and Upsample blocks, all enhanced by the C2PSA mechanism. The neck's primary role is to combine features from different scales and forward them to the head for final prediction [20].

The head is the final component of YOLOv11 and plays an essential role in generating predictions. It is responsible for determining the object class, calculating the objectness score, and accurately predicting the bounding boxes for detected objects [21].
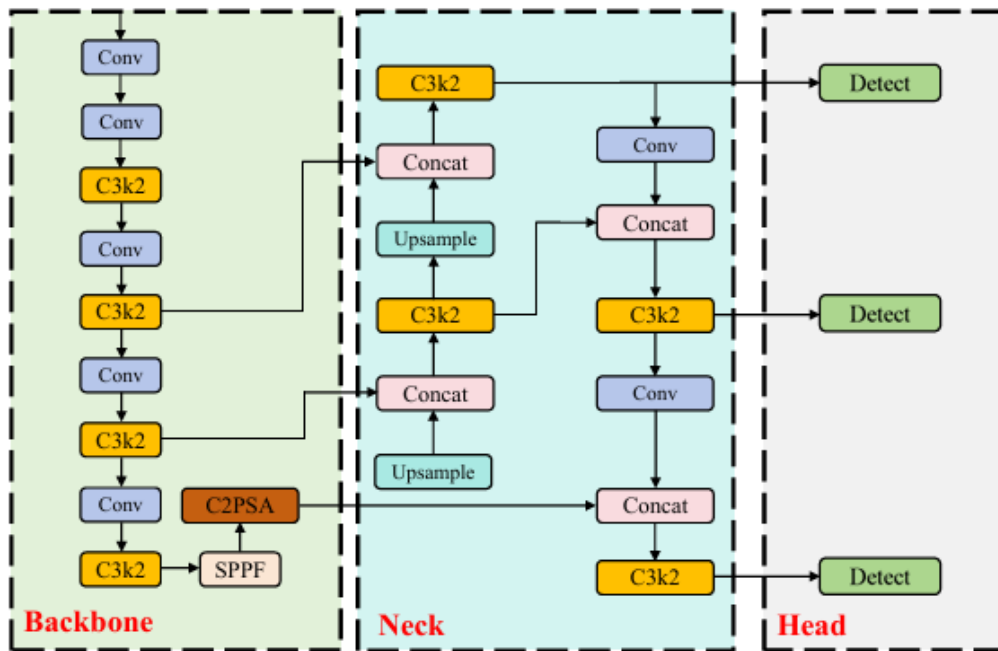
Figure 2 – Structure of YOLOv11[22].

One of the features of YOLOv11 is the C3PSA module, which provides efficient feature extraction and an advanced attention mechanism for better accuracy. It adopts an anchor-free design and a refined decoupled head for improved localization and classification. Also, optimized loss functions, including VFL and DFL, further enhance precision and stability [22].The model is optimized for modern GPUs [23,24], boosting speed and reducing latency for fast, real-time performance. This makes YOLOv11 perfect for applications like video surveillance and autonomous systems [25,26] that need quick and accurate object detection.

3 Dataset and processing

3.1. Image database
In this study, the UAVSOD-10 dataset was utilized, containing aerial imagery captured by UAVs to facilitate small object detection through deep learning techniques. The UAVSOD-10 dataset contains 844 images and 18,234 annotated instances, each labeled with horizontal bounding boxes (HBB) in VOC format [27]. The image widths range from 1,000 to 4,800 pixels, with a resolution of approximately 0.15 meters. Scale differences [28] in objects of the same or different categories are apparent. The width of the smallest object in image instance is 9 pixels, the biggest width is 312 pixels, and the mean width is 74.85 pixels. The images were captured in a mountainous area of the Liuzhi Special Economic Zone, Guizhou Province, China. To enhance the model's generalization ability and account for various natural conditions, the dataset includes images from different types of terrain, such as mountains, forests, and snowfields. This approach enables the model to be trained on data that represents diverse environments, improv-

ing its ability to detect people in complex natural landscapes [28].

The model was trained using the Roboflow [29, 30] platform for data annotation. To accelerate learning, the transfer learning technique was applied, enabling pre-trained models to be adapted for the task of detecting people in images captured by drones. Training was conducted on a system with an Intel Core i9 processor [31] and an NVIDIA GeForce RTX 4090 GPU [32], providing the necessary computational power for effective training. The training hyperparameters were as follows: 600 epochs, a

batch size of 16, and a learning rate of 0.01. Various data augmentation techniques, such as rotation, scaling, and brightness variation, were employed to improve the model's ability to handle different lighting conditions and object orientations [32].

Object scales were compared by calculating the area ratio of the object bounding box pixels to the total image. As shown in Figure 3, the image scale is enhanced by segmenting it into pixels within a rectangular grid. YOLO models typically process images at varying scales, where the images undergo magnification ranging from zero to 6x [33].

Figure 3 – Examples of images showing aerial photographs taken with a drone, at zero and 6x magnification.

The training set, consisting of 717 images, is composed of diverse locations in the suburbs of China, including mountainous and forested areas, captured at altitudes ranging from 13 to 30 meters. The validation set, made up of 84 images, is carefully selected to represent a wide range of environmental conditions, supporting the model's generalization across different landscapes. The test set, containing 81 images, is used as a benchmark for evaluating the model's performance in real-world scenarios. The dataset is focused on people detection, ensuring precise and reliable identification from dynamic aerial perspectives.

3.2. Performance of YOLOv8/v11

The Raspberry Pi 5 is a powerful single-board computer designed for high-performance and real-time processing. It features a 64-bit Broadcom BCM2712 processor (Cortex-A76, up to 2.4 GHz) and a VideoCore VII GPU (800 MHz), offering significant improvements over previous models. With 4 GB or 8 GB LPDDR4X-4267 RAM, it efficiently handles multitasking and large datasets. The PCIe 2.0 interface supports external accelerator integra-

tion, enhancing data processing capabilities. Despite a 5A and 5V power requirement, the Raspberry Pi 5 remains compact and efficient for various applications [34-37].

To deploy YOLOv8 and YOLOv11 on Raspberry Pi 5, the trained models were converted into OpenVINO-compatible format. Using OpenVINO's Model Optimizer, the best.pt file was transformed into an Intermediate Representation (IR) model, optimizing it for efficient execution on resource-constrained devices.

OpenVINO (Open Visual Inference and Neural Network Optimization) is an Intel toolkit that optimizes deep learning models for CPUs, GPUs, FPGAs, and VPUs. It converts models from frameworks like TensorFlow and PyTorch into an IR format using the Model Optimizer, and the Inference Engine ensures efficient execution. Integrated with Raspberry Pi 5, OpenVINO enhances inference efficiency, reducing computational overhead and enabling real-time processing using its BCM2712 processor [38] and VideoCore VII GPU [39]. Figure 4 shows the object detection system using Raspberry Pi5.
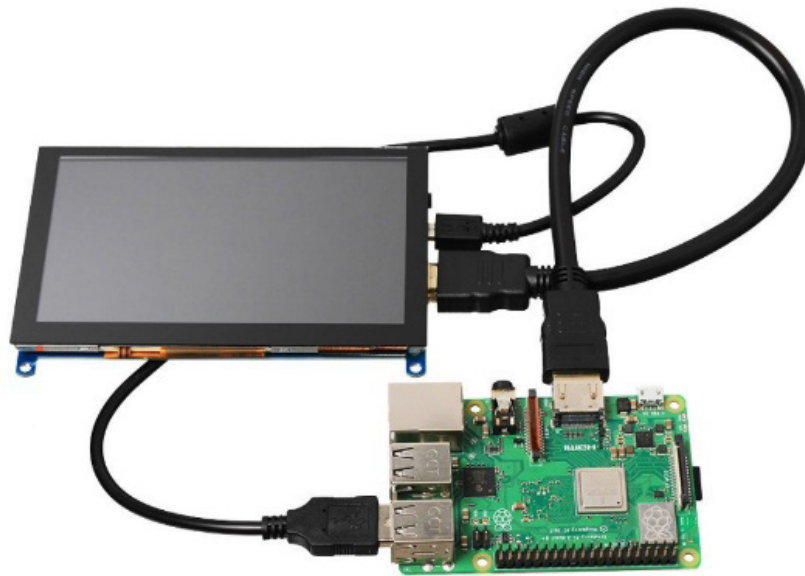
D.M. Zhexebay *et al.*

Phys. Sci. Technol., Vol. 12 (No. 1-2), 2025: 142-153

Figure 4 – Human detection system using Raspberry Pi 5.

After the model was converted to the OpenVINO format, the best_yolov8s_openvino_model was deployed on the Raspberry Pi 5. Test images stored in./test/images, and their corresponding YOLO-format annotations in./test/labels were used for evaluation. A Python script on Raspberry Pi 5 handles the entire object detection process : it loads and preprocesses images, performs inference using the YOLO model via OpenVINO, and then compares the predicted bounding boxes with ground truth annotations [40,41]. This comprehensive workflow allows for a detailed assessment of the model's accuracy and performance in real-time object detection on resource-constrained hardware [42].

For each test image, the following steps are performed: the image is loaded into memory, processed through the YOLO model to obtain predicted object coordinates, and compared with ground truth annotations. Bounding boxes are visualized, with predictions in green and actual annotations in red, providing a clear assessment of detection accuracy [43,44]. The inference time for each image is recorded to evaluate real-time performance. Finally, processed images with bounding boxes are saved in the. /results directory for further analysis. This approach ensures a comprehensive evaluation of both detection accuracy and processing efficiency.

4 Results

In this section, we evaluate the performance of the YOLO models for addressing the object detection task in real-time applications. Figure 5 presents the detection results of the YOLOv8 and YOLOv11 models in identifying people from UAV imagery under various environmental conditions. In Figure 4, the red bounding boxes represent manually labeled ground truth annotations, while the blue boxes indicate the objects detected by the trained models.

The results shown in Figure 5 indicate that the detection capabilities of the YOLOv8 and YOLOv11 models are acceptable and can be applied in various environmental conditions. The FPS values for each of the tested models are presented in Table 1, enabling a comparison of their processing speeds.

As shown in Table 1, the YOLOv8n and YOLOv11n models achieve the highest FPS (10.50 and 11.04 respectively), indicating their acceptable processing speed and suitability for real-time detection tasks in comparison with other models. Figure 6 presents the results of the confusion matrics and accuracy curves of the YOLOv8n and YOLOv8s models. The x-axis represents the true class labels of the samples, while the y-axis indicates the predicted results.
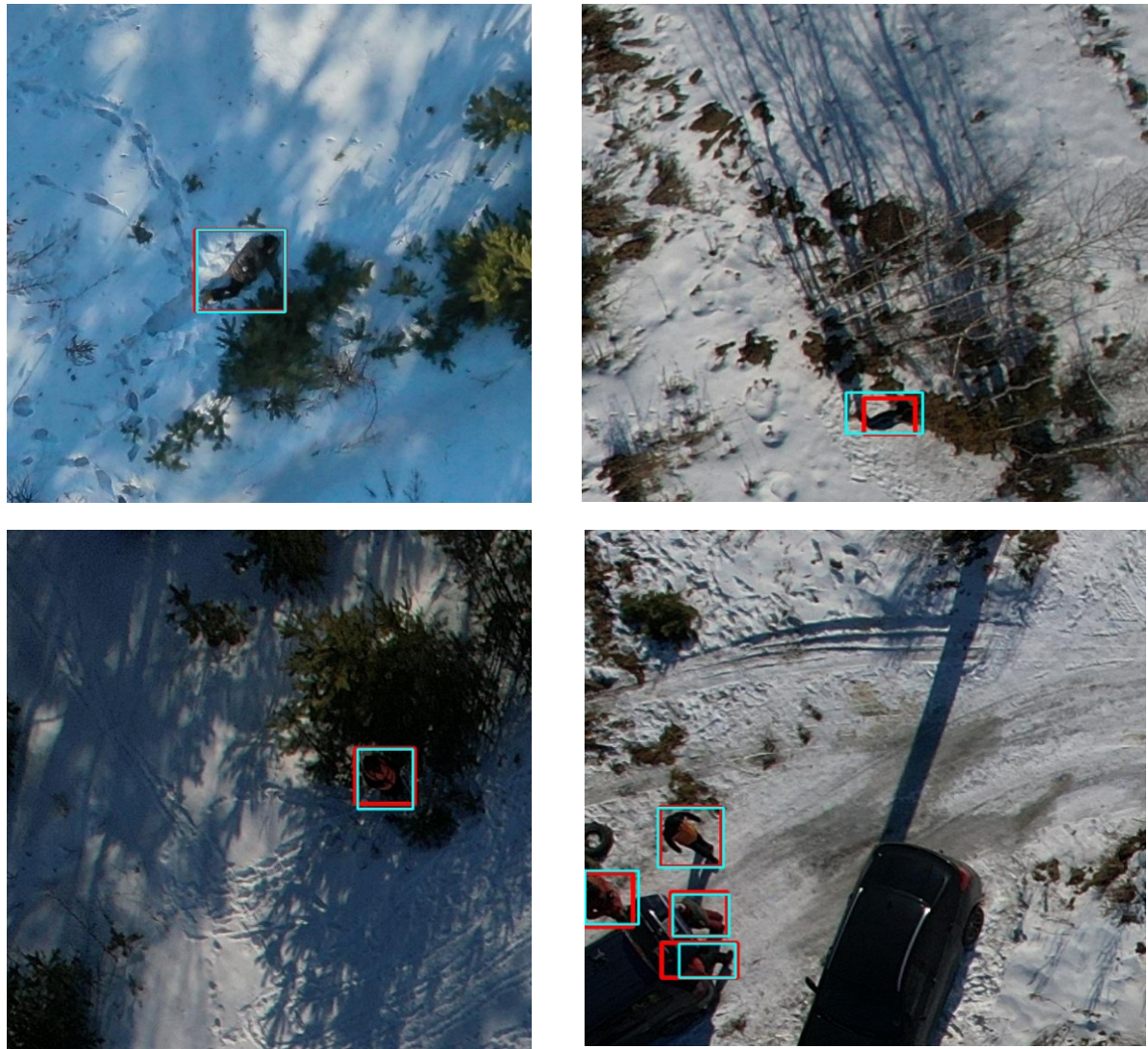
Figure 5 – Object detection comparison of YOLOv8n/v11n and YOLOv8s/11s models in snow-covered landscapes. Red boxes are ground truth labels, blue boxes are detected objects.

Table 1 – FPS values of the tested YOLOv8 and YOLOv11 models.

Model	FPS
YOLO 11s	5.24
YOLO 11n	11.04
YOLO v8s	4.95
YOLO v8n	10.50

(a)

(b)

(c)

(d)
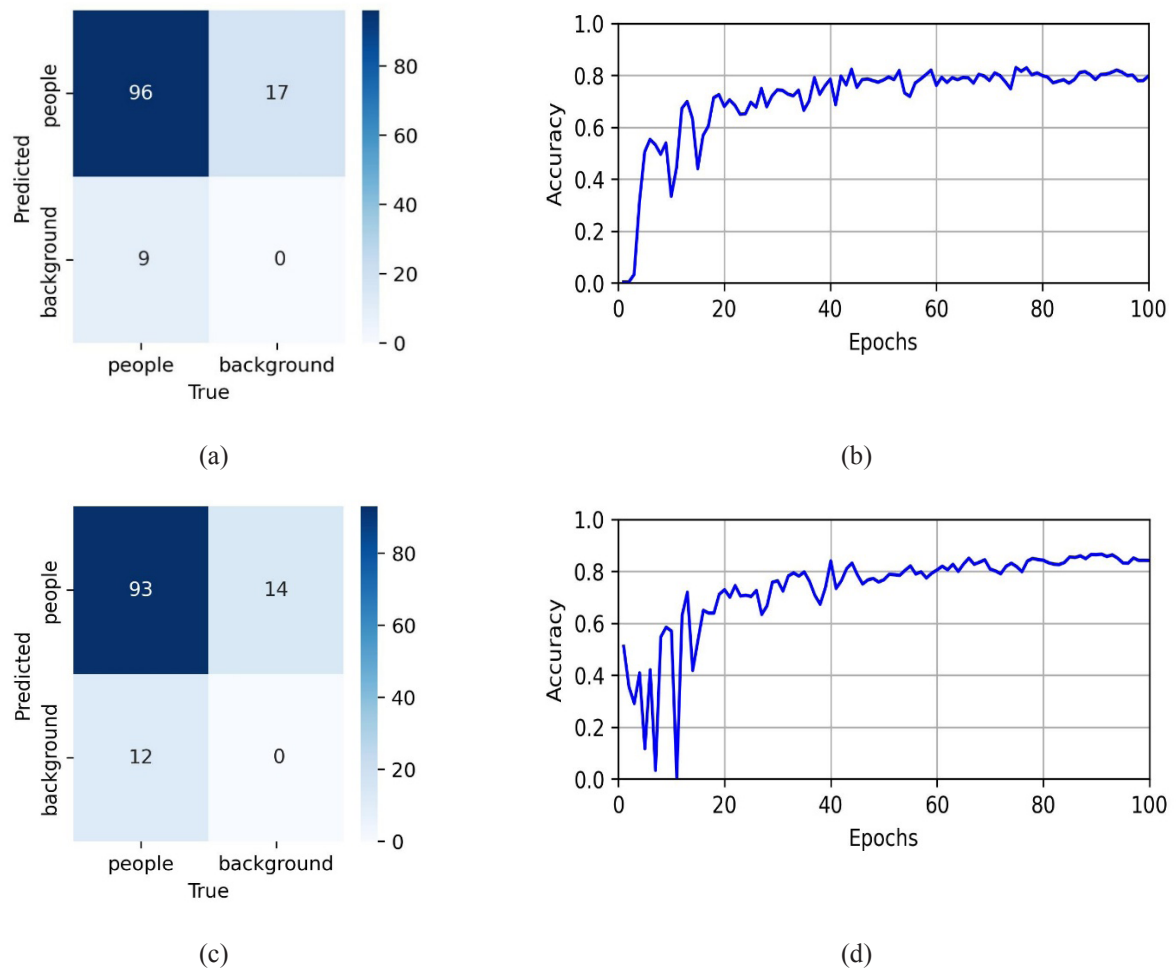
Figure 6 (a, c) – YOLOv8n/s confusion matrix; (b, d) – Accuracy curve.

The confusion matrices (a) and (c) show that YOLOv8n detects 96 people, with 17 background and 9 people misclassified, while YOLOv8s identifies 93 people, with 14 background and 12 people misclassified. The accuracy curves (b) and (d) depict the training process over 100 epochs, showing a quick initial improvement before gradually stabilizing around 80%. Figure 6 presents the results of the confusion matrics and accuracy curves of the YOLOv11n and YOLOv11s models.

The confusion matrics (a) and (c) present that YOLOv11n recognizes 94 people and YOLOv11s recognizes 95, with 19 and 22 background instances as people and 11 and 10 people as background, respectively. The accuracy curves (b) and (d) show training progress over 100 epochs, with accuracy stabilizing above 80% after 80 epochs. Figure 8 provides a comparison of the efficiency of YOLOv8n/s and YOLOv11n/s models, showcasing their performance in terms of accuracy and processing speed.

(a)

(b)

(c)

(d)
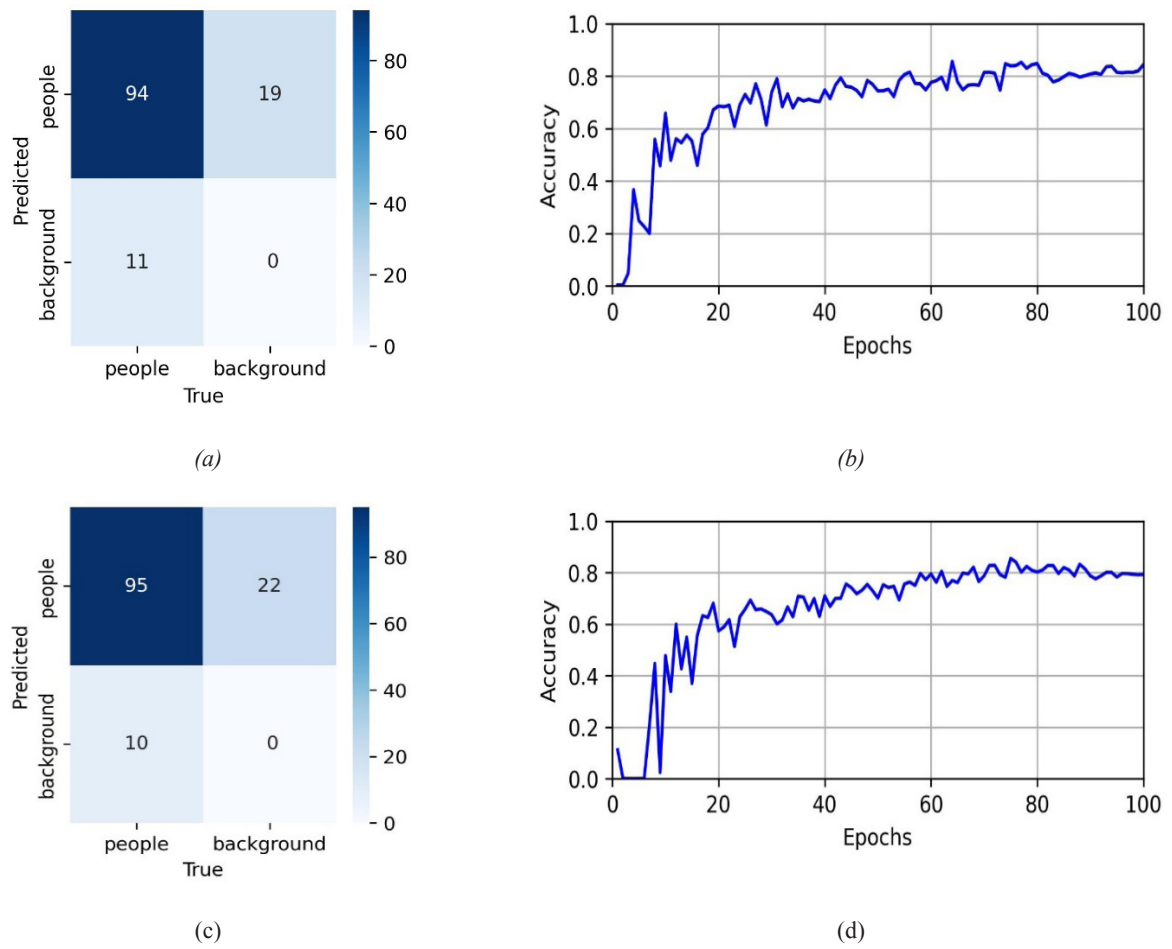
Figure 7 (a, c) – YOLOv11n/s confusion matrix; (b, d) – Accuracy curve.
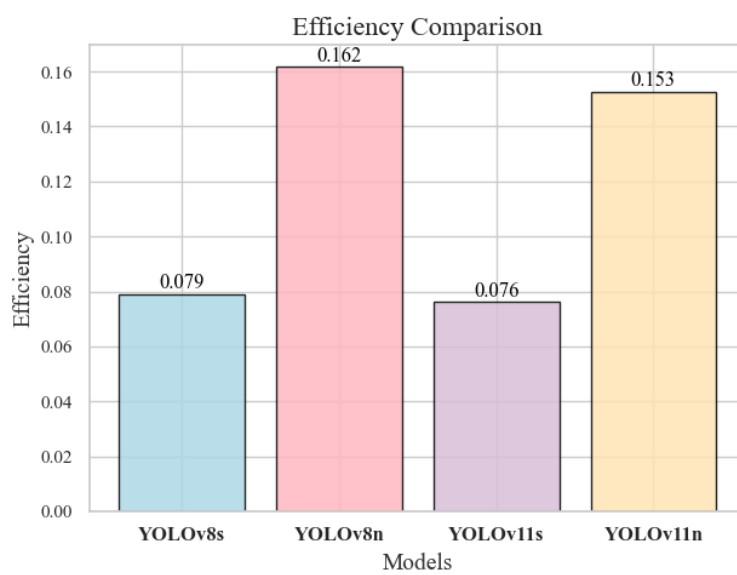
Figure 8 – Efficiency Comparison of models YOLOv8/11.

Figure 8 demonstrates that YOLOv8n and YO-LOv11n achieve the highest FPS and accuracy compared to the other evaluated models. Meanwhile, YOLOv8s and YOLOv11s exhibit slightly lower FPS but maintain competitive accuracy, balancing speed and precision in object detection.

5 Conclusion

In this article, we have evaluated the performance of YOLOv8n/v8s and YOLOv11n/11s models for human detection in UAV-captured imagery across diverse natural landscapes. The results showed that both YOLO series achieved comparable accuracy between 80% and 82%, with YOLOv8n and YO-LOv11n demonstrating the highest FPS. These models exhibited higher efficiency, balancing processing speed and detection accuracy for real-time UAV applications. Their successful deployment on a Rasp-berry Pi 5 using the OpenVINO framework confirmed their feasibility for real-time object detection in resource-constrained environments.

Future work includes integrating YOLOv8n and YOLOv11n models with FPGA to enhance performance, accuracy, and efficiency for real-time object detection while optimizing computational speed and power consumption for UAV applications.

References

1. Muzammul M., Assam M., Qahmash A. Quantum-inspired multi-scale object detection in UAV imagery: advancing ultra-small object accuracy and efficiency for real-time applications //IEEE Access. – 2024. – Vol. 10. – P. 2173 – 2186. https://doi.org/10.1109/ACCESS.2024.3523405

2. Wang Y., Zhang J., Zhou J. Urban traffic tiny object detection via attention and multi-scale feature driven in UAV-vision // Scientific Reports. – 2024. – Vol. 14. – Is. 1. – Art. 20614. https://doi.org/10.1038/s41598-024-71074-2

3. Wang J., Yang H., Wu M., Wang S., Cao Y., Hu S., Shao J., Zeng C. UR-YOLO: an urban road small object detection algorithm // Pattern Analysis and Applications. – 2024. – Vol. 27. – Is. 4. – Art. 121. https://doi.org/10.1007/s10044-024-01324-6

4. Han T., Dong Q., Sun L. Senselite: A YOLO -based lightweight model for small object detection in aerial imagery // Sensors. – 2023. – Vol. 23. – Is. 19. – Art. 8118. https://doi.org/10.3390/s23198118

5. Chang Y., Li D., Gao Y., Su Y., Jia X. An improved YOLO model for UAV fuzzy small target image detection // Applied Sciences. – 2023. – Vol. 13. – Is. 9. – Art. 5409. https://doi.org/10.3390/app13095409

6. Sun W., Dai L., Zhang X., Chang P., He X. RSOD: Real-time small object detection algorithm in UAV-based traffic monitoring // Applied Intelligence. – 2022. – Vol. 52. – Is. 4. – P.8448-8463. https://doi.org/10.1007/s10489-021-02893-3

7. Ansah P. A. K., Appati J. K., Owusu E., Boahen E. K., Boakye-Sekyerehene P., Dwumfour A. SB-YOLO-V8: A multilayered deep learning approach for real-time human detection // Engineering Reports. – 2025. – Vol. 7. – Is. 2. – Art. e70033. https://doi.org/10.1002/eng2.70033

8. Vijayakumar A., Vairavasundaram S. Yolo-based object detection models: A review and its applications // Multimedia Tools and Applications. – 2024. – Vol. 83. – No. 35. – P. 83535-83574. https://doi.org/10.1007/s11042-024-18872-y

9. Zeng S., Yang W., Jiao Y., Geng L., Chen X. SCA-YOLO: A new small object detection model for UAV images // The Visual Computer. – 2024. – Vol. 40. – No. 3. – P. 1787–1803. https://doi.org/10.1007/s00371-023-02886-y

10. Jiang C., Ren H., Ye X., Zhu J., Zeng H., Nan Y., Sun M., Ren X., Huo H. Object detection from UAV thermal infrared images and videos using YOLO models // International Journal of Applied Earth Observation and Geoinformation. – 2022. – Vol. 112. – Art. 102912. https://doi.org/10.1016/j.jag.2022.102912

11. Chang Y., Li D., Gao Y., Su Y., Jia X. An improved YOLO model for UAV fuzzy small target image detection // Applied Sciences. – 2023. – Vol. 13. – Is. 9. – Art. 5409. https://doi.org/10.3390/app13095409

12. Wang C. Y., Liao H., Wu Y. H., Chen P. Y., Yeh I. A new backbone that can enhance learning capability of CNN. 2020 IEEE // CVF Conference on Computer Vision and Pattern Recognition Workshops (CVPRW). IEEE. – 2020. – P. 390-391. https://doi.org/10.48550/arXiv.1911.11929

13. Lin T. Y., Dollár P., Girshick R., He K., Hariharan B., Belongie S. Feature pyramid networks for object detection // Proceedings of the IEEE conference on computer vision and pattern recognition. – 2017. – P. 2117-2125. https://doi.org/10.1109/CVPR.2017.106

14. Liu S., Qi L., Qin H., Shi J., Jia J. Path aggregation network for instance segmentation //Proceedings of the IEEE conference on computer vision and pattern recognition. – 2018. – P. 8759-8768. https://doi.org/10.1109/CVPR.2018.00913

15. Feng C., Zhong Y., Gao Y., Scott M. R., Huang W. Tood: Task-aligned one-stage object detection //2021 IEEE/CVF International Conference on Computer Vision (ICCV). – IEEE Computer Society. -2021. – P. 3490-3499. https://doi.org/10.1109/ICCV48922.2021.00349

16. Wang S., Qu Z., Gao L. Multi-spatial pyramid feature and optimizing focal loss function for object detection //IEEE Transactions on Intelligent Vehicles. – 2023. – Vol. 9. – Is. 1. – P. 1054-1065. https://doi.org/10.1109/TIV.2023.3282996

17. Wang X., Song J. ICIoU: Improved loss based on complete intersection over union for bounding box regression // IEEE Access. – 2021. – Vol. 9. – P. 105686-105695. https://doi.org/10.1109/ACCESS.2021.3100414

18. Yue M., Zhang L., Huang J., Zhang H. Lightweight and efficient tiny-object detection based on improved YOLOv8n for UAV aerial images // Drones. – 2024. – Vol. 8. – No. 7. – P. 276. https://doi.org/10.3390/drones8070276

19. Trinh C. D., Do Le T. M., Do T. H., Bui N. M., Nguyen T. H., Ngo Q. U., Bui D. T. Improving YOLOv8 Deep leaning model in rice disease detection by using Wise-IoU loss function // Journal of Measurement, Control, and Automation. – 2025. – Vol. 29. – No. 1. – P. 1-6. https://doi.org/10.3390/agriengineering6010018

20. Wei W., Huang Y., Zheng J., Rao Y., Wei Y., Tan X., OuYang H. YOLOv11-based multi-task learning for enhanced bone fracture detection and classification in X-ray images // Journal of Radiation Research and Applied Sciences. – 2025. – Vol. 18. – Is. 1. – Art. 101309. https://doi.org/10.1016/j.jrras.2025.101309

21. Khanam R., Hussain M. An overview of the key architectural enhancements //arXiv preprint arXiv:2410.17725. – 2024. https://doi.org/10.48550/arXiv.2410.17725

22. He L., Zheng L., Xiong J. FMV-YOLO: A Steel Surface Defect Detection Algorithm for Real-World Scenarios // Electronics. – 2025. – Vol. 14. – No. 6. – P. 1143. https://doi.org/10.3390/electronics14061143

23. Turlykozhayeva D. A., Akhtanov S. N., Zhanabaev Z. Z., Ussipov N. M., Akhmetali A. A routing algorithm for wireless mesh network based on information entropy theory // IET Communications. – 2025. – Vol. 19. – No. 1. –Art. e70011. https://doi.org/10.1049/cmu2.70011

24. Zahoruiko L., Martianova T., Al-Hiari M., Polovenko L., Kovalchuk M., Merinova S., ... Yeraliyeva B. Mathematical model and structure of a neural network for detection of cyber attacks on information and communication systems // Informatics Control Measurement in Economy and Environment Protection. – 2024. – Vol. 14. – No. 3. – P. 49-55. https://doi.org/10.35784/iapgos.6155

25. Kuzminykh V., Koval O., Havrylko Y., Xu B., Yepifanova I., Zhu S., Yeraliyeva B. Synchronization of event-driven management during data collection // Informatyka, Automatyka, Pomiary w Gospodarce i Ochronie Środowiska. – 2024. – Vol. 14. – No. 4. – P. 121-129. https://doi.org/10.35784/iapgos.6656

26. Vasylkivskyi M. V., Horodetska O. S., Savytska L. A., Savina N. B., Kalizhanova A., Komada P. Method to improve information security in fiberoptic systems and networks // Photonics Applications in Astronomy, Communications, Industry, and High Energy Physics Experiments 2024. – SPIE, 2024. – Vol. 13400. – P. 201-207. https://doi.org/10.1117/12.3054856

27. Tymchenko L., Kokriatska N., Pavlov S., Tverdomed V., Lisovenko I., Khomyuk I., Issakozhayeva I. Modified parallel-hierarchical transformation algorithm for processing of optical imaging // Photonics Applications in Astronomy, Communications, Industry, and High Energy Physics Experiments 2024. – SPIE, 2024. – Vol. 13400. – P. 158-163. https://doi.org/10.1117/12.3054898

28. Chen S., Sun Q., Liu M., Tao M., Li Y., Xing M. Superpixel segmentation of marine SAR images based on local fuzzy iteration and edge information for target detection // IEEE Journal of Selected Topics in Applied Earth Observations and Remote Sensing. – 2024. – Vol. 17. – P. 16917-16931. https://doi.org/10.1109/JSTARS.2024.3450548

29. Dong Z., Liu M., Chen S., Tao M., Wei J., Xing M. Occluded SAR target recognition based on center local constraint shadow residual network // IEEE Geoscience and Remote Sensing Letters. – 2025. – Vol. 22. – P. 1-5. https://doi.org/10.1109/LGRS.2025.3532763

30. Liu Y., Tao M., Zhou Y., Zhao L., Su J., Wang L. RFI Localization Scheme for Dual-Channel SAR System based on Alternating Constraints Optimization // 2024 IEEE International Conference on Signal, Information and Data Processing (ICSIDP). – IEEE, 2024. – P. 1-4. https://doi.org/10.1109/ICSIDP62679.2024.10868155

31. Duisebayev T., Ibraimov M., Khaniyev B., Tileu A., Alimbetova D. Development of memory elements based on surface-modified nanostructured porous silicon // WSEAS Transactions on Electronics. – 2024. – Vol. 15. – P. 63-69. https://doi.org/10.37394/232017.2024.15.8

32. Andrushchenko M., Selivanova K., Avrunin O., Palii D., Tymchyk S., Turlykozhayeva D. Hand movement disorders tracking by smartphone based on computer vision methods // Informatyka, Automatyka, Pomiary W Gospodarce I Ochronie Środowiska. – 2024. – Vol. 14. – P. 5-10. http://doi.org/10.35784/iapgos.6126

33. Turlykozhayeva D. A., Akhtanov S. N., Baigaliyeva A. N., Temesheva S. A., Zhexebay D. M., Zaidyn M., Skabylov A. A. Evaluating routing algorithms across different wireless mesh network topologies using NS-3 simulator // Eurasian Physical Technical Journal. – 2024. – Vol. 21, No. 2. – P. 70-82. https://doi.org/10.31489/2024No2/70-82

34. Turlykozhayeva D., Akhtanov S., Zhexebay D., Ussipov N., Baigaliyeva A., Wójcik W., Boranbayeva N. Evaluating machine learning-based routing algorithms on various wireless network topologies // Photonics Applications in Astronomy, Communications, Industry, and High Energy Physics Experiments 2024. – SPIE, 2024. – Vol. 13400. – P. 236-245. https://doi.org/10.1117/12.3058676

35. Ussipov N., Akhtanov S., Zhanabaev Z., Turlykozhayeva D., Karibayev B., Namazbayev T., Tang X. Automatic modulation classification for MIMO system based on the mutual information feature extraction // IEEE Access. – 2024. https://doi.org/10.1109/ACCESS.2024.340044

36. Ussipov N., Akhtanov S., Turlykozhayeva D., Temesheva S., Akhmetali A., Zaidyn M., Tang X. MEGA: Maximum-Entropy Genetic Algorithm for Router Nodes Placement in Wireless Mesh Networks // Sensors. – 2024. – Vol. 24, No. 20. – P. 6735. https://doi.org/10.3390/s24206735

37. Turlykozhayeva D., Temesheva S., Ussipov N., Bolysbay A., Akhmetali A., Akhtanov S., Tang X. Experimental performance comparison of proactive routing protocols in wireless mesh network using raspberry Pi 4 // Telecom. – MDPI, 2024. – Vol. 5, No. 4. – P. 1008-1020. https://doi.org/10.3390/telecom5040051

38. Sabibolda A., Tsyporenko V., Smailov N., Tsyporenko V., Abdykadyrov A. Estimation of the time efficiency of a radio direction finder operating on the basis of a searchless spectral method of dispersion-correlation radio direction finding // IFToMM Asian conference on Mechanism and Machine Science. – Cham: Springer Nature Switzerland, 2024. – P. 62-70. https://doi.org/10.1007/978-3-031-67569-0_8

39. Seidaliyeva U., Ilipbayeva L., Utebayeva D., Smailov N., Matson E. T. LiDAR Technology for UAV Detection: From fundamentals and operational principles to advanced detection and classification techniques // Sensors. – 2024. https://doi.org/10.3390/s25092757

40. Seidaliyeva U., Ilipbayeva L., Taissariyeva K., Smailov N., Matson E. T. Advances and challenges in drone detection and classification techniques: A state-of-the-art review // Sensors. – 2023. – Vol. 24, No. 1. – P. 125. https://doi.org/10.3390/s24010125

41. Temirzhanov A., Sadykov B., Zholdybayev T., Duisebayev B., Ussabayeva G., Kerimkulov Z. STM32F407 microcontroller based multichannel analyzer for spectroscopy // Physical Sciences and Technology. – 2024. – Vol. 11, Nos. 3-4. – P. 21–28. https://doi.org/10.26577/phst2024v11i2b03

42. Solodovnik A. A., Leontyev P. I., Useinov B. M., Kadyrmin A. D., Zyryanov R. O. Application of electronic receivers for recording infrared images of celestial phenomena at the CAR of the NKU // Physical Sciences and Technology. – 2023. – Vol. 10, Nos. 1-2. – P. 50–57. https://doi.org/10.26577/phst.2023.v10.i1.07

43. Saitov E. B., Zikrillayev N. F., Ayupov K. S., Yuldoshev I. A. Determination of the resistance of external parameters to the degradation of the parameters of silicon photocells with input nickel atoms // Physical Sciences and Technology. – 2022. – Vol. 9, Nos. 1-2. – P. 30–36. https://doi.org/10.26577/phst.2022.v9.i1.04

44. Al-Aish A. K. T., Amjed Kamil H. A new system to the spectroscopy analysis with multiple X-ray of free electron laser // Physical Sciences and Technology. – 2024. – Vol. 11, Nos. 3-4. – P. 86–91. https://doi.org/10.26577/phst2024v11i2b010

Information about authors:

Zhexebay Dauren, PhD is a Researcher at the School of Electronics and Information, Northwestern Polytechnical University (Xi'an, China), e-mail: Dauren.zhexebay@gmail.com

Skabylov Alisher, PhD is d Researcher at the School of Electronics and Information, Northwestern Polytechnical University (Xi'an, China), e-mail: Skabylov.alisher@gmail.com

Turlykozhayeva Dana, PhD is a Senior researcher at the School of Electronics and Information, Northwestern Polytechnical University (Xi'an, China) e-mail: Turlykozhayeva.dana @gmail.com

Bolysbay Aslan, BS in Physics is a Researcher at the School of Electronics and Information, Northwestern Polytechnical University (Xi'an, China), e-mail: Bolysbay.aslan@kaznu.edu.kz

Turmaganbet Ulpan (corresponding author), MS in Physics is a Researcher at the School of Electronics and Information, Northwestern Polytechnical University (Xi'an, China), e-mail: uturmaganbet@gmail.com

Namazbayev Timur, MS in Physics is a Senior researcher at the School of Electronics and Information, Northwestern Polytechnical University (Xi'an, China), e-mail: namazbayev.timur@gmail.com

Mingliang Tao, PhD is a Professor at the School of Electronics and Information, Northwestern Polytechnical University (Xi'an, China), e-mail: mltao@nwpu.edu.cn

CONTENTS